

KATHOLIEKE UNIVERSITEIT
LEUVEN

**Arenberg Doctoral School of Science, Engineering & Technology**
Faculty of Engineering
Department of Electrical Engineering (ESAT)

# Data-Driven Multimodal Signal Processing With Applications To EEG-fMRI Fusion

**Bogdan MIJOVIĆ**

Dissertation presented in partial
fulfillment of the requirements for
the degree of Doctor
in Engineering

May 2012

# Data-Driven Multimodal Signal Processing with Applications To EEG-fMRI Fusion

**Bogdan MIJOVIĆ**

Jury:
Prof. dr. Paul Sas, chairman
Prof. dr. Sabine Van Huffel, promotor
Prof. dr. Johan Wagemans
Prof. dr. Marc Moonen
Prof. dr. Wim Van Paesschen
dr. Maarten De Vos
Prof. dr. Marc Van Hulle
Prof. dr. Danilo Mandić
(Imperial College, The United Kingdom)
Prof. dr. Dejan Popović
(Aalborg University, Denmark)

Dissertation presented in partial fulfillment of the requirements for the degree of Doctor in Engineering

May 2012

© KU Leuven – Faculty of Engineering
Arenbergkasteel, B-3001 Leuven-Heverlee, Belgium

Alle rechten voorbehouden. Niets uit deze uitgave mag worden vermenigvuldigd en/of openbaar gemaakt worden door middel van druk, fotokopie, microfilm, elektronisch of op welke andere wijze ook zonder voorafgaande schriftelijke toestemming van de uitgever.

All rights reserved. No part of the publication may be reproduced in any form by print, photoprint, microfilm or any other means without written permission from the publisher.

Legal depot number D/2012/7515/46
ISBN number 978-94-6018-510-6

*Knowledge is in the end based on acknowledgement.*

*Ludwig Wittgenstein*

# Acknowledgments

However weird it sounds, this page will be the mostly read page of my thesis. See? You are reading it now! But, since no success is possible without support, let's start with acknowledging it.

There are so many people around that I owe my thanks to. However, I have to start with one, so let it be my supervisor, Sabine Van Huffel. There are several things I have to thank her for. First of all, she had enough trust to let me come to this group and start my research. Second, I was not constrained by any means, and I was allowed to explore and direct my research to any field I currently felt interested in. Finally, the organizations of her social events brought me closer to the people from the group, I had difficulties to fit in in the first place.

When mentioning people who are responsible for my arrival to Belgium, I cannot leave out the coauthors of my first journal paper I wrote back there in Belgrade, at the faculty of electrical engineering, professors Dejan and Mirjana Popović. Also, they are responsible for my first academic steps, and it's their guilt mostly that I ended up in science. Thanks for the great time I had in your lab BMIT, where I also finished my master thesis.

Thereafter, special thanks go to my closest collaborators and coauthors. To mention a few, I will start with Katrien Vanderperren. Well, everybody is already well aware that most of my journal papers have passed a thorough rewriting from her side. Besides, thanks for the great atmosphere in the office, which you managed to achieve, together with Bori, of course. Finally, thanks to both of you for great dinners, I hope they are not going to stop right now. Dikke merci, mates!

I thank to Maarten De Vos, for all the difficult times he gave me with his both positive and (mostly) negative critique of my work. Most of the "fine" works, and additional experiments in my work started from his ideas, believes and disbelieves. Also, thanks for all the unselfish discussion which you face each time you come to Leuven for a weekend. I know that in those moments you feel more like having fun and drinking beer - Sorry for that.

Last, but not the least, Ivan Gligorijević, my flatmate, and coauthor. Thanks for all the time we spent together, for all the discussion, parties, good times-bad times... you know. Thanks for standing all the moments when I don't give up on my point of view, although I might have been wrong. However, I am never wrong, just maybe not always fully right ◡̈.

On the professional side, I owe my thanks to psychologists who had enough patients to talk to the guy who speaks another scientific language. It was a difficult time in the beginning, when I was lost in space with all these neuroscience stuff. These thanks go especially to Peter Stiers, Johan Wagemans, Bart Machilsen, and, of course, Nikolay Novitskiy. I am very happy to have spent time in discussion with you guys, I learned A LOT!

Further on, I thank my jury to reading the thesis. I also appreciate all the very useful comments, which can also serve as directions to my further research. Thanks for the nice discussion we had during my preliminary defence, and for managing to synchronize your agendas, so that everybody was allowed to present on the preliminary defence.

Then, I owe greatest gratitude to all the ex-YU guys from Leuven, Brussels, Belgrade and all around the world I spent my free time with. I can't express how lucky I am to be surrounded with such a group of great people! Thanks for all the basketball games, travels, coffee, beers, teretana, bleja. If I wouldn't have had all this great and fulfilled free time, it would've been so much harder to focus on my doctorate when it's needed. Well, possibly I could have given up. So, guys (and girls, of course) - Macani, hvala onoliko. Baš ste likovi.

I also thank my mother and father for their unconditional support. Mama i tata hvala na podršci i što često verujete u smisao svega što je besmisleno... Then, Pavle and Ksenija, well, 20 years of growing up... there's too much to say, so only a couple of words won't work. One of the most important things I learned is how to concentrate fast and deeply in a really fuzzy environment. Still I would like to mention my aunt, Seka, who took apparently a good care of me when I was a child, ljubi tetka čedo svoje ◡̈.

Sofija influenced my development as a person in a particular way, teaching me a couple of ultra-important facts, like "You're stupid to worry now, because everything is gonna work out just fine". It's probably not the best advice in the world in general, but it indeed *works out just fine* for me. And a couple of them more, like "Lako ćemo" and "Srediće se". Great, no? Also, thanks for all the difficult moments, because, you know, it helps one grow stronger ◡̈.

It was my great pleasure to meet Marina and Bane - better known as najveći carevi Leuvena. There's so much to thank them for. I don't even know where to start. Food - Lunches, dinners, bbq's, chikcken wings (home made and burned to perfection - oh, so great), birthday parties, all the other parties... Thanks for all

the help in any kind of all the weird situations I am capable of ending up in. Well, thanks for even being willing to listen about it in the first place. Thanks for all the support and for being there when I needed somebody, especially in the first months of my stay in Belgium, when nobody else was around.

Na kraju, posvetio bih ovu tezu babi i dedi, iako bi oni više voleli da sam lekar ili direktor elektrane u Obrenovcu.

Bogdan Mijović
Leuven, May 2012

# Abstract

Most cognitive processes in the brain are reflected through several aspects simultaneously, allowing us to observe the same process from different biological phenomena. The diverse nature of these biological processes suggests that a better understanding of cerebral activity may be achieved through multimodal measurements. One of the possible multimodal brain recording settings is the combination of electroencephalography (EEG) and functional magnetic resonance imaging (fMRI), which is one of the main topics of this thesis.

Two groups of EEG-fMRI integration approaches are possible. The first group, commonly called model-based techniques, are very popular due to the fact that the results from such analyses confirm or disprove a specific hypothesis. However, such hypotheses are not always available, requiring a more explorative approach to analyze the data. This exploration is possible with the second group of approaches, the so-called data-driven methods.

The data-driven methods used in this work are based on blind source separation (BSS) and, more specifically, on independent component analysis (ICA) techniques. Besides the fusion of EEG and fMRI data, also the application of ICA to several types of single-channel and two-channels signals is studied. However, to be able to use ICA for these specific applications, modifications to the algorithm or to the way the data are used as input, are needed.

Physiological signals are often measured from only one or a few electrodes, like, e.g., the electromyogram (EMG) measuring muscle activity. One of the limitations of ICA, however, is that it can extract independent components only when the number of sources embedded in the data is lower than, or equal to the number of recorded channels. In case of single-channel signals, this assumption is not satisfied. To solve this issue, in the first part of this thesis, we propose the use of empirical mode decomposition (EMD) to decompose a single-channel signal into a set of oscillatory modes, after which ICA is used to extract the underlying components. This method can also be extended to bivariate (or even multivariate) signals and is illustrated and validated in this thesis on data from baby cries, EEG and EMG data.

The second part of this work is devoted to the application of ICA to EEG-fMRI fusion. EEG and fMRI data are structured together into one matrix and then jointly decomposed with ICA. This so-called JointICA algorithm [23] is first thoroughly validated on data from a simple visual detection task. The results of these analyses are compared to literature, and different aspects of the algorithm's performance are discussed.

JointICA is then used in a more complicated setting - the study of perceptual grouping. More specifically, the neural mechanisms of contour integration, i.e., the grouping of local edges into global contours are investigated. A modification of the algorithm is also proposed, allowing the comparison of different task conditions presented during the experimental paradigm. This allows to pinpoint detailed spatio-temporal differences and similarities across the presented conditions.

# Samenvatting

De meeste cognitieve functie in de hersenen kunnen op verschillende manieren bestudeerd worden. De diversiteit van biologische processen gerelateerd aan dezelfde cognitieve activiteit suggereert dat een dieper begrip van hersenactiviteit kan bekomen worden met multimodale metingen. Een van de mogelijkheden is de combinatie van electroencephalography (EEG) en functionele magnetische resonantie beeldvorming (fMRI), dat een van de belangrijkste thema's was in deze thesis.

Twee grote groepen aan methoden voor EEG-fMRI integratie kunnen onderscheiden worden. De eerste groep, vaak de model-gebaseerde techniekengenoemd, zijn zeer populair doordat de resultaten van zulke analyse direct een welbepaalde hypothese kunnen bevestigen of ontkennen. Echter, zulke hypothese is niet altijd mogelijk, en wanneer het niet mogelijk is, is een meer exploratieve benadering van data-analyse nodig. Zulke exploratie is mogelijk met de tweede groep methode, de zogenoemde data-gedreven methoden.

De data-gedreven methoden die in dit werk gebruikt zijn, zijn gebaseerd op blinde bron schatting (BSS) technieken en, meer bepaald, op onafhankelijke component analyse (ICA). Naast de integratie van EEG en fMRI data, werd ook de toepassing van ICA voor verschillende een- en twee-kanaals signalen bestudeerd. Echter, om ICA voor deze specifieke toepassingen te gebruiken, moeten wijzigingen aangebracht worden aan het algoritme of aan de manier waarop de inputdata gebruitk wordt.

Physiologische signalen worden vaak slechts met behulp van een of enkele electrode opgemeten, zoals bijvoorbeeld het electromyogram (EMG) dat spieractiviteit opmeet. Een van de beperkingen van ICA is dat het enkel onafhankelijke componenten kan schatten wanneer het aantal bronnen in de data kleiner is dan, of gelijk aan, het aantal meetkanalen. Voor eenkanaals signalen geldt deze hypothese niet. Om dit probleem om te lossen, stellen we in het eerste deel van de thesis het gebruik van empirische mode ontbinding (EMD) voor om eenkanaals signalen te ontbinden in een aantal oscillerende modes, waarna ICA kan gebruikt worden om de onderliggende componenten te schatten. De methode kan ook uitgebreid worden naar bivariate (en zelfs mutlivariate) signalen en is geïllustreerd aan de

hand van baby-schreeuwen, EEG en EMG data.

Het tweede deel van het werk werd toegewijd aan de toepassing van ICA voor EEG-fMRI integratie. EEG en fMRI data kunnen in een gegevensmatrix gestructureerd worden, en beide modaliteiten kunnen dan samen ontbonden worden met behulp van ICA. Dit zogenoemde jointICA algoritme [23] werd eerst grondig gevalideerd aan de hand van data opgemeten tijdens een eenvoudige detectie taak. De resultaten van deze analyses werden aan de hand van de literatuur gevalideerd en verschilllende aspecten in verband met de performatie van het algoritme werden bestudeerd.

Daarna werd jointICA voor een ingewikkelder probleem gebruikt - de studie van perceptuele groepering. Meer precies, de neuronale mechanismen voor contour integratie, of - nog anders gezegd, de groepering van locale randoriëntering in globale contouren werden bestudeerd. Een aanpassing aan het jointICA algoritme werd ook voorgesteld, dat de vergelijking van verschillende taakcondities tijdens experimentele paradigmas toelaat. Dit nieuwe algoritme laat ons toe in detail de spatiotemporele gelijkenissen en verschillen tussen verschillende condities te bestuderen.

# Резиме

Већина когнитивних процеса у људском мозгу се рефлектује на неколико начина, што нам омогућава да посматрамо један исти процес кроз различите биолошке феномене. Различитосто ових процеса указује да се мождана активност може боље пратити уз помоћ мултимодалних мерења, где се неколико физиолошких сигнала посматра у истом временском периоду. Једна од могућих комбинација мултимодалних мерења је симултано мерење електроенцефалограма (ЕЕГ) и функционалне магнетне резонанце (фМР). Изучавање овог комбинованог мерења је једна од основних тема ове тезе.

Постоје две групе могућих приступа интеграцији ЕЕГ-а и фМР-а. Прву групу представљају тзв. тхенике базиране на моделовању. Оне су популарне из разлога што резултати из овакве анализе могу да докажу или оповргну почетну хипотезу. Међутим, проблем настаје када немамо довољно информација о моделу који желимо да испитујемо, па нам је, према томе, неопходан више експлоративни приступ, који нас не ограничава условима које поставља модел. Овакав истраживачки приступ је могућ коришћењем друге групе интеграционих техника, тзв. подацима-вођене методе.

Подацима-вођене методе које се користе у овој тези су технике "слепог издвајања изворних сигнала" (Blind Source Separation (BSS)). Ове методе подразумевају да је мерени сигнал добијен суперпозицијом изворних сигнала, и покушава да раздовоји мерени сигнал на те саставне компоненте. Прецизније, користе се методе "анализе независних компонената" (Independent Component Analysis (ICA)). Осим за потребе интеграције (фузије) ЕЕГ и фМР сигнала, примена ICA метода на неколико типова једноканалних и двоканалних мерења је анализирана у овој тези. Међутим, да бисмо користили ICA методе у ове сврхе, модификација алгоритма је неопходна у смислу промене облика улазног сигнала.

Физиолошки сигнали се често снимају само са једном, или малим бројем електрода (нпр. електромиограм (ЕМГ) који мери мишићну активност). Међутим, једно од основних ограничења ICA методе је у томе што она подразумева да је број изворних сигнала, чијом је суперпозицијом мерени

сигнал добијен, мањи или једнак броју мерених сигнала. У случају једноканалних мерења, ова претпоставка очигледно не може бити задовољена. Да бисмо решили овај проблем, у првом делу ове тезе је предложено да се емпиријска декомпозиција у осцилаторне модове (Empirical Mode Decomposition (EMD)) користи да разложи улазни сигнал. ICA се затим примењује да издвоји саставне компоненте. Овај метод може бити проширен за употребу на двоканалним и вишеканалним сигналима. Валидација оваквог приступа је извршена на ЕЕГ и ЕМГ сигналима, као и неким вокалним сигналима.

Други део ове тезе је посвећен примени ICA алгоритама на фузију ЕЕГ и фМР сигнала. У овом приступу, ЕЕГ и фМР сигнали су уклопљени у једну заједничку матрицу, а потом су заједно декомпоновани, користећи ICA алгоритме. Прво је изведена темељна валидација овог приступа, који се зове "JointICA" [23] на примеру једноставног експеримента визуалне детекције. Резултати добијени у овој студији су потом упоређени са резултатима из литературе добијених стандардним техникама. Поред тога, различити аспекти перформанси овог алгоритма су испитиване и дискутоване.

JointICA је затим употребљена у компликованијој експерименталној поставци - перцепционо груписање. Испитивани су неурални механизми интеграције контуре, односно груписање локалних ивица у глобалне контуре. Предложена је и модификација JointICA алгоритма, која дозвољава упоређивање различитих експерименталних услова, током експерименталне парадигме. Ова модификација омогућује истицање детаљних просторно-временских разлика и сличности између различитих експерименталних поставки.

# Contents

**Acknowledgments** i

**Abstract** v

**Samenvatting** vii

**Резиме** ix

**Contents** xi

**1 Introduction** 1

1.1 Physiological Signals . . . . . 1

1.2 Blind Source Separation . . . . . 2

1.2.1 Background . . . . . 2

1.2.2 BSS approaches . . . . . 5

1.2.3 Single-Channel BSS techniques . . . . . 6

1.2.4 BSS in multimodal applications . . . . . 7

1.2.5 Multidimensional BSS . . . . . 7

1.3 Aims of the thesis . . . . . 8

1.4 Chapter-by-chapter overview . . . . . 9

1.5 Personal Contributions . . . . . 10

**2 Decomposition Techniques: Mathematical Background and Application 13**

2.1 1-D Decomposition Techniques . . . . . 13

2.1.1 Dictionaries and Atoms . . . . . 14

2.1.2 Empirical Mode Decomposition . . . . . 16

2.2 Application of EMD to vocal signals (phonetic baby cry) . . . . . 18

2.2.1 Introduction to baby cry signals . . . . . 18

2.2.2 Materials and Methods . . . . . 20

2.2.3 Results . . . . . 21

2.2.4 Discussion . . . . . 24

2.2.5 Conclusion on the Baby Cry study . . . . . 26

2.3 2-D Decomposition Techniques . . . . . 27

2.3.1 Principal Component Analysis (PCA) . . . . . 27

2.3.2 Independent Component Analysis (ICA) . . . . . 27

2.3.3 Multivariate Empirical Mode Decomposition . . . . . 33

2.4 Conclusion . . . . . 34

**3 Combining ICA with EMD for Single-Channel Decomposition 37**

3.1 EEMD-ICA for Source Separation from Single-Channel Recordings 37

3.1.1 Introduction . . . . . 37

3.1.2 Methods . . . . . 39

3.1.3 Simulations . . . . . 43

3.1.4 Real-life application of EEMD-ICA . . . . . 53

3.1.5 Conclusion . . . . . 56

3.2 Generalization of the EEMD-ICA algorithm to 2-Channel Data . . 57

3.2.1 Methods . . . . . 57

3.2.2 Results . . . . . 58

3.2.3 Discussion . . . . . 59

3.3 Conclusion . . . . . 61

**4 Introduction to EEG-fMRI Integration 63**

4.1 Introduction . . . 63
4.2 Visual system . . . 64
4.3 EEG signals . . . 66
4.3.1 Typical EEG rhythms and artifacts . . . 68
4.3.2 Event-related potentials . . . 69
4.4 fMRI signals . . . 70
4.4.1 Basis of magnetic resonance . . . 71
4.4.2 Acquisition of anatomical images . . . 74
4.4.3 Acquisition of functional images . . . 75
4.5 EEG Preprocessing . . . 76
4.5.1 Gradient-artifact removal . . . 76
4.5.2 Ballistocardiogram artifact . . . 77
4.5.3 Algorithms for the BCG-artifact removal . . . 78
4.6 fMRI Preprocessing . . . 83
4.6.1 Data Preparation . . . 83
4.6.2 Statistical Analysis . . . 85
4.7 EEG-FMRI Integration . . . 86
4.7.1 Spontaneous and task-related activity in fMRI . . . 87
4.7.2 Coupling of spontaneous activity in EEG and fMRI . . . 88
4.7.3 Task-related EEG-fMRI coupling . . . 89
4.8 Conclusion . . . 94

**5 EEG-fMRI Data Acquisition 95**

5.1 Simultaneous acquisition of EEG and fMRI . . . 95
5.1.1 Equipment . . . 95
5.1.2 Data acquisition parameters . . . 97
5.2 Experimental data . . . 98

5.2.1 Task paradigms . . . . . 99
5.2.2 Overview of acquired data . . . . . 101
5.3 Conclusion . . . . . 103

**6 JointICA for EEG-fMRI Fusion 105**

6.1 Introduction . . . . . 106
6.1.1 Simultaneous EEG-fMRI . . . . . 106
6.1.2 Integration approaches . . . . . 106
6.1.3 The present study . . . . . 107
6.2 Materials and Methods . . . . . 108
6.2.1 Tasks . . . . . 109
6.2.2 Data acquisition . . . . . 109
6.2.3 EEG processing . . . . . 109
6.2.4 fMRI processing . . . . . 109
6.2.5 JointICA . . . . . 110
6.2.6 ICASSO Analysis . . . . . 111
6.2.7 Evaluation Strategies . . . . . 112
6.3 Results . . . . . 114
6.3.1 Application of JointICA – Simultaneously Recorded Data . 114
6.3.2 Application of JointICA –Non-Simultaneous Recordings . . 120
6.3.3 JointICA Experiment – Investigating the Influence of the ICA Algorithm . . . . . 123
6.3.4 JointICA Experiment – Central Linking Hypothesis and Randomization . . . . . 125
6.3.5 JointICA Experiment - Robustness and Consistency analysis 127
6.4 Discussion . . . . . 133
6.4.1 Application of JointICA – Simultaneously Recorded Data . 133
6.4.2 Application of JointICA –Non-Simultaneous Recordings . . 134

6.4.3 JointICA Experiment – Investigating the Influence of the ICA Algorithm . . . 135
6.4.4 JointICA Experiment – Central Linking Hypothesis and Randomization . . . 137
6.4.5 JointICA Experiment – Robustness and Consistency analysis 138
6.5 Conclusion . . . 139

**7 A simultaneous EEG/fMRI Study on Local and Global Integration of Visual Information 141**

7.1 Introduction . . . 141
7.2 Methods . . . 144
7.2.1 Participants . . . 144
7.2.2 Task Paradigm . . . 144
7.2.3 Electrophysiology . . . 146
7.2.4 Functional MRI . . . 147
7.2.5 Data analysis part 1: Correlation Study . . . 148
7.2.6 Data analysis part 2: JointICA . . . 148
7.2.7 Data analysis part 3: Modified JointICA . . . 149
7.3 Results . . . 150
7.3.1 Visualization of Employed EEG and fMRI data . . . 150
7.3.2 Correlations . . . 150
7.3.3 JointICA . . . 151
7.3.4 Modified JointICA . . . 152
7.4 Discussion . . . 161
7.5 Conclusion . . . 162

**8 Conclusion and Future Work 163**

8.1 EMD-based source separation techniques . . . 163
8.2 BSS techniques for multimodal EEG-fMRI fusion . . . 165

8.3 Future work in the single-trial EEG-fMRI area . . . . . 166

**Bibliography** **171**

**List of Publications** **189**

**Curriculum Vitae** **193**

# Chapter 1

# Introduction

*This thesis focuses on the application of so-called Blind Source Separation (BSS) techniques to single-channel signals on the one hand, and multimodal, multi-channel signals on the other hand. To understand the results in the following chapters, this chapter first introduces some of the physiological signals that are used in the presented analyses. Afterwards, a general introduction to the BSS concept is provided. This concept is subsequently extended to both single-channel and multimodal data and also higher-order techniques are introduced. Finally, the aims of this thesis, a detailed chapter-by-chapter overview and personal contributions are listed.*

## 1.1 Physiological Signals

Physiological signals are signals that are generated by the human body and give an idea about the functioning of various physiological systems. In this section, the physiological signals that are used in this thesis, are introduced.

Many of these signals are electrophysiological, meaning that they provide a measure for the electrical activity of the physiological system under study. This electrical activity is typically generated by nerve or muscle cells, and can be measured by placing electrodes on specific locations on the body surface. Depending on the position, the recorded signals can originate from muscles, the heart, brain and so on. According to their origin, they can be divided in several categories, three of which are used in this thesis:

- The **electromyogram (EMG)** measures the electrical activity of the muscles (except the heart), which is caused by the electrical potential

generated in activated muscle cells. The signals can be analyzed to detect physiological abnormalities, activation level or to analyze the biomechanics of human or animal movement.

- The **electrocardiogram (ECG)** is a measure of the electrical activity of the heart. It is usually recorded from the chest of the patient (subject), but it can also be visible in other recorded signals (like EMG), in which case it is considered as an artifact (a signal which is not of interest).
- The **electroencephalogram (EEG)** allows recording the electrical activity of brain cells (neurons), by placing a number of electrodes on the scalp. It can provide information about spontaneous brain processes, as well about the brain's reaction to specific environmental stimuli. This evoked activity is called the event-related potential (ERP) and will be intensively used in this thesis.

Apart from the above-mentioned electrophysiological signals, another physiological signal will be used in this thesis, namely **functional magnetic resonance imaging (fMRI)**. This signal is measured with a magnetic resonance scanner and allows the identification of activated brain regions based on changes in blood oxygenation. More details about this method can be found in Chapter 4.

## 1.2 Blind Source Separation

### 1.2.1 Background

In our every-day experience, we are often faced with the problem where a number of stimuli (visual, auditory or others) are presented to us, mixed together, but where we want to focus on only one of them. The human brain is a very good signal processing tool in this regard. We can easily listen to several voices, for example, and at the same time follow the story of only one of them, or change our visual focus to the objects we are interested in. In the signal processing community, this problem of separating different sources from a mixture is called the Blind Source Separation (BSS) problem. It is usually explained through the "cocktail party problem", illustrated in Fig. 1.1. In this problem, several people are speaking at the same time during a cocktail party. This conversation is recorded with a number of sensors (microphones, in this case), and the goal is to isolate the speech coming from each person separately, without disturbances coming from the others. This process of separating the signals is called the demixing process.

This problem can be easily generalized to other problems present in nature. For example, Fig. 1.2 represents the recording of a set of EEG signals. The recorded

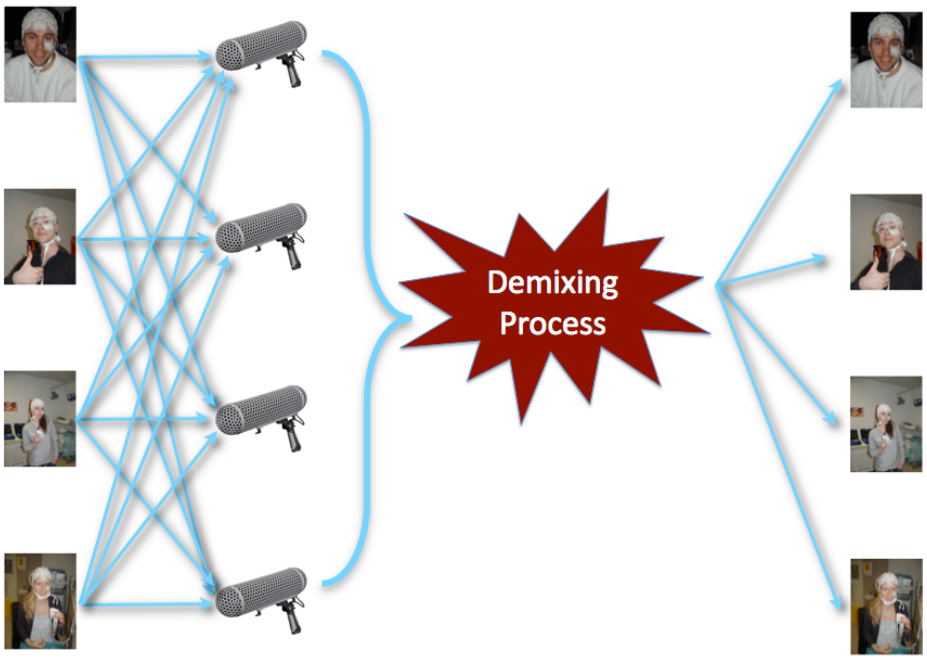


Figure 1.1: Cocktail Party Problem: A number of persons is speaking at a cocktail party at the same time. The conversation of all the people together is recorded by a number of sensors (microphones). The BSS problem comes down to separating this mixed speech into the constituent speech of every person separately.

signals are generated by a number of electrical sources (dipoles) hidden inside the brain, but, unfortunately, represent a mixture of these dipole signals, propagated through the gray matter, skull and scalp. The goal of BSS in this case, would be to separate the recorded EEG data into sources, corresponding to individual dipoles.

In mathematical terms, this problem can be described as follows. Let us assume that the data consist of a number of variables that we have observed together. Let us denote the number of variables by $n$ and the number of observations by $T$. We can then denote the data by $x_i(t)$, where the indices take the values $i = 1..n$ and $t = 1..T$. The dimensions $n$ and $T$ can be very large. Now, we want to find the function mapping variables from an $n$-dimensional space (we call the signals in this space $x$) to an $m$-dimensional space (signals $s$), such that the transformed variables give information on the data that are otherwise hidden in the original dataset. In other words, the transformed variables should be the underlying components that describe the essential structure of the data. Ideally, these sources describe different physical phenomena that were involved in the signal generation process. In this

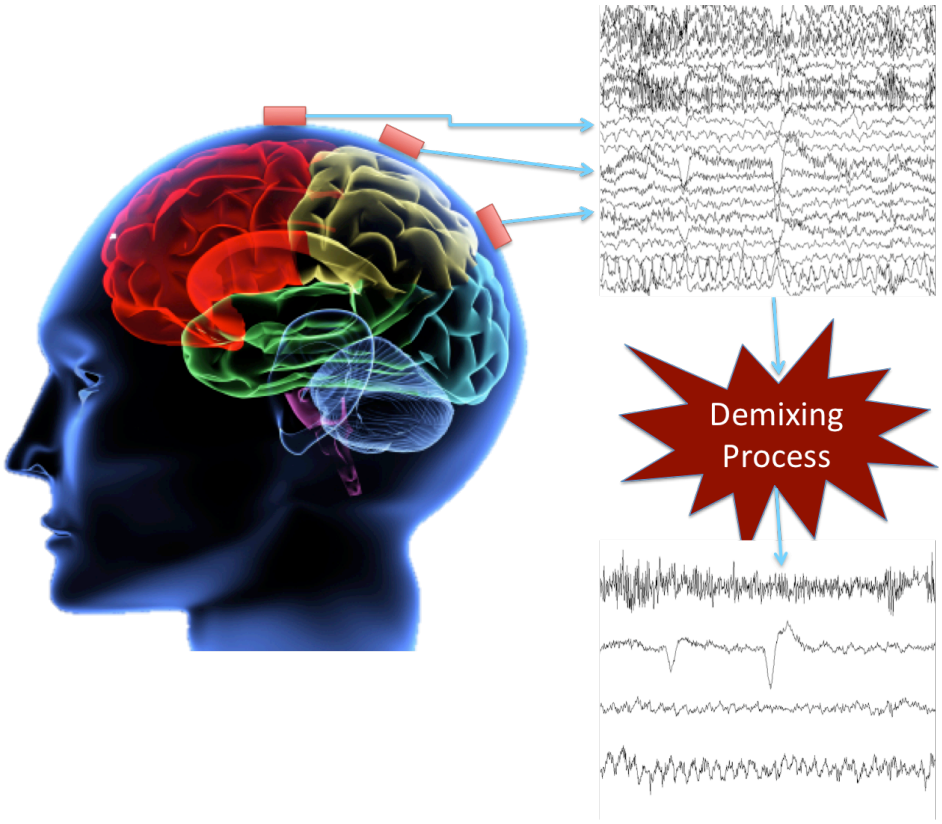


Figure 1.2: Illustration of BSS problem on EEG data. A number of EEG signals are recorded from the scalp. Their underlying sources are extracted (demixing process) with independent component analysis (ICA - see Section 1.2.2). The resulting components represent different physiological sources, more specifically muscle activity (first component), eye blinks (second) and epileptic seizure activity (fourth).

thesis, only linear mappings are explored, which means that the $n$ recorded signals are obtained as linear combinations of the $m$ sources (see Eq. 1.1).

$$\begin{pmatrix} x_1(t) \\ x_2(t) \\ \vdots \\ x_n(t) \end{pmatrix} = \mathbf{A} \begin{pmatrix} s_1(t) \\ s_2(t) \\ \vdots \\ s_m(t) \end{pmatrix} \tag{1.1}$$

where the elements of the matrix $\mathbf{A}$ represent the coefficients that "mix" the sources $s_j$ into the recorded signals $x_i$. This matrix $\mathbf{A}$ is therefore called the mixing matrix.

For the sake of simplicity, we will demonstrate here the problem assuming only three different sources. Let $x_1(t)$, $x_2(t)$ and $x_3(t)$ be the observed signals, and $s_1(t)$, $s_2(t)$ and $s_3(t)$ be the original (physical) sources. As mentioned before, the $x_i(t)$ can be represented as a linear mixture of sources $s_i(t)$ in the following way:

$$\begin{aligned} x_1(t) &= a_{11}s_1(t) + a_{12}s_2(t) + a_{13}s_3(t) \\ x_2(t) &= a_{21}s_1(t) + a_{22}s_2(t) + a_{23}s_3(t) \\ x_3(t) &= a_{31}s_1(t) + a_{32}s_2(t) + a_{33}s_3(t) \end{aligned} \tag{1.2}$$

The goal of BBS is then to find the original sources which construct these mixtures. However, since we have only limited knowledge about the physical system under study, both the sources $s_j$ and the coefficients $a_{ij}$ are unknown. As such, BSS aims at finding an *unmixing* matrix $\mathbf{W}$ for which $\mathbf{W} = \mathbf{A}^{-1}$ with coefficients $w_{ji}$, such that we can separate the $s_j$ as in Eq. 1.3.

$$\begin{pmatrix} s_1(t) \\ s_2(t) \\ s_3(t) \end{pmatrix} = \mathbf{W} \begin{pmatrix} x_1(t) \\ x_2(t) \\ x_3(t) \end{pmatrix} \tag{1.3}$$

### 1.2.2 BSS approaches

As explained above, both the matrix $\mathbf{A}$ and the sources $s_j$ in Eq. 1.1 are unknown. As such, the problem presented in Eq. 1.1 is ill-posed and cannot be solved without imposing additional assumptions. Several assumptions in this context are possible, of which two will now be shortly explained.

**Orthogonality** One of the principles to extract sources from recorded signals is to impose orthogonality between the extracted sources. One such technique is called principal component analysis (PCA) [66, 153]. It tries to explain as much information as possible with only a couple of components. In other words, this technique tries to find one variable describing as much of the signal variability as possible, then the next one is orthogonal to the first variable, and describes as much as possible of the residual after extraction of the first variable, etc. Therefore, this method is also often used as a dimensionality reduction method, in which case only several first variables are retained, while all the rest are replaced by zeros.

**Statistical Independence** Another assumption that is commonly used (as also in this thesis) is the assumption of statistical independence. This means that we extract sources of which the values of any of the source components give no information at all on the values of any other component. In reality, perfect statistical independence is not easily obtained, so we try to maximize the independence between the sources. BSS methods used for this purpose are called independent component analysis (ICA) approaches [91], and are explained in more detail in Chapter 2. An illustration of the result of ICA applied to EEG data is also given in Figure 1.2.

### 1.2.3 Single-Channel BSS techniques

From Eq. 1.1 and from Figs. 1.1 and 1.2, it seems that multiple sensors are needed to record the mixed signals necessary for solving the BSS problem (based on, e.g., statistical independence like in ICA). In fact, it is most commonly assumed that the number of sources is always lower than or equal to the number of recorded mixtures. Otherwise, the linear system in Eq. 1.1 would be ill-posed.

However, in some cases the number of observed channels can be lower than the number of underlying sources. In an extreme case, the number of measured signals is only 1. EMG, e.g., can for practical reasons often only be measured from one electrode. If such EMG signal would then be corrupted by specific artifacts (e.g., ECG), information from only one channel would be available to remove these artifacts. Therefore, it would be interesting if we could adapt the BSS techniques to be used for this purpose, since, as mentioned before, these methods are originally intended for multi-channel signals. In order to obtain such multi-channel signals, several decomposition techniques exist to map the 1-dimensional (1D) data into a 2-dimensional (2D) space.

The two techniques we use further for this purpose are Wavelet analysis and Empirical Mode Decomposition. Wavelet analysis is a technique that allows decomposing a signal in different frequency bands. More specifically, one-dimensional wavelets map a single-channel signal into a certain wavelet dictionary, composed of scaled and shifted versions of the so-called mother wavelet. The coefficients obtained for each scale will then constitute the rows of the input (measured) matrix. This approach will be further explained in Chapters 2 and 3.

Another possible method for expanding a single channel signal into a multi-channel input matrix is the recently introduced Empirical Mode Decomposition [89]. This technique maps single channel data into the space of so-called Intrinsic Mode Functions (IMF), which describe the frequency content of the signal. Similarly to wavelets, each IMF can be used as one row of the input matrix for the BSS algorithm. This approach will also be further explained in Chapters 2 and 3.

### 1.2.4 BSS in multimodal applications

Understanding the processes that are going on in the human body, requires the combination of several types of observations. For this reason, since several years, biomedical signal processing research started to focus on multimodal approaches. One such multimodal approach, especially used in neuroscience research, is the combination of electroencephalography (EEG) and functional magnetic resonance imaging (fMRI). The non-invasive character of these two modalities makes their combination not only harmless and painless, but also especially suited for widespread research in both clinical and experimental applications. Moreover, the complementarity between the high temporal resolution of the EEG and the high spatial resolution of the fMRI, allows obtaining a more complete picture of the processes under study.

To analyze the combination of these two datasets, several BSS techniques have already been proposed. A detailed overview of these approaches will be given in Chapter 4, but in this thesis, special attention is given to the so-called JointICA method. The general principle of this method is to concatenate the corresponding EEG and fMRI data per subject, and then include the data from several subjects together in one matrix. Subsequently, ICA is applied to these data in order to jointly extract sources from both modalities [23]. The JointICA approach is better elaborated in Chapters 6 and 7.

### 1.2.5 Multidimensional BSS

The BSS approaches and modifications presented in the previous sections, only allow source extraction from two-way data. This property, however, poses a certain limitation when applying these BSS approaches to physiological datasets, since such data often incorporate more than two modes. In the case of EEG recordings, for example, data are acquired from different electrodes (spatial mode), at different time instants (temporal mode), in response to different stimuli (trial mode), from different subjects (subject mode), etc. To preserve this multi-way structural information in the analyses, higher-order arrays (or tensors) can be used to store the data and higher-order decomposition techniques should be applied. One such higher-order approach is the Canonical Polyadic Decomposition (CPD), also known as Canonical Decomposition or Parallel Factor Analysis (PARAFAC) [101]. This method decomposes three- or higher-order tensors into a set of distinct atoms, which ideally represent different physiological sources. PARAFAC has the advantage of being unique under very mild conditions and has already been applied in several biomedical applications (e.g., [56, 51]). PARAFAC has not been explicitly used for the results presented in this thesis, but is introduced here to clarify some of the suggestions made in Chapter 8. In addition, it also has been successfully applied to some of the data presented in Chapter 5 as described in [186].

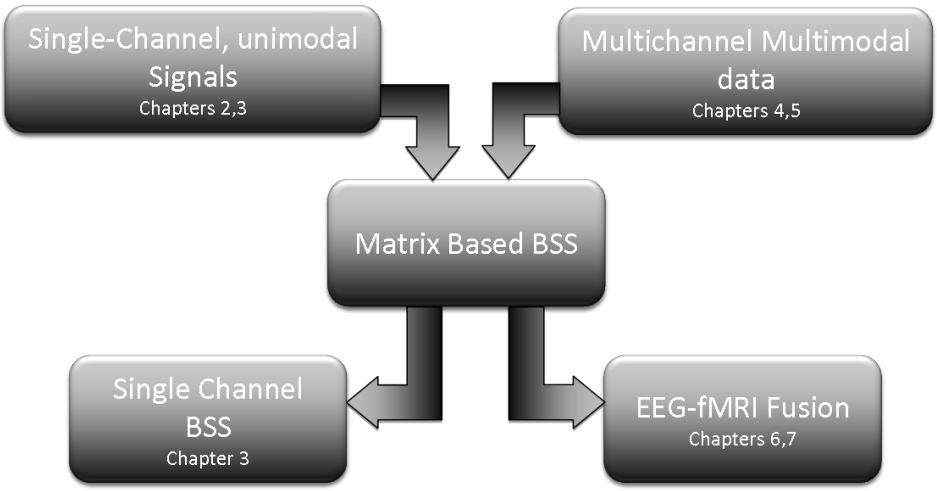


Figure 1.3: Outline of the thesis. On the one hand, single-channel blind source separation is solved by mapping the single-channel data into a 2D space, and then solving the matrix-based BSS problem. On the other hand, the multimodal multi-channel BSS problem is solved by arranging the data into a 2D matrix space, after which the matrix-based BSS problem is solved.

## 1.3 Aims of the thesis

This thesis focuses on matrix-based blind source separation techniques. These techniques are used to solve two more general decomposition problems:

1. Blind Source Separation of single-channel signals
2. Multimodal Multivariate Blind Source Separation for EEG-fMRI fusion

The single-channel BSS issue is solved in Chapter 3 by first expanding the single-channel data into matrix space, and then solving the BSS problem (see Fig. 1.3).

The multimodal EEG-fMRI fusion is achieved through composing one matrix that contains both EEG and fMRI data, and then using BSS algorithms to decompose the resulting matrix. This method is explained better in Chapters 6 and 7.

## 1.4 Chapter-by-chapter overview

**Chapter 2** provides the mathematical background on different 1-D and 2-D decomposition techniques. Furthermore, this chapter introduces the empirical mode decomposition (EMD) and ensemble empirical mode decomposition (EEMD) techniques. The application of EEMD to investigate the correlation between the amplitude and instantaneous frequency of the neonatal cry during venous blood sampling is provided.

**Chapter 3** In this chapter a new algorithm for source separation of single channel signals (EEMD-ICA) is introduced and validated through numerous simulations and also several real-life examples. Finally, the EEMD-ICA method is extended so that it can be used for source separation from 2-channel signals.

**Chapter 4** first introduces the physiological measures of EEG and fMRI that are explored further in the thesis. The advantages and disadvantages of both modalities are also explained, and the need for EEG-fMRI integration is motivated. The challenges one has to overcome in the preprocessing phase of both modalities are presented. Finally, the existing integration methods are overviewed in detail.

**Chapter 5** describes the protocol of data acquisition used in studies described further on in the thesis. Information about the recording parameters is given, together with information about the subjects, and the visual stimulations presented to the subjects, with the overview of the dataset.

**Chapter 6** presents an extensive validation study on the JointICA algorithm for EEG-fMRI fusion. The discussion is provided to "why" and "how" the algorithms perform, and an answer to the following questions is provided: Under which conditions does it perform better or worse? Which algorithms are to be used? How to assess the quality of the acquired dataset?

**Chapter 7** fuses the EEG and fMRI recordings for the study of perceptual grouping. Also, three different techniques are compared: correlation, regular JointICA, and a modified version of JointICA.

**Chapter 8** reviews the work presented in this thesis, and proposes the directions for future research and exploration.

## 1.5 Personal Contributions

My own contribution in this work ranges from the initial data acquisition until the final interpretation of the obtained results. In addition, I was involved in several other studies which were not included in this thesis as to preserve a certain coherence. Also these studies will be listed below.

The work on the vocalization signals of neonates was performed in close collaboration with Mitchel Silva from the Division M3-BIORES: Measure, Model & Manage Bioresponses, KU Leuven, and Karel Allegaert from the Department of Pregnancy, Foetus and Newborn. In this work, the correlation between the amplitude and instantaneous frequency of the infant cry was investigated during venous blood sampling. This resulted in papers published in *Early Human Development* [174] and *Methods of Information in medicine* [138]. The latter work exploits the EMD method, and it is included in this thesis in Chapter 2.

One of my main contributions is shown in Chapter 3, presenting the work on joining Empirical Mode Decomposition and Independent Component Analysis for the purpose of single-channel recordings. The performance of this method is shown on numerous simulations, and the application on real-life signals is shown. The results of this study have been published in *IEEE Transactions on Biomedical Engineering* [134]. The extension of this method to the application for 2-channel signals is also proposed, and published in the proceedings of the *IEEE EMBS* conference [135].

I started working on the integration of EEG and fMRI signals as a part of the KU Leuven EEG-fMRI IDO project (05/010). In the initial phase, the data acquisition was performed by colleagues from collaborating groups. However, before the official end of the project, I also got involved in the acquisition, after the other co-workers had left. Apart from the IDO project, I was also involved in the COST action NeuroMath, giving me the opportunity to attend some of this action's workshops, where several of our abstracts were presented.

One of my major contributions was the validation study on JointICA (cf. Chapter 6). This study helped me to better understand the functioning of data-driven techniques for the application of EEG-fMRI integration. JointICA was validated at several levels, and the interpretability of the obtained results was shown. Criteria were also proposed to assess whether the obtained results are reliable. This study has been published in *NeuroImage* [136].

Thanks to the experience gained in the above-mentioned studies, I was invited to submit an overview of EEG-fMRI integration techniques. This overview is partly presented in Chapter 4 and is accepted for publication in *Proceedings of Macedonian Academy of Sciences*.

After validating the JointICA approach [136], JointICA has been modified and used

in an ongoing study on local and global integration of visual information, presented in Chapter 7. The study is still in progress, and only preliminary results are shown. This ongoing study was performed in close collaboration with Bart Machilsen and professor Johan Wagemans of the Laboratory of Experimental Psychology.

In a study on the extraction of single trial ERP information [186], the use of PARAFAC on single trial ERP data was introduced and validated with a classification procedure based on different conditions in the experimental paradigm. This study was initially performed by my colleague Katrien Vanderperren. Nevertheless, I was involved in acquiring the data, preprocessing and summarizing the obtained results. This study has been submitted in revised form to *Psychophysiology* [186]. Another integration study conducted within our EEG-fMRI IDO project, was based on single trial P1 and N1 information. The results of this work indicated that simultaneous EEG-fMRI can separate visual processing at 100-200 ms after stimulus onset from the rest of the information processing in the brain. More details have not been included in this thesis, but can be found in a paper published in *NeuroImage* [149].

# Chapter 2

# Decomposition Techniques: Mathematical Background and Application

*This chapter introduces the mathematical concepts used in this thesis. First, some techniques for mapping the one-dimensional data into two-dimensional space are described. Then, in Section 2.2 the application of the EMD algorithm for processing the vocal signals of cries is demonstrated. This section presents the work published in [138, 174]. Thereafter, an overview of the blind source separation techniques used in this thesis is provided.*

## 2.1 1-D Decomposition Techniques

As explained in Chapter 1, one way to apply blind source separation techniques to 1D signals, is to first extend them to the two-dimensional space. This can be done by decomposing the signal into multiple, spectrally distinct, functions. Here we propose several ways to do this extension.

A signal in one dimension can be represented by a row vector $s \in \mathbb{R}^{1\times n}$. If this signal still contains different signal components, one could exploit the available time and frequency information contained in the signal. We review some concepts, as they can also be used as building blocks for more complex decomposition techniques.

Let $s(t)$, $(t = 1, ..., n)$ be a one-dimensional time signal of length $n$. This may also be viewed as a vector in $\mathbb{R}^n$. By decomposition techniques, we assume the

techniques which are used to decompose this signal into elementary waveforms that better represent the features embedded in the signal. Traditional methods to do this decomposition involve the decomposition in one of the orthogonal bases (e.g. Fourier basis, orthogonal wavelet bases etc.). This decomposition may be viewed as follows: Given the basis list of $n$ waveforms, represent $s$ as a linear combination of these waveforms. The waveforms in the list are linearly independent, making this representation unique. For these bases, forward and backward transformations exist which transform the signal $s$ from time domain to frequency domain (in the case of Fourier basis), and backwards. In this chapter, we give an overview of these techniques in an alternative, but more intuitive way.

### 2.1.1 Dictionaries and Atoms

We call a *Dictionary* a collection of parametrized waveforms $\mathcal{D} = (\phi_\gamma : \gamma \in \Gamma)$, where $\phi_\gamma$ are discrete time signals of length $n$, which are called atoms. Also, $\gamma$ is the index of the atom in a dictionary. In a Fourier dictionary, $\gamma$ denotes a frequency index, in a wavelet case it is a time/scale joint index, or it can also be jointly time/frequency index. A lot of different dictionaries have been introduced, but we list the most commonly used ones.

#### Fourier Dictionary

The analytic expression of the continuous Fourier transform is very well known, and is given by:

$$\hat{f}(\omega) = \int_{-\infty}^{+\infty} f(t) e^{-i\omega t} dt \tag{2.1}$$

In the discrete case, a Fourier dictionary is a set of frequency atoms, described by $\gamma = (\omega, \nu)$, where $\omega = [0, 2\pi)$ describes the frequency, and $\nu \in \{0, 1\}$ describes the phase type (sine or cosine):

$$\phi_{(\omega,0)} = cos(\omega t), \quad \phi_{(\omega,1)} = sin(\omega t) \tag{2.2}$$

To decompose, we let $\gamma$ run through all the cosines at frequencies $\omega_k = 2\pi k/n, k = 0, ..., n/2$, and all the sines of the frequencies of $\omega_k, k = 1, ..., n/2 - 1$.

### Wavelet Dictionaries

Wavelet dictionaries belong to the group of time-scale dictionaries. They are demonstrated here for the case of the second derivative of the Gaussian function, commonly called the *Mexican Hat* wavelet. The function is described with $\psi(t) = \left(1 - t^2\right) e^{-\frac{t^2}{2}}$. This function $\psi$ is then called a *mother wavelet*, and the wavelet functions are derived from the mother wavelet as $\psi^{a,b}(t) = \|a\|^{-\frac{1}{2}} \psi\left(\frac{t-b}{a}\right)$. As $a$ changes, the function $\psi^{a,b}$ covers different frequency ranges (the smaller the $a$, the higher the frequency). This coefficient is called the scaling factor. Changing the parameter $b$ allows moving the wavelet function in the time domain. Therefore, this parameter is called *translation*.

Similarly to Eq. 2.1, the wavelet function can be described as

$$\hat{f}(a,b) = \|a\|^{-\frac{1}{2}} \int_{-\infty}^{+\infty} f(t)\psi\left(\frac{t-b}{a}\right) dt \tag{2.3}$$

with additional requirements that

$$\int_{-\infty}^{+\infty} \psi(t)dt = 0 \tag{2.4}$$

and

$$\int_{-\infty}^{+\infty} \|\psi(t)\|^2 dt < \infty \tag{2.5}$$

The last two conditions allow the inverse transformation. The first condition implied the finite energy of the wavelet $\psi(t)$, and the second condition realizes a band-pass filter (it is zero-mean).

**Orthonormal Wavelets** In the discrete case, the wavelet dictionary can then be described with the coefficients of translation and scaling of the *Mother wavelet*. Each atom $\gamma$ is parametrized with $a$ describing the scale (in terms of different frequency content), and $b = [0, n]$ indicating location. Here, $\gamma$ runs through the collection of *Mother wavelets* with dyadic scales ($a_j = 2^j/n, j = j_0, ..., log_2(n) - 1$), and locations which are integer multiples of the scale ($b_{j,k} = k \cdot a_j, k = 0, ..., 2^j - 1$). This basis is also orthonormal. A lot of different (more complicated, and more suitable for different applications) wavelets exist. A broad overview of their analysis and synthesis functions can be found in [40].

**Stationary Wavelets** From Eq. 2.3, it is apparent that the scalar product is used to compute the signal power at a certain sample explained by a given wavelet. This means that the wavelet will better explain a certain event in the signal if the two are perfectly aligned. However, in the case of discrete wavelets, the shift between the adjacent atoms is too large ($n/2^j$), i.e. the two adjacent atoms are *far* from each other for the whole wavelet width at a certain scale. Therefore, continuous wavelets are proposed with the hope that all the events are able to be captured more accurately. In this case, at the level $j$ there are $n$, instead of $2^j$ shifts, the width being $n/2^j$. This means that each wavelet atom is shifted by only one sample. thus the wavelet shape is always exactly aligned with the feature of interest, and therefore provides a superior presentation. An overview of continuous, as well as discrete wavelet dictionaries can be found in [40].

### 2.1.2 Empirical Mode Decomposition

The decomposition techniques described above are meant to decompose the signal into a set of predefined basis functions. This poses a limitation that the events in the observed signal should correspond closely to the atoms of the particular (wavelet, Fourier or other) dictionary. Another decomposition technique, which is used to decompose the signal into its oscillatory modes without imposing any prior information is called *Empirical Mode Decomposition* (EMD) [89]. Contrary to wavelets and Fourier transform, where the signal is decomposed into atoms from a predefined dictionary, EMD does not impose such restrictions on the analyzed signal. Therefore, this method is described as *data-driven*. EMD has been successfully applied in a number of applications in various disciplines. The range of the disciplines is rather broad, ranging from meteorology [38, 65], to image processing [118], and biomedical signal processing [19, 131, 138].

This method adaptively decomposes a given time signal $s(t)$ into a set of oscillatory modes, called *Intrinsic Mode Functions* (IMF). We can say that EMD maps the signal into a space spanned by the IMFs. These functions are *mono-component* in the sense that each function is supposed to contain only one frequency at the time, called *instantaneous frequency* (IF). Additionally, the set of IMFs is *local*, *orthogonal* and *complete*. The *completeness* assumes that the signal is fully described with these IMFs (no information loss is present), and it is guaranteed by the fact that the signal $s(t)$ can be reconstructed by simply summing all IMFs together. Local property assures that the very local non-stationary events are captured with the method. Orthogonality implies that two different IMFs are never correlated.

The intrinsic mode function is a function defined by the two following rules:

1. The number of extrema and zero-crossings in the whole signal can differ at most by 1, and

2. At each time instant, the mean value of the envelope defined by local maxima and the one defined by local minima is zero

The process of extracting the IMFs from the given time signal $s(t)$ is called the *sifting* process, and the procedure is as follows for the $i^{th}$ component:

1. Define the residual to be equal to the signal $r_0(t) = s(t)$
2. Set $i = 1$
3. Detect all the extrema in the $r_{i-1}(t)$
4. Define the upper envelope by connecting all the maxima and interpolating in all the other points using a cubic spline interpolation method
5. Define the lower envelope similarly to the upper envelope, just using local minima.
6. compute $h_{i,1}(t) = r_{i-1}(t) - m_{i,1}(t)$, where $m_{i,1}(t)$ is the mean of upper and lower envelopes.
7. If $h_{i,1}$ does not satisfy the conditions for being the IMF, repeat the process as $h_{i,2}(t) = h_{i,1}(t) - m_{i,2}(t)$, where $m_{i,2}(t)$ is the mean of the upper and lower envelopes of $h_{i,1}$. Repeat the process iteratively until $h_{i,k}(t) = h_{i,k-1}(t) - m_{i,k}(t)$ satisfy the IMF conditions.
8. The extracted IMF becomes $c_i(t) = h_{i,k}(t)$. Form the residual $r_i(t) = r_{i-1}(t) - c_i(t)$.
9. If $r_i(t)$ contains more than one extremum, increase $i$ by one ($i = i + 1$), and go back to point 3.
10. The set of IMFs and a residual are successfully extracted.

After this process, the signal $s(t)$ may be written as $s(t) = \sum_{i=1}^{n} c_i(t) + r_n(t)$. The output of such a procedure is shown in Fig. 2.3. The top panel represents the original signal, decomposed in the first 5 IMFs, and the residue. In this figure, the process is stopped after extracting first 5 IMFs. However, the procedure can be continued until the residue is a monotonic function.

### Ensemble Empirical Mode Decomposition

One of the major drawbacks of the original EMD is the frequent appearance of mode mixing, which is defined as a single IMF either consisting of widely disparate scales, or a signal of a similar scale residing in different IMF components. This

is a consequence of the interpolation used in the sifting process. To overcome this problem, the advanced noise-assisted data analysis method is proposed, called Ensemble Empirical Mode Decomposition (EEMD) [191], which defines the IMF as an ensemble of trials, each consisting of the signal plus a white noise of finite magnitude. The algorithm is as follows:

1. Define a number of ensemble members ($N$)
2. Set $i = 1$
3. Generate random noise sequence of the standard deviation $\sigma$, and add it to the original signal.
4. Apply EMD and derive the $IMF_i$ set.
5. If $i \leq N$, $i = i + 1$, go back to item 3.
6. Obtain the averaged IMF set, by averaging over the members of the ensemble.

Taking into account properties of white noise, noisy components are expected to cancel out and a set of noise- free IMF's is derived. Increasing the ensemble would give more accurate estimates of IMF's, but the computational efficiency is decreased.

One of the major drawbacks of the EMD algorithm is that it is purely intuitive, and still misses mathematical background. Although by EEMD the mode-mixing problem appears to be solved, it poses new challenges to the mathematical understanding of the procedure [41]. A solution to this problem is proposed by Daubechies et al., [41], who introduced, so-called, synchrosqueezed wavelets. In this work a family of IMF-type functions (IMT) is defined and a decomposition of a given signal into the set of these functions using synchrosqueezed wavelets is performed. This method is called an *EMD-like decomposition tool*. The exploration of the EMD and EEMD methods is still under development. The EEMD algorithm is available online via [181].

## 2.2 Application of EMD to vocal signals (phonetic baby cry)

### 2.2.1 Introduction to baby cry signals

One of the most important tools for infants to communicate is vocalization. In neonates, vocalization is mainly manifested through crying, and research has been done on the relationship between stress states and acoustic cry features. Bellieni et

al., [16] were able to document that newborns with a higher DAN (Douleur Aigue du Nouveau-né) score during venous blood sampling (heel lancing) also had a higher fundamental frequency and a correlation was found between the pain intensity (DAN-score) and the normalized Root Mean Square value (RMS). Facchini et al., [70] looked to the relation between the DAN score and the occurrence of noise patterns in the sound spectrograms. These noise patterns were chaotic and showed discontinuous parts in the crying signal, caused by a highly turbulent flow in the larynx. Results indicated that newborns with a higher DAN score showed more noise patterns.

Baby cry is the result of the interaction between controls of different areas in the brain, respiratory control and vocal fold vibrations. At early stage, it is believed that a cry is the result of a respiratory action and the effect of air going through a pipe, causing the vocal folds to vibrate, resulting in a cry bout [139] (the vocalization produced during one expiration). The more the neural system matures, the more laryngeal control can be exerted resulting in manipulation and modulation of the cry signal. However, the observations on maturational aspects of the cry signal are limited and conflicting [16, 190]. The development of the central neural system has been linked with the extent of vocalization control [190]. Based on the cry production model of Golub described in the work of Moller and Schonweiler [139] and Barr et al. [12], decoupling between variations in fundamental frequency and intensity contour during crying indicates cortical control. Decoupling is referred to as the absence of coupling between fundamental frequency variation and intensity contour during phonetic crying. In this cry model, cry production is controlled by a three level processor structure, in which the lower level can be subdivided into the subglottal, glottal and supraglottal cry production areas. The mid-processor is involved in physiological inputs like pain, blood levels and respiratory constraints, while the feed-back processes are part of the upper-processor level, especially auditory feedback.

In this study, we assessed the relation between the energy envelope of the cry bout and frequency variation within the same bout using the method introduced by Huang [89], called Empirical Mode Decomposition (EMD). This is done in order to establish the relation between the resulting correlation coefficients of these variables with clinical indicators of pain (mean behavioral pain scale - MBPS) after venous blood sampling (or stress expression). In this way, the difference between the painful cry and a cry which is a consequence of only stress and fear theoretically could be established.

The study in which these relations are estimated with the more standard methods on the same dataset is given in [174].

### 2.2.2 Materials and Methods

#### Data Set

The vocalization was recorded in 24 term neonates in whom a venous blood sampling was performed on the $3^{rd}$ day of life for routine metabolic screening. All babies were born in the University Hospital of Leuven (U.Z. Leuven). The study was approved by the Ethical Board of the University Hospitals, and neonates were only included after written consent of the parents. In order to participate in the project, babies had to have minimal gestational age of at least 37 weeks, no complications during pregnancy, a 1- and 5- minutes APGAR score above 7, and a minimal birth weight of 2.5 kg.

The vocalization from the babies was recorded up to three minutes after the venous puncture, with a sampling rate of 44000 Hz at a distance of 0.5 meters from the baby's head.

In infant cry analysis there are three types of vocalization as described in [105]: phonation (voiced cries), hyperphonation (high pitched cries) and disphonation (turbulence, voiceless cries). In order to evaluate the relation between the variation in the frequency and amplitude of the cry, only manually selected voiced cry bouts (phonations) are used. The total number of cry bouts extracted for this work was 800.

#### Preprocessing and Data Analysis

In the preprocessing step all the signals were first band-pass filtered using a 6th order Butterworth filter with lower and upper cut-off frequencies being 200 Hz and 2500 Hz respectively. After filtering, the signal was downsampled to 11025 Hz.

After the EEMD has been applied and the set of IMF's has been extracted, instantaneous frequencies (IF) and instantaneous amplitudes (IA) have been computed for each cry bout separately. The regular way to compute IA's and IF's from the IMF's is to apply the Hilbert Transform (HT), which behaves well when applied to IMF's since they are monotonic and locally symmetric to the zero level. However, in time instants where large and fast changes in amplitude occur, cubic spline fitting, which is incorporated in the sifting process is not able to follow these changes and hence IMF's are not always ideal. Due to this phenomenon, the HT will give non-accurate instantaneous frequencies in those places.

To overcome these problems the time-frequency spectrum has to be averaged in some way. This can be achieved using Gaussian windowing as in [89] which will concentrate the averaged spectrum of the particular window in the center of that window.

Another way to average the spectrum is to reassign it, as proposed by Auger [10] and Rilling [164]. This method relies on the principle that frequency values around the observed point have no reason to be symmetrically distributed around that point, as Gaussian averaging supposes. Therefore, their average should not be assigned to this point, but rather to the center of gravity of the observed domain. This is done by windowing the data in the overlapping windows for each IMF separately, and the power of the signal in a certain window is assigned to the center of gravity of that window, instead of the geometrical center of the window, as it is the case with Gaussian smoothing. In this work we used the reassigned spectrogram.

#### Computing Correlations

After extracting the IMF's the reassigned spectrogram is derived, as explained above. After this is done, we followed the changes in the IMFs that contain information about the fundamental frequency (between 400 and 900 Hz) and studied how these changes correlate with the Intensity Contour (IC). IC is defined as the envelope of the signal in time domain. To compute this envelope, we first computed the absolute value of the signal, and then filtered it with the 8th order low-pass Butterworth filter at cut-off frequency 80 Hz.

Once the envelopes and frequencies have been computed, we were interested in the correlations between them. To compute these correlations, we calculated the averaged values of the frequencies and amplitudes over half-overlapping windowed epochs of 512 data points (i.e. 46 ms), using a Hamming window. The correlations are then then computed between those averaged values.

### 2.2.3 Results

In this section we present the results of signal processing as well as the computed correlations between the intensity contour of the voice signal and the instantaneous frequency of the modes containing the fundamental frequency. The cry bout with correlated, or uncorrelated instantaneous amplitude and frequency are shown in Figs. 2.1 and 2.2 respectively.

An example of the EMD decomposition of one cry bout (the extraction of the first 5 IMFs) is shown in Fig. 2.3. From the IMF set, the $3^{rd}$ and $4^{th}$ intrinsic modes were observed to carry most of the fundamental frequency information (400 to 900 Hz), and are therefore most interesting to investigate. This is illustrated in Fig. 2.5.

In Figs. 2.4 and 2.5 we show the spectrogram of a randomly chosen cry bout from the database before and after reassignment respectively. It is obvious that in the

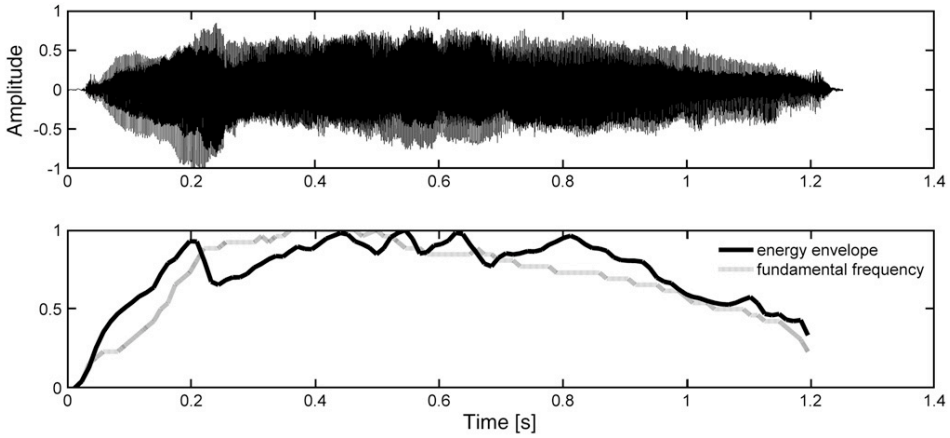


Figure 2.1: Coupled cry bout showing its waveform with corresponding energy envelope and frequency variation (both normalized for visualization). The cross correlation-coefficient is 0.77.

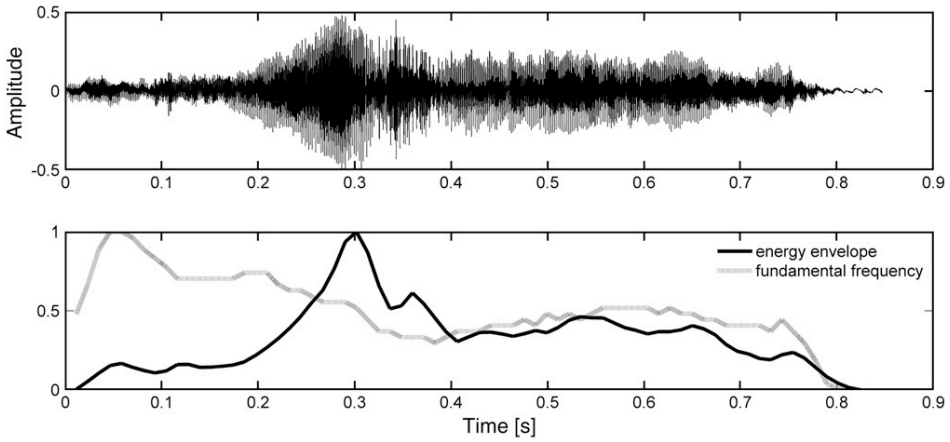


Figure 2.2: Decoupled cry bout showing its waveform with corresponding energy envelope and frequency variation (both normalized for visualization). The cross-correlation coefficient is 0.12.

reassigned spectrogram blurring is significantly suppressed, which allows us to observe frequencies of the intrinsic modes more accurately and to easily compare it with the intensity contour of the voice signal.

Table 2.1 presents the mean correlations between the fundamental frequency and the intensity contour over all cry bouts for each subject. Corresponding standard

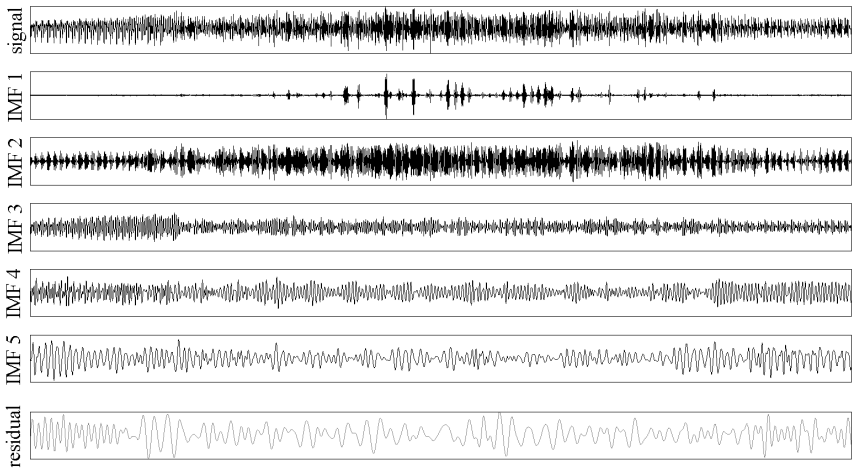


Figure 2.3: The first five extracted IMFs from one of the cry bouts. The residual after these 5 IMFs is shown in the bottom panel. It is apparent from this figure that the IMFs with the highest frequency content are extracted first.

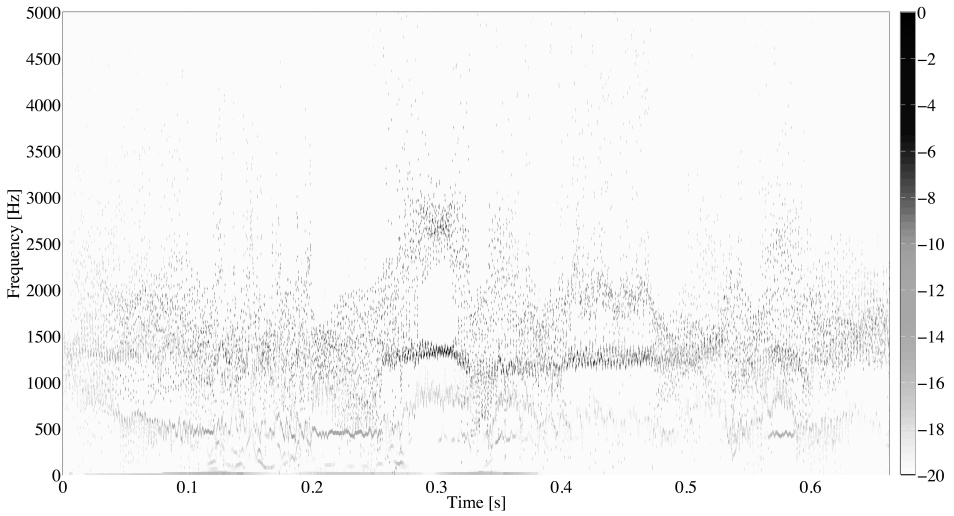


Figure 2.4: Spectrogram of the EMD treated signal before reassignment.

deviations are also given in the third column of the table.

Additionally, we checked whether there is a relation between the correlation coefficients of the babies and their MBPS scores. Therefore, in the last column in

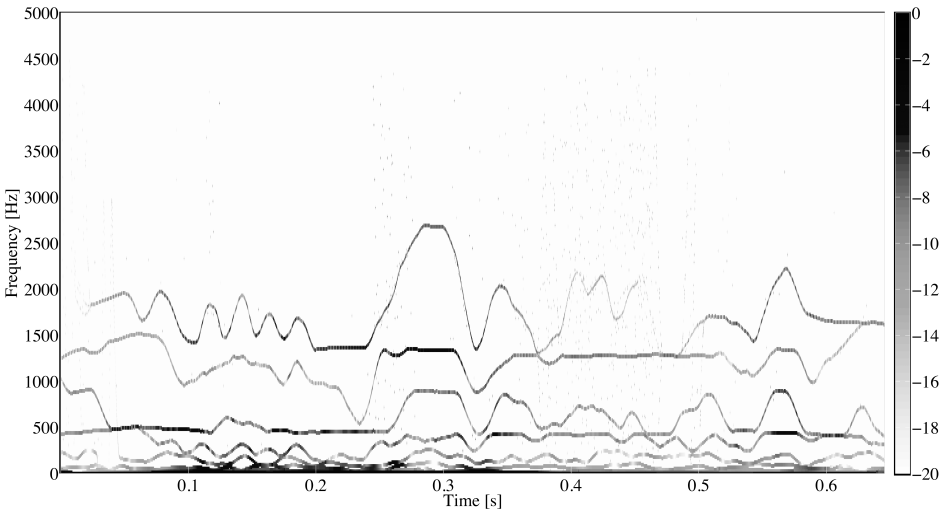


Figure 2.5: Spectrogram of the EMD treated cry signal after reassignment. The different lines represent different IMF's.

Table 2.1 we add the corresponding MBPS values. To better visualize a relationship between the results in Table 2.1, we plot the ratio of the mean correlation value and standard deviation from Table against the corresponding MBPS value (Fig. 2.6). The correlation between the two mentioned measures is significant (0.55 with the p-value of 0.006).

### 2.2.4 Discussion

We showed the application of the EMD technique to newborn cry signals. In the particular case illustrated in Fig. 2.5, the reassigned spectrogram shows that IMF 3 and 4 seem to partially overlap in the frequency domain, however in different time instants (see Fig. 2.5). Since the fundamental frequency of the cry is located in this particular frequency band, those two modes mutually switch the essential information on the fundamental, implying that the fundamental frequency can be found in both of these modes. This is not always the case, since sometimes only one of these modes is dominant.

When calculating the mean value of the correlation between the IC and frequency variation a great spread is observed, ranging between 0.37 ($\pm$0.14) and 0.83 ($\pm$0.07), while the MBPS value also varied between 3 and 10.

In addition, a considerably high standard deviation of the correlations is observed

| Subject no. | Mean value | Standard deviation | MBPS |
|---|---|---|---|
| 1 | 0.6116 | 0.2266 | 3 |
| 2 | 0.6584 | 0.1774 | 3 |
| 3 | 0.5629 | 0.2626 | 4 |
| 4 | 0.6831 | 0.1698 | 5 |
| 5 | 0.7754 | 0.1927 | 6 |
| 6 | 0.8138 | 0.1754 | 7 |
| 7 | 0.6806 | 0.1758 | 7 |
| 8 | 0.6213 | 0.2002 | 7 |
| 9 | 0.6832 | 0.1173 | 7 |
| 10 | 0.5641 | 0.3019 | 8 |
| 11 | 0.3683 | 0.1405 | 8 |
| 12 | 0.6359 | 0.1725 | 8 |
| 13 | 0.7286 | 0.1916 | 8 |
| 14 | 0.3852 | 0.2159 | 8 |
| 15 | 0.8226 | 0.0795 | 8 |
| 16 | 0.7754 | 0.1303 | 9 |
| 17 | 0.7514 | 0.0837 | 9 |
| 18 | 0.7765 | 0.1668 | 9 |
| 19 | 0.7946 | 0.1109 | 10 |
| 20 | 0.6969 | 0.1584 | 10 |
| 21 | 0.7097 | 0.0754 | 10 |
| 22 | 0.8391 | 0.0709 | 10 |
| 23 | 0.8052 | 0.0826 | 10 |
| 24 | 0.6906 | 0.1216 | 10 |

Table 2.1: Mean values and standard deviations of the correlations between the fundamental frequency and the intensity contour and MBPS value for each subject

compared to the mean correlation per subject. This indicates a high intra-subject variability. Taking the ratio between the mean correlation value and the standard deviation gives information about the consistency of the investigated cry bouts during crying sequence. By plotting this ratio against the MBPS values (Fig. 2.6), a trend can be seen that infants with a higher MBPS score show a higher mean/standard deviation ratio. This indicates that babies with higher MBPS score have higher mean and lower standard deviation of correlation between IC and frequency. In other words the IC and frequency are more coupled in more stressed infants. This is a careful statement as more data is required to validate this. Wolf suggested that prior to one month of age, infant cries are highly reflective and undifferentiated, but that shortly afterwards cries progressively reflect various psycho-physiological states like hunger and pain [190]. In contrast, Bellieni et al.

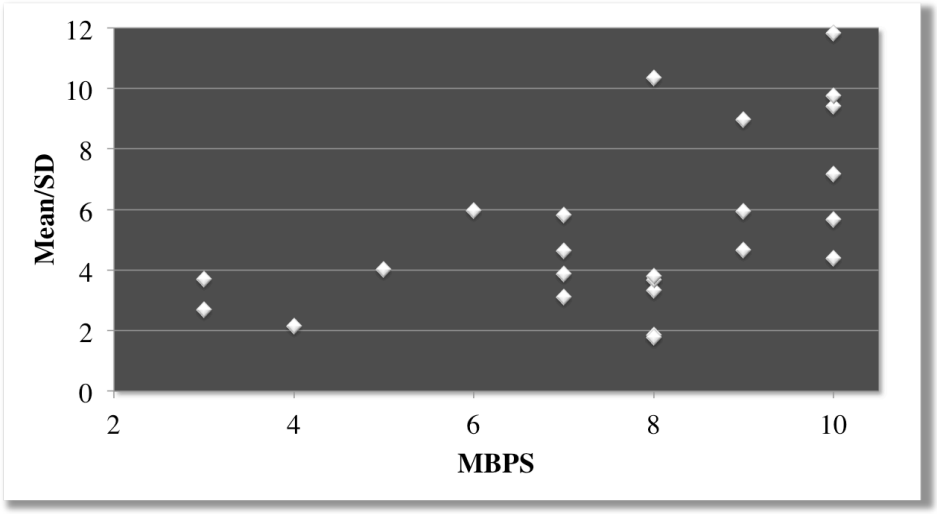


Figure 2.6: The ratio of the mean value and standard deviation of the correlations over all cry bouts for a particular subject with respect to the MBPS value.

were able to document a correlation between cry features and DAN score in term neonates [16].

The same problem, using a classical autoregressive spectral estimation method, has been introduced in [174], including a more detailed clinical interpretation of the problem. Compared to the results obtained in that work, EMD allowed to better relate the correlation between frequency and intensity contour with MBPS, thereby showing a more positive trend. Also, the statistical significance ($p<0.006$) is achieved by using the output of the EMD analysis. However, the statistically significant relation was not detected when more standard methods were used.

### 2.2.5 Conclusion on the Baby Cry study

In this section, we demonstrated the application of the EMD algorithm to the human vocal signals (phonetic baby cries). The cries are recorded during the venous blood sampling of the neonates. The correlation of the frequency to the power of cries are compared to the mean behavioral pain scale (MBPS) and a certain trend could be observed. However, the results from this study are only indicative, and this study should be regarded only as a demonstration.

## 2.3 2-D Decomposition Techniques

### 2.3.1 Principal Component Analysis (PCA)

Principal Component Analysis (PCA)[153, 66] is used to decompose the set of observations (variables) into the space where these variables are mutually orthogonal. This means that the originally correlated variables are uncorrelated in the new space. The number of extracted components can be equal to the number of originally recorded signals. The PCA solution can be derived either by eigenvalue decomposition, or with singular value decomposition (SVD), usually after data centering. PCA transforms the data in a new coordinate system, such that the greatest variance by any projection of the data comes to lie on the first coordinate (called the first principal component), second greatest variance lies on the second coordinate, and so on. It is mostly used as a tool for data reduction in exploratory data analysis. The data reduction is obtained by retaining the first several components, while discarding the others.

Let $\mathbf{X}$ be the data matrix where the mean has been subtracted, $\mathbf{X} \in \mathbb{R}^{N \times J}$, with rank $R$. PCA computes the matrices $\mathbf{B} \in \mathbb{R}^{N \times R}$ and $\mathbf{S} \in \mathbb{R}^{J \times R}$, such that:

$$\hat{\mathbf{X}} = \mathbf{B}\mathbf{S}^T, \quad \text{s.t.} \quad \|\mathbf{X} - \mathbf{B}\mathbf{S}^T\|^2 \quad \text{is minimal} \tag{2.6}$$

However, matrix $\mathbf{B}$ is not uniquely defined for the case that $R < I - 1$, but matrix $\mathbf{S}$ normally is, since the components are sorted according to the amount of explained variance of the signal.

### 2.3.2 Independent Component Analysis (ICA)

As described in Chapter 1, Independent Component Analysis (ICA) is a BSS technique that starts from the assumption that each of the observed signals is obtained as a linear mixing of mutually independent sources, contrary to PCA, which imposes orthogonality between the derived components:

$$x_i = a_{1i}s_1 + a_{2i}s_2 + \ldots + a_{ki}s_k, \quad \forall i \in [1, n] \tag{2.7}$$

using the vector notation, we get the same notation as in Eq. 2.6, where $\mathbf{A}$ is called the mixing matrix, and $\mathbf{S}$ represents the matrix of sources. Therefore, we try to estimate the demixing matrix $\mathbf{W}$, such that it solves the problem.

$$\hat{\mathbf{S}} = \mathbf{W} \cdot \mathbf{X} \tag{2.8}$$

In the ideal case, where the number of sources is equal to the number of measured channels, $\mathbf{W} = \mathbf{A}^{-1}$. Otherwise, matrix $\mathbf{W}$ is a pseudo-inverse of $\mathbf{A}$.

To be able to solve the ICA problem, several assumptions must be made:

1. The sources are mutually independent. This, by definition, means that the joint distribution of all the sources is equal to the product of all the distributions separately. Taking that we have $k$ sources, that means that

   $$p(s_1, s_2, ..., s_k) = p(s_1) \cdot p(s_2) \cdots p(s_k)$$

   where $p(a)$ describes the probability distribution of the variable $a$.

2. In the ICA model, at most one of the independent sources is allowed to undergo *Gaussian* distribution. This is because all the higher-order cumulants of the variable with Gaussian distribution are equal to zero, and the ICA model makes use of exactly these higher-order cumulants to estimate the independent sources.

3. In the ICA model, we start with the assumption that the mean value of the recorded signal, and independent sources equals zero.

Also, a couple of features of ICA algorithms should be noted, and they are:

1. The estimated independent components cannot be sorted. The reason of this is simply that by introducing the permuting matrix $\mathbf{P}$, we can write $\mathbf{X} = \mathbf{A}\mathbf{P}^{-1}\mathbf{P}\mathbf{S}$, and therefore $\mathbf{X} = \left(\mathbf{A}\mathbf{P}^{-1}\right) \cdot (\mathbf{P}\mathbf{S})$, which means that $\mathbf{P}\mathbf{S}$ can also represent the matrix of sources.

2. It is often the case that the number of measured signals is greater than the number of sources, but the number of sources is not explicitly known. Therefore, several methods exist (like Akaike Information Criterion (AIC), Minimum Description Length (MDL), or ICASSO[86]), that help us estimate the number of independent sources.

#### Pre-whitening

Most ICA algorithms require a pre-whitening step. This step is used after the centering of the data to "decorrelate" the measured signals, actually to rotate the

coordinate system as to diagonalize the covariance matrix. For the matrix $\mathbf{Q}$ we say that it is *white* if it satisfies:

$$Cov\{\mathbf{Q}\} = E\,\mathbf{Q}\mathbf{Q}^{-1}$$

=I

The whitening may be achieved in the following way. Denote by $\mathbf{C}$ the covariance matrix of $\mathbf{X}$:

$$\mathbf{C} = E\left[\mathbf{X}\mathbf{X}^T\right] \tag{2.10}$$

By applying the *Eigenvalue Decomposition* (EVD) to $\mathbf{C}$, we obtain

$$\mathbf{C} = \mathbf{E}\mathbf{D}\mathbf{E}^T \tag{2.11}$$

where $\mathbf{E}$ is the orthogonal matrix of the *eigenvectors*, and $\mathbf{D}$ is the diagonal matrix of eigenvalues.

Now, we define $\mathbf{C}^{1/2}$, such that $\mathbf{C}^{1/2}\left(\mathbf{C}^{1/2}\right)^T = \mathbf{C}$. From Eq. 2.11, we have that $\mathbf{C}^{1/2} = \mathbf{E}\mathbf{D}^{1/2}$. If we compute now the covariance of $\mathbf{C}^{-1/2}\mathbf{X}$, we get [91]

$$\begin{aligned} Cov\left(\mathbf{C}^{-1/2}\mathbf{X}\right) &= E\left[\left(\mathbf{C}^{-1/2}\mathbf{X}\right)\left(\mathbf{C}^{-1/2}\mathbf{X}\right)^T\right] \\ &= E\left[\left(\mathbf{C}^{-1/2}\mathbf{X}\right)\left(\mathbf{X}^T\mathbf{C}^{-1/2}\right)\right] \\ &= \mathbf{C}^{-1/2}E\left[\mathbf{X}\mathbf{X}^T\right]\mathbf{C}^{-1/2} \\ &= \mathbf{C}^{-1/2}\mathbf{C}\mathbf{C}^{-1/2} \\ &= \mathbf{I} \end{aligned} \tag{2.12}$$

Therefore, the matrix $\mathbf{B} = \mathbf{C}^{-1/2}$ is the whitening matrix.

Some ICA algorithms use the PCA solution as the whitening matrix solution, since it also decorrelates the measured signals $\mathbf{X}$.

### Measures of independence

In order to estimate the demixing matrix $\mathbf{W}$ that unmixes the measured signals $\mathbf{X}$ into the original sources $\mathbf{S}$, it is necessary to define the measure of independence.

Some algorithms (Infomax [15]) use neural networks to estimate the maximum likelihood. However, other ICA algorithms (JADE [30]) set all the $4^{th}$ order cross-cumulants to zero, or (FastICA [143] ) use the $4^{th}$ order cumulant(*kurtosis*) as a measure of non-Gaussianity. But, how is non-Gaussianity connected to independence?

The *Central Limit Theorem* states that a mixture of (non-Gaussian) sources (recall that the sources in ICA model are assumed to be non-Gaussian) has more Gaussian-like distribution, than each of the sources separately. Suppose we want to estimate only one source, $s_i$. From Eq. 2.8, we have

$$\hat{s}_i = w_i^T \mathbf{AS} \tag{2.13}$$

where $w_i^T$ is one column of the demixing matrix that gives the solution $s_i$. We also see from Eq. 2.13 that $s_i$ is a linear combination of all the sources given in $\mathbf{S}$, with the coefficients given as $w_i^T \mathbf{A}$. However, since the $s_i$ itself is one of the rows in $\mathbf{S}$, $w_i^T \mathbf{A}$ should be the column vector with only one non-zero element (to select for our source $s_i$). It is impossible to estimate $w_i$, since also the mixing matrix $\mathbf{A}$ is unknown. For this reason, in practice, we try to estimate vector $w_i$ such that it maximizes the non-gaussianity of $w_i^T \mathbf{X}$. According to the above mentioned *Central Limit Theorem*, such a vector would provide the maximally "unmixed" source, and they would correspond to the vector $w_i^T \mathbf{A}$ with only one non-zero element.

**The Likelihood of the ICA model** It is possible to formulate directly the likelihood in the noise-free ICA model, which was done in [156], and then estimate the model by a maximum likelihood estimation. In our case, the likelihood takes the form

$$L(\mathbf{W}) = \prod_{t=1}^{T} \prod_{i=1}^{n} \log p_i \left( w_i^T \mathbf{x}(t) \right) \tag{2.14}$$

$p_i$ are the probability density functions of $s_i$ (they are assumed to be known here). The logarithm of the likelihood is more commonly used because it is algebraically simpler.

$$\log L(\mathbf{W}) = \sum_{t=1}^{T} \sum_{i=1}^{n} \log p_{xi} \left( w_i^T \mathbf{x}(t) \right) + T \log |\det \mathbf{W}| \tag{2.15}$$

Here $T$ is the number of time samples in $\mathbf{X}$. The term $\log |\det \mathbf{W}|$ in the likelihood comes from the classical rule for (linearly) transforming random variables and their densities[151]: If $\mathbf{x}$ is a random vector with density $p_x$, then for any matrix $\mathbf{W}$, the density of $\mathbf{S} = \mathbf{WX}$ is given by $p_x (\mathbf{WX}) |\det \mathbf{W}|$.

**Joint Diagonalization** Here the definition of joint diagonalization is given, because it will be needed in the further text. Observe the set of $K$ matrices, of dimension $n \times n$ : $\theta = \{\mathbf{M}_1, ..., \mathbf{M}_K\}$. The *joint diagonality* criterion is defined for a matrix $\mathbf{V}$, of dimension $n \times n$ as a non-negative function of $\mathbf{V}$:

$$X(\theta, \mathbf{V}) \triangleq \sum_{k=1}^{K} off\left(\mathbf{V}^H \mathbf{M}_k \mathbf{V}\right) \tag{2.16}$$

where the operater $off$ on the $n \times n$ matrix $\mathbf{M}$ with the elements $\mathbf{M}_{ij}$ is defined as $off(\mathbf{M}) \triangleq \sum_{1 \le i \ne j \le n} |\mathbf{M}_{ij}|^2$.

**Kurtosis as a measure of non-gaussianity** In our case, all of our sources and measured signals have zero-mean. Therefore, the kurtosis can be written as

$$kurt\{y\} = E\left[y^4\right] - 3E\left[y^2\right]^2 \tag{2.17}$$

For Gaussian variables, the *kurtosis* has a value 0. For non-Gaussian variables, the *kurtosis* has a non-zero value. It can be positive (then we speak about super-Gaussian), or negative (sub-Gaussian variables). Therefore, the absolute value of the *kurtosis* can be taken as a measure of non-gaussianity. We say that the larger the absolute value of *kurtosis*, the more it deviates from the Gaussian distribution, and in accordance to the *Central Limit Theorem*, it is most likely that such a source is "unmixed". The properties of *kurtosis* for the two independent variables ($y_1$ and $y_2$) are the following:

$$\begin{aligned} kurt(y_1 + y_2) &= kurt(y_1) + kurt(y_2) \\ kurt(\alpha y_1) &= \alpha^4 kurt(y_1) \end{aligned} \tag{2.18}$$

where $\alpha$ is a constant.

### Algorithms for solving the ICA problem

Numerous different algorithms for solving the ICA problem are available. The most common ones, used in this work, are described below.

**Information Maximization Algorithm - Infomax** An ICA algorithm which is based on information maximization is called Infomax [15]. This algorithm is based on maximizing the output entropy (or information flow) of a neural network

with non-linear outputs. Assume that $\mathbf{X}$ is the input to the neural network whose outputs are of the form $g_i\left(w_i^T\mathbf{X}\right)$, where the $g_i$ are some non-linear scalar functions. Infomax then maximizes the entropy of the outputs:

$$L_2 = H\left(g_1\left(w_1^T\mathbf{X}\right), ..., g_n\left(w_n^T\mathbf{X}\right)\right) \tag{2.19}$$

If the non-linear functions $g_i$ are well chosen, Eq. 2.19 also represents a solution to the ICA model. In several papers (e.g. [29, 152]), it is shown that this principle is equivalent to the maximum likelihood estimation. This equivalence requires that the non-linearities $g_i$ used in the neural network are chosen as the cumulative distribution functions corresponding to the densities of the sources $f_i$, meaning that $g_i' = f_i$. In this work, $g_i$ is mostly chosen to be the sigmoid function.

In layman's terms, this algorithm maximizes the information in each of the estimated sources, and minimizes the mutual information between the components using neural networks. At the same time, these components are estimated as to satisfy the maximum likelihood criterion.

**Fast Fixed-Point Algorithm for ICA - FastICA** FastICA [143, 92, 182] algorithm minimizes the *gaussianity* of the estimated *independent source* by maximizing the absolute value of the kurtosis in a gradient approach. It estimates sources one at the time. Basically, this algorithm starts from a random value for $w_1^T$. Then, the direction is computed in which the absolute value of the $kurt\left(w_1^T\mathbf{Z}\right)$ grows most significantly. Here, the matrix $\mathbf{Z}$ is obtained by whitening the matrix $\mathbf{X}$. The gradient of the absolute value of the *kurtosis* can be easily computed:

$$\frac{\partial |kurt\left(w_1^T\mathbf{Z}\right)|}{\partial \mathbf{W}} = 4kurt\left(kurt\left(w_1^T\mathbf{Z}\right)\right)\left[E\left\{\mathbf{Z}\left(w_1^T\mathbf{Z}\right)^3\right\} - 3w_1\|w_1\|^2\right] \tag{2.20}$$

It can be shown that in the stable point of the algorithm, the gradient of the *kurtosis* must be in the direction of $w_1$, meaning that it should be equal to $w_1$ multiplied by a constant. Therefore, Eq.2.20 may be rewritten as

$$w_1 \propto E\left\{\mathbf{Z}\left(w_1^T\mathbf{Z}\right)^3\right\} - 3w_1\|w_1\|^2 \tag{2.21}$$

The vector $w_1$ in each iteration is divided by its norm, to mantain convergence, and therafter it is updated by

$$w_1 \leftarrow E\left\{Z\left(w_1^T Z\right)^3\right\} - 3w_1 \tag{2.22}$$

This algorithm converges very quickly and it does not need any additional tuning, contrary to other gradient-based algorithms.

**Second Order Blind Identification - SOBI** The SOBI algorithm is introduced in [179]. The assumption made by SOBI is that the sources are mutually uncorrelated, but intrinsically autocorrelated. Since uncorrelation is a weaker condition than independence (sources may be uncorrelated, but still dependent), this algorithm is not considered an ICA algorithm.

The method first estimates covariance matrices of the pre-whitened signal at different time-lags ($\mathbf{C}(\tau), \tau \in \{1, 2, ..., K\}$), and computes the unitary matrix $\hat{\mathbf{U}}$, by jointly diagonalizing the set of $\mathbf{C}(\tau)$. The sources are then obtained by

$$\hat{\mathbf{s}} = \hat{\mathbf{U}}^H \mathbf{B}\mathbf{X} \tag{2.23}$$

where $\mathbf{B}$ is the whitening matrix.

**Joint Approximate Diagonalization of Eigenmatrices - JADE** This approach, diagonalizes the matrices of the $4^{th}$ order cumulant. It basically minimizes all the cross-cumulants between the sources. However, computing the cumulant matrices is more complicated than the correlation matrices, because of their 4-dimensional nature. Therefore, the cumulant matrices, used by JADE, are defined as follows. Let $\mathbf{X}$ be the measured signal (for example $M$ channels times $T$ time-instants). The cumulant matrix $\mathbf{Q_{ij}}$ is defined as:

$$\mathbf{Q_{ij}} = (x_i \circ x_j \circ \mathbf{X})\, \mathbf{X}^T, \quad 1 \leq i \leq M, \quad 1 \leq j \leq M \tag{2.24}$$

here "$\circ$" denotes the *Hadamard product*, which represents the element-by-element multiplication. The elements of vectors $x_i$ and $x_j$ are first multiplied, and then the resulting vector is in the same manner multiplied with the rows of matrix $\mathbf{X}$. This algorithm is introduced in [31].

### 2.3.3 Multivariate Empirical Mode Decomposition

The Extension of the EMD technique to multichannel data has also been proposed. The complex EMD algorithm [177] effectively applies real-valued EMD to the signals corresponding to the positive and negative frequency component of the spectrum of analytical signals. However, this method does not guarantee the same number of IMFs in the "positive" and "negative" set. The rotation invariant complex EMD

(RI-EMD) [4], extends the real-valued EMD to the complex (bivariate) domain in a generic way. In this algorithm, the extrema are chosen to be the points where the angle of the derivative of the complex signal becomes zero. Since all the operations are performed directly in the complex field, this method provides a single set of complex IMFs. A generalization of RI-EMD [4], also termed the bivariate EMD [163], separates fast rotating components of a complex signal from slowly rotating ones. The reader should note here that the rotations of the complex signals represented in 3 dimensions (the third dimension being time) is equivalent to oscillations of the 1-dimensional signal represented in 2 dimensions (the third dimension being time). Envelope curves are obtained by projecting a bivariate signal in multiple directions and interpolating their extrema. The local mean is calculated by averaging the envelope curves, and is then subtracted from the original signal repeatedly to sift out rotating components within the signal. The method is described by Fig. 2.7 (borrowed from [163] with permission). The major advantage of bivariate EMD is that it has the ability to extract common oscillatory modes from both input signals, and capture them in the same, complex, IMF set. This implies that the number of extracted IMFs is the same for both input channels. The RI-EMD can be viewed as a version of the bivariate EMD.

Trivariate EMD is proposed in [159]. This technique estimates the local mean and envelopes by taking projections along multiple directions in three-dimensional space. This is achieved by a lattice that is created by taking equidistant points on multiple longitudinal lines on the sphere.

Finally, the extension to n-variate EMD (called multivariate EMD or MEMD) is proposed in [160]. Here the multiple $n$-dimensional envelopes are generated by taking signal projections along different directions in $n$-dimensional spaces. These are then averaged to obtain the local mean. These multivariate extensions to the EMD algorithm are actually generalizations of the bivariate EMD algorithm [163] and trivariate EMD [159]. The code for MEMD is freely available from `http://www.commsp.ee.ic.ac.uk/mandic/research/emd.htm`.

## 2.4 Conclusion

In this chapter, in Section 2.1, we first introduced several methods for mapping one-dimensional data into two-dimensional space. This step is one of the possible preprocessing steps for application of the matrix-based blind source separation techniques to 1D signals. Among others, a fairly new method for decomposing a 1D signal into its oscillatory modes, called empirical mode decomposition (EMD), is introduced. The application of this method to vocal signals is demonstrated in Section 2.2. Finally, in Section 2.3, several matrix-based blind source separation techniques are introduced. These techniques will be extensively used in the following chapters of this thesis.

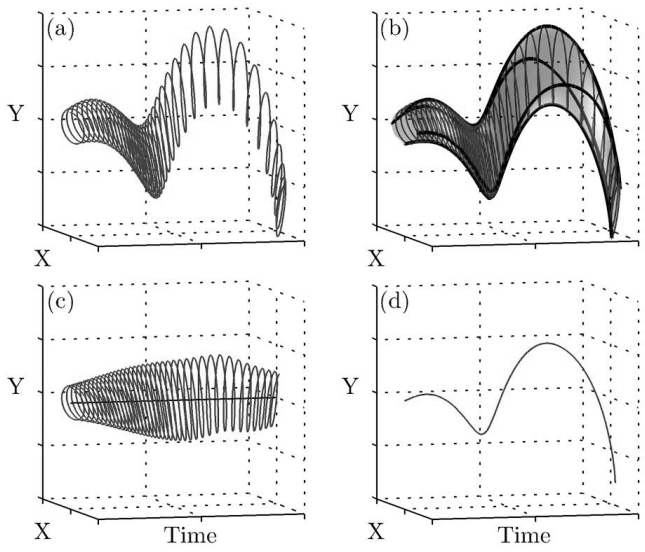


Slika 2.7: The figure is borrowed from [163] with permission ©[2007] IEEE. Principle of the bivariate extensions of EMD. (a) A complex signal represented in 3 dimensions. (b) Signal enclosed in its 3-D envelope. The black thick lines stand for the envelope curves that are used to derive the mean. (c) Fast rotating component. (d) More slowly rotating component corresponding to the mean of the tube in (analogue to the mean of the positive and negative envelopes in the original EMD algorithm) (b).

# Chapter 3

# Combining ICA with EMD for Single-Channel Decomposition

*In this chapter, we introduce a new algorithm for blind source separation of single-channel signals in Section 3.1. The performance of the EEMD-ICA method is evaluated through a simulation study, and compared to the other available single-channel separation methods. Finally, in Section 3.2 we propose the extension of the method to two-dimensional signals. The work from these chapters has been published in [134, 135].*

## 3.1 EEMD-ICA for Source Separation from Single-Channel Recordings

### 3.1.1 Introduction

A signal measured on the human body often represents a mixture of activity coming from several independent sources. Our task is then to unmix contribution sources in order to closer follow the activity of interest. In multichannel recordings, such as Electroencephalogram (EEG), this problem is efficiently handled by employing *Blind Source Separation* (BSS) techniques to unmix the given signal into sources (see, e.g., [97, 27, 51]).

*Independent Component Analysis* (ICA) is a BSS technique that extracts statistically independent sources (called independent components) from a set of recorded signals. Standard algorithms tackle the problem when the number of recording

sites (channels) is larger than or equal to the number of sources. On the other hand, there is a group of algorithms called "under-determined ICA", that can recover more signals than channels available (see [46] and references therein). In the limit, the goal can be the extraction of independent sources from a single-channel recording. Examples are cleaning the Electromyogram (EMG) signal contaminated by an Electrocardiogram (ECG) artifact [195, 176], especially from the electrodes placed on the left side of the back. The ECG artifact is very prominent in this case. Another example is in single-channel deep brain recordings where the neuronal-spikes are very low Signal to Noise Ratio *SNR* signals and are difficult to separate from noise [166, 111]. It could also be useful in preprocessing when applied to the multi-channel signals (cleaning the eye-artifacts from the EEG signal, extraction of ERP's etc).

The adaptation of ICA to single-channel signals, called Single Channel ICA (SCICA), has already been proposed in the literature [44]. It has two major drawbacks: first, the algorithm assumes stationary sources, and second the sources are assumed to be disjoint in the frequency domain. These assumptions, however do not always hold in applications.

Another possible approach to decomposing a signal of interest into different sources, which we pursue in this thesis, is as follows. If a multichannel recording can be created from a single channel signal, ICA might be used to select the signal components which are independent from each other. One way to decompose a single-channel signal into multiple components is to decompose it into different spectral modes (e.g. using a Wavelet transform or Empirical Mode Decomposition (EMD) [89]).

As explained in the Section 2.1.2, EMD is a signal analysis tool which is able to decompose any time series into a set of spectrally disjoint oscillatory modes, called Intrinsic Mode Functions (IMF). This means that two different IMFs do not overlap in the frequency domain at any time-point. The advantage of EMD, compared to wavelets, is that the EMD is a data driven algorithm. It decomposes a signal in a natural way without prior knowledge about the signal of interest embedded in the data series [75].

In this section, a new technique for single-channel signal analysis is proposed, that first decomposes the given signal into *spectrally disjoint* modes using EMD algorithm, and then ICA is applied to extract *statistically independent sources*. The source extraction capabilities of such a method are studied in depth. In particular, the performance is compared to wavelet-ICA (WICA) and SCICA by means of an extensive simulation study. Additionally, the performance of the algorithm in two real-life applications is also shown.

### 3.1.2 Methods

In this section we first revise some existing methods SCICA and WICA in subsections **SCICA** and **Wavelet-ICA (WICA)** and then we describe the new method EEMD-ICA in subsection **Ensemble EMD-ICA (EEMD-ICA)**.

#### Independent Component Analysis (ICA)

Independent Component Analysis (ICA) is a building-block in all the other algorithms. The mathematical background about techniques used here is given in Chapters 1 and 2. As mentioned there, the goal of ICA is to separate instantaneously mixed signals from the channel matrix $\mathbf{X}$ into their independent sources $\mathbf{S}$, such that $\mathbf{X} = \mathbf{AS}$, where $\mathbf{A}$ is called the mixing matrix, without prior knowledge. It is possible to estimate the contributing sources from the mixtures provided they are statistically independent of each other. In this section, the FastICA algorithm [143, 92, 182] is used. Also SOBI [179] and JADE [31] were tested, but FastICA proved to yield the best results in the general case.

#### SCICA

Single Channel ICA (SCICA) is an adaptation of the ICA algorithm to single-channel signals [44]. The algorithm is explained as follows.

First, the signal $x(t)$ is separated into a sequence of contiguous blocks $\mathbf{x}$, each having length $N$, which is to be treated as a sequence of vector observations. Then, the matrix $\mathbf{X}$ is formed as a set of observations $\mathbf{x}(k)$, $k = 1, 2, ..., K$ as follows:

$$\begin{aligned} \mathbf{x}(k) &= [x(k\tau), ..., x(k\tau + N - 1)]^{\mathrm{T}} \\ \mathbf{X} &= [\mathbf{x}(1), ..., \mathbf{x}(K)]^{\mathrm{T}} \end{aligned} \tag{3.1}$$

where $k$ is the block index, $\tau$ is a time delay , and $(K\tau + N - 1)$ is the length of the original signal. Note that the performance of the SCICA algorithm significantly depends on these parameters. However, in the paper where the algorithm is originally introduced [44], the authors leave to readers to set these parameters based on their own experience. Each row of the matrix $\mathbf{X}$ corresponds now to a single observation. Thereafter the FastICA algorithm is applied to the matrix $\mathbf{X}$ to derive the mixing and unmixing matrices $\mathbf{A}$ and $\mathbf{W}$ ($\mathbf{X} = \mathbf{AS}$, $\mathbf{S} = \mathbf{WX}$). The rows of the matrix $\mathbf{W}$ represent the inverse filters, which are used to extract the

particular source of interest. It is achieved by simply convoluting the signal $x(t)$ with the corresponding row of the matrix $\mathbf{W}$, like in Eq. 3.2.

$$s(t)_i = w_i * x(t) \tag{3.2}$$

where $w_i$ is the $i^{th}$ row of the matrix $\mathbf{W}$.

FastICA also provides the mixing matrix $\mathbf{A}$ as an inverse (or the pseudo-inverse if the number of sources and the number of channels differ) of $\mathbf{W}$ $\left(\mathbf{A} = \mathbf{W}^{-1}\right)$. Therefore we can convolve the extracted source $s(t)_i$ with the $i^{th}$ column of the matrix $\mathbf{A}$ to backreconstruct its contribution to the original signal (see Eq. reffiltering2).

$$\hat{x}(t)_i = a_i * s(t)_i \tag{3.3}$$

In Eq. 3.3, $i$ represents the $i^{th}$ column of the mixing matrix $\mathbf{A}$. When we subtract the first derived source from the original signal, we can extract the second one from this deflated signal and so on.

**Algorithm 1** SCICA

1. First split the time series $x(t)$ into a sequence of contiguous blocks $\mathbf{x}(k)$
2. Apply the FastICA algorithm to this matrix, to derive the unmixing matrix $\mathbf{W}$
3. Extract the particular source of interest by convoluting the original signal $x(t)$ with the corresponding row of the matrix $\mathbf{W}$.
4. To obtain the appearance of the desired source in the signal $\hat{x}(t)_i$, convolve the extracted source $s(i)$ with the $i$-th column of the matrix $\mathbf{A}$.
5. Subtract the contribution of the source $s(i)$ to the signal $x(t)$, redefine this newly obtained signal, and repeat the steps from 1 to 4 to further extract other sources from the new signal $x$ obtained after this subtraction.

This algorithm assumes that the signal is stationary and that it is composed of spectrally non-overlapping sources. In this case filters can be derived with pass-bands which correspond to frequency bands of these sources. SCICA estimates these filters and convolves the signal to extract the sources one by one. The algorithm is therefore blind deconvolution, rather than blind source separation technique. It is shortly outlined in **Algorithm** 1 and discussed in detail in [44].

### Wavelet-ICA (WICA)

Since the wavelet analysis is based on very similar ideas as the EMD, i.e. to decompose the signal into components of disjoint spectra, it was natural to compare

the performance of the EEMD-ICA algorithm with the WICA algorithm. First, the choice of the mother wavelet function is necessary. The best way of choosing it is that it corresponds in shape with the source we are interested in. Note that with no a priori knowledge of the signal of interest, it is very hard to make the best decision.

After choosing the appropriate mother wavelet, also the order of the Wavelet transform has to be chosen. Then the signal $x(t)$ is decomposed into spectrally distinct components using a wavelet decomposition. The ICA algorithm is then applied to the derived wavelet components $X$. The ICA algorithm again provides us with mixing and unmixing matrices $\mathbf{A}$ and $\mathbf{W}$, and the matrix of independent components $\mathbf{S}$ as an output, where the matrix of wavelet components ($\mathbf{X}$) satisfies the equation $\mathbf{X} = \mathbf{AS}$, and $\mathbf{S} = \mathbf{WX}$. Note that the interpretation of the mixing matrix $\mathbf{A}$ here is different. It does not mix sources into different channels, but into the set of wavelet components instead. If the number of extracted wavelet components is $N$, then the formula that connects the signal $x(t)$ and the sources $\mathbf{S}$ is given by:

$$x(t) = \underbrace{[11 \cdots 1]}_{N} \mathbf{AS} \tag{3.4}$$

where the matrix $\mathbf{X} = \mathbf{AS}$ is obtained from $x(t)$ using the wavelet transformation. After selecting the sources of interest (this part has to be done manually, or by exploiting a priori knowledge about the source of interest), the appearance of the particular source in the signal is achieved by multiplying that source with the corresponding column of the mixing matrix $\mathbf{A}$ (to derive its appearance in the wavelet components) and consequently summing over all the newly derived wavelet components, like in Eq. 3.5. Contrary to the SCICA algorithm, this algorithm makes no assumption on spectral characteristics of the sources. Assumptions about the statistical properties depend on the ICA algorithm used in the second step of the method. The algorithm is shortly described in **Algorithm** 2.

$$\hat{x}(t)_i = \underbrace{[11 \cdots 1]}_{N} \mathbf{A}_{(:,i)} \mathbf{S}_{(i,:)} \tag{3.5}$$

### Ensemble EMD-ICA (EEMD-ICA)

As introduced in Chapter 2, Empirical Mode Decomposition (EMD) is a single-channel technique [89], that decomposes any complicated time series into a finite

**Algorithm 2** Wavelets-ICA (WICA)

1. Select the mother wavelet and the order of the Wavelet transform.
2. Apply the Wavelet decomposition to generate the input matrix for the ICA algorithm.
3. Perform the FastICA algorithm to the set of wavelet components and derive the corresponding mixing and unmixing matrices **A** and **W**.
4. Select the source(s) of interest and multiply it with the corresponding columnd of the mixing matrix **A** to back-reconstruct its appearance in the set of wavelet components.
5. Sum over all the rows of this matrix to back-reconstruct the appearance of the particular source in the original signal (see Eq. 3.5).

set of *oscillatory modes*, called Intrinsic Mode Functions (IMF). One of the major drawbacks of the original EMD algorithm is that it is highly sensitive to noise. Therefore, a more robust, noise-assisted version of the EMD algorithm, called Ensemble EMD (EEMD), was introduced [191]. In this chapter, we denote the standard deviation of the identically distributed white noise added in the EEMD algorithm at each iteration by SD. The ratio of the noise SD to the SD of the signal will be further referred to as a *noise parameter* (*np*).

After EEMD is performed and a set of averaged IMFs is derived (last IMF being only the monotonic function with at most one extremum) FastICA is applied to the whole set of IMFs. The ICs are extracted, as well as the mixing and demixing matrices, **A** and **W**, as described in the previous Section **Wavelet-ICA (WICA)**. After selecting the ICs of interest, the signal is reconstructed first by multiplying it by the mixing matrix to derive a new IMF set, in which only the ICs of interest are present. Summing over the newly derived IMF set, similarly as shown in the Section **Wavelet-ICA (WICA)**, the appearance of the desired source in the original signal is obtained.

No IMF subset has been preselected as an input of the ICA algorithm in order to keep this part of the algorithm as automatic as possible. We select afterwards the independent component (IC) we are interested in. Note that this part has to be done by visual inspection unless some features of the signal of interest are known. The reconstruction of the signal is then straightforward. We multiply the independent component vector with the mixing matrix to regenerate the IMF set, now containing only the component of interest, and then simply add all of these IMFs together to obtain the reconstructed signal (see Eq. 3.6). This algorithm, as well as Wavelet-ICA makes no assumption on spectral characteristics of the sources. Statistical properties of the obtained sources estimates depend on the ICA algorithm used.

$$\hat{x}(t)_i = \underbrace{[11\cdots1]}_{N} \begin{bmatrix} \hat{IMF}_{1i} \\ \hat{IMF}_{2i} \\ \vdots \\ \hat{IMF}_{Ni} \end{bmatrix} = \underbrace{[11\cdots1]}_{N} \mathbf{A}_{(:,\mathbf{i})}\mathbf{S}_{(\mathbf{i},:)} \tag{3.6}$$

**Algorithm 3** EEMD-ICA

1. Perform EEMD to obtain an avarage of the ensemble of IMFs
2. Perform the FastICA algorithm to the IMFs and derive the corresponding mixing and unmixing matrices $\mathbf{A}$ and $\mathbf{W}$
3. Select the independent component (source) of interest and multiply it with the corresponding column of the mixing matrix $\mathbf{A}$ to back-reconstruct its appearance in the IMF set
4. Sum over all the newly derived IMFs to reconstruct the appearance of the source of interest in the original signal (see Eq. 3.6)

### 3.1.3 Simulations

To evaluate the performance of the EEMD-ICA method and to compare its performance in an objective way with the other available methods as outlined in Section 3.1.2 (WICA and SCICA), we performed the following two essentially different simulations. In **"Extraction of an oscillation-type source"** the signal of interest we aim to extract is a stationary signal of oscillatory type. As example we chose the extraction of a seizure event from a real-life background EEG signal contaminated by muscle artifact. In this case, the signal of interest is a stationary signal of oscillatory type which is representative for different physiological signals such as blood pressure, respiration, EEG $\alpha$-rhythm, even heart rate series in some cases etc. In the second simulation, described in **"Extraction of a spike-type source"**, the signal of interest we want to extract is spiky. As an example, we focus on the extraction of ECG artifacts from real-life EMG signals. Simply subtracting the derived artifact from the original signal yields the artifact-free EMG data. This spiky type of data is representative for a whole class of artifact removal problems such as extraction of ECG artifacts from other physiological signals like EEG, the extraction of interictal spikes in EEG signals, spiky type seizure detection in neonatal EEG [57], as well as spike detection in intracranial electroneural signals captured during deep brain recordings [166].

In the simulations below, the signals always represent the mixture of two sources: the signal we want to extract $a(t)$, and another, unwanted signal which is considered

to be noise $b(t)$ in the following way

$$x_\lambda(t) = a(t) + \lambda b(t), \tag{3.7}$$

with $\lambda \in \mathbb{R}$ being a proportion factor, and $x_\lambda(t)$ being a mixed signal, i.e. an input to the algorithm. An important measure here is the *Noise-to-Signal Ratio* (*NSR*) which is defined as follows:

$$NSR = \frac{RMS(\lambda \cdot b(t))}{RMS(a(t))}. \tag{3.8}$$

Changing $\lambda$ alters the *NSR* of our simulated signals. The *NSR* measure is used here rather than the more common *Signal-to-Noise Ratio* (*SNR*) to equally emphasize the behavior of the signal in the range of *NSR* from 0.05 to 1 (the power of noise is 5% to 100% of the signal power), and the range of *NSR* from 1 to 2 (100% to 200%). Note that *NSR* is simply the inverse of *SNR*.

The simulation performance is expressed in terms of the Relative Root Mean Squared Error (RRMSE):

$$RRMSE = \frac{RMS(a(t) - \hat{a}(t))}{RMS(a(t))} \cdot 100[\%], \tag{3.9}$$

where $\hat{a}(t)$ is the estimate of the signal of interest.

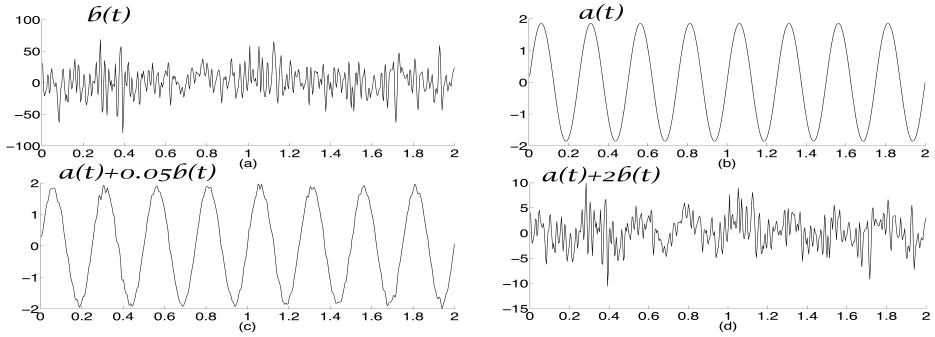


Figure 3.1: (a) Simulated background brain signal with the muscle artifact - signal $b(t)$, (b) Sinusoidal signal - $a(t)$, (c) Signal $x(t)$ for $NSR = 0.05$, (d) Signal $x(t)$ for $NSR = 2$

### Simulations setup

**Extraction of an oscillation-type source** To simulate the extraction of oscillation-type components, we consider here the extraction of a seizure event from single-channel brain recordings. The brain signal consists of awake background electrical activity from a normal subject contaminated by muscle artifact. The simulated muscle artifact was superimposed on real-life brain background activity. This defines the noise part $b(t)$ in this simulation. The amplitude of the muscle artifact was chosen in a realistic way. Epileptic activity can be modeled in two ways - either as spiky activity, or as a pure sinusoid. Here the epileptic activity was modeled as a $4Hz$ sinusoidal waveform. The frequency of the background electrical activity ranges from 0 to $30Hz$, so the spectra of the sinusoid and the background activity were overlapping. The sinusoidal signal is in these simulations denoted as $a(t)$. Signals $a(t)$ and $b(t)$, as well as the mixed signals for different *NSR*'s are shown in Fig. 3.1. In further text, this simulation will be called *"oscillation"*.

**Extraction of a spike-type source** To simulate the extraction of spiky-type sources, we mixed a pure real-life EMG signal (signal $b(t)$) with a simulated ECG artifact - a spike-train (signal $a(t)$) for different *NSR* values, as described above. The spike-train signal was a real-life QRS complex recorded from the EMG electrode repeated every 0.75 seconds, and zero padded in between. The mentioned single-spike is extracted from the EMG electrode while no muscle activity was present. These signals are shown in Fig. 3.2. The frequency spectrum of the EMG signal is broad-band $(10 - 180Hz)$ with more or less equally distributed power over the whole range, while the spike-train is a narrow-band signal $(5 - 30Hz)$. Note that the spectra of these two signals are also overlapping. In further text, this simulation will be called *"spike"*

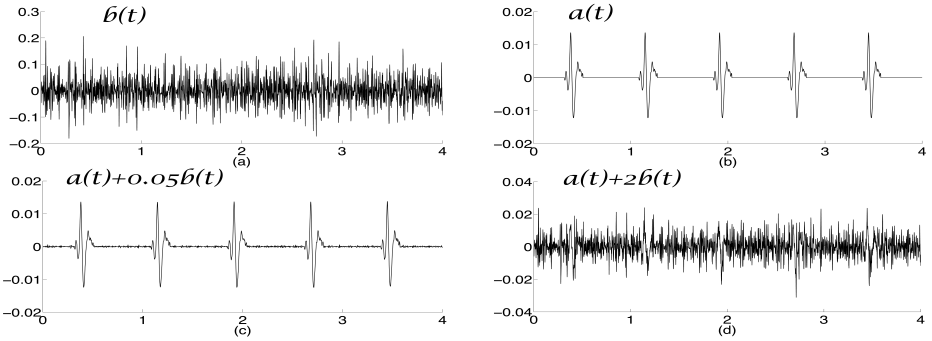


Figure 3.2: (a) Pure EMG - signal $b(t)$, (b) Spike-train - signal $a(t)$, (c) $x(t)$ for $NSR = 0.05$, (d) $x(t)$ for $NSR = 2$

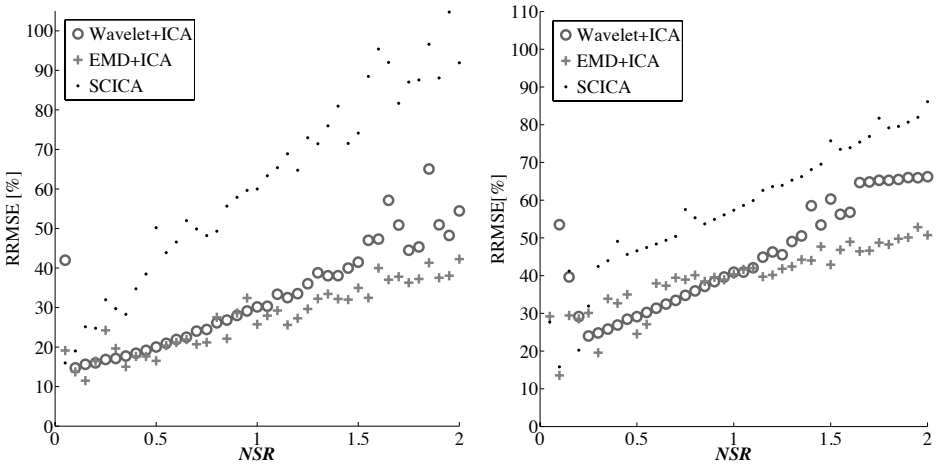


Figure 3.3: Performance comparison of the single-channel BSS algorithms for the simulation described in simulations "*oscillation*" (left) and "*spike*" (right)

### Parameter Settings

In all the simulations, the number of independent components in FastICA to be extracted was set to 5. In the SCICA algorithm the values for $K$ and $\tau$ were set to 10 and 1 respectively (these values yielded the best performance in terms of RMSE). The mother wavelet used in the WICA algorithm was Daubechies 6, and the order of the wavelet transform was set to 8. In the EEMD-ICA simulations the *np*-value used was set to 2. The number of IMFs was usually observed to be between 8 and 15 components and it only depends on the complexity of the signal (if the signal is only the sinusoid, the number of IMFs will theoretically be 1 and the residue, which is the mean value). Also, the *NSR* was set to increase from 0.05 to 2 with steps of 0.05.

### Simulations Results

Fig. 3.3 shows the performance of all the algorithms outlined in Section 3.1.2 as a function of *NSR* for the simulations in the Sections *"oscillation"* and *"spike"* respectively. Additionally, Fig. 3.4 compares the performance of the EEMD-ICA algorithm for two different *np* values (0.2 and 2), as this is a crucial parameter.

Figures 3.5 and 3.7 illustrate the EEMD decompositions of the mixed signal from the simulation *"oscillation"* and *"spike"* respectively for the $NSR = 1$ before applying the ICA algorithm. The first row shows the original signal, and the other

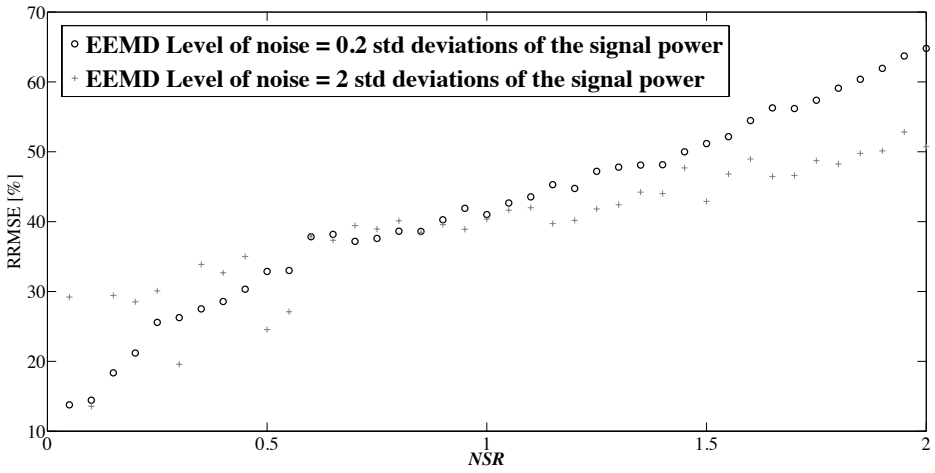


Figure 3.4: Comparison of the EEMD-ICA algorithm for different levels of added noise for spike-type simulation

rows show different IMFs. Figures 3.6 and 3.8 show the extracted independent components after applying FastICA and signal reconstruction. In both simulations the signal of interest is captured in the first component.

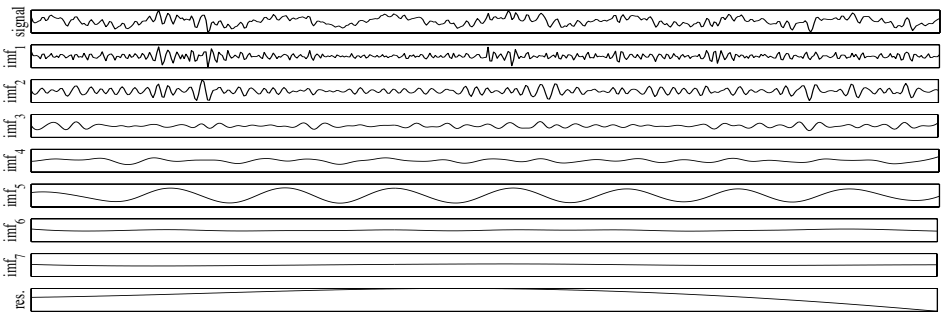


Figure 3.5: The EEMD decomposition of the signal composed of background EEG, muscle artifact, sinusoidal seizure and noise for $NSR = 1$

In Figures 3.9 and 3.10 the result of applying WICA is shown for oscillatory and spike-type signal extraction simulations respectively.

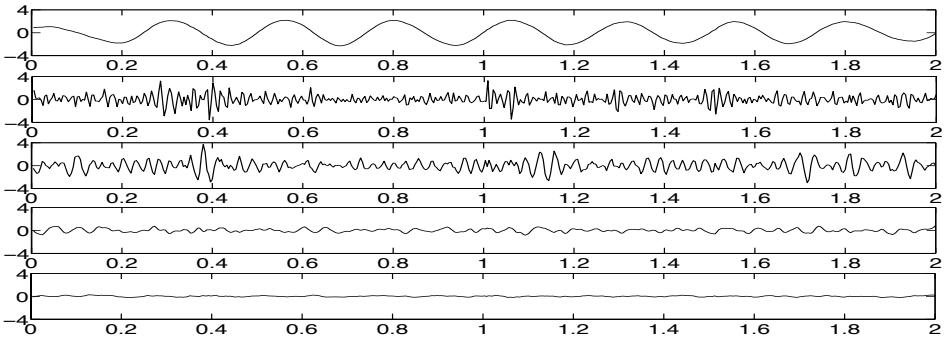

Figure 3.6: Sources extracted with the EEMD-ICA decomposition of the signal from simulation 1 for $NSR = 1$

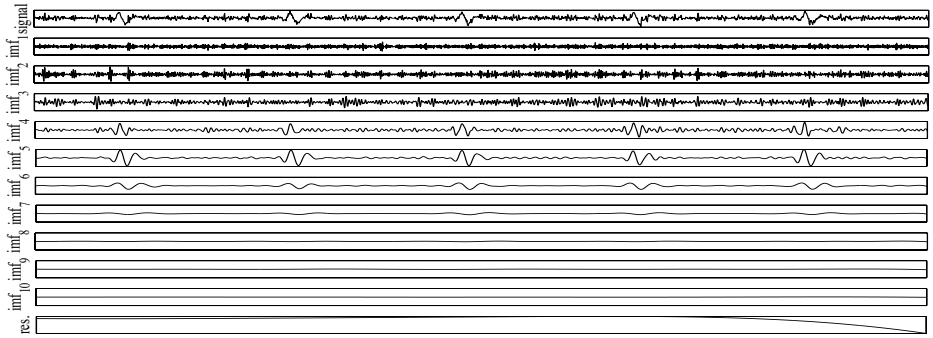


Figure 3.7: The EEMD decomposition of the EMG signal with ECG artifact ($NSR = 1$)

### Simulations Discussion

Compared to other algorithms in our simulations, EEMD-ICA performs best for high *NSR*. For low *NSR* EEMD-ICA performs similarly to WICA, although the tuning of the *np* may significantly increase the accuracy of the results. The reason for this is that a very high amount of noise is added for making an ensemble ($np = 2$) in EEMD, and the noise could not be canceled out correctly. From Fig. 3.4, it is clear that the algorithm's performance depends on this factor, and that performance for low *NSR*s can be significantly enhanced by reducing *np*. This is also one of the drawbacks of the EEMD-ICA algorithm in the sense that this parameter has to be chosen correctly in order to achieve the best performance, although the inexperienced user can choose any value between 0 (the regular EMD) and 2 and obtain a satisfactory result. One way to choose the *np* is to set it to be equal to the NSR of the signal itself. If no knowledge of the noise power is present

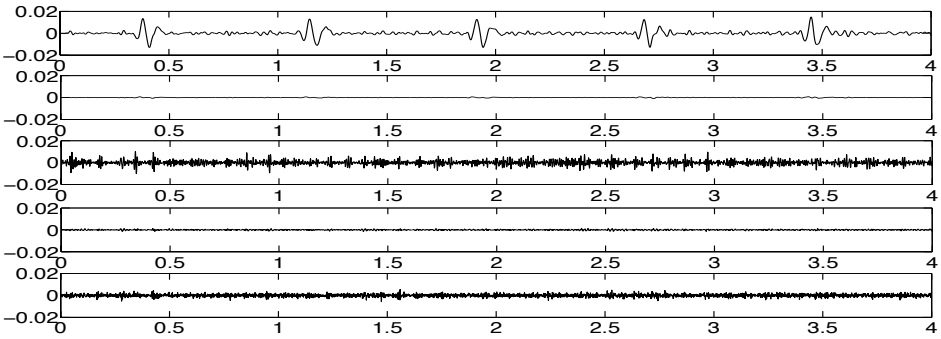


Figure 3.8: Sources extracted with the EEMD-ICA decomposition of the signal from simulation 2 for $NSR = 1$

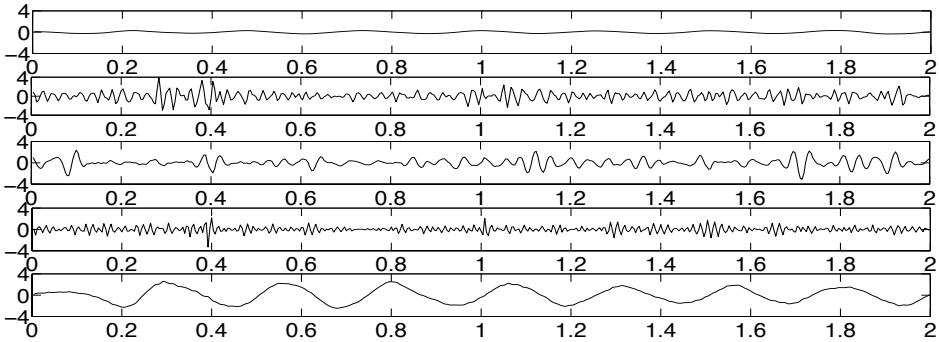


Figure 3.9: Sources extracted with the WICA decomposition of the signal from simulation 1 for $NSR = 1$

either the regular EMD technique might be used, or several $np$ values could be explored, until the best separation is achieved. In the literature [191] it is also shown that the $np$ should be smaller if the signal to be extracted has high frequency behavior and larger if the signal we want to extract is of low frequency content.

The SCICA algorithm performed clearly worse than other algorithms in both simulations. The problem with this approach is that it yields two major limitations. First, the algorithm assumes stationarity of the data, and second, it is not able to separate components with overlapping spectra. In the first simulation (*"oscillation"*) SCICA under-performed due to significant spectral overlapping of the data, although the signals to be extracted were stationary. In the second simulation (*"spike"*) its performance was more comparable to that of the other algorithms, although it was inferior to that of the EEMD-ICA algorithm due to the non-stationarity and spectral overlapping of the data from the simulation.

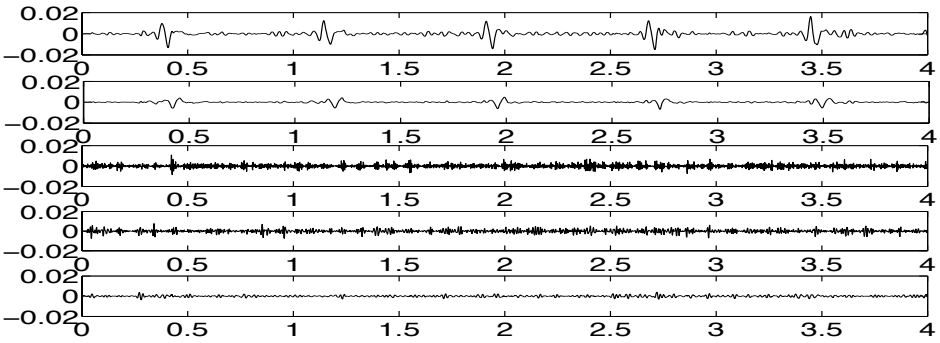


Figure 3.10: Sources extracted with the WICA decomposition of the signal from simulation 2 for $NSR = 1$

It is worth noting that in the second simulation (*"spike"*), the modeled ECG artifact was always spread over a number of ICs for the examples under study in WICA simulations (see Fig. 3.10), contrary to EEMD-ICA which could capture the signal of interest into one component only (Fig. 3.8). It is also obvious that in the first simulation ("*oscillation*"), the sinusoidal signal extracted with the EEMD-ICA algorithm (illustrated in Fig. 3.6) was much smoother than the one extracted with WICA (Fig. 3.9), despite the fact that the RRMSE in the simulation was almost equal for the particular case ($NSR = 1$). However, the WICA algorithm seemed to slightly outperform EEMD-ICA in the spiky-type source extraction simulation in the low *NSR* range. Therefore we show in Fig. 3.4, that by tuning the *np* parameter, the performance of EEMD-ICA can be significantly increased in this range. This tuning will weaken the performance for high *NSR*, although it will still be better than the one of WICA ($RRMSE = 50.73$ for $np = 2$ and $RRMSE = 64.79$ for $np = 0.2$ for EEMD-ICA, and $RRMSE = 66.22$ for WICA, Fig. 3.4). Both the shape and the amplitude of the ECG artifact peak in the EMG simulation were almost perfectly recovered using the EEMD-ICA algorithm, contrary to the other methods, where the extracted spikes were mostly changed both in shape and amplitude.

The advantage of EEMD over wavelets is that EEMD breaks the signal into its oscillatory modes, and therefore we expect the EEMD-ICA algorithm to outperform WICA in the case of oscillatory signals, which are very common in the field of biomedical data. Additionally, EEMD has a data-driven, instead of a predefined basis, contrary to wavelets and is able to deal with very local variations in the signal oscillations.

Since the spike-type data are not localized in frequency (simulation *"spike"*, figure 3.7), EEMD will yield local oscillations in several IMFs. The latter ICA processing will capture these oscillations in only one independent component. Here the reader

might argue that there is no obvious reason that variations in different IMFs can be extracted by independent component analysis.

To address this question, we refer to the work of Daubechies et al.[42]. In that paper, they consider the use of the ICA algorithms Infomax [15] and FastICA on the BOLD (Blood Oxygen Level Dependent) signal in fMRI data. These algorithms are the two most widely used ICA algorithms to analyze fMRI data, although other more general ICA algorithms exist that assume less about components in the sense of their probability distribution function, like JADE [31], and can separate mixtures into independent components for which FastICA and Infomax fail (FastICA and Infomax work well if the sources have "*generalized normal distribution*", excluding Gaussian distribution). However, Infomax and FastICA showed to outperform JADE when separating the biological signals coming from different physiological sources, which don't have statistically independent distributions per se. The issue is, that the variations in BOLD signal in different brain areas have no physiological reason to be statistically independent. Daubechies et al. show that the superior performance of Infomax and FastICA in fMRI is linked to their ability to handle effectively sparse components rather than independent components as such. Therefore we also expect FastICA performed after the EEMD to pick up local oscillations from different IMFs, caused by spike appearance in the decomposed signal, as spikes are sparse in nature, and to capture them in only 1 independent component. This discussion will be continued in Chapter 6.

When it comes to oscillatory signals, it is obvious that the EEMD algorithm is able to extract the pure sinusoid itself (simulation *"oscillation"*, Fig. 3.5) and therefore EEMD-ICA will always give a good result in extracting the oscillatory data. It is also clear that the post-processing based on ICA might not improve the result, but the oscillatory signal is still preserved, what is apparent from Fig. 3.8. The question then arises: Why do we need the ICA-step?

To answer this question, we will provide an additional simulation where we want to separate a single spike from a sinusoid and noise. In this simulation we mixed 3 signals: the single spike in the middle of the signal, with the sinusoid and the background EEG activity from simulation *"oscillation"*.

The first row in Fig. 3.11 shows the original signal, where the spike is poorly (almost not) visible, and the other rows present the extracted IMFs. It is important to notice that the EEMD was not able to separate the spike from the sinusoid-like seizure and that the sinusoid is present in two IMF channels. It is evident that no simple arithmetical operation can be applied to IMFs to separate the spike from the sinusoid. However, if we apply FastICA (Fig. 3.12), the spike is isolated in one channel, the sinusoidal seizure in another one, and the background EEG in the third channel. The sinusoid is apparently not perfectly recovered and is still distorted in the time instant of the spike appearance, due to the fact that the chosen spike had similar width as the period of the sinusoid. However, making use

of this decomposition would allow spike-type, or oscillatory-type seizure detection algorithms to perform significantly better.

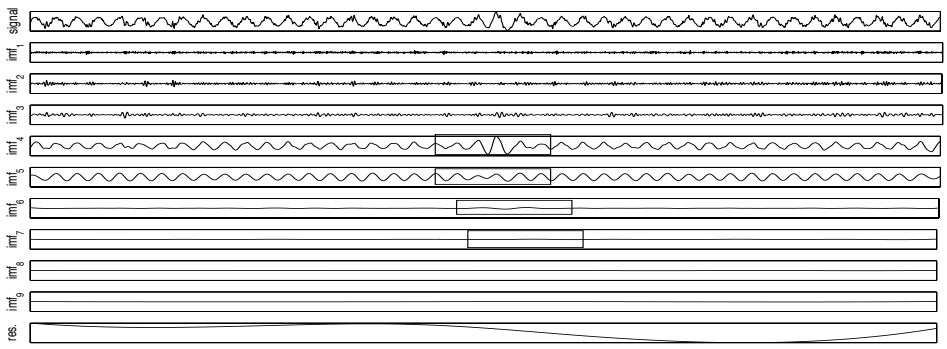


Figure 3.11: EEMD of the single spike mixed with the sinusoid and the background EEG signal

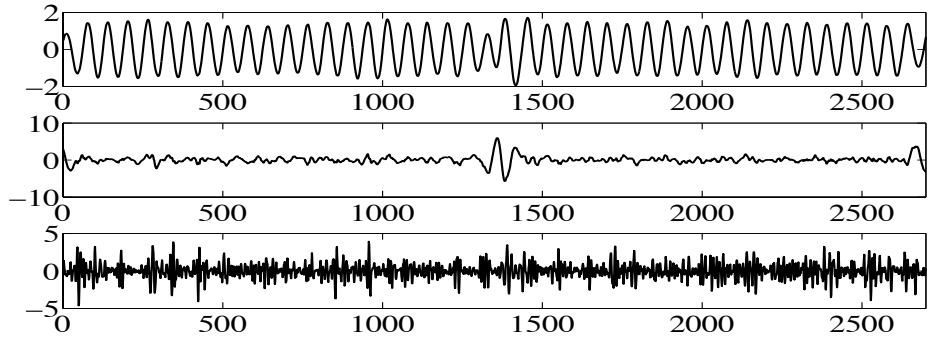


Figure 3.12: The EEMD-ICA decomposition of the single spike mixed with the sinusoid and the background EEG signal

We would like to stress here that applying the ICA technique on the IMF set makes sense only if the original sources and the IMFs are mutually linearly dependent, i.e. that the set of IMFs and the set of independent components span the same row-space, which is difficult to prove. Further more, EEMD itself is mathematically not well established. The performance of the algorithms is only proven in practice and through different simulation studies. Our simulations show, however, that combining EEMD and ICA clearly enhances source separation, and this will be further illustrated in some real-life examples in the following sections.

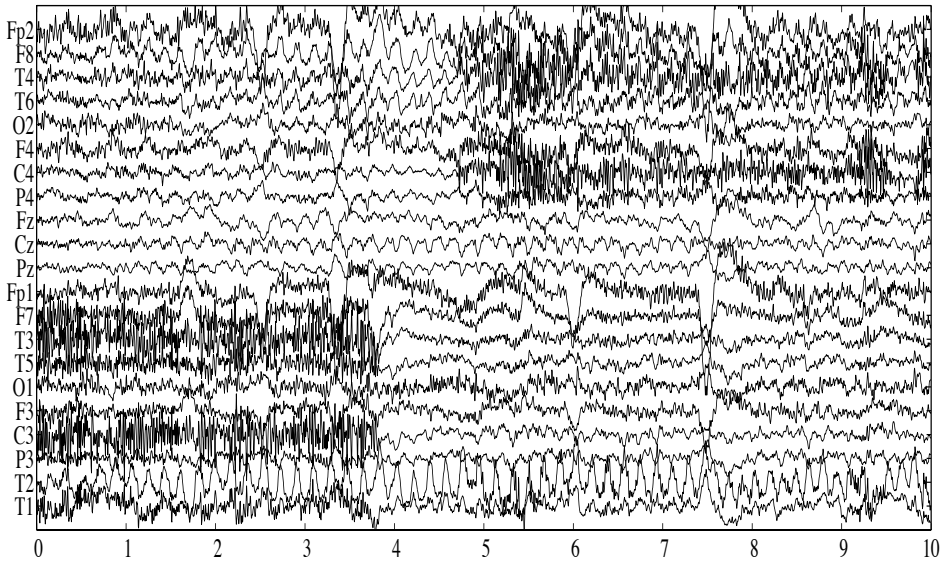


Figure 3.13: 10 seconds of 21 channel EEG recordings

### 3.1.4 Real-life application of EEMD-ICA

We will now illustrate the performance of the proposed EEMD-ICA algorithm on 2 real-life applications. In the first case we apply the EEMD-ICA algorithm to one of the EEG channels contaminated by muscle artifact, eye artifact, and seizure activity. We aim to separate this information into different sources. In the second case we will demonstrate how our new method performs in the case separating the ECG artifact from the EMG recordings, this time in-vivo. In the EEMD-ICA algorithm, the number of independent components to be extracted was set to 7 in the example "*EEG recording*" because we were interested in 3 different sources and not all of them would appear in the first 5 IC's. In the example "*EMG recording*", the number of IC's to be extracted was set to 5.

#### Real-Life examples

**EEG recordings** In Fig. 3.13, 10 seconds of 21-channel scalp EEG recordings from a long-term epilepsy monitoring unit are shown. This recording contains ictal activity from a patient with Mesial Temporal Lobe Epilepsy (MTLE), contaminated with eye blinks and muscle artifact. The sampling rate was $250Hz$. Although the single channel technique in this case is not necessary, we chose this example because lower spatial sampling can be required in wireless systems applications,

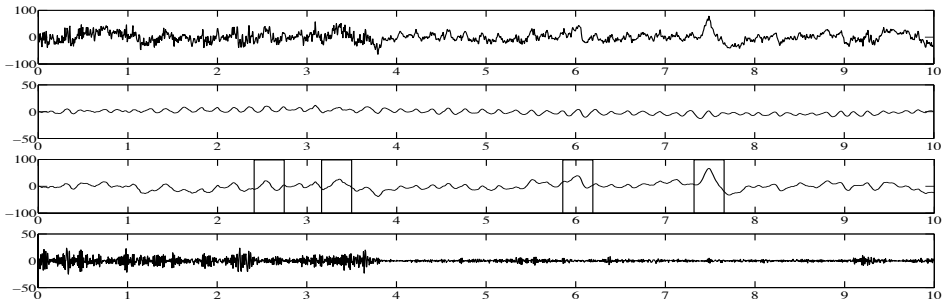

Figure 3.14: $21^{st}$ EEG channel decomposed in independent components. First row - original channel, second row - seizure event, third row - eye artifact (rectangles), fourth row - muscle activity

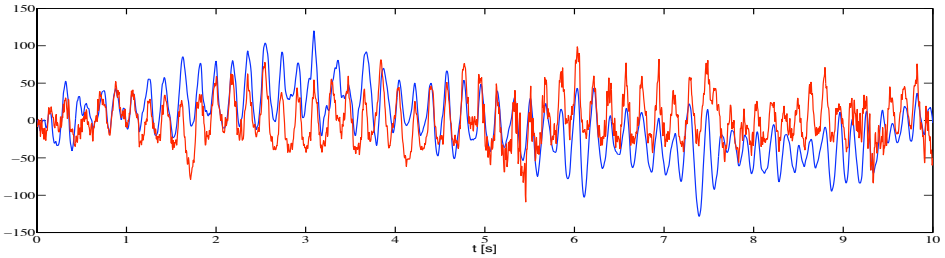


Figure 3.15: Extracted seizure activity (blue) extracted from channel T1, plotted against T2 channel of the EEG recording (red). It is clear that the extracted activity is in phase with the activity from channel T2.

and our technique might be of use. Also, it enables us to further validate our technique. Eye-artifacts can be observed around 2.5, 3.5, 6 and 7.5 seconds, and are most emphasized in the Fp1 and Fp2 channels, as expected. Seizure activity is constantly present (T2 channel), and muscle activity starts on one side of the head. We will extract all underlying signals from channel T1 by applying EEMD-ICA, because their contributions are rather weak in this channel and therefore a successful extraction of these sources is most challenging.

**EMG recording** In the upper trace of Fig. 3.16 we give a recording of 100 seconds of the EMG signal contaminated with the ECG artifact. This recording corresponds to the phase immediately after the muscle activity, when the muscle is still not in the completely relaxed state. The muscle is not in complete rest however, and therefore the power of the EMG signal is still fairly high. This is a very useful

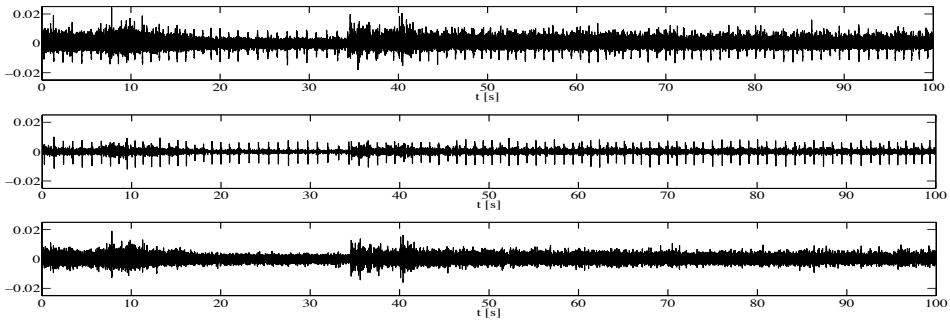


Figure 3.16: EMG recording. Upper trace - original EMG signal, middle trace - extracted ECG artifact, lower trace - cleaned EMG signal. $np$ was set to 0.5

application of our algorithm, because otherwise the EMG activity here cannot be accurately studied. In the middle trace of this figure the extracted ECG artifact is shown, and the lower trace shows the cleaned EMG signal obtained by subtracting the extracted artifact from the original signal.

### Results and Discussion

We showed results of applying our technique to real-life examples. In Fig. 3.14, the T1 channel of the EEG recordings is decomposed. After applying the EEMD-ICA algorithm, 7 independent components were extracted among which we show 3 to back reconstruct the signals shown in the same figure, representing the seizure event, eye artifact and muscle activity respectively. We can clearly notice a successful separation of the important components. The extracted oscillatory activity is in phase with the seizure activity visible in the T2 channel, see Fig. 3.15. This confirms that this is related to the seizure. This is an interesting result, since channels T1 and T2 are located on the opposite sides of the head. This means that the seizure has been picked up from the averaged reference despite the very low $SNR$. It is also clear that the eye artifact is more clearly (although not perfectly) expressed than in the original signal and that the muscle activity is well separated. We would like to stress here that these artifacts (e.g. eye-artifact) can sometimes be more clear in other leads (Fp1 and Fp2). However, in some cases (e.g. in neonates), EEG is recorded only with 8, and sometimes even with as few as 2 leads. In these cases it is very difficult to capture all the brain activity clearly, and our algorithm can be beneficial.

Fig. 3.16 shows the EMG signal contaminated by the ECG artifact. In the middle trace of this figure the extracted ECG artifact is shown, and the lower trace shows the cleaned EMG signal obtained by subtracting the extracted artifact from the

original signal. We see that the ECG artifact is successfully removed from the signal without distorting the original shape and amplitude of the EMG signal. After applying the EEMD-ICA algorithm, 4 sources were detected, only one of them containing the ECG artifact. As one can think that some EMG activity is also mixed into the ECG source, Fig. 3.17 zooms in a 1 second of the signal from Fig. 3.16 to show the performance of the proposed algorithm in detail. In the same figure the extracted artifact and the clean version of the EMG are shown. It is clear that the spike is accurately isolated (red trace), and that the cleaned EMG closely follows local variations of the original EMG in the places where the spike is not present. The channel in which the spike appears still contains some small oscillations that are not spike-related. However, these oscillations are very slow and small in amplitude, so they do not significantly change the shape of the EMG signal, and therefore will not influence various measures of the EMG activity derived afterwards. The computed ratio of the standard deviation of the cleaned EMG signal to the standard deviation of the ECG artifact is 1, which is fairly high. The *np* in these applications was set to 0.5.

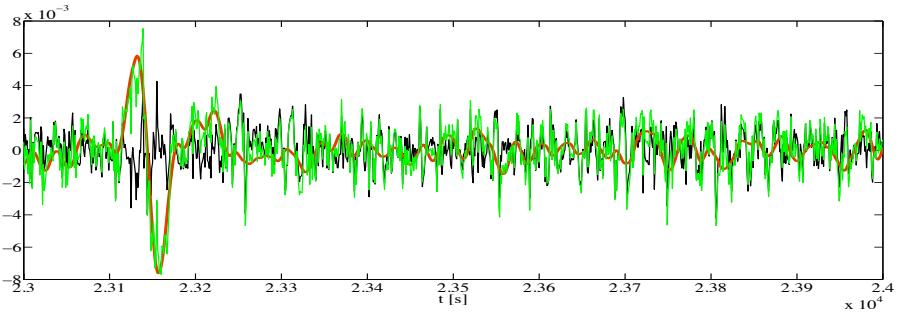


Figure 3.17: The figure shows enhanced part of the real-life EMG signal, contaminated by the ECG artifact (green), Extracted ECG artifact (red) and cleaned EMG signal (black)

### 3.1.5 Conclusion

A new method for single-channel signal decomposition into its independent components, which combines EEMD [89, 191] and Independent Component Analysis, EEMD-ICA is presented. We showed the good performance of the method and compared it to two other available algorithms for decomposing single-channel signals, Wavelet-ICA (WICA) [115] and Single Channel ICA (SCICA) [44] through various simulations. Of the three algorithms, SCICA had the worst performance. The WICA technique, although comparable with the EEMD-ICA, shows a weaker performance in our simulations. We provided 2 real-life examples

and our technique exhibited a very strong separation power, and proved to be succesful for oscillatory as well as spike-type source extraction in biomedical signal processing.

## 3.2 Generalization of the EEMD-ICA algorithm to 2-Channel Data

In this section we extend the EEMD-ICA approach to 2-channel EMD-ICA. We will show the extraction capabilities of the algorithm on 2-channel EEG signals and we will discuss the benefits and improvements compared to single-channel EMD-ICA. The work is published in [135].

### 3.2.1 Methods

#### 2-channel EMD-ICA

After bivariate EMD [163] has been performed (as explained in Chapter 2), our data is stored in a 3D array. The dimensions are spatial (different channels), times time, times frequency (the set of IMFs). There are several ways how to proceed from this point, and perform a data reduction and independent component analysis. The fact that after Complex EMD, the set of IMFs contains common oscillations from both channels allows us to meaningfully perform the Singular Value Decomposition (SVD) , and thus to reduce the dimensionality in the third dimension (IMFs) [47]. This can also be done with PCA or other data-reduction methods. This way we perform the dimension reduction, and still keep the highest variance information for each channel separately. When the data reduction has been performed, the data is stored in a new matrix, which is obtained by merging both sets of reduced IMFs (putting them on top of each other). After this, ICA is applied and a set of common independent sources has been extracted. The reader should note that all the processes are reversible, so the appearance of each source in each of the original channels can be back-reconstructed.

#### Data

To demonstrate the performance of the 2-channel EEMD-ICA, we used the same epileptic EEG data as shown in Fig. 3.13. In this setup, however, we added another channel to observe what is the benefit of using 2-channel EMD-ICA. The second channel we used was F4. This lead is interesting because its position is at the right

side of the head (contrary to T1) and the artifacts in this channel are still present, but different than in T1.

Additionally, we give an example of cleaning the ECG artifact from the EMD data (similarly as presented in Fig. 3.16). However, in this section, the corresponding ECG channel is additionally used as a reference, and it is fed into 2-channel EMD-ICA together with the EMG channel. Both EMD and ECG channels are normalized before introduced to the 2-channel EMD-ICA.

### 3.2.2 Results

**EEG signals with seizure** In Fig. 3.14, the T1 channel of the EEG recording from Fig. 3.13 is decomposed. After applying the EMD-ICA algorithm, 7 independent components were extracted among which we show 3 to back reconstruct the signals shown in the same figure, representing the seizure event, eye artifact and muscle activity respectively. We can clearly notice a successful separation of the important components. The extracted oscillatory activity is in phase with the seizure activity visible in the T2 channel (as shown in Fig. 3.15). This confirms that this is related to the seizure. This is an interesting result, since channels T1 and T2 are located on the opposite sides of the head. This means that the seizure has been picked up from the averaged reference despite the very high noise-to-signal ratio. It is also clear that the eye artifact is more clearly (although not perfectly) expressed than in the original signal and that the muscle activity is well separated. We would like to stress here that these artifacts (e.g. eye-artifact) can sometimes be more clear in other leads (Fp1 and Fp2). However, in some cases (e.g. in neonates), EEG is recorded only with 8, and sometimes even with as few as 2 leads. In these cases, it is very difficult to capture all the brain activity clearly, and our algorithm can be beneficial.

Fig. 3.18 shows the 2 independent components when FastICA only is applied to channels T1 and F4. It is obvious that there are more than 2 sources present and that FastICA was unable to successfully disjoint them, since we only gave two channels as an input. Then we show the result when 2-channel EMD-ICA algorithm is performed. EMD-ICA has extracted 7 components, 5 of which are shown in the Fig. 3.19.

**EMG signals with the ECG artifact** An additional demonstration of the 2-channel EMD-ICA is presented for cleaning the ECG artifact from the EMG sigmal in Fig. 3.20. It is obvious that the ECG artifact is successfully extracted from the EMG signal. Only the ECG signal is extracted, while the EMG activity is left intact. Especially, it is interested to see the QRS event, extracted at the time instant around the sample 7000. At this time instant it is even impossible to visually

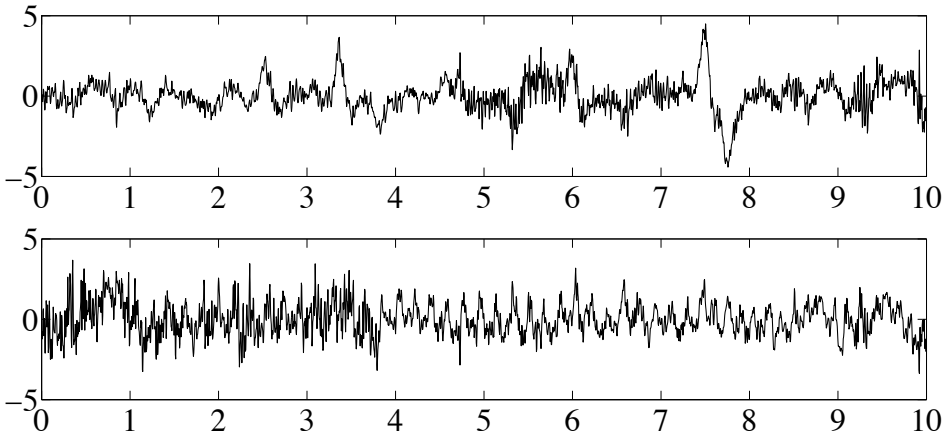


Figure 3.18: The independent sources extracted by applying the FastICA algorithm to EEG channels T1 and F4

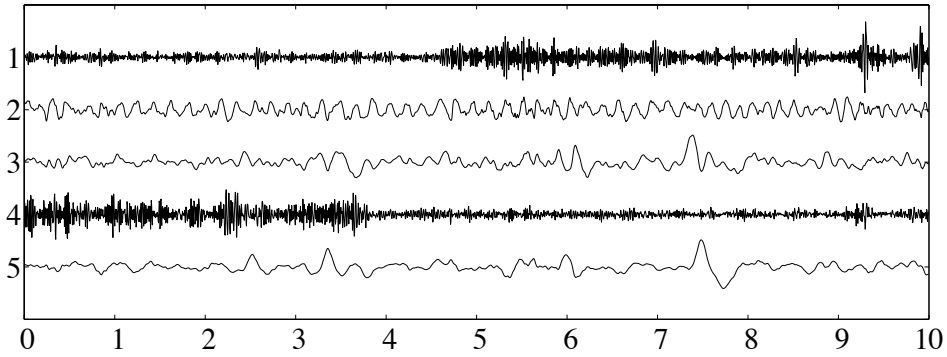


Figure 3.19: The 5 out of 7 independent sources extracted from EEG channels T1 and F4 by applying 2-channel EMD-ICA

see the ECG artifact. However, we can deduce it based on the distance between consecutive heart beats.

### 3.2.3 Discussion

Fig. 3.15 shows the decomposition of channel T1 into independent sources. The seizure activity and muscle activity are nicely captured. The extracted oscillatory activity is in phase with the channel T2. This proves that the captured activity is indeed the seizure. The eye artifacts are also more clearly (although not perfectly)

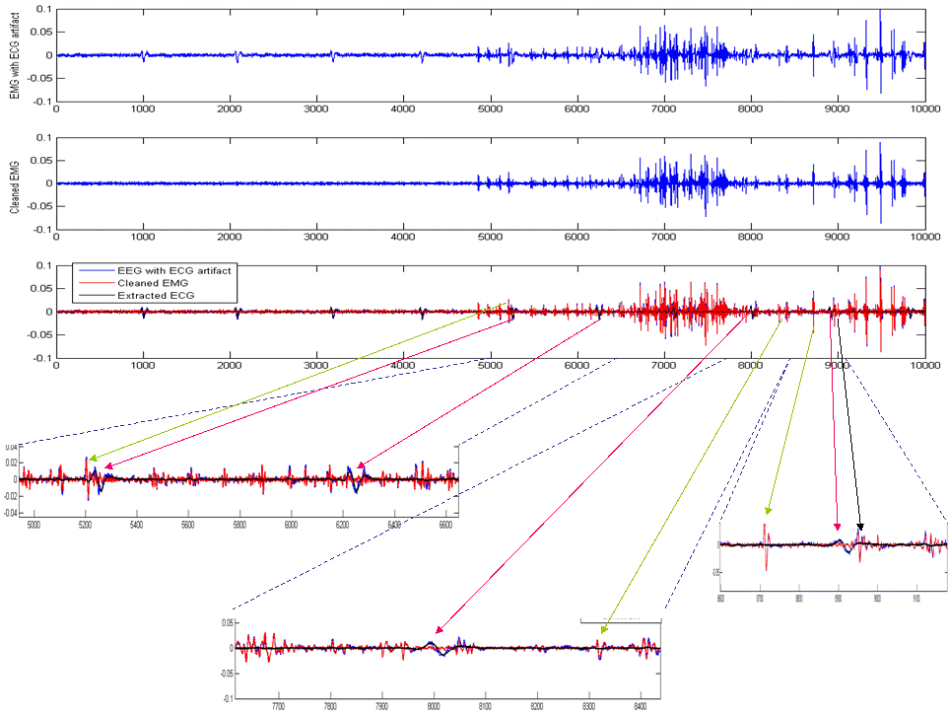


Figure 3.20: The performance of the 2-channel EMD-ICA algorithm for removal of the ECG artifacts from the EMG signal. In this case, the recorded ECG signal was used as the reference. The original EMG signal contaminated with the ECG artifact is presented in the top panel. The "cleaned" EMG is presented in the second panel. The third panel shows these two signals in blue and red respectively, together with the extracted ECG artifact in black. Additionally, some parts of the signal are shown enhanced, so the the good separation is made more clear. The red arrows point to show the good extraction of the ECG artifact. The green arrows and the black arrow point to the muscle firings that are ignored by the ECG extracted component.

isolated. However, this performance is enhanced by performing 2-channel EMD-ICA on channels T1 and F4 (see Fig. 3.19).

The performance of the 2-channel EMD-ICA is shown in Fig. 3.19. Channels T1 and F4 are given as inputs. It is clear that the eye artifacts (sources 3 and 5) are more clearly isolated than in the case of single-channel EMD-ICA (especially the artifacts appearing around 2.5 and 3.5 seconds). The eye-artifact channel is decomposed into two components, one of which (source 3) allows better reconstruction of the separate appearance of the artifact in the two observed channels. Good extraction

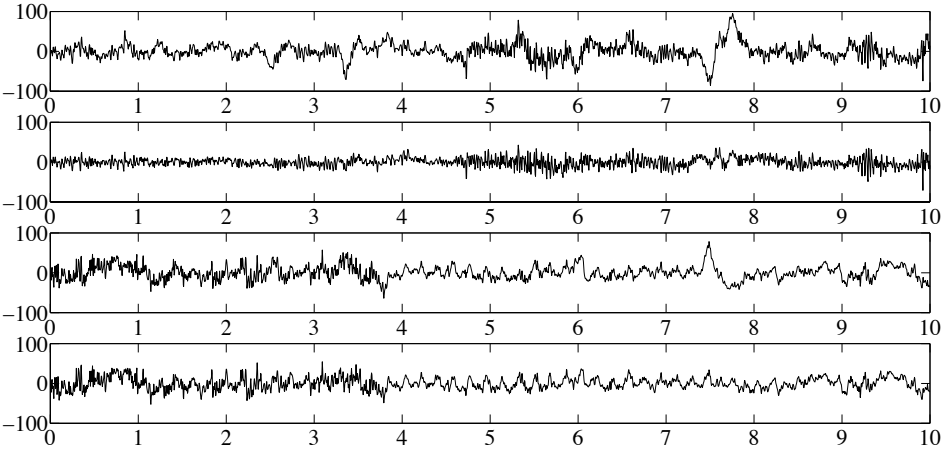


Figure 3.21: Channels T1 and F4 (traces 1 and 3) with cleaned eye-artifacts (traces 2 and 4) using two-channel EMD-ICA. Only the eye artifact is removed, but the seizure and muscle artifact are still present

of the eye-artifact is obvious from Fig. 3.21. Both channels are shown (channel F4 in trace 1, and channel T1 in trace 3). The corresponding channels after cleaning the eye artifact are shown in traces 2 and 4 respectively. It is obvious that other artifacts are not removed after cleaning the eye-artifact. Beside the eye-artifact, the muscle activity from the right side of the head (where the electrode F4 is positioned) is also nicely captured (trace 1 in Fig. 3.19). The sources which had already been extracted before by applying the single-channel EMD-ICA to the channel T1 (muscle artifact on the left side of the head and the seizure activity) are still present in 2-channel EMD-ICA. Therefore we can conclude that the 2-channel EMD-ICA makes better estimation of the common sources (eye-artifact), while the activity present in each channel separately is still preserved.

The results from the study on extracting the ECG artifact from the EMG signal are only preliminary, and are shown in Fig. 3.20. It is apparent that the algorithm is very selective towards extracting the ECG artifacts, while leaving the EMG parts unchanged. The algorithm shows a potential to be used for this purpose, but a more extensive study is needed.

## 3.3 Conclusion

In this chapter, the EEMD-ICA technique for decomposing the single-channel data into its constituent sources is introduced. The performance of this algorithm

is shown in several simulation settings as well as in 2 real-life signals. It is also compared to other available methods for single-channel source separation.

Additionally, in Section 3.2 this algorithm is extended to 2-channel signals. It is shown that it preserves the extraction of the independent sources from each channel separately. Also, it enhances the performance of common dynamics present in both input channels. As it was the case with single-channel EEMD-ICA, this extension is also shown to be capable of extracting more sources than channels recorded, and that it outperforms the single-channel method if more channels are available. This allows for analyzing sources in spatially under-sampled signals, which opens new possibilities in biomedical signal analysis.

As already mentioned in Chapter 2, multivariate extensions of the EMD algorithm (MEMD) have also been proposed [159, 160]. The application of the multivariate EMD algorithm to seizure detection in EEG signals is shown in [162]. The potential of this technique lies in separating oscillatory activity from the EEG signals, such as alpha band activity, or oscillating seizure activity. In [51], it is shown that the seizure localization can be done by first expanding matrix EEG data into 3D-tensor space using wavelet analysis, and then combining applying PARAFAC technique to extract the the seizure components. Since in this chapter it was shown that for oscillatory data, the EMD method outperforms wavelets as a preprocessing tool, the MEMD-PARAFAC tool might be promising for both seizure activity, and alpha-band activity extraction.

# Chapter 4

# Introduction to EEG-fMRI Integration

*This chapter presents an introduction to the physiological origin of the EEG and fMRI signals. Also the acquisition problems are specified, and the solution to these problems is reviewed. Different artifacts arising from simultaneous acquisition of these modalities are described. The necessary preprocessing for both modalities, together with the artifact removal algorithms are also provided. The need for the multimodal integration of these modalities is justified and finally an overview of existing symmetric and asymmetric integration approaches is provided. The work presented in this chapter is mostly compound from the manuscript published as [137, 184].*

## 4.1 Introduction

The synchronized neural firing can be measured with the electroencephalogram (EEG) as event-related potentials (ERP) with high temporal resolution. This neural activity is also accompanied by a regional increase in cerebral blood flow, which can be indirectly measured as a Blood Oxygenation Level Dependent (BOLD) signal with functional Magnetic Resonance Imaging (fMRI). Contrary to EEG, fMRI has high spatial, but very low temporal resolution. Simultaneous measurement of both can provide deeper insight into function and dysfunction of brain dynamics [180], due to the complementary nature of these signals.

In recent years, several integration approaches have been proposed. The earliest proposed methods were EEG-informed fMRI and fMRI-informed EEG analysis.

These approaches are asymmetric, meaning that one of the modalities is considered to be prior knowledge to improve the results in the other modality.

Another set of integration approaches do not use one of the modalities as prior knowledge and are thus considered to operate more symmetrically. These approaches are therefore commonly referred to as EEG/fMRI fusion. Popular methods for this purpose are data-driven signal processing techniques, which are already well-established for processing EEG and fMRI separately. The advantage of simultaneous measurements has already been exploited in numerous cognitive neuroscience applications (an overview is provided in [180]). There is also an increasing trend of using integration techniques for medical applications. For instance, the integration of EEG and fMRI allows localizing epileptic activity based on spike-triggered fMRI [17].

In this chapter, we first introduce the physiology of the visual system, since this system is explored in the following chapters. Then both EEG and fMRI signals are introduced- how they are measured, what is their physiology etc. Thereafter, we present the preprocessing steps which are necessary to obtain a sufficient quality of the simultaneously recorded data. As the reader will see, these steps are far from trivial. Finally, a broad overview of the existing integration techniques is provided, as an introduction to the following chapters about EEG-fMRI fusion.

## 4.2 Visual system

In this section, the visual system is shortly described, because this system is the focus of the research presented in later chapters.

The first organ involved in the visual system is the eye. The eye is a complex biological device that focuses light from external objects in the field of view onto a light-sensitive medium, which is composed of an array of visual receptors. Light entering the eye is refracted as it passes through the cornea. It then passes through the pupil (controlled by the iris) and is further refracted by the lens. The cornea and lens act together as a compound lens to project an inverted image onto the retina.

The retina consists of a large number of photoreceptor cells which contain particular protein molecules called opsins. Opsins absorb photons and transmit a signal to the photoreceptor cell through a signal transduction pathway, resulting in hyperpolarization of the photoreceptor.

Different populations of ganglion cells in the retina send information to the brain through the optic nerve. About 90% of the axons in the optic nerve go to the lateral geniculate nucleus in the thalamus. Another population sends information to the

superior colliculus in the midbrain, which assists in controlling eye movements, as well as other motor responses.

The optic nerves from both eyes meet and cross at the optic chiasm, at the base of the hypothalamus of the brain. At this point the information coming from both eyes is combined and then splits according to the visual field. The corresponding halves of the field of view (right and left) are sent to the left and right halves of the brain, respectively, to be processed. That is, the right side of primary visual cortex deals with the left half of the field of view from both eyes, and similarly for the left brain. A small region in the center of the field of view is processed redundantly by both halves of the brain.

Information from the right visual field (now on the left side of the brain) travels in the left optic tract. Information from the left visual field travels in the right optic tract. Each optic tract terminates in the lateral geniculate nucleus (LGN) in the thalamus.

The lateral geniculate nucleus (LGN) is a sensory relay nucleus in the thalamus of the brain. The LGN consists of six layers in humans. Layers 1, 4, and 6 correspond to information from the contralateral (crossed) fibers of the nasal retina (temporal visual field). Layers 2, 3, and 5 correspond to information from the ipsilateral (uncrossed) fibers of the temporal retina (nasal visual field). Layer 1 contains cells of the optic nerve of the opposite eye and are concerned with depth or motion. Layers 4 and 6 of the LGN also connect to the opposite eye, but to the cells of the optic nerve, which are responsible for color and edges. By contrast, layers 2, 3, and 5 of the LGN connect to the cells of the optic nerve for the same side of the brain as its respective LGN. In between these six layers are smaller cells that receive information from the cells responsible for color in the retina. The neurons of the LGN then relay the visual image to the primary visual cortex (V1) which is located at the back of the brain in the occipital lobe around the calcarine sulcus. The LGN is not just a simple relay station but it is also a center for processing; it receives reciprocal input from the cortical and subcortical layers and reciprocal innervation from the visual cortex.

The optic radiations, one on each side of the brain, carry information from the thalamic lateral geniculate nucleus to layer 4 of the visual cortex. There is a direct correspondence from an angular position in the field of view of the eye, all the way through the optic tract to a nerve position in V1. At this juncture in V1, the image path ceases to be straightforward; there is more cross-connection within the visual cortex.

The visual cortex is the largest system in the human brain and is responsible for processing the visual image. It lies at the rear of the brain, above the cerebellum. The region that receives information directly from the LGN is called the primary visual cortex, (also called V1 and striate cortex). Visual information then flows through a cortical hierarchy. These areas include V2, V3, V4 and area V5/MT.

These secondary visual areas (collectively termed the extrastriate visual cortex) process a wide variety of visual primitives. Neurons in V1 and V2 respond selectively to bars of specific orientations, or combinations of bars. These are believed to support edge and corner detection. Similarly, basic information about color and motion is processed here.

As visual information passes forward through the visual hierarchy, the complexity of the neural representations increases. Whereas a V1 neuron may respond selectively to a line segment of a particular orientation in a particular retinotopic location, neurons in the lateral occipital complex respond selectively to complete object (e.g., a figure drawing), and neurons in visual association cortex may respond selectively to human faces, or to a particular object.

Along with this increasing complexity of neural representation may come a level of specialization of processing into two distinct pathways: the dorsal stream and the ventral stream. The dorsal stream, commonly referred to as the "where" stream, is involved in spatial attention (covert and overt), and communicates with regions that control eye movements and hand movements. More recently, this area has been called the "how" stream to emphasize its role in guiding behaviors to spatial locations. The ventral stream, commonly referred as the "what" stream, is involved in the recognition, identification and categorization of visual stimuli. However, there is still much debate about the degree of specialization within these two pathways, since they are in fact heavily interconnected.

The schematic representation of the visual system is given in Fig. 4.1. The visual cortex will be examined in more detail in the Chapters 6 and 7.

## 4.3 EEG signals

Neurons possess specific electrical properties which cause their activity to produce electrical fields. These fields may be recorded by means of electrodes either at a short distance from the sources (local field potentials or LFPs), either from a longer distance, at the cortical surface (electrocorticogram or ECoG) or at the subject's scalp. The latter is most commonly called the EEG and provides a measure for the electrical communication between neurons as a function of time. However, the occurring potential changes can only be detected if many neurons synchronously de- or hyperpolarize. Therefore, it is believed that the EEG is specifically generated by the synchronous firing of many vertically oriented large pyramidal cells in the cortex. These cells are aligned in such a way that they amplify each other's extracellular field [73]. A small fraction of the summation of the resulting currents penetrates through the meningeal coverings, spinal fluid and skull to the scalp, causing different parts of the scalp to be at different potential levels. By putting

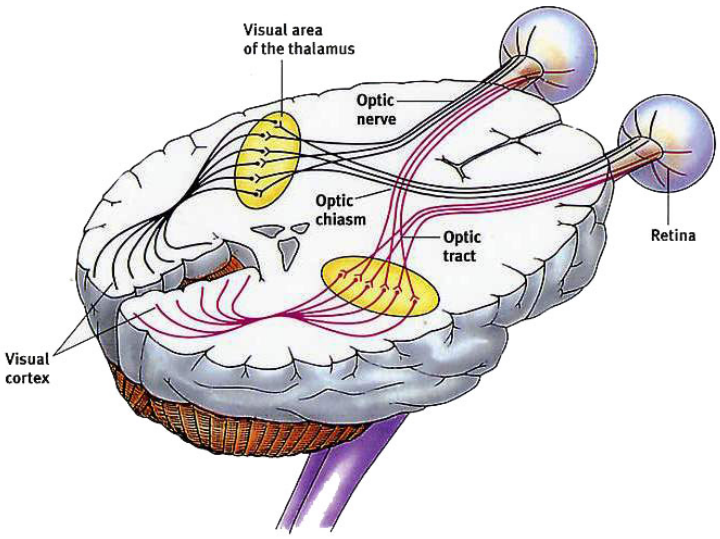


Figure 4.1: Schematic representation of the visual system. Picture from [194]

electrodes on the scalp, these potential differences can be measured as a function of time, thereby yielding the EEG.

To position the electrodes on the scalp, the International Federation of Societies for Electroencephalography and Clinical Neurophysiology has recommended a standardized electrode setting, commonly called the international 10-20 system [94, 150]. This system, illustrated in Figure 4.2, proposes electrode placement based on intersections at 10 or 20% intervals of distances between specific anatomic landmarks on the head. As such, 21 electrode positions are obtained, each indicated with a combination of two or three letters an/or digits. The first letter normally corresponds to the specific region the electrodes are located on. As such, F indicates electrodes on the frontal lobe, P on the parietal, T on the temporal and O on the occipital lobe. The letter C indicates the electrodes on the central line. For most electrodes, a second letter or a digit is added to this letter; a Z for all electrodes on the midline and odd and even numbers for electrodes on the left and right hemisphere, respectively. For setting a larger number of electrodes on top of these 21 positions, additional electrodes are equidistantly placed in between the above electrodes and the same naming approach is preserved.

Since the aim of EEG is to measure potential differences on the scalp, one or several reference electrodes have to be used. Different reference electrode placements have been used in literature, such as using the vertex (Cz), linked-ears, average reference, etc.

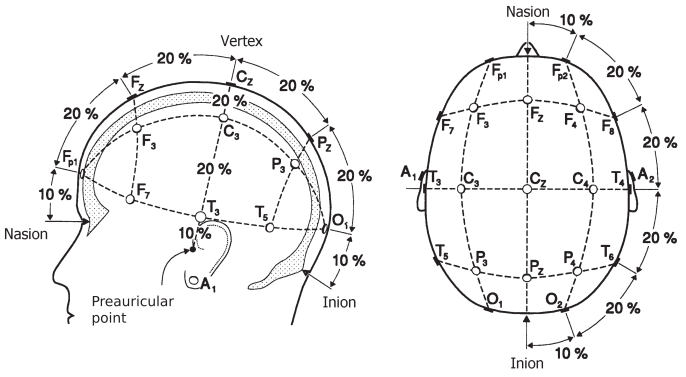


Figure 4.2: Side and top view of the standard EEG electrode placement according to the 10-20 international system. The placement is based on a grid of lines, generated by connecting specific anatomical landmarks such as the nasion, inion and preauricular points, that mutually intersect at 10 and 20% intervals of their length. The electrodes are put at these intersections (from [123]).

### 4.3.1 Typical EEG rhythms and artifacts

One of the advantages of EEG is that it is a reasonably cheap and simple way to measure brain function. Its typical patterns are relatively well studied, which allows diagnosing several brain disorders based on visual inspection of the EEG. A number of these typical patterns are specifically characterized by their different frequency ranges. Brain rhythms between 0.5 and 4 Hz are called delta waves, those between 4 and 8 Hz theta and the oscillations between 8 and 13 Hz alpha waves. Further, also beta waves ranging from 13-25 Hz and gamma waves at frequencies above 25 Hz exist. The brain waves range are shown in Fig. 4.3. In healthy adults, the amplitudes of these brain rhythms can change over states such as sleep and wakefulness or even evolve with age.

Looking at the other side of the picture, EEG also suffers from a number of limitations. First, from the above explanation about the generation of electrical brain activity,it is already clear that scalp EEG measurements record only a portion of the underlying brain activity. In addition, the spatial resolution of EEG is rather low, due to the limited number of electrodes only present on the scalp.

Another problem of EEG lies in the fact that it measures potential differences, without making a distinction between brain and other sources. These recorded potentials not generated by the brain, are called artifacts and can sometimes

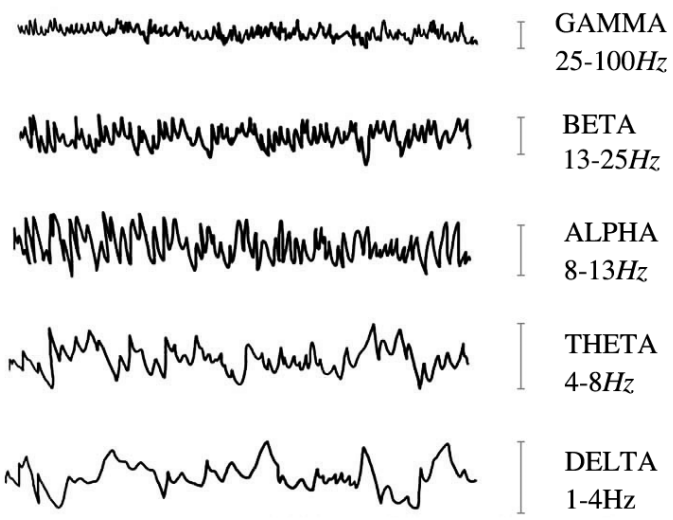


Figure 4.3: Frequency range of different brain waves.

completely cover the brain activity of interest. Origins of these artifacts can be twofold: physiological and non-physiological. Non-physiological artifacts are mainly related to power line interference or malfunctioning of the recording equipment, while physiological artifacts are caused by parts of the body itself. This latter category includes, among others, artifacts coming from eye blinking and eye movement and artifacts caused by muscle contraction. Fortunately, signal processing techniques are successfully used to remove or suppress these artifacts and recover the underlying brain signals [45, 49, 132].

### 4.3.2 Event-related potentials

EEG is used in many applications that require a measure for brain function. It has shown its value for the analysis of sleep disorders, long-term monitoring of epilepsy patients and research in the field of neuro-pharmacology. One particular field for which EEG has been used extensively is the study of event-related potentials (ERPs), responses in the brain to specific motor, sensory or cognitive events [120]. These ERPs are rather small, especially compared to the background EEG activity. Therefore, procedures for extracting the ERPs from the EEG signals are needed. The most straightforward approach to achieve this, is to simply average over a set

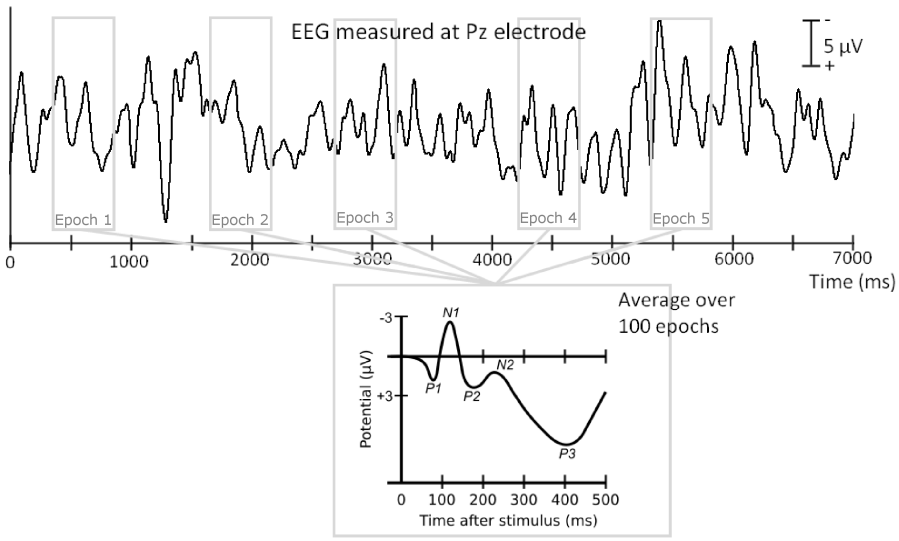


Figure 4.4: Illustration of averaging procedure for the extraction of ERPs. Stimuli are presented to the subjects and the resulting responses are averaged. The most common ERP components are also indicated in the figure.

of event trials, thereby emphasizing the activity of interest and cancelling out the other ongoing neural processes and noise (visualized in Figure 4.4). Besides this approach, which is used to express the average brain response to a certain stimulus, to investigate processes like learning and habituation, some studies focus more on single-trial ERP data. Obtaining these single trial ERPs, however, requires more advanced signal processing techniques.

ERP signals can be characterized by the amplitude, latency and spatial distribution of specific ERP components. These ERP components are the positive and negative deflections constituting the ERP waveform. They are usually represented by the letter P or N, depending on their polarity, plus a number indicating their latency or order. The most common ERP components are also indicated in Figure 4.4.

## 4.4 fMRI signals

Functional magnetic resonance imaging (fMRI) is a non-invasive technique that allows localizing active brain regions. It is not only used in experimental research for assessing brain function in, e.g., visual or cognitive tasks but also in pre-surgical examinations. Its physical basis is the phenomenon of nuclear magnetic resonance (NMR) or simply called magnetic resonance (MR). In the following sections, first

the physics of MR will be briefly described, after which the principles of both MRI and fMRI will be explained. This explanation is based on [80, 146, 157], but for a more detailed background the reader is directed to specific MRI literature, such as [95, 148].

### 4.4.1 Basis of magnetic resonance

#### $T_1$-weighting

The hydrogen atom is the most relevant atom for MRI and fMRI, due to its abundance in the human body as a part of water molecules. The nucleus of this hydrogen atom consists of one single proton, that is characterized by a certain mass, a positive electrical charge and, like all protons and neutrons, an angular momentum or a spin. Since moving electrical charges produces a magnetic moment, also the spinning, positively charged hydrogen nuclei will possess such a moment and, therefore, interact with an externally applied magnetic field $B_0$. At the atomic level, some of the protons will align with the field (lower energy state) and others will align against the field (higher energy state), as such canceling each other out. However, a slight majority will align with the field so that the net result is an alignment with the external field. The larger this external field, the bigger will be the difference in energy levels and the larger the majority aligned with the field. The total magnetic field of the excess protons is called the magnetization $M_0$. In addition, the external magnetic field $B_0$ will also cause the protons to precess or rotate around the field direction. The frequency of this precession is called the Larmor frequency and is directly proportional to the strength of $B_0$:

$$\omega_{Larmor} = -\gamma_H B_0 \tag{4.1}$$

where $\gamma_H$ is the gyromagnetic ratio, which is a nuclei-specific constant (for hydrogen atom, $\gamma_H = 42.6 \frac{MHz}{T}$).

Applying an additional, oscillating, magnetic field $B_1$ (also referred to as an electromagnetic radio frequency (RF) pulse) tuned to the Larmor frequency, transmits energy to the nuclei, causing some of the protons to jump to the higher energy state. In addition, the precession of the nuclei will be brought in phase. As a result, at the macroscopic level, the magnetization vector $M_0$ (that we consider originally aligned with $B_0$ along the Z-direction), spirals down to the XY-plane (with $B_1$ in the X-direction). This is illustrated in Fig. 4.5, where the magnetization vector is presented in a rotating frame (meaning that the reference system is set so that the spiral movement does not exist).

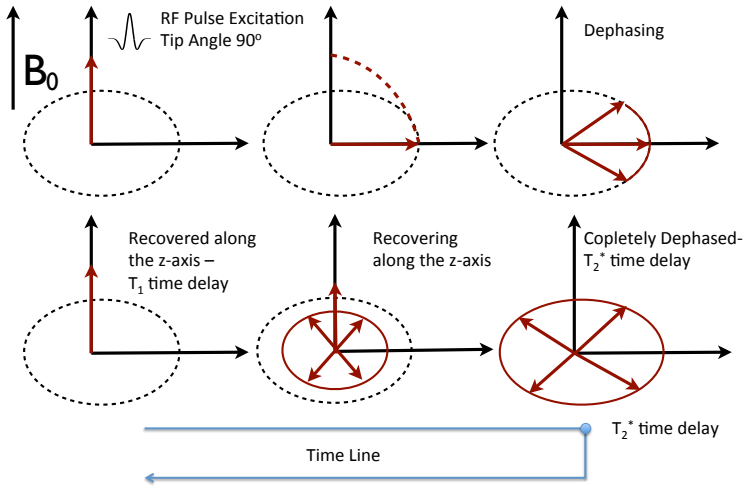


Figure 4.5: Schematic representation of the magnetization going down to the XY-plane when an oscillating magnetic field is applied and the dephasing in the XY-plane due to nuclei interactions and field inhomogeneities. The time line starts in the upper left panel, then proceeds to the upper right corner, and then back to the lower left corner (as depicted).

Removing the RF pulse causes some of the protons to return back to the lower energy state, thereby releasing a photon. On the macroscopic level, this corresponds to the magnetization vector recovering back to $M_0$ along the Z-direction at the expense of the component in the XY-plane. This releases the originally absorbed RF energy, partly as electromagnetic radiation, partly heating up the surrounding tissue. The magnetization recovers with the following formula:

$$M_z(t) = M_0 \left(1 - e^{-\frac{t}{T_1}}\right) \tag{4.2}$$

The recovery of the Z-component to $M_0$ is called $T_1$ relaxation, because its time course is characterized by an exponential curve with a time constant $T_1$. This $T_1$ is unique for every tissue and indicates the time after the excitation pulse when 63.2% of the magnetization is again aligned with $B_0$, as shown in Fig. 4.5.

The $T_1$-weighted scans, are basic MRI scans that differentiate fat from water (fat being bright and water being dark). The fat-water contrast can be enhanced

by introducing another (inversion) pulse, leading to the following magnetization recovery function:

$$M_z(t) = M_0 \left(1 - 2e^{-\frac{t}{T_1}}\right) \tag{4.3}$$

In this case, first the $180^o$ pulse is applied to invert the longitudinal magnetization $M_0$ in the negative direction. After the "inversion time" ($TI$), the transversal pulse ($90^o$) is applied, to obtain the transverse magnetization. Since the $T_1$ constant for fat is much smaller than the $T_1$ constant for water, the $TI$ time is chosen such that the influence of fat is cancelled (it will obtain no transversal magnetization, due to absence of the longitudinal magnetization at the time-instant when the transversal pulse is applied). Therefore, the fat-water contrast will be enhanced. This concept is used in the Magnetization Prepared Rapid Gradient Echo (MP-RAGE) sequence.

### $T_2$- and $T_2^*$-weighting

As explained above, applying the oscillating magnetic field $B_1$ brings the precession of the protons in phase. The precession rate of these protons depends on the strength of the magnetic field they experience.

However, spins are not always aligned and in phase, because they experience a different magnetic field throughout the tissue. These field variations can be time-constant and time-varying. Time-constant field variations may arise due to imperfections in magnet design (inhomogeneity of $B_0$). However, even if $B_0$ is fully homogenic, the tissue being imaged can distort the fields as a result of their magnetic properties.

In contrast to this fixed field variation, other mechanisms can also lead to the (time-varying) field inhomogeneity. This is due to the fact that protons are slightly magnetic, or due to diffusive movement of spins in microscopic magnetic field inhomogeneities. This mechanism is referred to as "spin-spin" relaxation.

Therefore, after the transversal pulse $90^o$ has been applied, the sum of the individual magnetization vectors is going to decrease due to this progressive dephasing, resulting in the decay of NMR signal (Fig. 4.5). This dephasing is the consequence of both time-constant and time-varying field changes, and both these phenomena will contribute to the decay time constant $T_2^*$.

However, using a special combination of excitation pulses, known as a spin-echo pulse sequence, it is possible to measure the signal decay time constant arising only from the time varying changes in the magnetic field to quantify $T_2$. The initial transverse magnetization will decay to zero as follows:

Table 4.1: The approximate values of the $T_1$ and $T_2$ constants for different tissue types.

| Tissue Type | Approximate $T_1$ value in $[ms]$ | Approximate $T_2$ value in $[ms]$ |
|---|---|---|
| Gray matter of cerebrum | 920 | 100 |
| White matter of cerebrum | 780 | 90 |
| Cerebrospinal fluid (similar to pure water) | 4200-4500 | 2100-2300 |
| Oxygenated blood | 1350 | 200 |
| Deoxygenated blood | 1350 | 50 |

$$M_{xy}(t) = M_{xy_0} e^{-\frac{t}{T_2}} \tag{4.4}$$

Therefore, after a time $T_2$, the transverse magnetization vector value drops to around 37% of its initial value.

The $T_2$ time and $T_2^*$ constant are connected with the following equation.

$$\frac{1}{T_0^*} = \frac{1}{T_2} + \gamma \delta B_0 \tag{4.5}$$

The standard values of these time-constants for some tissues are given in Table 4.1.

### 4.4.2 Acquisition of anatomical images

The above explained time constants are tissue dependent and can thus be used to make brain images allowing to distinguish between different anatomical regions and tissue types. These time constant maps are obtained by selecting appropriate recording parameters such as the most optimal pulse sequence and a proper repetition (TR) and echo time (TE). The TR is the time between two consecutive RF pulses while TE is related to specific pulse sequences like the spin-echo and gradient-echo characteristics. To encode the spatial location, strong magnetic field gradients are applied. These gradients, provided in all directions, cause nuclei at different locations to rotate at different speeds. Since these spatially varying rotation frequencies are known, they can be used to accurately determinate spatial location. More information on the acquisition of MRI can be found in [95, 148].

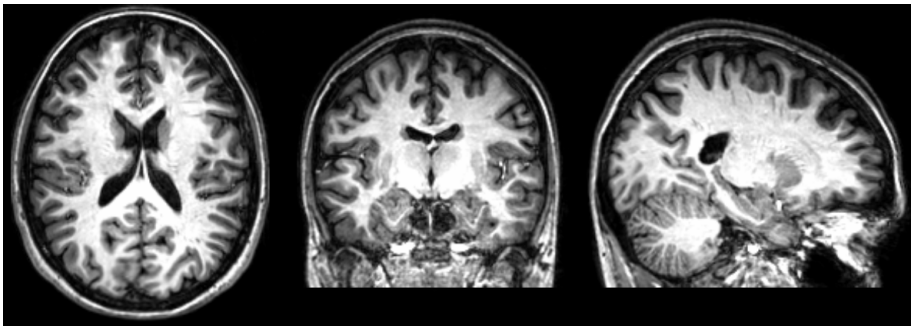

Figure 4.6: Example of a $T_1$-weighted MR image, with from left to right: an axial, a coronal and a sagittal slice.

An example of a $T_1$-weighted image is given in Figure 4.6. The size of the voxels (three-dimensional version of a pixel) in this image is $3 \times 3 \times 3$ mm.

### 4.4.3 Acquisition of functional images

fMRI is based on local-field disturbances, which are the consequence of changes in blood flow volume and blood oxygen concentration as measures for brain activity. These phenomena will be explained in this section.

Neurons in the brain consume oxygen. This oxygen is continuously supplied to the neurons by the blood in which the oxygen is attached to haemoglobin molecules. When neuronal activity increases, also more oxygen is needed. This additional oxygen is provided by an increased blood flow, leading to an increased concentration of oxygenated blood in the capillaries surrounding the active brain areas. Since oxygenated and deoxygenated blood have different magnetic properties, their difference in concentration can be measured with an MR scanner. More specifically, the oxygen concentration in the blood affects the magnetic environment of the hydrogen nuclei. As a consequence, low oxygen concentrations will cause faster dephasing of the protons and thus a lower $T_2^*$ time constant. To remind the reader, this dephasing is due to field imperfections, which are the consequence of tissue distortion, and not spin-spin interactions. Therefore neither $T_1$- or $T_2$-weighted imaging techniques are able to capture this phenomenon. MR images reflecting $T_2^*$ will be brighter in active brain areas (longer $T_2^*$), an effect that is called the blood oxygen level dependent (BOLD) effect. These MR images are obtained with the gradient echo planar imaging sequence, which is especially sensitive to the $T_2^*$ constant.

In reality, the signal time course following neuronal activation, is not limited to a simple increase and decrease. It follows a specific pattern, the so-called

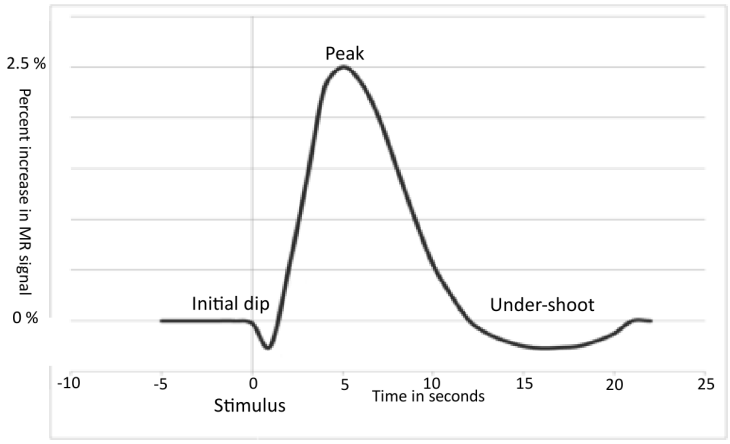


Figure 4.7: Illustration of the haemodynamic response after the perception of a specific stimulus (adapted from [88]).

haemodynamic response, that can be visualized with the haemodynamic response function (HRF). The physiology behind the course of this response (illustrated in Figure 4.7) is, however, only partially understood.

## 4.5 EEG Preprocessing

### 4.5.1 Gradient-artifact removal

When recorded simultaneously with fMRI, EEG data are highly contaminated with artifacts. Radio-frequency (RF) and gradient artifacts, which may have amplitudes 10 to 100 times larger than the EEG signal itself, occur due to switching magnetic fields during fMRI acquisition. These artifacts occupy a broad frequency spectrum, which overlaps with the frequency spectrum of the EEG information. It is shown that fourth-order low-pass filtering with a cutoff point as low as 13 Hz cannot suppress imaging artifact in ECG signals and gives considerable ECG signal distortion [71]. In this context, EEG and ECG signals have similar spectral content so similar results would be expected for EEG.

Nevertheless, since this artifact is invariant over time, a subtracting procedure based on an average artifact template (proposed in [2]) works reasonably well in most applications. This method consists of two stages. First, an average artifact waveform is calculated over a fixed number of epochs and in the second step, this waveform is subtracted from the EEG for each epoch. Adaptive noise cancelling

is then optionally used to attenuate any residual artifact. The top panel of Fig. 4.8 shows 5 seconds of the acquired EEG signal inside the magnetic field with gradients. The same EEG signal segment, after successful gradient artifact removal and low pass filtering (30Hz) is shown in the bottom panel of Fig. 4.8. One can observe that the amplitude of the signal is significantly reduced (from around 2mV down to only a few micro-volts).

### 4.5.2 Ballistocardiogram artifact

A bigger challenge is posed by the ballistocardiogram (BCG) artifact, produced by cardiac pulse-related movement of the scalp electrodes inside the magnetic field. This artifact is still visible after the gradient artifact has been removed (Fig. 4.8 - bottom panel). With every heart beat, the electrodes are slightly displaced, therefore producing the artifact, which follows closely the QRS complex on the ECG lead. Therefore, measuring ECG inside the magnetic field and detection of the QRS complex helps with removing this artifact. Not only the exact cause of this movement is still a matter of investigation, the removal of this artifact is also a problematic issue, reported in many simultaneous EEG/fMRI studies (e.g. [53]). Many methods have already been proposed for this purpose. However, before the algorithms for BCG artifact reduction can be applied, the QRS events have to be properly detected.

For this reason, ECG is measured simultaneously with EEG with one lead, and the method for detecting QRS on this lead can be summarized as follows. The ECG data is first filtered, and then a complex ECG signal is constructed by applying the k-Teager energy operator. In this way a specific amplitude-frequency ratio is emphasized. Then, three different thresholds are computed from this complex signal, and QRS peaks are detected each time the amplitudes exceeds the sum of these three thresholds. Further details can be found in [147].

Although this procedure showed high sensitivity and specificity in [147], in our study the method failed in several datasets, meaning that the artifacts stayed partly misaligned. These problems are mostly caused by the bad ECG signal quality. The ECG wire is the longest one, and in the strong magnetic field it is mostly subjected to artifacts which may lead to saturation. However, since this artifact is also present on the EEG leads, instead of creating the template only from the ECG lead, it may be created taking more channels into account, therefore enhancing the correlation. The second problem might be the fact that an average template is used for the correlation and that this template is not updated in between the two alignment steps.

We, therefore, propose the improved iterative method for the correlation-based alignment [136]), based on the following steps. If the initial detection is bad (i.e. more than 20% of the QRS are wrongly detected), the detection step can

be performed taking either another electrode, or a set of additional electrodes. Afterwards, the detection should be checked for missing R-peaks, and these should be added either automatically (e.g. based on a mean RR-distance), or manually. Redundant R-peaks also have to be removed. After all this has been done, the correlation-based alignment (including one or more EEG channels) can be performed again to correct the misaligned peaks.

### 4.5.3 Algorithms for the BCG-artifact removal

The algorithms for the BCG-artifact removal can be roughly subdivided in two groups. The first group of algorithms is based on channel-wise artifact template subtraction. The way this artifact template is generated differs among different approaches. The first study [3] aimed at constructing a dynamic average artifact template (similarly to what has been used for gradient artifact removal). Variations on this average template followed based on median filtering [68] and Gaussian weighted averaging [82]. Finally, the Optimal Basis Set (OBS) of principal components for the template creation is suggested [147]. This technique relies on the idea that principal component analysis (PCA) applied to all artifact occurrences in each channel separately makes it possible to capture the temporal variations of the BCG artifact. The resulting averaged ERP over one subject with its standard deviation is shown in Fig. 4.10 before and after BCG artifact removal. It is apparent that the standard deviation significantly reduces. This is especially obvious during the prestimulus interval (-100 $ms$ - 0 $ms$), where the baseline is flat after the BCG artifact is removed, whereas the oscillations are visible when the OBS is not performed.

The methods from the second group are based on blind source separation (BSS) techniques. Several algorithms can be used for this purpose. The most widely reported blind source separation technique for BCG artifact removal is Independent Component Analysis (ICA) [175, 17, 125]. This method is used to recover underlying sources of the recorded data, assuming that these sources are mutually statistically independent. ICA applied to EEG data contaminated with BCG artifacts can potentially identify both brain- and artifact related sources, given that they are independent, thereby cleaning up the EEG by removing the artifactual sources.

However, most ICA algorithms assume stationarity of the underlying sources. Since the BCG artifact shows a considerable spatial variation across its occurrence [185], satisfying this assumption can be problematic. For this reason, it was suggested to apply OBS prior to ICA [55], instead of applying ICA directly on the EEG data. This approach would combine the strengths of both methods, removing the major part of the artifact with OBS and its residuals with ICA.

In [185], several methodological issues are clarified regarding the different approaches with an extensive validation based on ERPs. Also the advantages of applying ICA

after OBS is discussed and compared. Most attention in this work was focused on task-related measures, including their use on trial-to-trial information. Both OBS and ICA proved to be able to yield equally good results. However, ICA methods needed more parameter tuning, thereby making OBS more robust and easy to use.

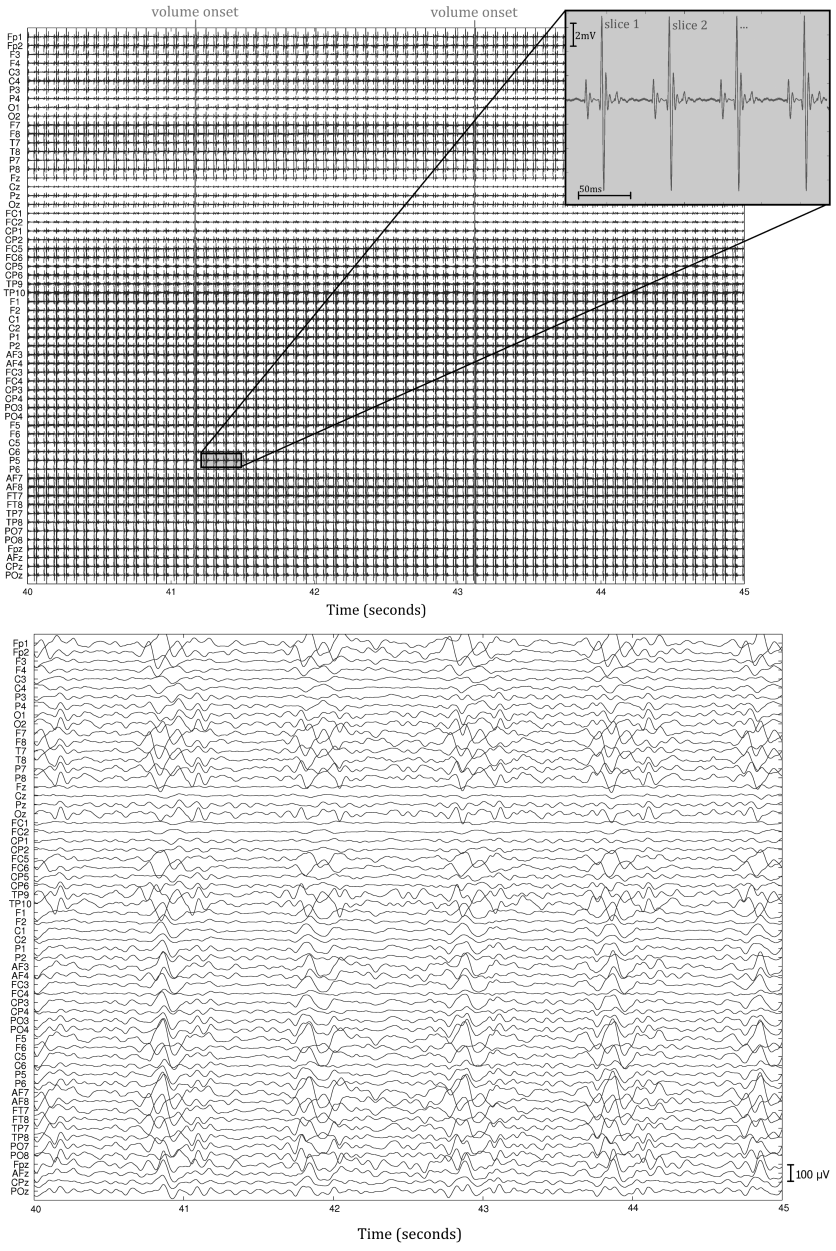


Figure 4.8: Top plot - EEG data segment recorded inside the scanner during the fMRI acquisition. Gradient artifacts are clearly visible. Bottom plot - EEG signal after gradient artifact reduction and low-pass filtering. The major residual artifact in this plot is the ballistocardiogram artifact.

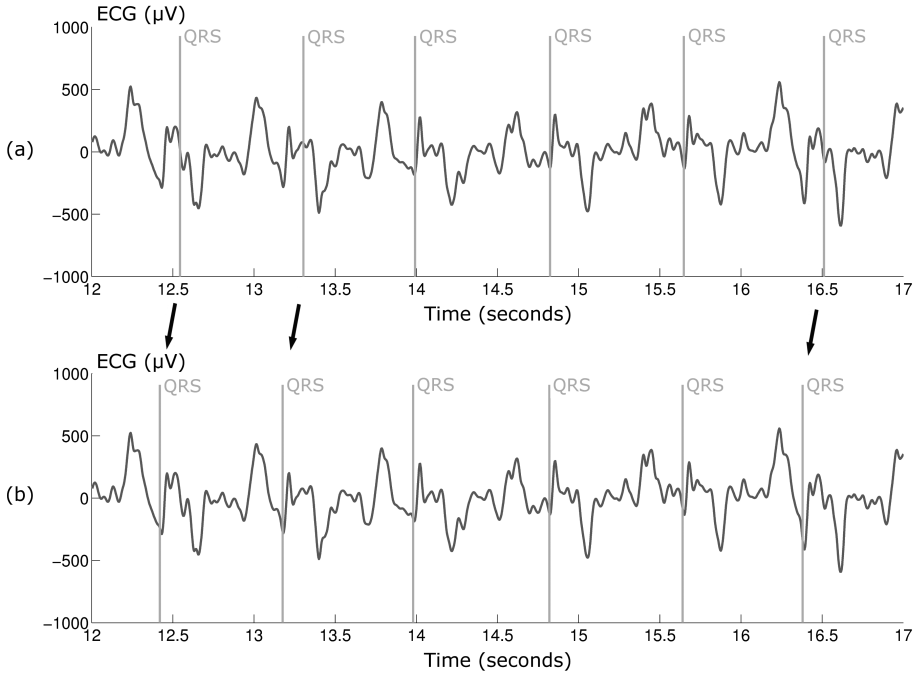


Figure 4.9: (a) Five seconds fragment of ECG data with green marks corresponding to detected QRS complexes obtained with regular detection. Three of the detected QRS complexes (3,4 and 5) are correctly placed. However, the other three are missplaced. (b) Same ECG fragment with new QRS timings obtained after the improved correction procedure.

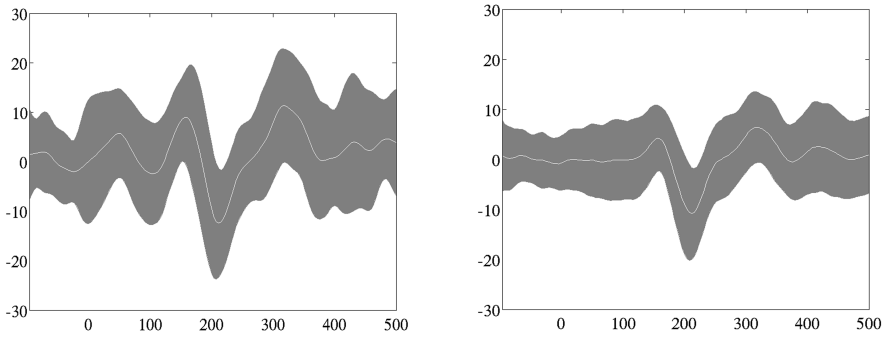


Figure 4.10: Averaged single-subject ERP (white) with its standard deviation (gray) over trials before removing the BCG artifact with the OBS method (left). The average ERP of the same subject after the BCG artifact removal is shown in the right panel.

## 4.6 fMRI Preprocessing

### 4.6.1 Data Preparation

When it comes to preprocessing the fMRI data, other difficulties are encountered. Several steps are required from acquisition of the fMRI image, until the data can be fused with ERPs. These steps are now shortly reviewed.

**Slice-Time correction** The acquisition of one complete fMRI volume requires the successive acquisition of a specific number of slices, and the whole volume is acquired in around 1.5 to 3 seconds. This means that the difference in time when the first slice and the last slice are acquired, is in the order of 2 seconds. Therefore, in some studies, "slice time correction" is applied to compensate for this delay. This means that each slice is interpolated to the specific time-instant in each acquisition (most usually the acquisition time of the first slice, or the acquisition time of the intermediate slice).

**Spatial Realignment** After the slice time correction, the "spatial realignment" of the acquired images has to be performed. Although all the necessary precautions have been taken to prevent the head motion, displacements up to several millimetres can still occur. This can lead to unwanted changes in some voxels, and therefore this has to be corrected for. What is most commonly used in practice is to select one acquired volume as a reference scan, and to realign all the other volumes to this reference volume.

Six parameters are estimated for this purpose (3 for rotation, and 3 for translation). These parameters are estimated such that the least squares error is iteratively minimized. The full description of the algorithm can be found in [81]. After the parameters have been estimated, they are applied back to the images based on interpolation. Fig. 4.11 shows the evolution of the six parameters over scans.

**Coregistration** with the anatomical image can also be applied. This step can even be skipped, but it is useful to visualize the brain activations overlaid over the anatomical image. A rigid-body transformation is used for co-registration, including three translations and three rotations along the different axes. The illustration of coregistration is provided in Fig. 4.12.

**Normalization** To compare the results obtained in different subjects, it is necessary to map all of their brains into the same space. Usually, all the brains are mapped into a common template space (e.g. Montreal Neurological Institute (MNI) template).

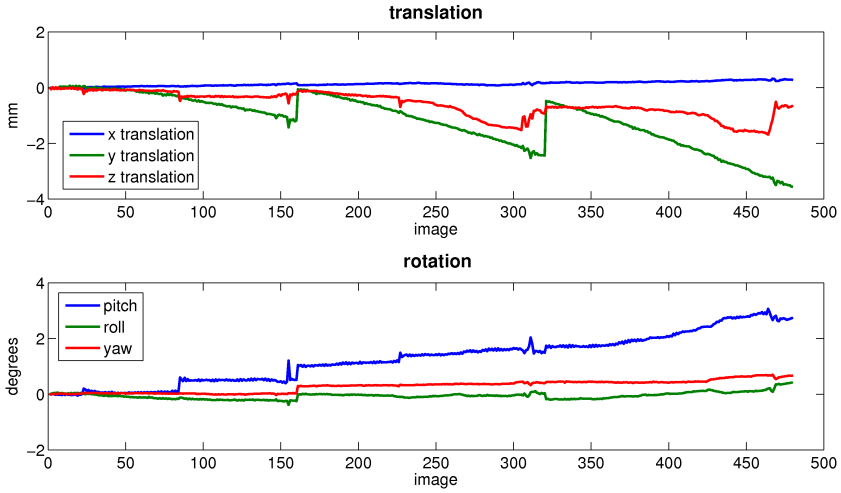


Figure 4.11: Evolution of the six spatial realignment parameters used for movement artifact correction of the fMRI data. Both the three parameters for translation and the three for rotation, are shown.

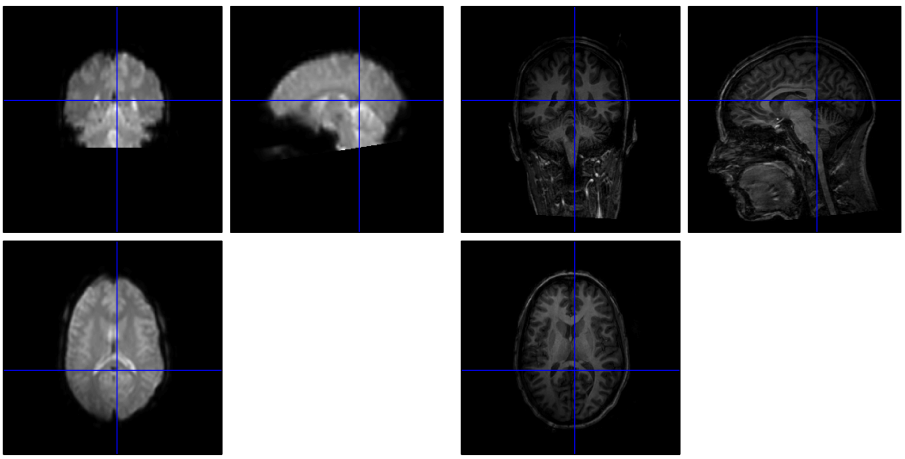

Figure 4.12: Illustration of the correspondence between functional (left) and anatomical (right) images after the application of co-registration.

This process of mapping all the brains into the same template is called normalization. The normalization can be applied to either anatomical or functional images.

For the purpose of normalization, 12 parameters of the affine transforms are estimated (including, scaling, skewing, and others). They are afterwards applied to the anatomical and functional images.

**Spatial Smoothing** After all these steps, the functional images are usually spatially smoothed. The smoothing is achieved by convolving the fMRI image by a Gaussian kernel of a specified width. This step is mostly performed to artificially introduce more correlations between the neighbouring voxels, which is important in the following step, where the active voxels are identified through statistical analysis.

### 4.6.2 Statistical Analysis

**Detecting active brain regions** The identification of active brain regions with fMRI is complicated by the fact that the increase in BOLD response related to neuronal activation is only 2-5% of the total signal. As such, the images need to be carefully preprocessed (see previous section) and statistical analyses are needed to detect regions with an increased blood flow. One of the most widely used methods in this context, is based on generating a general linear model (GLM) for the fMRI signal. This GLM is constructed by creating a signal based on time points of interest (e.g., time instances of presented stimuli) and convolving this signal with a model for the HRF. The fMRI signal in each voxel is then statistically compared with this GLM and the resulting statistical map can be thresholded to retrieve the activated brain areas.

Next to this GLM-based approach, also blind source separation (BSS) methods like independent component analysis (ICA) and canonical correlation analysis (CCA) have been applied to fMRI data [21, 80]. These methods have the advantage that no model of the HRF has to be assumed and no timing information about the origin of activation is needed. Although statistical analysis cannot be used for exploratory purpose, until today it is accepted as most widely used approach, since the conclusions derived in this way are scientifically strong.

A schematic representation of all the analysis steps, including the statistical analysis, is shown in Fig. 4.13.

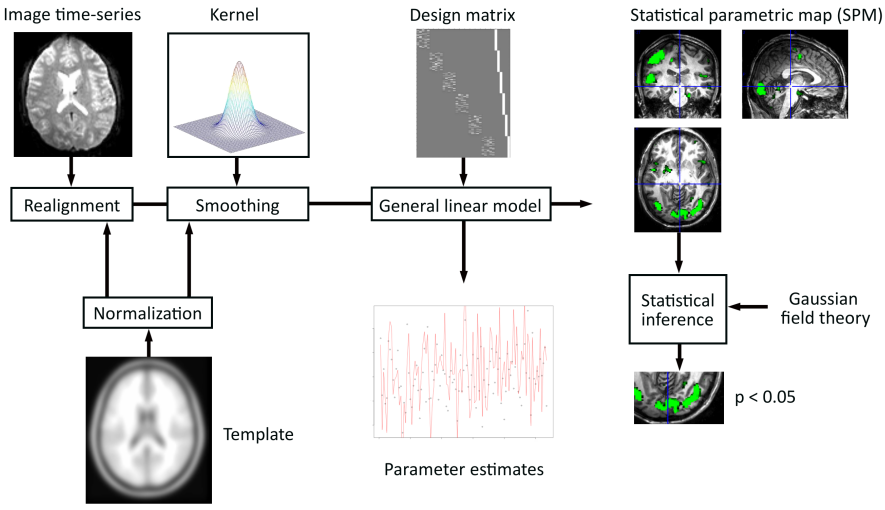


Figure 4.13: Schematic representation of analysis steps that need to be followed to obtain a quantification of activated brain regions, based on raw fMRI images (based on [81]). The images are first slice-time corrected (not shown), realigned and co-registered with their anatomical image. Subsequently, normalization is applied by aligning the images to a template and finally the images are smoothed based on a Gaussian kernel. To analyze the fMRI data, a general linear model is constructed and fitted to the data. Applying statistics to the resulting parameter estimates, yields so-called statistical parametric maps which can be thresholded to investigate the activated brain regions in detail.

## 4.7 EEG-FMRI Integration

The need for EEG and fMRI integration is justified by two major reasons. First, these modalities are complementary in their spatio-temporal characteristics. This comes from the fact that EEG is measured with a very high temporal resolution, whereas with fMRI only one 3D image is acquired every 1-2 seconds. On the other hand, EEG is measured on the scalp, and it is measured with up to 256 sensors (electrodes), whereas the fMRI imaging techniques provides spatial recordings from inside the brain, with the accuracies of down to only several millimetres. The second reason for this coupling is that they both measure (directly or indirectly) different aspects of brain activity, and it is of interest to explore how these two measurements are related.

The fMRI and EEG research nowadays can be roughly divided in two groups. The first group is the research of the ongoing spontaneous brain activity (usually called

as resting-state research), and the research of the brain activity during carrying a particular task (task-related activity).

### 4.7.1 Spontaneous and task-related activity in fMRI

**Spontaneous Activity in fMRI** The answer to why one would be interested in research of the resting-state activity, when the brain does "nothing" is very simple. First, the task-related increases in brain activity are lower than 5%. This means that by investigating only the task-related activity, we actually study only a minor component of total brain activity. The other reason is that it has been confirmed by several groups that the spontaneous activity of the corresponding contra-lateral brain areas highly correlate in time-domain. In that sense, for example, the activity in the left somatomotor cortex is highly correlated with the activity of the right somatomotor cortex, and with the medial frontal area. Similar conclusions are drawn for visual and auditory areas (see [76] and [183] for review).

This spontaneous activity is specifically organized in different spatial maps (for example default mode network, motor areas, visual areas and auditory areas), and in that sense they are significantly different from white noise in the spatial domain. Moreover, their temporal activity also significantly differs from white noise behavior, in the sense that it follows a $1/f$ frequency distribution, meaning that there is a decrease in power at higher frequencies.

**Interference of spontaneous and task-related activity** It was recently shown [78] that the single-trial task related BOLD variability is highly influenced by the ongoing spontaneous brain activity. The data in this study were recorded during two different task blocks. In one block (the passive block), the subjects were asked to simply watch a movie. During another task (the active task), they were required to press a button with their right index figure, every time there was a transition between major events in the movie.

During the active task, they found "expectedly" the activity in the left motor cortex (due to right index finger press). In the passive task, they identified all the areas that correlate with the left motor cortex area during the resting-state. Then, they simply subtracted the activity of these correlated areas during the active task, from the left motor cortex. It was shown that the average BOLD estimate of the activity in the left motor cortex remained the same as when they did not subtract the spontaneous activity from the active task. However, the variability in the trial-to-trial BOLD resposnes was significantly lower. This is depicted in Fig. 4.14 (the figure is borrowed with permission from [76]).

In a later study, this group showed on the same data set that this spontaneous activity is correlated with human behaviour. More specifically, the strength of the

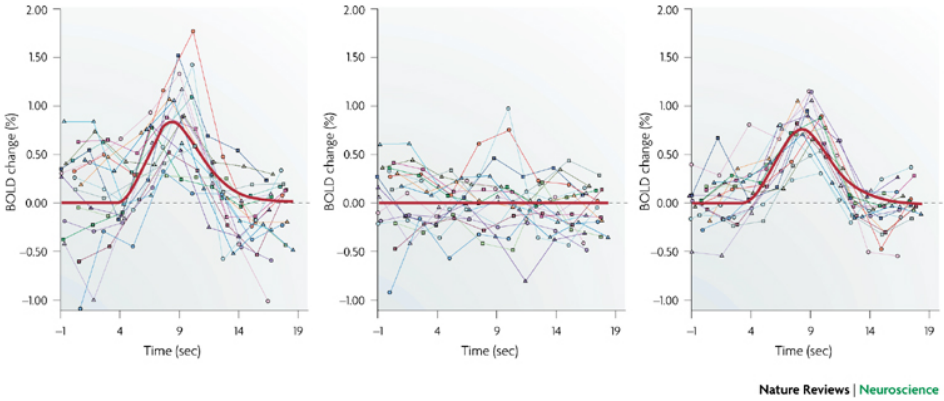


Figure 4.14: Coherent spontaneous fluctuations account for variability in event-related BOLD responses. a | Raw left somatomotor cortex event-related blood oxygen level dependent (BOLD) responses for 18 right-handed button presses from a single subject. b | The corresponding activity in the right somatomotor cortex during each button press can be used as an approximation of the ongoing spontaneous activity in the left somatomotor cortex. c | Left somatomotor cortex responses after subtraction of spontaneous fluctuations measured in the right somatomotor cortex show a decrease in variance and an increase in signal-to-noise ratio. The thick red line in each graph represents the best fit gamma function to all data points. The figure is borrowed with permission from [76]

spontaneous activity upon each button press was found to be correlated with the force used for this same button press [77].

### 4.7.2 Coupling of spontaneous activity in EEG and fMRI

As noted before, BOLD is actually not a direct measure of neuronal activity. It arises from the differences in magnetic properties of oxygenated and de-oxygenated haemoglobin. When the haemoglobin is oxygenated, the oxygen molecules "protect" the surrounding magnetic field from the influence of iron that is used to carry them. However, once the haemoglobin is de-oxygenated, the iron affects the magnetic field in a stationary way, therefore introducing the change in the $T_2^*$ time constant.

The first EEG-fMRI coupling was examined by correlating the spontaneous changes in the BOLD signal to the changes in power of high-frequency oscillations in EEG. For example, the power of brain electrical activity in the alpha frequency band fluctuates at the frequency of 8-12 $Hz$, but the power, or amplitude, of these frequency bands fluctuates at much slower rate, also exhibiting 1/f behaviour, and are correlated mostly across the visual cortex [83, 141, 107, 106]. Also the

correlation of higher frequency oscillations are shown later, for example gamma-range (60-100 $Hz$) [170]

More recently, Scheeringa et al. [171] examined the influence of single-trial BOLD responses in respect to the phase and the amplitude of the spontaneous EEG activity in the alpha frequency band. They found that the trial-to-trial fluctuations are related to the changes in amplitude of the alpha frequency band power. However, these differences could be explained by the spontaneous BOLD activity, rather than the difference in single-trial responses. On the other hand, they showed that visual stimuli (which are constructed to stimulate early visual areas - V1/V2), arriving at the peak phase of alpha cycle, yield a lower BOLD response compared to the ones presented in the trough phase of the cycle.

In another study they constructed the stimulation paradigm known to induce sustained changes in neuronal synchronization across a wide range of frequencies [170]. What they showed is that trial-to-trial BOLD fluctuations correlated positively with trial-to-trial fluctuations in high-EEG gamma power (60-80 $Hz$) and negatively with alpha and beta power. Additionally, they showed that these correlations independently contributed to explaining BOLD variance. However, it is still an open question whether trial-to-trial fluctuations of task-related BOLD signal correlate with the spontaneous EEG fluctuations, or whether simply the spontaneous BOLD activity, which is overlapping with the task-induced BOLD activity, correlates with the spontaneous EEG fluctuations.

### 4.7.3 Task-related EEG-fMRI coupling

It has been suggested the first time in 1889 [165], that the neuronal activity is accompanied with the regional increase in cerebral blood flow. Since 1991, these changes can be measured with fMRI. The question, however, remains how are these spontaneous changes in indirect measures of oxygenation related to electrical measures of neuronal activity.

The idea of integrating measured task-related EEG and fMRI signals is then additionally supported by the research of Logothetis et al. [117], who showed in macaque monkeys that the local field potential (LFP) recordings relate linearly with the BOLD signal. Since then, for integration of the simultaneously recorded EEG and fMRI signals in humans, several approaches have been proposed. Most commonly, presented approaches can be divided in three different groups.

#### EEG-informed fMRI analysis

The first group represents the integration-by-prediction approaches (or EEG-informed fMRI analysis). In this type of analysis, certain features of the single

trial ERP components are used as predictors (regressors) for the statistical fMRI analysis. This approach is schematically presented in Fig. 4.15 (figure borrowed from [54] with permission). One can, for example, use the changes in only one of the ERP features. In [55] for instance, the amplitude of the N1 component – the minimum of the interval of 15-85 $ms$ is determined, and then the mean of the preceding (-80 $ms$-0) and succeeding (85-200 $ms$) positivity windows are subtracted. The computed values are subsequently used as regressors for fMRI analysis.

Other studies combined two ERP component features. In [99], it was shown that N2- and P3- based fMRI analysis shows activations in different brain areas, corresponding to different aspects of voluntary selection. In [149], the P1- and N1-based regressors were used to separate the activations of the visual system at the latency of 100-200 $ms$.

Also the combination of three regressors can also be used, like in (Eichele, 2005), where P2- (170 $ms$), N2- (200 $ms$), and P3- (320 $ms$) based regressors predicted spatially different patterns during auditory oddball task. The features used for regressors in this kind of analysis are usually amplitudes, as mentioned above, but latencies of the certain components can also be used (e.g. [18, 188]). The main challenge of the integration-by-prediction approaches is to try to find the feature, upon which it is possible to disentangle the trial-to-trial fluctuations of different peaks, and in respect to noise. This problem is also addressed in [186, 50].

### fMRI-informed EEG analysis

The second group of EEG-fMRI integration approaches consists of fMRI-informed EEG analysis approaches. In these approaches, the information obtained from the fMRI measurements is used to constrain the equivalent dipole or distributed estimates of the EEG sources. In [20] the P300 generators are localized in visual target and distractor processing. Another application is shown in [48], where the relevance vector machines are used to predict single-trial ERP responses from the fMRI measurements.

### EEG-fMRI Fusion

The obvious drawback of these two groups of approaches is, however, that they force the information from one modality onto another one. Therefore, these approaches are also called *asymmetric*, and they cannot be considered as full integration approaches, since there is no temporal forward model that will start from both information, and fuse them in the sense that they exploit the underlying dynamics of both of them symmetrically.

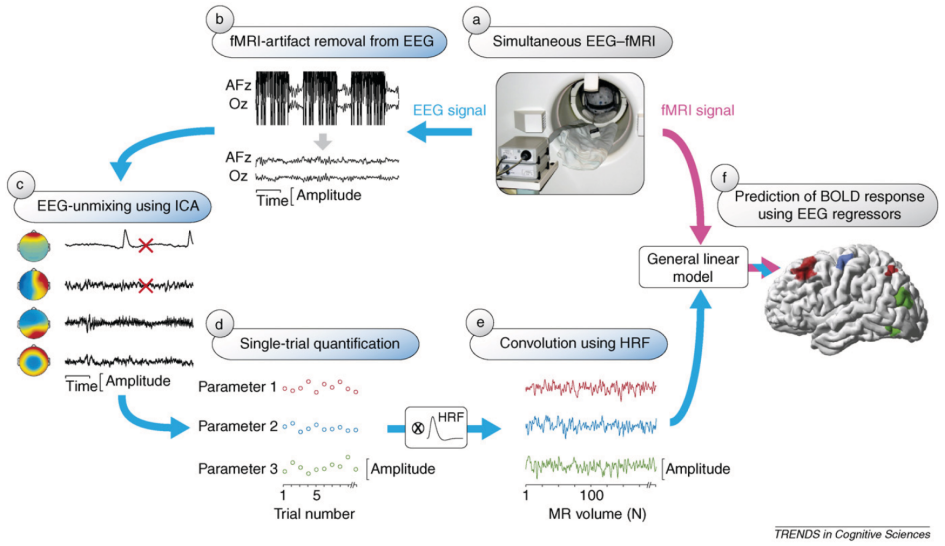


Figure 4.15: The EEG-informed fMRI analysis. EEG and fMRI data are recorded simultaneously. After acquisition, the EEG data follows the blue-arrow preprocessing path. The fMRI data is added only after the EEG data features are extracted and convolved with the haemodynamic response function. The fMRI data follows the pink arrow path.

The third group of integration approaches consists of the joint data-driven analysis of ERP and fMRI maps derived from the response to a particular stimulus. This group of approach we call the *symmetric* approaches, or the *EEG-fMRI fusion* approaches. Several methods have already been proposed for this purpose, and they can be based on modeling (as in e.g. [43]), or BSS techniques, such as ICA or CCA. These methods employ both modalities at the same time.

All the methods described from this point on, in this chapter, are considered as EEG-fMRI fusion approaches

**Model-based approaches** An example of model-based approaches is given in [43]. In that work, Variational Bayesian learning scheme is exploited to retrieve the common EEG-fMRI information from the joint EEG-fMRI dataset. The model follows the assumption that the temporal and spatial information can be separated. A common spatial profile is extracted, since this profile is introduced as unknown hierarchical prior on both (EEG and fMRI) markers of cerebral activity. The method is first assessed through simulation data, and thereafter verified in the EEG and fMRI recordings of an epileptic patient, where the intracranial EEG

recordings are used for validation.

**The CCA-based approach** to fusion is presented in [36, 37]. Given the two datasets $X_1$ and $X_2$, CCA tries to find linear combinations $X_1W_1$ and $X_2W_2$ that maximize the pair-wise correlation. In this approach, $X_1$ and $X_2$ are the set of average ERPs and task-related fMRI contrast maps over subjects. In [36] for example, it is shown using this method, that the N2 and P3 ERP peaks during the auditory oddball task are related with temporal and motor areas in fMRI. A more general correlation-based method is proposed in [127]. In that work 3-dimensional EEG (subjects x time x frequency) and fMRI (subjects x time x space) data are used (see also [51]). It is shown that alpha-band activity of EEG is closely correlated with the temporal activity of fMRI, thereby activating parieto-occipital complex, thalamus and insula.

**Parallel-ICA approaches** Besides the above-mentioned CCA approaches, different ICA approaches have also been proposed. Contrary to the CCA, ICA employs measures of higher order statistics (independence), rather than just second-order statistics (correlation). The ICA approaches can be divided in two groups: Parallel- and Joint-ICA approaches. In parallel ICA approaches the data for both modalities are first preprocessed separately, and then the connections between the modalities are made afterwards. In [67], after the independent components are extracted, the relations are made based on correlations between trial-to-trial fluctuations in the time domain (Fig. 4.16). The drawback of this method, however, is that it does not allow any interference between modalities during the decomposition step.

Another parallel ICA approach has been proposed in [109]. This approach is very similar to the previous one, with a difference that the components are linked in spatial and temporal model using variational Bayesian techniques. This allows results for one modality to be used as priors for another one (results from ICA decomposition of the EEG modality can be used as priors for fMRI and vice versa). This fact makes this method integration, rather than data-fusion approach. In [109] the simulation study is provided and the results are discussed.

The parallel approach which imposes constraints during the parallel decomposition is proposed in [116]. As in previous cases, this approach also applies the ICA algorithm to the two modalities separately. However, contrary to other Parallel-ICA approaches, the correlations between the corresponding mixing vectors of the two modalities are forced during the separate decompositions. Therefore, the connections are made more symmetrically than in the above-mentioned parallel ICA approaches.

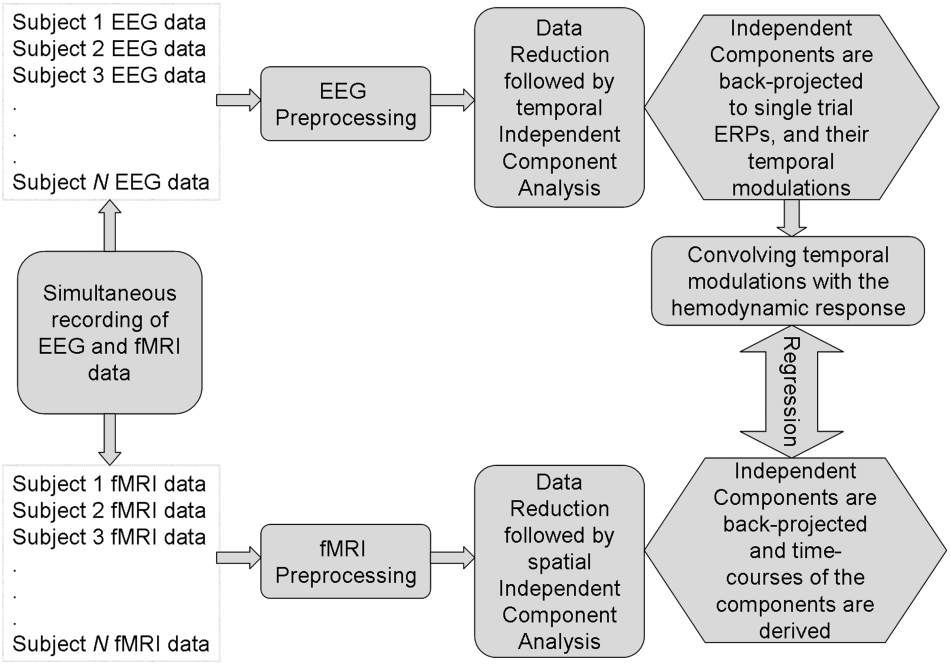


Figure 4.16: Schematic representation of the Parallel-ICA algorithm, proposed by [67]. It is apparent from the picture that the EEG and fMRI data are first preprocessed separately, and the connections are defined only in the last step – regression.

**JointICA approach** Another interesting fusion approach to this problem is called joint independent component analysis (JointICA) ([23, 136]. JointICA identifies the independent components of both modalities simultaneously, and connects them in an integrated fMRI-ERP result, where each fMRI independent component is associated to an ERP-derived time course. This approach is schematically shown in Fig. 4.17. The method assumes that the different wave components (peaks) of the ERP and the spatial components in a statistical brain activation map (activation sites) of the same stimulus co-vary. This is either because they are generated in the same brain region or because the BOLD active areas had participatory roles in ERP activity, without necessary being the source of a particular ERP wave.

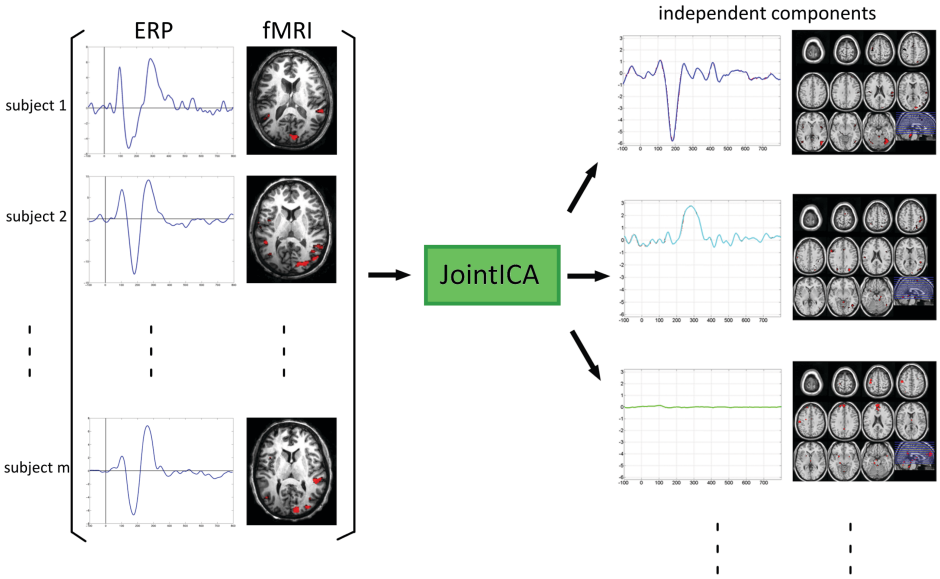


Figure 4.17: Schematic representation of the application of the JointICA method to average ERPs and fMRI maps from m subjects. On the left the matrix with the concatenated ERP and fMRI data per subject is shown, which is (after upsampling of the ERPs and normalization) fed into JointICA. On the right some examples of resulting components are presented, each consisting of an ERP and an fMRI part.

## 4.8 Conclusion

In conclusion, the simultaneous EEG-fMRI recordings combine two very important markers of brain activity. These recordings also allow for enhancing the spatio-temporal resolution, with which the brain activity can be observed. Several integration techniques have already been proposed for this purpose. Some of these techniques are reviewed in this chapter, together with the necessary preprocessing schemes for each modality. The underlying assumptions for several integration and fusion techniques are explained and discussed. Also the results obtained from these algorithms are described, and their applicability is illustrated.

# Chapter 5

# EEG-fMRI Data Acquisition

*This chapter describes the necessary procedures for the simultaneous acquisition of the EEG and fMRI data, together with the used equipment. Additionally, the data acquired for the purpose of studies presented in the following chapters are described. The data described here have already been used in the following published or submitted papers [136, 137, 149, 185, 186, 184].*

## 5.1 Simultaneous acquisition of EEG and fMRI

As explained in the previous chapter, many EEG-fMRI applications benefit from simultaneously acquiring both modalities. A major breakthrough in this context was accomplished by Ives et al. [93], when they showed for the first time the feasibility of acquiring EEG data inside an MR scanner. Since then, much progress has been made, such that nowadays several EEG systems for simultaneous EEG-fMRI acquisition are commercially available. Nevertheless, a number of technical and safety-related challenges had to be solved. The resulting acquisition setup and some related technical aspects will be highlighted in this section (based on [145, 180], without going into details). In addition, the specific acquisition parameters adopted in this study, will be discussed.

### 5.1.1 Equipment

Standard EEG instrumentation consists of a set of electrodes, an acquisition system to amplify and digitize the EEG signals, a system (e.g., a computer) to visualize and analyze the recordings and a number of leads and wires to connect all these

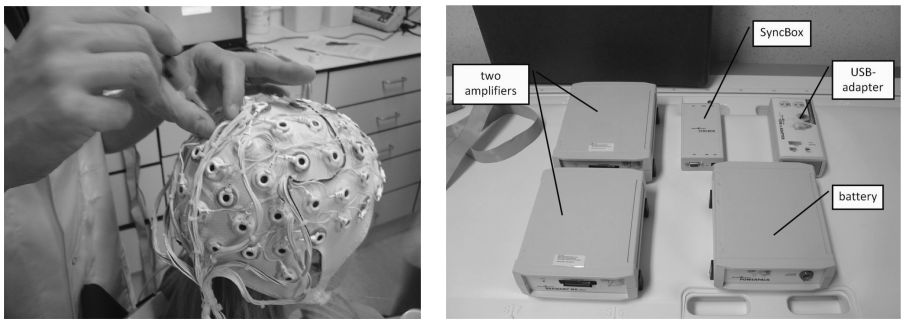


(a) (b)

Figure 5.1: (a) Picture of an electrode cap (BrainCap MR) with 64 ring electrodes. Electrolyte gel has to be used to optimize the signal quality during measurements; (b) Picture of different parts of the BrainAmp MR+ system. Two battery powered amplifiers are used and connected to the computer via the USB adapter. In addition, the synchronization box allows synchronizing the EEG data with the clock of the MR system.

components. The electrodes can be stuck to the subject's scalp or can be mounted in an electrode cap, as illustrated in Figure 5.1(a). To ensure good signal quality during the EEG measurements (i.e., minimize the impedances), the EEG electrodes must be filled with a conductive electrolyte gel.

The bore of the MR scanner can be seen as a "hostile" environment for recording the EEG data [180]. More specifically, all elements of the EEG hardware are exposed to both a constant and a varying magnetic field and to the RF pulses emitted during fMRI acquisition. Different approaches can be adopted to cope with this "hostility", thereby dividing the currently available MR-compatible EEG systems into two main categories. In addition, any use of ferromagnetic materials has to be avoided.

A first category of systems are the ones of which the biggest part is located in the scanner control room. A clear advantage of this approach is that putting the amplifier system outside the strong magnetic field avoids the necessity of a specific MR-compatible design for the amplifiers. However, this setup requires the use of long electrode leads and an opening for these leads in the MR filter panel, respectively causing bigger gradient artifacts and possibly leading to leakage of RF energy.

In this study, a system based upon the second approach is used. More specifically, the EEG data were collected using the BrainAmp MR+ system (BrainProducts, Munich, Germany), of which some parts are visualized in Figure 5.1(b). The battery powered amplifiers of this system are positioned inside the scanner bore.

In addition, the signals going from the amplifiers to the recording computer are fed through fibre optical cables, which have the advantage of being immune against magnetic or RF coupling. The amplifiers of this system are specifically designed to be used in the MR environment while all other electrically critical components of the EEG system can be put in the control room. When attaching the electrodes to the amplifiers, sandbags can be used to fixate the corresponding leads in order to avoid additional movement artifacts.

Regardless of the followed approach, a number of small details also have to be taken care of. First of all, the selected imaging sequence can have an effect on the subject's safety, since a badly chosen sequence can cause serious heating at the border between the scalp and the electrolyte gel [133]. Moreover, any type of loops that could cause additional currents, albeit in the electrode leads or in any other cable, should be avoided [60].

It has also been shown that synchronizing the EEG-amplifier clock to the MR scanner control-device clock improves the removal of the gradient artifacts [6, 33, 124]. Therefore, the BrainAmp MR+ System also includes a synchronization box, as can be seen in Figure 5.1(b).

Furthermore, to prevent head movements and resulting distortion of both EEG and fMRI data, it is important to take care of the subject's comfort. Therefore, when a subject is lying supine in the scanner, a cushion is used to minimize the pressure of the electrodes on the head. In addition, the subject is provided with earplugs to avoid harmful effect from the scanner's acoustic noise.

### 5.1.2 Data acquisition parameters

Besides the above-mentioned synchronization aspect, also the detection of the true onset of the gradient artifacts is essential for fully capturing their shape. This is important since a successful removal of the artifacts highly depends on an accurate construction of the artifact template. The gradient artifacts cover a broad frequency spectrum ranging from very low frequencies until several thousand Hertz [2]. To avoid aliasing and at the same time capture the major part of these artifacts, EEG data were measured using an analog hardware filter between 0.1 and 250 $Hz$ and a sampling rate of 5 $kHz$.

The experiments were performed at the University Hospital Gasthuisberg of the KU Leuven (Leuven, Belgium). For validation purposes, the EEG data were acquired in two different situations: inside the MR scanner simultaneously with fMRI and in the scanner control room, in absence of the magnetic field. Regardless of the situation, the EEG data were collected from 62 standard scalp sites using the above explained BrainAmp MR+ system. In both cases, electrode impedances were kept always below 10 $k\Omega$, and usually below 5 $k\Omega$. In Fig. 5.2 the software

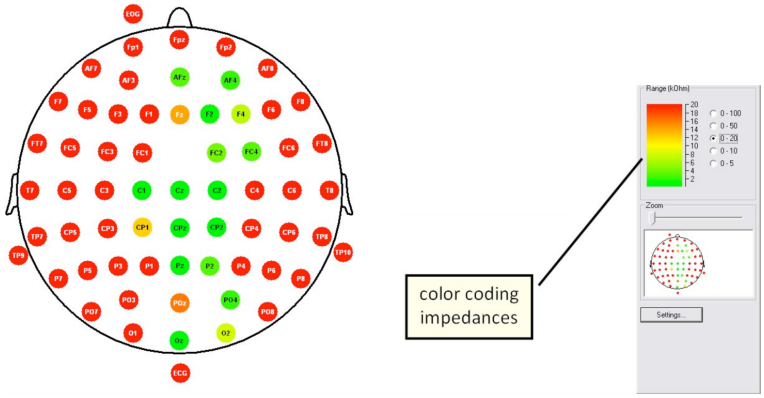


Figure 5.2: Software interface used to yield an indication about the electrode impedance. The scale is shown on the right - from 0 to 20 kω color range from green to red. Also, the electrode position used in the measurements is clearly visible.

interface for setting up the EEG cap is shown. The color depicts the impedance of the electrodes - the greener the electrode, the lower the impedance. Also the MR scanner and the fMRI acquisition parameters are detailed below.

The 62 unipolar electrodes employed in this setup were arranged according to the international 10-20 system . In addition, the EOG was measured below the left eye and an ECG electrode was put on the left scapula. All 64 channels were recorded with FCz as reference and Iz as ground (see Figure 5.2).

The simultaneous measurements were performed in a Philips 3T Intera whole-body scanner (Royal Philips Electronics, Amsterdam, the Netherlands). 160 EPI images composed of 28 slices of $3 \times 3 \times 4.5$ mm voxel size and 4.8 mm slice thickness were recorded with ascending slice order with a TR of 1.95 s (for the detection task) and a TR of 2 s (for the grouping task). Also here the MP-RAGE sequence was used to acquire anatomical images (230 coronal slices, TE = 4.6 ms, TR = 9.7 s).

## 5.2 Experimental data

First, the employed task paradigms will be described after which the actual available data will be listed.

### 5.2.1 Task paradigms

The different stimulation paradigms were generated and presented to the participants with the Presentation software (Neurobehavioral Systems, Albany, CA, USA).

#### Detection task

The first task was a visual detection paradigm with segments of circular black-and-white checkerboard stimuli presented one at a time in randomized sequences to one of the four quadrants of the visual field [62]. As such, there are upper left (UL), upper right (UR), down left (DL) and down right (DR) stimuli. In addition, a large circular black-and-white checkerboard was presented as a central stimulus (CE) on the middle part of the screen. Subjects were instructed to fixate the cross in the middle of the screen and to press a button upon detection of each of these stimuli. In the simultaneous measurements, also empty events were used in order to provide a baseline for the fMRI event-related analysis. The figure during empty events was not different from the inter-stimulus interval, i.e., a gray screen with a fixation cross.

The stimuli (see Fig. 5.3) were presented in four blocks and per run 100 stimuli (20 of each type) were shown to the participants. In each condition the stimulus was presented for 150 ms and the inter-stimulus interval (ISI) varied between 900 ms and 2400 ms. In each acquisition block, 61 empty stimuli are included. This, together with the fact that there are 5 different kinds of stimuli, gives rise to effective ISI, as shown in [187]. The average appearance of the consecutive stimuli of the same type is 6.8 seconds, taking into account that the central stimulus activations overlap with each of the other stimuli separately. The presentation paradigm was randomized across subjects, as well as across sessions (inside versus outside). A more detailed description of the task can be found in [149].

#### Grouping task

The purpose of this task was to obtain a better understanding of the mechanisms underlying two-dimensional shape perception. In the early twentieth century, a number of local and global grouping principles that contribute to visual perception have been postulated [100, 189]. By using stimuli of which the structure detection involves local and global grouping, we hope to reveal the spatio-temporal dynamics behind these grouping principles.

We used MATLAB (v 7.1; The MathWorks, Natick, MA, USA) and GERT, the Grouping Elements Rendering Toolbox [59], to construct arrays of non-overlapping Gabor elements on a uniform grey background (Fig. 5.4). The arrays comprised

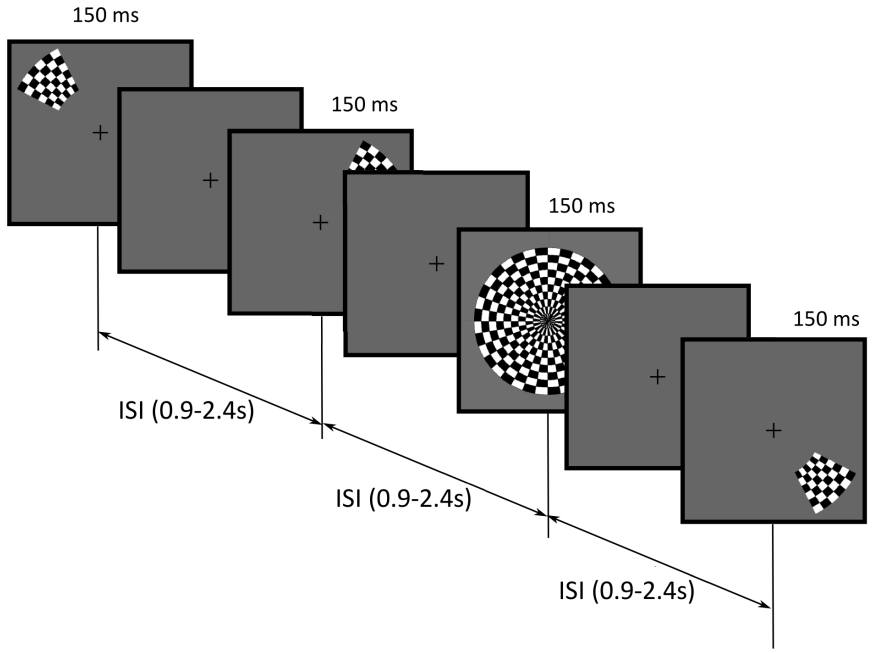


Figure 5.3: Schematic representation of a fragment of detection task paradigm. Five types of stimuli are alternated with empty events and with an ISI between 900 and 2400 ms.

496 x 496 pixels and subtended approximately $10^o$ of visual angle. Each Gabor element was defined as the product of a sine wave luminance grating (frequency of 3 cycles per degree of visual angle) and a circular Gaussian (standard deviation of 3 arcminutes). A subset of 45 Gabor elements was positioned along the contour outline of an artificial shape. The shape outlines were generated by plotting the sum of 5 radial frequency components (each sine wave having a random phase angle) in polar coordinates. After rescaling the surface area to one eighth of the array size we co-localized the center of mass of each shape with the center of the array.

Next, the remainder of the array was populated with Gabor elements. To ensure a homogeneous spacing of Gabor elements throughout the array, we adjusted the number of elements inside and outside the shape outline separately for each shape. The number of interior elements ranged between 60 and 72, the number of exterior elements between 507 and 542. No stimuli were included for which the mean local density - here defined as the average Euclidean distance from each element to its

five nearest neighbors - differed more than 1 arc min between interior, contour, and exterior elements.

In each display, all interior and exterior elements had the same orientation. Three different types of arrays were obtained (Fig. 5.4) by manipulating the orientations of the contour elements. In the local + global (LG) condition (Fig. 5.4(b)), all contour elements were aligned along the outline of the embedded shape. In other words, each pair of adjacent contour elements is locally aligned, and the entire set of contour elements results in a global shape. In the global only (GO) condition (Fig. 5.4(c)), only half of the contour elements was aligned along the outline of the embedded shape and every other element was oriented orthogonal to the outline. This still yields a global percept of a closed contour, but without any local alignment between adjacent contour elements. In the no-contour (NC) condition (Fig. 5.4(a)), all elements on the embedded shape were oriented parallel to the other elements in the array.

Subjects were asked to perform four blocks of each task version. They were instructed to focus on the fixation cross in the middle of the screen and press a button upon appearance of each of the catch stimuli (Fig. 5.4(d)). These catch stimuli were introduced to ensure that the participants' attention was kept to the screen. To avoid that participants would only focus on a small region of the display, we randomized the position of the circles across trials. In addition to the different stimuli explained above, also a number of blank events were included, for the same reason as the empty events in the detection task. The number of blank events and structure, non-structure and catch stimuli was randomized between task blocks. The same task blocks were, however in a different order, used for every subject. As such, the total number of stimuli is equal for all subjects, yielding 500 trials for the LG task and 500 for the version GO task, of which 8% were catch stimuli, 24% structure and 48% non-structure. The ISI varied between 2 and 2.4 seconds (in steps of 40 $ms$) and stimuli were shown for 200 $ms$.

### 5.2.2 Overview of acquired data

#### Study 1: Detection task

Twenty-six healthy subjects (11 female and 15 male, aged 18-44) with no history of neurological or cardiological disorders participated in this study. Written informed consent was obtained in accordance with the local ethical committee guidelines. During the simultaneous measurements subjects were lying supine in the scanner on a cushion that ameliorated the pressure from the EEG electrodes on the head, and with soft cushions to the side to restrict head movement in the coil. Subjects were provided with earplugs and headphones to avoid any harmful effect from the fMRI acoustic noise. Eighteen out of these 26 subjects additionally participated

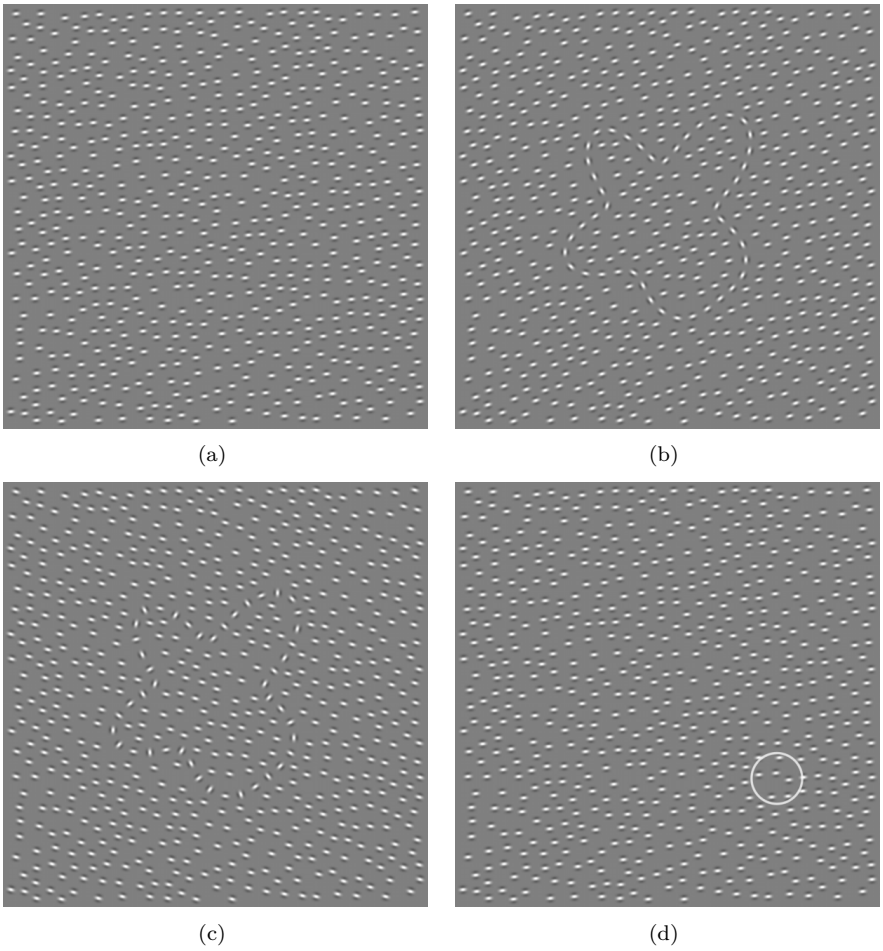

(a) (b)

(c) (d)

Figure 5.4: Example stimuli for the different array types. (a) no-contour (NC) stimulus in which all Gabor elements have the same orientation. (b) local + global stimulus (LG), obtained by aligning the elements on the contour parallel to their local tangent at the contour. (c) global only stimulus (GO), in which every other contour element is oriented parallel to or orthogonal to the shape outline. (d) catch stimulus, is always a no-contour stimulus with a small circle overlaid at a random location. Catch trials are not included in the analyses.

in a session where only EEG was acquired outside of the scanner room with the same presentation paradigm. In the outside session, the subjects were seated in front of the computer screen. The visual angle was as close as possible to the one in the inside session. The refresh rate of the screen was 60 Hz in both cases. The computer room was dark, and there was no environmental noise during the task execution. The experimental circumstances were optimized such that they maximally correspond between the two (inside the scanner, and outside the scanner) conditions.

#### Study 2: Grouping task

In this study, only simultaneous EEG-fMRI data were acquired. 17 subjects (8 female and 9 male, aged 23-44) with no history of neurological or cardiological disorders were included. Written informed consent was obtained in accordance with the local ethical committee guidelines. Two of the original 17 datasets had to be eventually discarded due to insufficient signal quality or problems during acquisition, resulting in 15 datasets for further analyses.

## 5.3 Conclusion

In this chapter, the equipment for simultaneous acquisition of EEG and fMRI was introduced. In addition, details were given about the datasets that were acquired in the course of this work. More specifically, a visual detection task and a grouping task were employed. For validation purposes, part of the subjects not only performed the tasks during simultaneous EEG-fMRI measurements, but also outside the scanner room. In the next chapters, the analyses performed on these different datasets will be discussed.

# Chapter 6

# JointICA for EEG-fMRI Fusion

*Since several years, neuroscience research started to focus on multimodal approaches. One such multimodal approach is the combination of electroencephalography (EEG) and functional magnetic resonance imaging (fMRI). However, no standard integration procedure has been established so far. One promising data-driven approach consists of a joint decomposition of event-related potentials (ERPs) and fMRI maps derived from the response to a particular stimulus. Such an algorithm (joint independent component analysis or JointICA) has recently been proposed by Calhoun et al. [23]. This method provides sources with both a fine spatial and temporal resolution, and has shown to provide meaningful results. However, the algorithm's performance has not been fully characterized yet, and no procedure has been proposed to assess the quality of the decomposition. In this chapter, we therefore set out to answer why and how JointICA works. We show the performance of the algorithm on data obtained in a visual detection task, and compare the performance for EEG recorded simultaneously with fMRI data and for EEG recorded in a separate session (outside the scanner room). We perform several analyses in order to set the necessary conditions that lead to a sound decomposition, and to give additional insights for exploration in future studies. In that respect, we show how the algorithm behaves when different EEG electrodes are used and we test the robustness with respect to the number of subjects in the study. The performance of the algorithm in all the experiments is validated based on results from previous studies. This chapter is based on [136]*

## 6.1 Introduction

### 6.1.1 Simultaneous EEG-fMRI

As described in Chapter 4, EEG and BOLD changes can be measured simultaneously to benefit from their complementary properties. EEG measures electrical responses with a millisecond precision, but does not provide a precise spatial localization of the underlying cortical activity, since the electrode position is limited to the scalp surface. fMRI, on the other hand, measures local changes in brain hemodynamics with a very good spatial precision. However, the hemodynamic response is a slow signal and one Echo-Planar Image (EPI) is only acquired every few seconds. This is far below the brain reaction time to externally applied stimuli, thus making the analysis of detailed temporal brain changes during the reaction on external stimuli very difficult.

For this reason, the simultaneous acquisition of both EEG and fMRI is getting more and more popular, as their complementarity can provide deeper insight into function and dysfunction of brain dynamics [180, 145, 52]. This advantage has already been exploited in numerous applications. For instance, the combination of EEG and fMRI allows localizing epileptic activity based on spike-triggered fMRI [173, 104, 110, 17]. Other possible applications are the study of ongoing brain rhythms [82, 83, 107, 141] and cerebral activations during sleep [39, 114, 169]. Also the analysis of event-related brain responses based on multimodal information (e.g. [144, 55, 54, 23, 67, 140] becomes more and more popular.

### 6.1.2 Integration approaches

The overview of the existing integration approaches is given in Chapter 4. Therefore, here we mostly focus on JointICA itself.

JointICA identifies the independent components for both EEG and fMRI modalities simultaneously. To do this, it starts from ERP epochs in the temporal domain and fMRI activation maps in the spatial domain. In the original paper on JointICA [23], the method was applied to averaged ERP data from different participants. Although another possible application has been shown on single-trial simulation data by Moosmann et al. [140], in this chapter we will focus on the original algorithm on averaged data. The method assumes that the different wave components (peaks) of the ERP and the spatial components in a statistical brain activation map (activation sites) of the same stimulus co-vary, either because they are generated in the same brain region ([117] showed that the BOLD response is highly correlated with the group neuronal activity of the same brain region), or because the BOLD active areas had participatory roles in ERP activity, without necessary being the source of a particular ERP wave. Hence, it is believed that ICA will be able to

disentangle these components and connect the electrical activations (ERP peaks) to their corresponding chemical (BOLD) brain activation sites [23].

The hypothesis about this one-to-one relation between the physiological origin of both data sets and their statistical dependence, however, is not necessarily true, since there is no particular mathematical reason to ensure capturing different ERP peaks always together with their corresponding fMRI activation sites. First of all, spatial statistical independence among fMRI components alone cannot be justified in the sense that there is no physical reason for the spatial samples to correspond to different activity patterns with independent distributions (see [42]. Furthermore, the two signals (ERP and fMRI) are very different in nature from a signal processing point of view. As used in the JointICA algorithm in this work, ERP is a temporal signal and fMRI a spatial map (obtained from a General Linear Model - GLM analysis) without any temporal information and their probabilistic distribution functions are different. The reader should note here that generally it is also possible to use concatenated ERPs from multiple electrodes as an input to JointICA, as done in the simulation study by Moosmann et al., [140], therefore obtaining spatio-temporal ERP information. However, in this work, only ERPs from a single electrode are used.

Although JointICA was shown to provide meaningful results with real data when introduced as a tool for integrated ERP and fMRI data analysis [23, 26], the underlying ICA assumption that the ERP and fMRI information extracted in a single component are mutually dependent, and at the same time statistically independent among different components was not questioned. Also, the behavior and robustness of the algorithm were not investigated. For this reason, and because of a growing interest in the method for the integration of different multimodal datasets, also besides EEG-fMRI [79, 192, 28, 64], some more methodological concerns need to be explored.

### 6.1.3 The present study

In this chapter, we therefore explore and validate the performance of JointICA and its central assumption that physiological linking between ERP and BOLD amplitudes drives the extraction of multimodal components despite their intrinsically different temporal and spatial nature. We also show that the ICA algorithm used in the JointICA method (Infomax - [14]) plays a crucial role in this multimodal separation. To support this claim, we investigate the performance of JointICA when other well-known ICA algorithms are used (JADE – [30]; and FastICA [92], and show the disadvantages of these algorithms compared to the performance of Infomax.

To validate the meaningfulness of the JointICA results, we used a simple and well-established visual detection task with known ERP components and fMRI

activation sites. This task is well-suited for validation purposes, as consistent results have been repeatedly found in several earlier studies [61, 63, 149]. The dipole pair accounting for the C1 ERP wave was found to lie in the calcarine cortex. The early P1 wave dipole was situated in the dorsal extrastriate cortex of the middle occipital gyrus, and the late P1 dipole was found in the ventral fusiform gyrus. The dipole that accounted for the early N1 ERP wave, was localized in the parietal lobe near the intraparietal sulcus.

It is hypothesized that a large part of brain activity is reflected both in EEG and fMRI modalities, and the link between them can be established. This we refer to as the central linking hypothesis. If we can find components that reflect both EEG and fMRI activity, it provides evidence to support the central linking hypothesis. The contribution of the central linking hypothesis is evaluated first by randomly reassigning ERPs and fMRI activation maps over participants, thus destroying the amplitude link between the two modalities, and second by a comparison with an individual ICA analysis of both ERPs and fMRI maps, thus excluding any intermodal interaction. Furthermore, we investigate the effect of the ERP quality for JointICA by comparing recordings inside and outside of the scanner and the dependence of the JointICA results on the sample size.

Based on the results obtained with these different analyses we will discuss why and when (under which conditions) JointICA works well, hopefully providing a better understanding for potential future users.

## 6.2 Materials and Methods

The detailed data and task description is given in Chapter 5, Sections 5.2.2 and 5.2.1, and here only the most important details are listed for the sake of readability.

### Subjects

Twenty-six healthy subjects (11 female and 15 male, aged 18-44) with no history of neurological or cardiological disorders participated in this study. Eighteen out of these 26 subjects additionally participated in a session where only EEG was acquired outside of the scanner room with the same presentation paradigm. The computer room was dark, and there was no environmental noise during the task execution. The experimental circumstances were optimized such that they maximally correspond between the two (inside the scanner, and outside the scanner) conditions.

### 6.2.1 Tasks

Participants performed a simple visual detection task while in the scanner. Stimuli consisted of segments of circular black-and-white checkerboard stimuli presented one at a time in randomized sequences to one of the four quadrants of the visual field [149]. The duration of a presented stimulus was 150ms. A central stimulus was also present, but was not used for the purpose of this study. Subjects were asked to press a button upon detection of each of these stimuli. Per run 100 stimuli (20 of each type) were shown to the participants. The Inter-Stimulus Interval (ISI) varied between 900ms and 1900ms.

### 6.2.2 Data acquisition

Here is the short outline of the acquisition process, but for more details the reader should consult Section 5.2.1.

All subjects performed 4 runs of the visual detection task. During each experimental block, 160 echo-planar images (EPI) composed of 28 slices of 3 x 3 x 4.5 mm voxel size and 4.8 mm slice thickness were recorded with ascending slice order and 1.95 second repetition time (TR).

### 6.2.3 EEG processing

Preprocessing of the acquired EEG data was performed in the MATLAB 7.7.0 (R2008B) (The Mathworks Inc, Natick, Massachusetts, USA) environment with the EEGLAB 5.03 toolbox [58], as explained in Chapter 4

For the application of the JointICA algorithm, only the ERP data from the electrodes PO7 and PO8 were used to observe the activations corresponding to right and left visual fields respectively (one electrode per application of the method). The ERP belonging to the Oz electrode was additionally used because the C1 ERP peak, corresponding to the activations in the primary visual cortex, is observable only on the midline electrodes [126, 61, 63].

### 6.2.4 fMRI processing

fMRI analysis was performed with the statistical parametric mapping software (SPM5, Wellcome Department of Cognitive Neurology, London, UK) in MATLAB. The EPI time series were slice-time corrected, realigned, co-registered with anatomical images, normalized to the MNI template and smoothed with an 8-mm FWHM Gaussian kernel, as in explained in Chapter 4.

A stick function at the onset of the stimulus, as in traditional event-related fMRI studies, was used as regressor. First-order statistics were calculated by convolving the stick function at the stimulus timing with a canonical hemodynamic response function (HRF), separately for the 5 stimulus locations (upper-left – UL, upper-right – UR, lower-left – LL, lower-right –LR, and central stimulus - CC). No derivatives were used in the analysis. The 6 movement parameters (three for both translation and rotation) obtained during realignment were inserted in the model as covariates of no interest. As a result, the design consisted of $5 + 6 = 11$ variables per experimental block per subject. For each subject and condition, percent signal change (PSC) maps are then computed to be used in further analyses.

### 6.2.5 JointICA

JointICA has originally been proposed by [23]. It is implemented in the Fusion ICA Toolbox, available from `http://icatb.sourceforge.net`. The JointICA algorithm assumes that the electrical correlate of brain activation (expressed in the ERP components) and the hemodynamic response to brain activation (BOLD response) are generated by the same population of neurons. Hence, the amplitudes of the ERP wave (peak) and of the BOLD response invoked by an activated area will increase and decrease synchronously: a stronger ERP peak activation will yield a stronger BOLD response in this particular brain region, and vice versa. Additionally, JointICA will reveal regions that were not directly involved in the creation of the ERP, but participated in the source activity, and therefore covariate strongly with a particular ERP wave.

Following this assumption, we can concatenate the PSC fMRI maps, derived from contrasting the BOLD signal invoked by a particular stimulus with the background, with the average ERP response corresponding to the same stimulus. Prior to this concatenation, several additional steps (listed below) are required, in order to avoid the bias to a particular modality.

First, to compensate for the disproportion between the number of voxels in the fMRI map and the number of time samples in the ERP signal, the ERP data are upsampled using cubic spline interpolation. After upsampling, the data of the two modalities are normalized (divided by the root mean squared data of all subjects) and concatenated into a single vector for each subject. The data from all the m subjects are then stacked into an m by n matrix (m being the number of subjects, n the number of samples of our artificially created data), and finally fed into an ICA algorithm to solve the following linear mixing problem:

$$m \overbrace{\left\{\left[\mathbf{X}^{fMRI}\mathbf{X}^{EEG}\right]\right.}^{n} = \mathbf{A} \cdot \left[\mathbf{S}^{fMRI}\mathbf{S}^{EEG}\right] \tag{6.1}$$

**X** and **S** represent the matrices of, respectively, acquired and source signals, with their superscripts indicating their correspondence to the fMRI or ERP matrix part. Equation 6.1 assumes the same mixing matrix **A** for both modalities. As mentioned before, this means that the corresponding parts of the ERP peaks and the BOLD responses of the corresponding brain regions are assumed to be changing with the same dynamics across subjects.

Following what has been mentioned previously, the JointICA algorithm provides, as an output, independent components, each containing the sources of both modalities (EEG and fMRI). In the Results section, these components are always shown in paired figures, one containing the EEG, and the other one the fMRI information. Several ICA algorithms can be used in this setup. In this study we compare the results from the Information Maximization algorithm (Infomax), proposed by [14], Joint Approximate Diagonalization of Eigen-matrices (JADE; [30]) and FastICA [91].

### 6.2.6 ICASSO Analysis

ICASSO is a robustness analysis tool [86, 87] for ICA results. ICA algorithms iteratively try to maximize a cost function, and are subject to the risk of instable solutions due to suboptimal local maxima. ICASSO assesses the stability of the obtained solution by running the same ICA algorithm starting from different initial points and with different bootstrapping, a number of times (in our work 30), and analyses the differences between the multiple estimates of the independent components. ICASSO matches components across different runs by clustering them based on the absolute value of the correlation between squared source estimates. The clusters will be compact, if the correlations between different estimates of the same IC are very high. If, however, the correlation between different clusters is very high, one might consider performing an additional data reduction step, and repeat the analysis with a lower number of estimated independent components.

The algorithm also returns the stability index Iq for each estimated cluster. In the ideal case, the estimates are concentrated in mutually orthogonal clusters, in which case this index yields a value very close to 1. If the clusters grow wider and start mixing, this value drops.

The ICASSO toolbox performs the FastICA algorithm. However, we additionally adapted it to use it with Infomax. The toolbox has already been used for the analysis of fMRI data [35]. The ICASSO toolbox itself can be found at `http://research.ics.tkk.fi/ica/icasso/`.

### 6.2.7 Evaluation Strategies

1. ***Application of JointICA*** – *Simultaneously Recorded Data*

   To investigate the performance of JointICA, we start with applying it to the ERP and fMRI data recorded simultaneously. We visually validate the technique by comparing the activations obtained from JointICA when the PO8 electrode is used with what is established in the literature [126, 61, 63].

   According to the mentioned literature, primary visual areas are located around the calcarine sulcus, and correspond to the C1 ERP wave. However, this wave is difficult to be seen on the PO8 electrode, but it is present on the midline electrodes (Oz, POz). The C1 peak for the DL stimulus is positive, and has a peak latency of around 100ms [126]. The activations start between 65ms and 90 ms. Therefore, we performed JointICA also with the Oz electrode, and we verified resulting first brain activations for all 4 stimulus-types.

2. ***Application of JointICA*** – *Non-Simultaneously Recorded Data*

   The magnetic environment of the MRI scanner invokes severe artifacts in the recorded EEG signals that can only be removed at the risk of damaging the brain signals in the measurements. Both residual artifacts and damaged brain signals can interfere with the optimal performance of the JointICA analysis. To evaluate the magnitude of these unknown nuisance factors we also applied the JointICA analysis on EEG data free of the magnetic field artifacts and distortions.

3. ***JointICA Experiment*** – *Investigating the Influence of the ICA Algorithm*

   To more fully understand the performance of JointICA and to be able to explain how and why it works, we performed several additional analyses. To begin with, we tested the importance of the ICA algorithm used for JointICA. All the results reported so far were obtained with the Infomax algorithm [14]. We also tested the JointICA performance using two other well-known ICA algorithms: JADE [30], which maximizes the statistical independence of the components by diagonalizing the 4th order cumulant of the mixing matrix, and FastICA [91], which uses a fixed point iteration scheme. FastICA extracts sources based on their kurtosis, as does JADE, but the convex optimization problem is solved using a cost function, instead of diagonalizing the kurtosis matrix.

4. ***JointICA Experiment*** – *Central Linking Hypothesis and Randomization*

   To check the central linking hypothesis, we also applied the Infomax algorithm separately to ERP and fMRI data in order to show the difference for both modalities compared to the JointICA analysis on the simultaneously acquired data. Based on these analyses, we expect to understand whether the JointICA algorithm separates components and sources based on the interaction between

both modalities, or whether the separation of one of the modalities is influenced (or driven) by the separation of the other one.

As explained before (see equation 6.1), JointICA assumes that the average amplitudes of both EEG and fMRI responses have the same pattern across subjects. It is worth noting that the correlation between average ERP and BOLD amplitudes is also proposed by [11].To verify this hypothesis, we connected random simultaneously acquired ERP and fMRI data (corresponding to different subjects) and applied the algorithm to check how the decomposition is affected. In this case, the amplitudes of ERP and fMRI responses are not expected to change synchronously, since they come from different subjects.

5. ***JointICA Experiment*** - *Robustness and Consistency Analysis*

   Finally, we investigated the robustness of the method. There were two aspects that needed to be checked in this respect: One was to check the consistency of the ICA decomposition. As mentioned in the previous section, the ICASSO toolbox was used for this purpose as to check the consistency of the Infomax and the FastICA decompositions. Another point to investigate was how the decomposition is dependent on the number of subjects in the study, and how it affects the decomposition when the number of participants falls below the suboptimal level. Therefore we applied a leave-one-out procedure, and checked the consistency for every number of subjects from 26 to 12 for the simultaneously recorded data, and from 18 to 12 for the data where the outside recorded EEG is used. The subjects were left out at random, but from 26 to 18, only the subjects without outside recordings were dropped, so that the subsets of 18 subjects for inside and outside recorded ERP data consist of the same participants.

The number of extracted independent components was 26 for the simultaneous measurements, and 18 for the non-simultaneously recorded data. The optimal model order was checked with the Akaike Information Criterion (AIC), the Minimum Description Length (MDL) and the R-index (a heuristic Davies-Bouldin type relative measure for a "natural" number of clusters, as implemented in ICASSO). All three methods estimated the information dimension (the number of components that should be extracted) equal to the full dataset dimension. This same estimate was also made for the EEG modality alone, whereas the dimensionality of the fMRI data was mostly estimated to be between 4 and 6.

As a final check of the JointICA robustness performance, we masked a part of the fMRI data, and compared the results to the case where the values from the whole brain are used.

For all the additional analyses we will present and discuss the results only for the stimulus appearing in the down-left visual field, but the conclusions for other

stimuli remain the same. Moreover, since we are interested in the fusion of fMRI and ERP modalities, and therefore only in the independent components which show both ERP and fMRI activation, we concentrate in this work only on ICs which contain 90% of the total ERP IC energy in the time range of 50 - 350 $ms$.

In the following section (Results), in several places, correlation analysis is used to compare different independent components. In these comparisons, the corresponding independent components are matched based on the highest mutual correlation coefficient, i.e. the two independent components are corresponding if the correlation coefficient between these two is higher than if one of them is compared to any other one.

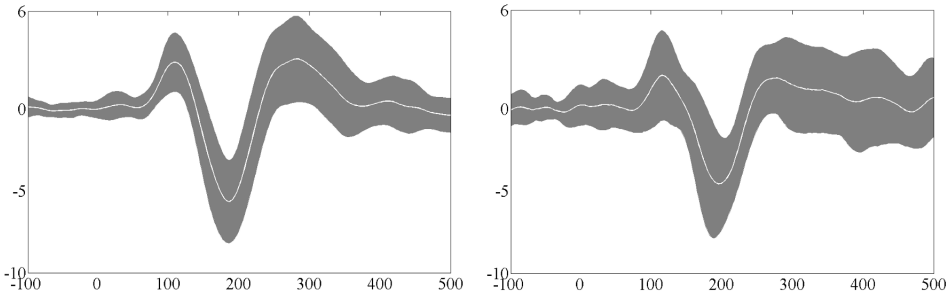


Figure 6.1: Average ERPs (white), and standard deviation (gray) extracted from the EEG data recorded outside the scanner room for 18 subjects (left), and from the simultaneously recorded EEG data for 26 subjects (right). The data are recorded on the PO8 electrode.

## 6.3 Results

### 6.3.1 Application of JointICA – Simultaneously Recorded Data

In this section, we present the results of the analyses on data for the simultaneous measurements in two ways. In Fig. 6.2, the JointICA decomposition is shown for the down-left visual field stimuli. The ERP data were derived from the electrode PO8, on which the P1, N1, and P2 ERP peaks are clearly visible, and the corresponding fMRI IC activations obtained from JointICA are shown.

Additionally, since the C1 ERP peak reflecting the initial bottom-up neural response of primary visual neurons located in the calcarine sulcus, is not visible on the more lateral PO8 electrode [61, 63], Fig. 6.3 integrates the first activation results of all four stimuli in different colors, corresponding to the C1 peak IC of the Oz electrode.

The detailed decomposition when the Oz electrode is used for the down-left stimulus is shown in Fig. 6.4.

Each subfigure in Fig. 6.2 a-f presents a specific fMRI IC activation, and the corresponding grand average ERP, together with the ERP IC wave (shown in yellow and blue respectively). Since only the positive expected fMRI activations are available in the literature which we use for validation, only the positive fMRI IC activations are also shown in this study. The reader should note that the Fig. 6.2c and Fig. 6.2d show the same independent component. They differ only in the slice that is taken to show the fMRI activations.

The locations of the fMRI IC activations in the brain are given in MNI coordinates in the figure captions, and anatomic areas are described. The P1 IC is associated with the activation in the right middle occipital gyrus (Brodmann Area 37). The N1 IC gives two components, the early one, associated with the right precuneus, cuneus and left lingual gyrus (BA 19, BA 7 and BA 18). During the late N1 ERP independent component, the areas in the right lateral occipital cortex (LOC) are active (BA 37). During this peak, also the activation in the somatosensory cortex (BA 3, 1 and 2) and primary motor cortex (BA 4) are visible. This activation is expected, since the subject was asked to press the button each time the stimulus appears. The component in Fig. 6.2e shows the ERP IC which appears as a transition from N1 to P2 ERP peak. This shows the activation in the right and left cuneus, and the right and left middle occipital gyrus. The P2 ERP peak is associated with the activations in the right middle occipital gyrus and right and left cuneus. These activations are expected, and are in line with previous findings in the literature [126, 61, 63]. It is interesting to note that the explained fMRI variance by the fMRI ICs shown in Fig. 6.2 was, 60%, while another 20% is explained by the activations in the early visual areas which did not belong to any of the ERP IC waves (extracted with the ERP data on PO8).

To further investigate the quality of the JointICA decomposition, in Fig. 6.3 we present the first fMRI activations that emerge in the fMRI spatio-temporal map, which can be considered the beginning of the visual activation. These activations correspond to the C1 ERP IC of the Oz electrode. The ERPs for down-left (DL), down-right (DR), upper-left (UL) and upper-right (UR) stimuli are presented in different colors. The corresponding ERPs with their C1 independent component are shown in the corners coinciding with the position in the visual field where the particular stimulus was presented, in colors describing the corresponding fMRI activation.

Fig.4 presents in detail all the activations derived with the ERP from the Oz electrode. Fig. 6.4a shows the fMRI IC activations around the calcarine sulcus that are associated with the C1 ERP independent component. The activated areas associated to the other ERP components (N1 early, N1 late and P2), correspond closely to the activations of the same ERP peaks, recorded on another electrode

(PO8), shown in Fig. 6.2.

To verify the correspondence of the fMRI maps of Fig. 6.2 and Fig. 6.4, the correlations between the independent components are calculated. The correlation values are 0.8 for the early N1 independent component, 0.73 for the late N1 component and 0.8 for the P2 component. In contrast, the C1 associated fMRI IC from the Oz analysis (Fig. 6.4a) does not correlate with the P1 associated fMRI component from the PO8 analysis (Fig. 6.2 a) (r=-0.12). This confirms that these two fMRI IC activation maps are entirely different, despite the fact that the fMRI data entered into the two analyses were identical and only the different ERPs could have caused this different result.

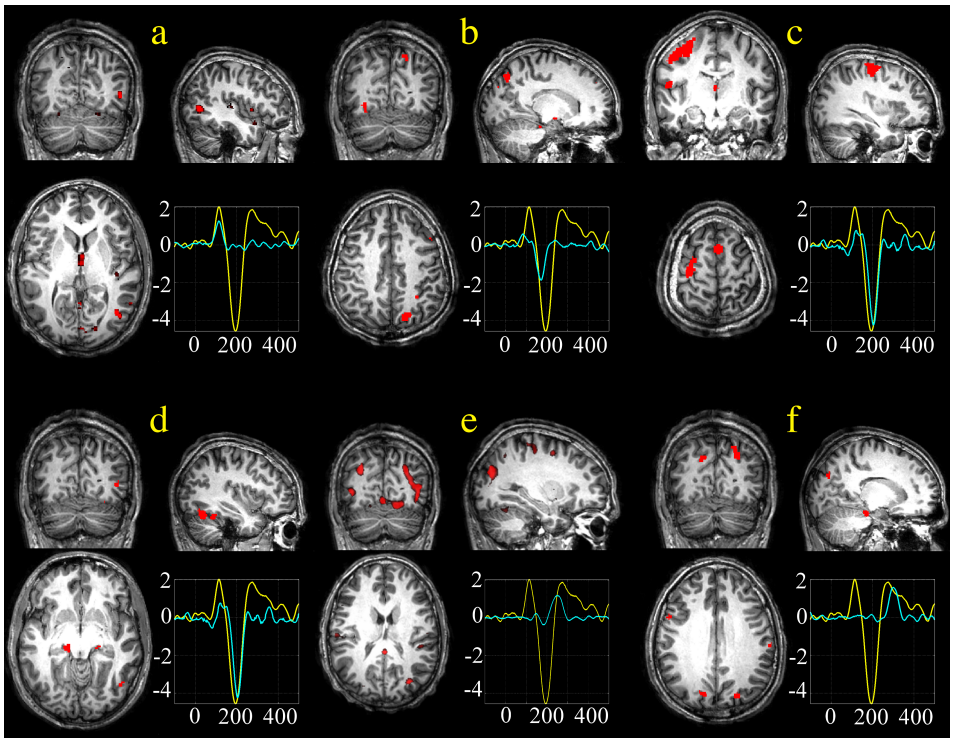


Figure 6.2: The results of JointICA for the simultaneously recorded data from the PO8 electrode for the down-left stimuli. Every extracted source contains an fMRI and an ERP part, shown in the different subfigures (a-f). Fig. 6.2-a shows the P1 ERP peak, and activation in the right middle occipital gyrus – lateral occipital complex (LOC) (BA37, MNI coordinates [44 -70 4]), and some activation in the right cerebellum (MNI [22 -70 -19]). Fig. 6.2-b shows ERP activity, partly corresponding to P1 and mostly to the early N1. The fMRI map shows the activity in the right precuneus (BA7, MNI [16 -78 40]), and right cuneus (BA19, MNI [21, -79 43]). Some activity is also present in left lingual gyrus (BA18, MNI [-31 -75 -8]). Fig. 6.2c and Fig. 6.2d show the activations corresponding to the P1 peak together with the late N1 component. Different slices are shown to depict motor and visual activations. The active fMRI areas in Fig. 6.2c are found in the right LOC (BA37, MNI [47 -67 -3]), and right cerebellum (MNI [32 -63 -19]). The fMRI activations in Fig. 6.2d are left postcentral gyrus - primary somatosensory cortex (BA 3, 1 and 2) and precentral gyrus - Primary motor cortex (BA4). Additionally, the insula (BA13, MNI [-56, -15, 16]) , and supplementary motor area (BA6, MNI [-47, 2, 50]) are activated. The ERP component in the Fig. 6.2e includes late N1 and early P2 activation. It activates the right and left cuneus (BA19, MNI [24 -83 36]), right and left middle occipital gyrus (BA19, MNI [45 -77 9]), and right cerebellum (MNI [17 -77 -15]). Finally, the P2 component is shown in Fig. 6.2f. It activates the right middle occipital gyrus (BA18, MNI [32 -86 2]), right and left cuneus (BA7, MNI [24 -83 36]) and right cerebellum (MNI [32 -68 -19]).

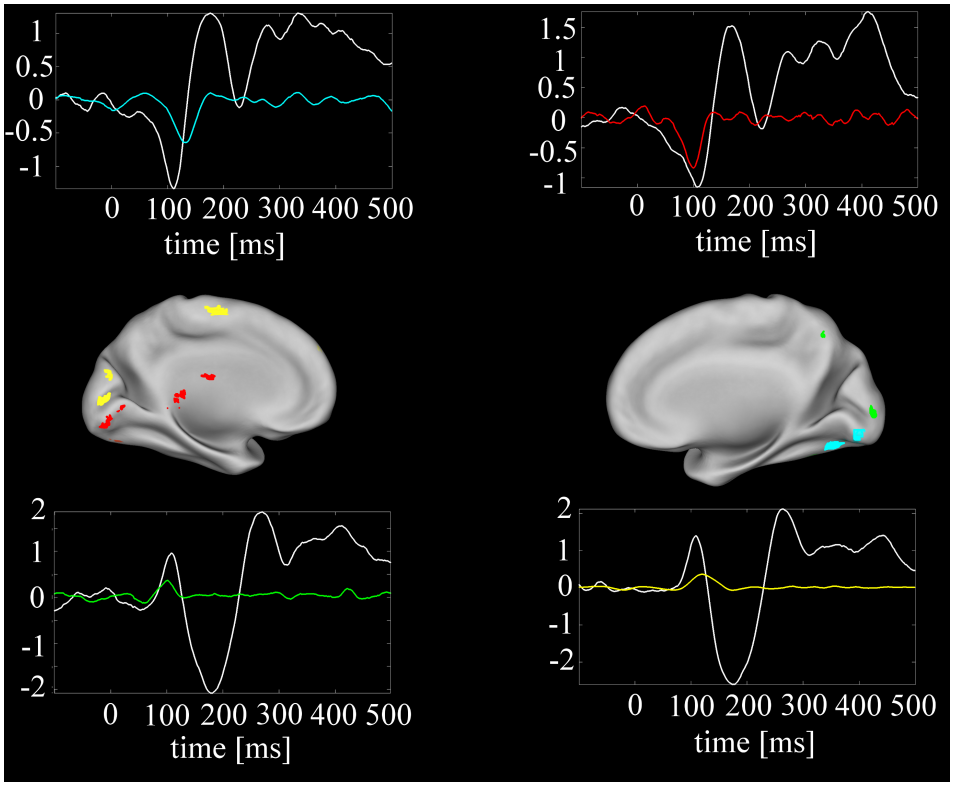


Figure 6.3: Brain activations for the simultaneously recorded data, corresponding to the C1 ERP wave for all 4 different stimuli (extracted with the Oz electrode). The offset starts around 60ms, and the latency of the peak is around 100ms. The grand average ERPs (in white), and the ERP C1 ICs (color) of the particular stimuli are shown in the corners of the figure, such that their position describes the corresponding stimulus (i.e., the ERP corresponding to the upper left stimulus is presented in the upper-left corner of the figures, and the down-left, down-right and upper-right stimuli are presented in the counterclockwise order). In the middle of the figure, the functional activations are plotted on the medial view of the inflated brain. Left and right hemispheres are presented on the left- and right-hand side, respectively. Each functional activation is painted in the same color as the corresponding C1 ERP IC.

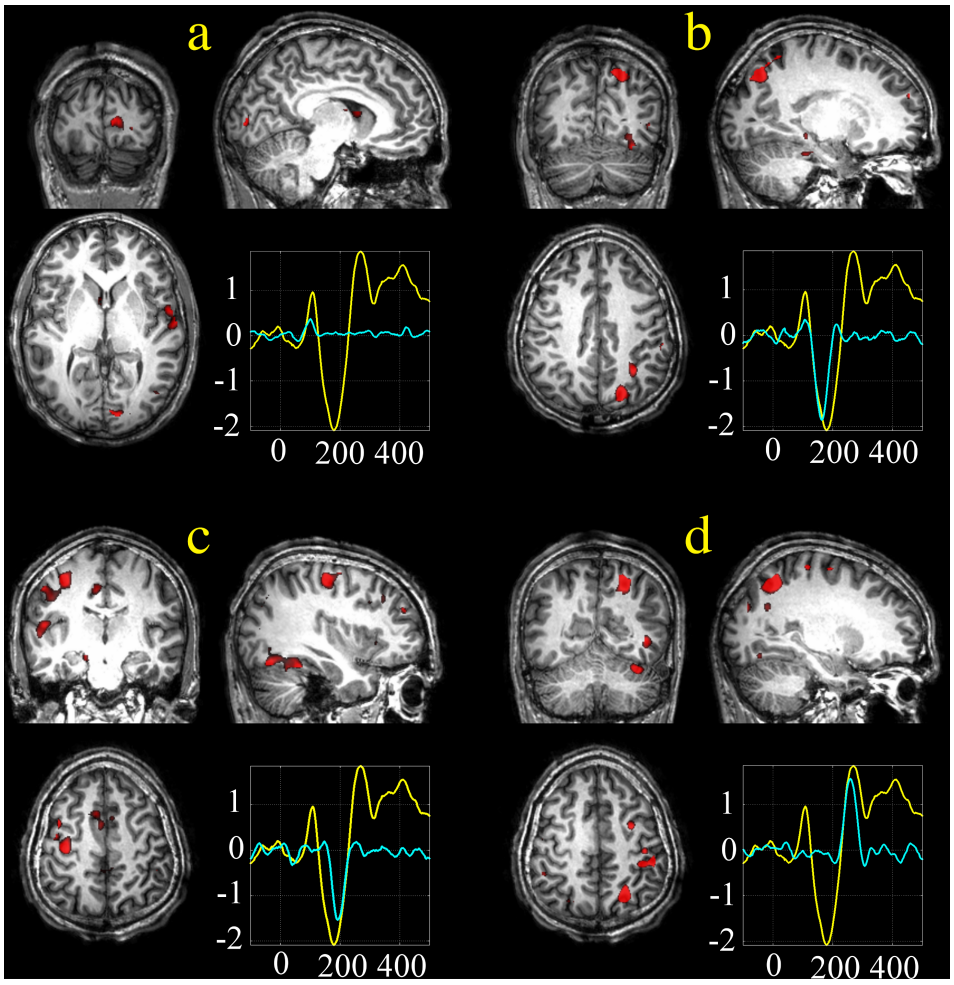


Figure 6.4: The results of JointICA for the simultaneously recorded data from the Oz electrode for the down-left stimuli. Every extracted source contains an fMRI and an ERP part. FFig. 6.4a shows the ERP wave containing the C1 peak. The corresponding fMRI activations are in the right upper lingual gyrus, around the calcarine sulcus – primary visual cortex (BA17, MNI [7 -93 5]). In Fig. 6.4-b, the early N1 component is present. The active fMRI areas are the right cuneus (BA7, MNI [18 -72 46]) and right lingual gyrus (BA18, MNI [28,-75 -9]). The late N1-related component (Fig. 6.4c), shows fMRI activations in the somatosensory cortex (BA3, 1 and 2) and primary motor cortex (BA4). The component in Fig. 6.4d shows P2 ERP activation, and the fMRI shows activity in the right cuneus (BA7, MNI [25 -63 53]).

### 6.3.2 Application of JointICA –Non-Simultaneous Recordings

In addition to the simultaneous acquisition, a non-simultaneous EEG measurement was performed for 18 out of the 26 subjects, in which the EEG data were recorded outside the scanner room, during the same task [9, 185]. The grand average ERPs of the inside and outside sessions are being compared in Fig. 6.1. The difference between the inside and the outside acquired ERPs can be due to magnetic field artifacts, as well as due to different environmental settings, like the scanner noise, or the supine versus upright position. The differences between the two grand average ERPs were much lower (RMSE=0.82), than the individual average ERPs of the corresponding subjects (mean RMSE across subjects was 1.81, with a minimum value of 0.97 and a maximal value of 3.1, see Fig. 6.1 for details).

To investigate the difference in quality between the data measured outside of the scanner room and the data measured inside the scanner, we computed the signal-to-noise ratios (SNRs) of the inside and the outside recorded ERPs for each subject. The SNR was computed such that the single trial ERP estimate was compared to the average ERP of the same subject. The provided SNRs are computed for the subset of 18 subjects, having both inside and outside recordings. The number of single trials in each average ERP was between 75 and 80 for both inside and outside recordings.The mean SNR for the inside data was $0.2484 \pm 0.0872$, whereas the SNR computed for the non-simultaneously measured data was $0.5385 \pm 0.2102$. The difference in the SNRs between the two datasets was significant ($p < 0.0001$).

Taking into account the higher SNRs for the outside compared to the inside data, and the greater similarity of the GA compared to single subject averages, we argue that the residual magnetic field artifacts in the inside case do affect the ERP signals. Therefore, we propose that it is relevant to make use of the outside recorded data to assess the influence of the magnetic field artifacts on the JointICA.

Fig. 6.5 shows the results of applying the JointICA algorithm to the fMRI data from the simultaneous measurement combined with the ERPs derived from the non-simultaneous measurement, again for the down-left stimulus condition. For an easier comparison, we overlaid the obtained fMRI ICs (blue) on top of the corresponding fMRI ICs obtained for the simultaneous measurements (red). The overlap between the two is shown in yellow. From this figure, it can be seen that the fMRI IC activations for the inside and outside measurements, corresponding to the same ERP IC waves, largely overlap. As it was the case for the inside recorded EEG, contra-lateral fMRI activation is visible in the middle occipital gyrus connected to the P1 peak. Activations are also present in the right cuneus and precuneus, associated with the N1 early peak, and the active regions in somatosensory and motor areas coincide with the N1 late activity. Also the P2 peak is mostly associated with the activations in left and right cuneus.

The fMRI ICs resulting from the analysis with the Oz electrode measurements

outside the scanner were also similar to the ones obtained in the corresponding analysis with the simultaneously recorded data (presented in Fig. 6.3 and Fig. 6.4). Therefore, these pictures are not additionally shown.

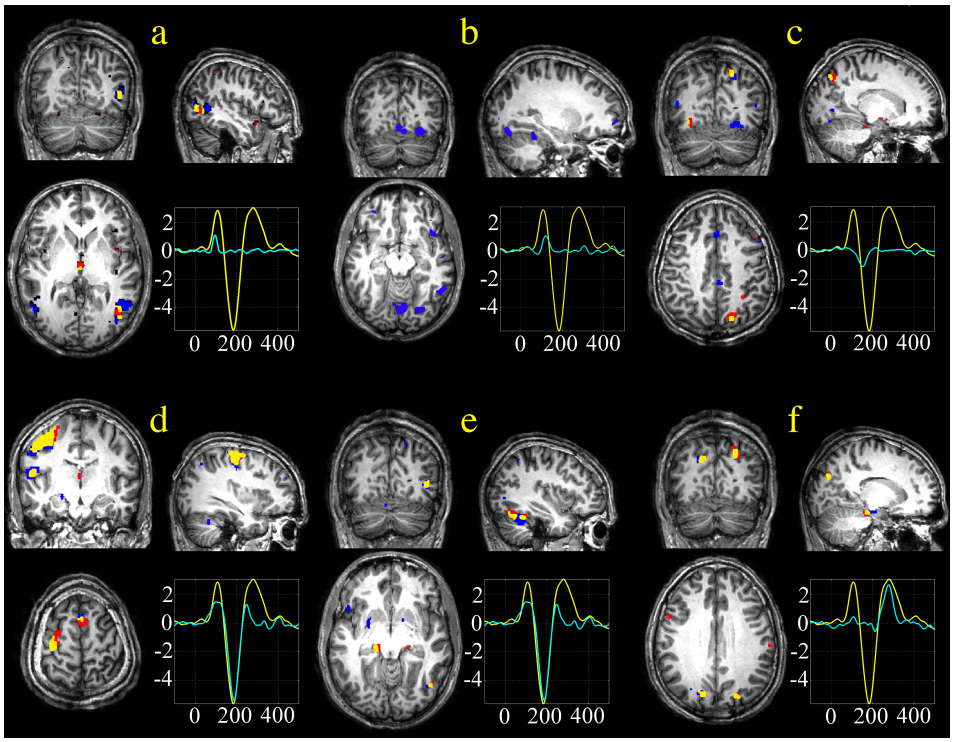


Figure 6.5: Each subfigure (a-f) shows the fMRI activation and the corresponding ERP IC from the non-simultaneously recorded data. The grand average ERP is shown in yellow. Concerning the fMRI activations, the activations from the simultaneous recordings (the same as in Fig. 6.2) are shown in red, the activations from the non-simultaneous measurements are presented in blue, whereas yellow shows the overlap between the two. The first activation (Fig. 6.5a) corresponds to the beginning of the P1 ERP wave (early P1 component). The fMRI shows activation in the right middle occipital gyrus (BA19, MNI [43 -77 4]), and in the left and right LOC (BA37). Fig. 6.5b shows activation corresponding to the late P1 peak. The associated fMRI active regions are right fusiform gyrus (BA19, MNI [33 -72 -19]) and some cerebellum regions (MNI [2 -77 -10]). The early N1-related components are shown in Fig. 6.5c. The fMRI activations are found in the right lingual gyrus (BA18, [21 -73 -9]), right precuneus (BA7, MNI [16 -80 37]), and right cuneus (BA19, MNI [19, -82, 43]). The late N1 component (Fig. 6.5d, Fig. 6.5e; Different slices are shown to depict motor and visual activations) shows activation in somatosensory and primary motor areas (BA 3, 1, 2 and 4), supplementary motor areas (BA6, MNI [-43, -5, 56]), the insula (BA13, MNI [-56, -15, 16]), together with visual activations in the right middle occipital gyrus (BA19, MNI 43 -77 4). The last, P2-related, component (Fig. 6.5f) shows activations in the left and right cuneus (BA19).

### 6.3.3 JointICA Experiment – Investigating the Influence of the ICA Algorithm

In Table 6.1, the cross-correlations between the independent components extracted by Infomax and FastICA (the left panel) and Infomax and JADE (the right panel) are shown. It is obvious that Infomax and FastICA yield similar components, with a mean cross-correlation value of 0.9815± 0.5811, whereas the results for Infomax and JADE are significantly different (mean correlation value of 0.7471±0.3736, p-value of unpaired t-test $< 0.0001$). The reported averages and standard deviations of the correlation values are corrected with the Fisher z-transformation throughout the manuscript.

Looking at the activations, the results from Infomax and JADE are different in the following sense: first, JADE did not yield specific P1-connected visual components. Second, JADE combined the P1 and early N1 ERP waves together in one component, but also their corresponding fMRI activations were combined in this same component. Third, the independent component revealing the late N1 peak in the ERP modality did neither show motor nor N1-associated visual activation. Instead, it yielded activation that was expected to belong to the P1 peak. The rest of the activations were similar.

Table 6.1: Correlations between the independent components derived from 26 subjects using different ICA algorithms. Left panel shows the correlation between the maps derived with Infomax and FastICA, whereas the correlations between maps derived by Infomax and JADE are shown in the right panel. The Mean and the Standard Deviation are corrected with the Fisher z-transformation.

| Infomax-FastICA correlation | | | | Infomax-JADE correlation | | | |
|---|---|---|---|---|---|---|---|
| 0.9877 | 0.9913 | 0.9929 | 0.9732 | 0.6886 | 0.4982 | 0.9573 | 0.9 |
| 0.9924 | 0.9435 | 0.9927 | 0.9603 | 0.8633 | 0.7468 | 0.904 | 0.4829 |
| 0.9901 | 0.9572 | 0.9961 | 0.9949 | 0.4245 | 0.8691 | 0.8338 | 0.6417 |
| 0.9965 | 0.7324 | 0.8976 | 0.9883 | 0.567 | 0.7786 | 0.5996 | 0.5846 |
| 0.9888 | 0.9927 | 0.989 | 0.9969 | 0.7537 | 0.6556 | 0.9065 | 0.5808 |
| 0.9175 | 0.8327 | 0.8767 | 0.9882 | 0.482 | 0.7524 | 0.7264 | 0.6168 |
| 0.9252 | 0.994 | | | 0.9166 | 0.549 | | |
| | | | | | | | |
| Mean = 0.9915±0.5811 | | | | Mean = 0.7471±0.3376 | | | |

Table 6.2: Correlations between independent components derived with JointICA and with solely one of the modalities. The left panel shows the correlations with EEG and the right panel with the fMRI modality. The Mean and the Standard Deviation are corrected with the Fisher z-transformation.

| | Correlations of the ERP ICA to the ERP modality from JointICA decomposition | | | | | Correlations of the fMRI ICA to the fMRI modality from JointICA decomposition | | | | |
|---|---|---|---|---|---|---|---|---|---|---|
| Simultaneously recorded data | 0.4281 | 0.5719 | 0.7727 | 0.7172 | 0.566 | 0.6260 | 0.6799 | 0.7633 | 0.4568 | 0.4744 |
| | 0.3293 | 0.8916 | 0.5565 | 0.7468 | 0.6938 | 0.6177 | 0.3914 | 0.6519 | 0.4928 | 0.4957 |
| | 0.8188 | 0.8726 | 0.8551 | 0.4571 | 0.9109 | 0.8107 | 0.524 | 0.6798 | 0.5974 | 0.4820 |
| | 0.6024 | 0.3320 | 0.8689 | 0.8546 | 0.6907 | 0.8586 | 0.4682 | 0.4519 | 0.5587 | 0.7827 |
| | 0.9249 | 0.8395 | 0.8351 | 0.8775 | 0.7544 | 0.6722 | 0.5638 | 0.595 | 0.3656 | 0.6578 |
| | 0.7429 | | | | | 0.5850 | | | | |
| | Mean = 0.7541±0.3539 | | | | | Mean = 0.6065±0.2205 | | | | |
| Nonslimultaneously recorded data | 0.7053 | 0.5980 | 0.6991 | 0.7598 | 0.6902 | 0.7618 | 0.8742 | 0.4981 | 0.5728 | 0.8800 |
| | 0.5234 | 0.6081 | 0.6119 | 0.6996 | 0.7680 | 0.4297 | 0.7714 | 0.4311 | 0.6687 | 0.8717 |
| | 0.8513 | 0.7717 | 0.7822 | 0.9031 | 0.8655 | 0.7292 | 0.4785 | 0.5672 | 0.5179 | 0.4747 |
| | 0.5925 | 0.7182 | 0.8572 | | | 0.8260 | 0.8244 | 0.5862 | | |
| | Mean = 0.7414±0.2465 | | | | | Mean = 0.6887±0.3177 | | | | |

Table 6.3: Correlation of the different ICA maps derived with JointICA on 26 subjects of the inside data, and the JointICA of the 26 subjects when the ERPs are connected to fMRI maps of the non-corresponding subjects. The Mean and the Standard Deviation are corrected with the Fisher z-transformation.

| | | | | | | | |
|---|---|---|---|---|---|---|---|
| 0.3876 | 0.3857 | 0.4404 | 0.3469 | 0.4766 | 0.6848 | 0.3612 | 0.3813 |
| 0.5896 | 0.5811 | 0.3192 | 0.4462 | 0.5405 | 0.3022 | 0.2639 | 0.3477 |
| 0.5498 | 0.7366 | 0.4559 | 0.6363 | 0.3695 | 0.4724 | 0.5217 | 0.4772 |
| 0.7252 | 4618 | | | | | | |
| Mean = 0.4833±0.1802 | | | | | | | |

### 6.3.4 JointICA Experiment – Central Linking Hypothesis and Randomization

Further, we compared the ERP and fMRI decompositions obtained with the JointICA analysis, to those obtained by applying Infomax to solely fMRI or inside and outside recorded ERP data. The correlations of the Infomax decomposition of the ERP and fMRI data obtained in separate and joint decompositions, corresponding to the down-left stimulus are shown in Table 6.2. The correlations between corresponding components from bi-modality and mono-modality analyses were significantly higher for the ERP only (0.7541±0.3539) compared to the fMRI only analysis (0.6065±0.2205) (p = 0.0018) for the inside case. In the case of 18 subjects (outside data), still the ERP only data were more strongly correlated (0.7414±0.2465), than the fMRI data (0.6887±0.3177), but this difference was not significant.

To further investigate the importance of the central linking hypothesis, the bottom row of Table 6.3 shows the correlation coefficients between the fMRI IC maps derived in a regular way with simultaneously recorded ERPs, and the fMRI IC maps derived with the same ERP data, but now randomly assigned to the fMRI maps (i.e. the fMRI and the ERP data of the subjects do not correspond to each other). Obviously, the correlation coefficient values are rather low, indicating that the amplitude changes in the ERP and fMRI components are closely related.

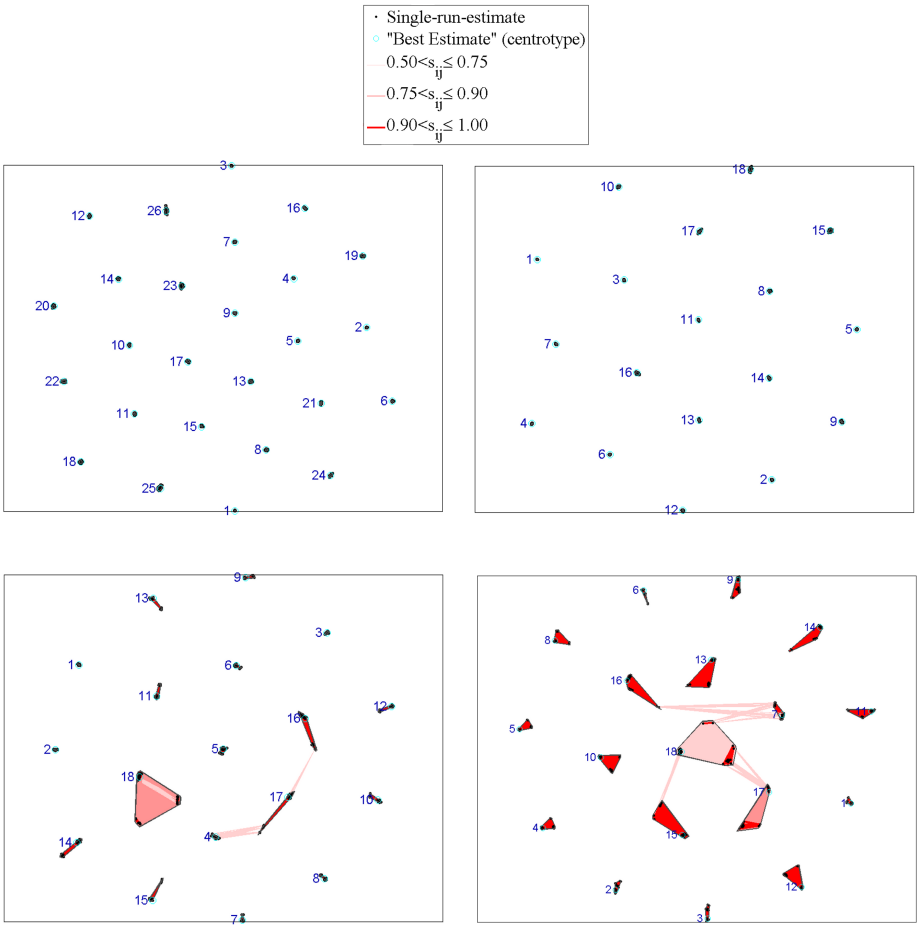


Figure 6.6: Cluster plots from the ICASSO analyses: a) Infomax, simultaneously recorded data, 26 subjects; minimal Iq value was 0.9989 b) Infomax, data recorded in separate sessions, 18 subjects, with minimal Iq value of 0.9536 c) Infomax, simultaneously recorded data, 18 subjects; minimal Iq was 0.8159 d) FastICA simultaneously recorded data, 18 subjects, with minimal Iq of 0.6287. Dots represent the estimates from a single iteration (there are 30 iterations), blue circles are the "best" estimate, taking into account the results from all 30 iterations. $s_{ij}$ denotes the correlation between the estimates. The figure shows that the IC estimates in panels a) and b) are focused to the same value, whereas the estimates in c) and d) are spread. Also, the connections between different clusters indicate the mixing between the estimates of different independent components.

### 6.3.5 JointICA Experiment - Robustness and Consistency analysis

To explore the robustness we performed several analyses, and we additionally employed the ICASSO method as described in the Methods section. The minimal Iq values are given in Table 6.5 for different numbers of subjects in the experiment (12 to 26 for the simultaneous, and 12 to 18 for the non-simultaneous measurements). Fig. 6.6 presents the results of the ICASSO analysis for different setups. The red and pink lines respectively describe stronger and weaker connections between the estimated clusters. If the decomposition is consistent, the between-cluster connections do not exist.

First, ICASSO showed that the decomposition for both the 26 inside recorded subjects, and 18 subjects where the ERPs were recorded in separate sessions were stable, with the smallest Iq values of 0.9989 and 0.9536, respectively (Fig. 6.6a-b). However, the ICASSO study provides only the information about the consistency of the decomposition itself, not about how is it influenced with respect to a different number of subjects. Therefore, we additionally checked the behavior of the decomposition when the number of subjects for the simultaneous measurement drops from 26 to 18. In this leaving-one-out procedure, always subjects without outside recording were left out, ending with the 18 subjects which have both inside and outside recordings. Beside this constraint, the subjects were left out completely at random. Since the difference between these two measurements is mostly reflected in the P1-related IC ERP and fMRI maps (see Fig. 6.2 and Fig. 6.5, and Table 6.4), we followed the behavior of the independent components, associated with this peak.

For the number of subjects being 25, not much was changed (see Tabel 6.5). Then, the decomposition becomes unstable with 24 subjects (minimal Iq of 0.7982). Closer inspection of the joint decomposition, revealed that the P1 peak, which was alone in the decomposition for 26 subjects (Fig. 6.2), got separated in 2 peaks, but the fMRI activations were not interpretable. The decomposition is still unstable, until the number of subjects drops down to 19 (minimal Iq 0.9573). At that point, the two P1 peaks are merged together again, but with no interpretable fMRI component. The same holds with the 18 subjects, and this decomposition is shown in Fig. 6.7. These 18 subjects in Fig. 6.7 are the same subjects, whose outside results are shown in Fig. 6.5.

We additionally compared in Fig. 6.6 the robustness of the Infomax decomposition for 18 subjects recorded in the non-simultaneous and simultaneous sessions (Fig. 6.6b-c), and also the FastICA decomposition of the 18 subjects recorded in the simultaneous session (Fig.6 d). This figure shows that the Infomax inside decomposition for 26 subjects and the decomposition for 18 subjects recorded in the separate sessions are stable, meaning that they yield a constant decomposition,

independently of the initialization of the Infomax algorithm (Fig. 6.6a-b). Fig. 6.6c shows that the Infomax decomposition of the simultaneous data is less robust than the one for the separate measurements, when an equal number of subjects (18) are used, with a minimal Iq of 0.8159.

A comparison of the results obtained by Infomax and FastICA on the simultaneous measurements (Fig 6c versus 6d) shows that the FastICA algorithm is more unstable than Infomax (minimal Iq is only 0.6287). It is worth noting at this point that, when FastICA ICASSO is applied to the dataset of 26 subjects, it gives a very stable performance (Iq of 0.9932).

When the number of subjects is further reduced (the decomposition with 12 subjects is shown in Fig. 6.8), the components in the simultaneous Infomax setting are getting merged together, and the decomposition becomes stable again (Iq=0.9435, see Table 6.5). Note that in Table 6.5, we always leave the same subject out, in both inside and outside recordings. The subject which was to be left out is chosen completely at random.

Fig 8-a shows that the ERP IC merges the P1 and early N1 ERP peaks, but also the corresponding fMRI ICs are merged (when compared to Fig. 6.2a and Fig. 6.2b). These activations are presented in Fig. 6.8-a in blue and green respectively. The overlaps with the decomposition with 12 subjects are presented in purple and yellow. Fig. 6.8b shows again the N1 late component, which shows the cuneus, precuneus, somatosensory and primary motor activation, same as Fig. 6.2c-d (shown in blue, overlap in purple). The same holds for Fig. 6.8c which shows the P2 ERP IC, and the corresponding fMRI IC maps, which correspond to the fMRI IC maps visible in Fig. 6.2f (shown in blue, overlap in purple).

It is also worth noting that for the non-simultaneous measurement, the Iq value is consistently high for all the number of subjects in the experiment from 12 to 18, whereas considerable variability in this value is present for the simultaneously measured data (Table 6.5).

As a last step in the robustness analysis, we checked how the decomposition is affected by masking a part of the fMRI data. We applied a mask that only included the occipital area, together with the cuneus and precuneus areas (the region where we expected our activation, without somatosensory and motor areas). The results did not change in the sense that the same fMRI ICs were connected to the same ERP ICs. The only difference was that somatosensory and motor areas were no longer present in any of the components. Therefore, the late N1 peak, for example, contained only the visual activations, as shown in Fig. 6.2d.

Table 6.4: The most important ERP peaks and their corresponding relevant activations retrieved from the simultaneously (left panel) and non-simultaneously (right panel) recorded data for the down left stimulus. All ERP peaks were identified on PO8 channel, except for the C1 peak of which the results were obtained with channel Oz. Regions like the cerebellum, which are less relevant for the present study, are not listed, here, but they can be found in Figs. 6.2 and 6.5 for the simultanous and non-simultanous data respectively. The fMRI activations are presented with their anatomical region, and their corresponding Brodmann area (BA), and can be seen in Figs. 6.2 and 6.5.

| Simultaneous data | | | Non-simultaneous data | | |
|---|---|---|---|---|---|
| ERP peak | Anatomical region | Brodmann | ERP peak | Anatomical region | Brodmann |
| C1 | Right upper lingual gyrus | BA 17 | C1 | Right upper lingual gyrus | BA 17 |
| P1 | Right LOC | BA 37 | P1 (early) | Right middle occipital gyrus | BA 19 |
| | | | | Right LOC | BA 37 |
| | | | | Left LOC | BA 37 |
| | | | P1 (late) | Right fusiform gyrus | BA 19 |
| N1 (early) | Right precuneus | BA 7 | N1 (early) | Right precuneus | BA 7 |
| | Right cuneus | BA 19 | | Right cuneus | BA 19 |
| | Left lingual gyrus | BA 18 | | Right lingual gyrus | BA 18 |
| N1 (late) | Right LOC | BA 37 | N1 (late) | Right middle occipital gyrus | BA 19 |
| | Left postcentral gyrus | BA 3,1,2 | | Left postcentral gyrus | BA 3,1,2 |
| | Left precentral gyrus | BA 4 | | Left precentral gyrus | BA 4 |
| | Left medial frontal gyrus | BA 6 | | Left medial frontal gyrus | BA 6 |
| | Left Insula | BA13 | | Left Insula | BA13 |
| P2 | Right cuneus | BA 19 | P2 | Right cuneus | BA 19 |
| | Left cuneus | BA 19 | | Left cuneus | BA 19 |
| | Right middle occipital gyrus | BA 18 | | | |

Table 6.5: The effect on consistency of the derived independent components when the number of participants is dropping from 26 to 18 observed through the Iq measure derived with the ICASSO analysis. The Iq stands for quality (stability) index. The index in the table is the lowest stability index for the dataset consisted of a particular number of subjects

| Number of components | Iq (simultaneous recordings) | Iq (non-simultaneous recordings) |
|---|---|---|
| 26 | 0.9989 | - |
| 25 | 0.9596 | - |
| 24 | 0.7982 | - |
| 23 | 0.7288 | - |
| 22 | 0.6736 | - |
| 21 | 0.8817 | - |
| 20 | 0.8817 | - |
| 19 | 0.9573 | - |
| 18 | 0.8159 | 0.9596 |
| 17 | 0.8964 | 0.9451 |
| 16 | 0.9524 | 0.9445 |
| 15 | 0.7565 | 0.9415 |
| 14 | 0.9533 | 0.9403 |
| 13 | 0.9518 | 0.9378 |
| 12 | 0.9435 | 0.9453 |

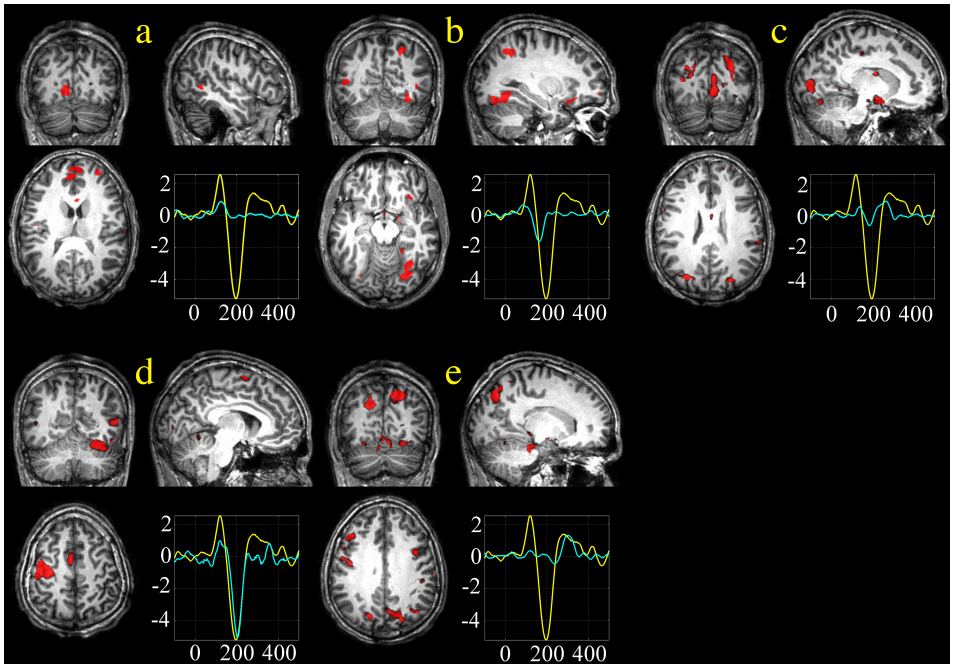


Figure 6.7: The JointICA results of the simultaneously recorded data for 18 subjects (the same subjects as in Fig. 6.5). Fig. 6.7a shows the activations in the left lingual gyrus (BA18, MNI [-11 -82 -3]), right middle occipital gyrus (BA37, MNI [48 -64 7]), with some additional frontal lobe activation. The ERP-related activation is connected to the P1 peak. Fig. 6.7b shows activity in the right fusiform gyrus (BA19, MNI [29 -76 -13]), right precuneus (BA7, MNI [26 -76 -16]) and left LOC (BA37, MNI [-51 -69 9]). The ERP activity is mainly connected to the early N1 peak. The activation in Fig. 6.7c is shown around the calcarine sulcus and bilateral activation is visible in the precuneus. Fig. 6.7d shows the somatosensory activity in Brodmann areas 3, 1 and 2, and in the primary motor cortex (BA4). Also, visual activity is shown in the inferior occipital gyrus (BA19, MNI [45 -72 -1]), and some cerebellum activity close to right fusiform gyrus. The ERP activation is connected to late N1 wave. The P2-related ERP activation (Fig. 6.7e) is mostly associated to the fMRI activation in the right and left precuneus (BA7).

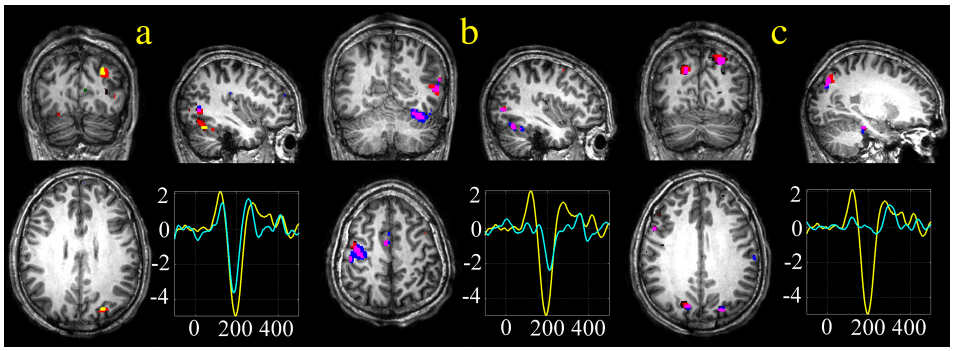


Figure 6.8: JointICA results of the simultaneously recorded data for 12 subjects (fMRI data shown in red). The blue and green activations correspond to the data obtained for the same peaks with 26 subjects. Yellow ERP data correspond to the grand average ERP, whereas the light-blue plot is a particular independent component. Fig. 6.8a shows the activations in the right and left fusiform gyrus, right middle occipital gyrus and right cuneus. fMRI activations corresponding to the P1 peak with 26 subjects (Fig. 6.2a) are shown in blue, and the early N1-related activations from Fig. 6.2b are presented in green. Yellow represents the overlapped area between red and green, and purple is the overlap between red and blue. Fig. 6.8b shows activity in the right middle occipital gyrus activation, somatosensory areas (BA3, 1 and 2) and in the primary motor area (BA4). Also some cerebellum activation is visible in the vicinity of the fusiform gyrus. Fig. 6.8c shows the fMRI IC activation in the left and right cuneus.

## 6.4 Discussion

In this study, we evaluated and presented the performance of JointICA, a recently proposed method for a symmetric integration of EEG and fMRI. To this end, we recorded EEG and fMRI data during a simple visual detection task. As this particular task is very well described in the literature [126, 62, 61, 63], we use this information to assess the relevance of the results in our experiments. For this reason, we did not additionally include a simulation study but for simulation studies of the algorithms used in this chapter, the reader is referred to [140, 42].

We compared the performance of JointICA for data acquired both simultaneously and non-simultaneously and investigated whether the decomposition was equally driven by both modalities, or solely by one of them. Moreover, we examined the validity and necessity of the assumptions that JointICA [23] relies on the amount of available data and the selection of the ICA algorithm. Further, we investigated the influence of the robustness and consistency of the decomposition obtained with JointICA, validated the central linking theorem, and we proposed the necessary conditions for a reliable decomposition.

### 6.4.1 Application of JointICA – Simultaneously Recorded Data

According to the literature and based on the characteristics of the presented task, the following activations are expected: the C1 peak should correspond to activity in the vicinity of the calcarine sulcus, whereas the early P1 peak is expected to activate the dorsal extrastriate areas of the middle occipital gyrus. Furthermore, the late P1 wave is known to be related to activations in the ventral fusiform gyrus, and the early N1 peak should yield activations of the parietal lobe, close to the intraparietal sulcus [126, 61]. In addition to this visual stimulation, our subjects were required to respond to the presented stimuli by pressing a button, which should evoke activation of the somatosensory and primary motor cortex.

The above expectations were consistently confirmed in our study both on simultaneously and non-simultaneously acquired data. However, as is shown in Fig. 6.2, the P1 ERP IC emerged as expected, but the activation connected to it was not complete in the sense that there was no activation in the ventral fusiform gyrus (as explained above).

Also in Fig. 6.3 and Fig. 6.4, we find the expected activations. It is clear that the C1 peak is positive for lower visual field stimuli, and negative for upper visual field stimuli. This comes from the fact that the activations which produce the C1 ERP peak lie on the opposite sides of the calcarine sulcus, and therefore their dipoles produce peak activations with an opposite polarity [32, 62]. It is also clear from Fig. 6.3, that the voxels associated with these early ERP components are located

in or very close to the calcarine sulcus in the contra-lateral hemisphere of the brain, as expected. Also, voxels in the upper bank of the calcarine sulcus are associated with the C1 aspect of the ERPs invoked by the lower-half visual field stimuli and voxels in the lower bank of the calcarine sulcus are associated with this component from the upper-half visual field stimuli.

As a further argument that these decompositions are valid, we showed that the early components in the analyses with the PO8 electrode (Fig. 6.2) and the Oz electrode (Fig. 6.3 and Fig. 6.4) do not correspond. On the other hand, we showed that the later fMRI ICs from the Oz analysis are spatially highly correlated with the fMRI ICs from the PO8 analysis (also visible in Fig. 6.4).

### 6.4.2 Application of JointICA –Non-Simultaneous Recordings

Making use of the EEG data measured outside of the scanner room, slightly improved the interpretability of the results and yielded spatio-temporal activations more consistent with the literature, specifically for the P1-related component. Earlier work by [126] showed that the P1 ERP wave is generated by two different regions. One region is found in the middle occipital gyrus (this activation is present in both inside and outside maps, Fig. 6.2a Fig. 6.5a). However, another region that contributes to the late P1 activation is located in the fusiform gyrus. This contribution can be clearly seen in Fig. 6.5b, but not in Fig. 6.2a, nor in any other subfigure of Fig. 6.2. It is also worth noting that the locations of the brain activation clusters shown in Fig. 6.5 are in strong agreement with the source localization that were obtained by Di Russo et al.[61] using dipole-modeling.

That the outside data yield more activation than the inside ERP data is further evident from the fact that the results were obtained with only 18 datasets, or 8 less than in the analysis with data measured simultaneously. To further substantiate this, we repeated the jICA analysis with inside EEG data with only 18 datasets (the subset of subjects which has both inside and outside recordings, as mentioned before). The results of this analysis did not yield the expected P1-related fMRI activity (Fig. 6.7). This was contrary to the non-simultaneous analysis in which the expected fMRI activation for the P1 wave was fully captured in the P1 IC (Fig. 6.5), despite that it included only 18 participants. This difference is probably due to residual scanner-related artifacts in the EEG data measured inside the scanner. Firstly, the quality difference of the ERPs recorded inside and outside the scanner room is obvious from Fig. 6.1 (especially from the pre-stimulus baseline variations), and from the SNR values provided in the Results section. Secondly, our previous work has shown that the quality of ERPs from EEG data recorded inside the scanner is strongly dependent on the procedures and parameter settings used for removing the artifacts and that the optimal settings vary from dataset to dataset [9, 185]. Of course, given the differences in position, (neuro)physiology

and measuring conditions between inside and outside EEG recordings, it cannot be excluded that some of the differences in the jICA result are also real differences that cannot be resolved with improved analysis and signal cleaning techniques. Taking this precaution into account, we believe that the results reported here constitute a good argument for acquiring EEG and fMRI data in separate sessions, as it may yield better results with fewer participants. However, under certain circumstances separate recordings are not recommended. E.g., there are many cognitive studies in which processes, such as habituation, learning and arousal state [55, 54], play an important role, and thus simultaneous measurements have to be performed. Also in some applications in clinical studies, simultaneous recordings are required. In both cases, it is essential to carefully optimize the data quality (e.g., [185] prior to further analyses.

### 6.4.3 JointICA Experiment – Investigating the Influence of the ICA Algorithm

Even though we know now which data properties are important to retrieve interpretable ICA components, this does not yet explain why exactly the JointICA method is able to extract these specific multimodal components. If one would consider general ICA assumptions, obtaining these components does not seem logical for the following reasons. First of all, the fMRI spatial activation maps in the brain have no mathematical ground to be fully statistically independent from each other (although this hypothesis is hard to check). This is why algorithms based on e.g. the diagonalization of 4th order cumulant matrices (like JADE), and therefore destruction of all the 4th order cross-cumulants between the obtained independent components, are not able to separate fMRI sources correctly. This behavior was shown previously [24, 69, 35], and the same result is confirmed here in Table 6.1. Although JADE does connect some components in the reliable way, other components are either merged together, or the ERP IC peaks are connected with non-corresponding fMRI IC activations (according to the expected activations based on the literature). Second, there is no reason to assume that ERP temporal peak components and fMRI spatial independent maps are statistically dependent, and will therefore be extracted into single independent component. For the above mentioned reasons, JADE is not the good choice for the JointICA algorithm, and therefore [23] used Infomax.

For the fMRI applications, the superior performance of Infomax, compared to other algorithms, has been shown by different groups [130, 24, 22, 42]. Daubechies et al., [42] showed on various simulations that the performance of Infomax is linked to its ability to effectively handle sparse components rather than independent components as such. FastICA algorithm has also been tested, and it showed more sensitivity to statistical independence of the data distributions with non-sparse data, but these distributions had no influence if the data used in the experiment

were sparse. An explanation for this can be found in the fact that Infomax and FastICA are based on minimizing the nonlinear objective function, which was tailored to satisfy the expected distribution of the target components, not strictly implying statistical independence between components [29] showed that it was possible to improve the Infomax estimates by tuning the nonlinearity to better match the underlying distributions). Specifically, since the data distribution of the target components was assumed to be super-Gaussian (sparse), a sigmoidal function is chosen for Infomax [130], as implemented in the Fusion ICA Toolbox. For this reason, we expect Infomax to perform not only well on the fMRI but also on the joint data, assuming the sparsity of both modalities.

This means that, for Infomax to work, it is sufficient that brain areas corresponding to higher ERP peak amplitudes also need to show stronger hemodynamic responses and vice versa, and that the number of activated voxels with respect to the total number of analyzed voxels is small. If the amplitude modulation over subjects is linearly dependent between both modalities, due to equation 6.1 they will be captured in the same row of the S matrix, i.e., in the same independent component, even if the mutual independence between all the estimated components is not satisfied. As such, we can conclude that JADE is less effective in connecting fMRI activations with their corresponding ERP waveforms than FastICA or Infomax. For the analysis of the performance of the algorithms on the fMRI data, with a number of simulations where sparsity/independence was questioned, we refer the reader to [42].

Concerning the FastICA algorithm, it pursues the same goal, using the concept of differential entropy (negentropy), again an information theoretic function, interpreted as a measure of non-Gaussianity of a distribution. FastICA practically estimates negentropy, based on maximum entropy principles [90]. This results in the use of nonlinearities that are practically equivalent to those required by Infomax. Hence the decomposition by these algorithms is almost indistinguishable when 26 subjects are used (see the correlations in Table 6.1).

The difference between the two algorithms is the complementary way of adapting the unmixing matrices within each iteration. FastICA uses the non-adaptive rule, whereas Infomax uses the adaptive rule. The adaptation additionally requires the choice of a learning rate sequence, thereby affecting the convergence speed. However, the adaptation may account for some non-stationary effects in the observed data, and is more robust to the choice of the initial point (as confirmed by the ICASSO analysis in our work (Fig. 6.6)). For a more theoretical explanation about the algorithms and methods the reader is directed to (Infomax - [14]; Fixed-Point approach [91, 34]).

### 6.4.4 JointICA Experiment – Central Linking Hypothesis and Randomization

To support our central-linking hypothesis that the strengths of activations in ERP and fMRI data are indeed highly correlated, we refer to work of Sadeh et al. [168] for visual brain activation in humans. They examined the correlations between ERP and fMRI measures in face-selectivity. What they found is that not only face-selective ERP and fMRI responses were highly-correlated, but also that these correlations were specific for distinct ERP latencies and distinct brain regions. Following the same logic, we believe that these findings hold for all brain activations and that different ERP peak components are highly connected to different fMRI regions. This was also confirmed in a similar study with auditory stimulation by Mayhew et al. [129] and in a visual study of [11].

In the context of the central-linking hypothesis, we were comparing the similarity of the components obtained from integrated and individual ERP and fMRI ICA analyses. Based on this, and on the better results obtained with the non-simultaneously compared to the simultaneously acquired data (Figs. 6.5 and 6.7), we hypothesize that the JointICA decomposition is more strongly influenced by the ERP characteristics. It therefore represents an additional argument for optimizing the quality of the ERP data.

Nonetheless, the decomposition of the single modality ERP data was still significantly different from what was obtained in the joint decomposition. This is evident from the fact that some of the peaks obtained in distinct components in the separate analysis, are merged in the joint analysis, thanks to the fMRI maps. This indicates that, although the ERP data are more similarly decomposed, the fMRI modality also influences the decomposition significantly, which additionally confirms the central linking hypothesis.

As mentioned in the results, only 60% of the fMRI in the simultaneously processed data was explained through the PO8 ERP components in Fig. 6.2, whereas additional 20% is explained through a single fMRI independent component that shows activations in the primary visual areas, but has no ERP activation on the PO8 electrode. This fact is very interesting, since it implies that the so-called ERP-blind fMRI activations can be captured with the ICs having flat ERP part.

However, if the Oz electrode is used for decomposition, this same fMRI IC is connected to the C1 ERP IC. Therefore, the central linking theorem is additionally supported in the sense that a major part of the fMRI signal energy (more 80% in total) can indeed be explained with the ERP activity through the JointICA method. Moreover, it implies that the decomposition is more driven with the ERP modality, and explains the difference in the fMRI maps extracted jointly with the ERP data and in a separate analysis.

Another way to picture the central-linking hypothesis was the randomization analysis. It is shown that the ICs yield very low correlations with the randomized data (Table 6.3), significantly worse compared to the correlation coefficients obtained by comparison of Infomax to JADE (Table 6.1), or Infomax decomposition of solely the fMRI data (Table 6.2). Additionally, when the data are randomized, the fMRI IC maps are connected to the wrong ERP independent components, or show no interpretable activation at all. This leads to the conclusion that the decomposition with randomized ERPs is worse than if no ERP information is used.

An additional indication that the ERP data are important for the algorithm, is given by the above-mentioned fact that different electrodes yield a different decomposition. This is shown in Figs. 2 and 4, visualizing the decompositions using electrodes PO8 and Oz respectively. However, these decompositions differ only in the early ERP components. When Oz is used, the fMRI IC shows activations around the calcarine sulcus (primary visual area), whereas if the PO8 electrode is used, the middle occipital gyrus (P1-related region) is activated. All the other activations (early N1, late N1 and P2) are similar between the two decompositions. The differences correspond well with the fact that the activations around the calcarine sulcus are connected with the C1 peak, which is visible on the midline electrodes (e.g., Oz), whereas the activations in the middle occipital gyrus give rise to the P1 peak that temporally overlaps with the C1, but is visible on the more lateral EEG electrodes (e.g., PO8). For more information about the expected occipital activations connected to the task used in this study, the reader is referred to [126, 62, 61, 63].

### 6.4.5 JointICA Experiment – Robustness and Consistency analysis

Our results show that increasing the number of subjects has a clear impact on the quality of the decomposition. Table 6.1 shows that FastICA and Infomax extracted very similar independent components. Therefore, we conclude that, if the dataset is sufficiently large, both algorithms are going to show a consistent performance and yield similar results (as explained in one of the previous subsections). If the dataset is insufficient, the decomposition becomes unstable and Infomax performs better in the sense of consistency.

Fig. 6.7 (the decomposition of 18 subjects, simultaneously recorded data), teaches us that, apart for the P1-related independent component, other components are similar to when 26 subjects are used (Fig. 6.2). That implies (together with what we have seen by reducing the number of subjects from 26 to 18), that by taking less subjects into account, the decomposition is not going to change completely for all the components, but only for some (unstable) components, in this case P1. Other components are going to preserve their associated activations. This is because

the information dimension is higher than the data dimension, and therefore it is no longer possible to separate the data into more independent components. This becomes even more obvious when the number of subjects drops to only 12 (Fig. 6.8).

As mentioned before, when JADE is used in JointICA, the ERP ICs and the fMRI IC maps are sometimes merged into one component, but sometimes also wrongly connected. The corresponding components in the Infomax decomposition with 12 subjects are only merged into one independent component. This is the consequence of a non-sufficient dataset. However, if more ERP ICs are merged into only one independent component, the corresponding fMRI ICs are also merged into the same component. Therefore, the decomposition can still be trusted.

Based on our research, we try to speculate on the test for the reliability of the decomposition. The decomposition can be considered reliable if it is found to be consistent (Iq above 0.9) systematically across consecutive numbers of subjects. This means that if the Iq value is high both in the experiment with N subjects and in the experiment with N+1 or N-1 subjects, the decomposition is reliable. In that sense, reliable decompositions are shown in Fig. 6.2, Fig. 6.5 and Fig. 6.8, while the decomposition in Fig. 6.7 is not (see Table 6.5 for details). The consecutive number of subjects ensures the robustness of the decomposition. The consistency can be checked for both the Infomax and FastICA algorithms to ensure the sufficiency of the dataset.

However, as this claim is heuristically derived, it should only be taken as a hint for the researcher. Additional check, e.g. checking the existence of some physiologically expected components by an expert, should also be performed.

## 6.5 Conclusion

In this study, we investigated the performance of JointICA for EEG-fMRI data on a visual detection task. We showed and compared the performance when the EEG was recorded both simultaneously with fMRI data and in a separate session (outside the scanner room). The importance of the ICA algorithm, which is used for the decomposition, is also analyzed and discussed. Although it was previously suggested to use Infomax, it was better explained in the Discussion section of this chapter why exactly this algorithm is the best choice. For this reason, its performance was also compared to FastICA and JADE. Additionally, we validated the central-linking hypothesis, and showed that the joint decomposition is mostly influenced by the ERP modality, and that therefore a good quality of the ERP data is highly desirable. It is also shown that the number of included subjects should be as high as possible, in order to obtain a complete decomposition. However, if the available number of subjects is not sufficient for the full decomposition, a

meaningful decomposition can still be obtained, and we proposed a way to check if the obtained decomposition can be reliable. Although in this case some independent components are merged together, the corresponding ERP and fMRI activations still belong to the same independent component.

# Chapter 7

# A simultaneous EEG/fMRI Study on Local and Global Integration of Visual Information

*In the previous section, the JointICA approach has been explained and validated [136]. In this chapter, we exploit JointICA for another, more complicated, task (the task of perceptual grouping, described in 5.2.1). Besides discussing the results obtained with JointICA, this approach is compared to other approaches (correlation-based approaches). Also, the JointICA has been slightly modified in two ways, and these new results are presented and discussed. This research is performed in collaboration with the Laboratory of Experimental Psychology, KU Leuven.*

## 7.1 Introduction

Vision science aims to understand how the brain translates the pattern of light on the retina into a stable, coherent and meaningful picture of the outside world. An intermediate step in this process is to determine which parts of the retinal image belong together. To describe how local elements are perceptually grouped into larger wholes, a number of grouping principles have been introduced by the Gestalt School in the early $20^{th}$ century (e.g., [100]). These principles include – among others – proximity, similarity and good continuation (Fig. 7.1).

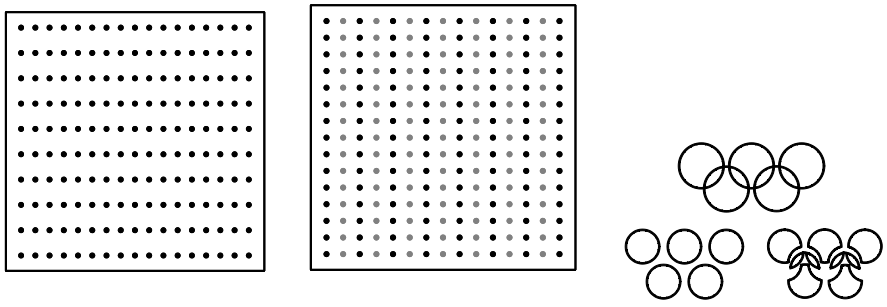

(a) (b) (c)

Figure 7.1: Illustrations of 3 Gestalt principles. (a) Proximity. The dots are perceived to group in horizontal lines, because the distance between the dots is smaller in the horizontal than in the vertical direction. (b) Similarity. The dots are grouped in vertical direction because of systematic luminance differences between adjacent columns. (c) Good continuation. The upper figure is perceived as a collection of 5 circles, rather than a collection of 9 more complex shapes, because we tend to see the lines continuing in their established direction

Our research investigates the neural mechanisms of contour integration, i.e. the grouping of local edges into global contours. Contour integration is strongly linked to the Gestalt principle of good continuation, the tendency to aggregate spatially aligned neighboring features into a continuous contour [189]. Good continuation has been studied extensively in the pathfinder or snake detection paradigm (introduced in [72]), in which participants have to detect a winding path in an array of randomly positioned elements. The strength of grouping by good continuation depends on a number of factors, such as the separation and relative orientation of local elements. More global contour properties also influence the grouping strength [85]). Straight contours are detected more easily than curved ones (e.g. [72, 84]) and changes in curvature direction impede path detection [154]. Longer paths [72] and closed contours (e.g., [103, 84, 155]) improve detectability.

Grouping of local elements into a global contour requires integration beyond the receptive field size of orientation selective neurons in primary visual cortex (V1). Field et al. [72] assumed that lateral connections between V1 neurons might enable this integration and, as such, provide the neural circuitry for contour integration. Empirical support for this view comes from Fitzpatrick [74]. He observed anisotropy in the striate cortex of the tree shrew. Neurons with the same orientation preference are more strongly interconnected. These connections also extend further than connections between neurons with a different orientation tuning. Schmidt, Goebel, Löwel, and Singer [172] obtained similar results in area 17 of the cat. In addition, they showed that the anisotropy is even more pronounced for neurons with spatially

aligned receptive fields. This synaptic architecture within V1 might enable the perceptual grouping of smoothly aligned edge elements. Further evidence for this idea comes from physiological studies that found enhanced neural responses in striate cortex when oriented gratings were flanked by collinear gratings outside the neuron's receptive field (e.g. [158]).

The integration of local elements into spatially extended contours has often been explained by a reinforcing cascade of lateral connections between V1 neurons (e.g., [113]). More recently, however, some authors have argued that a serial propagation through horizontal connections is probably too slow to explain the fast modulations by stimuli far outside the classical receptive field [7]. Probably, also extrastriate feedback connections to V1 play a role in contour integration [8]. This view of contour integration as a global-to-local process, mediated by feedback connections is supported by recent neurophysiological findings. Li, Piëch, and Gilbert [112] found that the enhancement of V1 responses to collinear contour elements disappeared under anaesthesia, highlighting the involvement of extrastriate areas in contour integration.

The involvement of both striate and extrastriate brain areas in contour integration has been observed in functional magnetic resonance imaging (fMRI) studies. Gabor elements that are arranged to form a closed shape outline elicit a stronger BOLD response than randomly oriented Gabor elements, both in object sensitive lateral occipital cortex (LOC) and in early retinotopic areas [5, 102]. Although fMRI has provided us with important knowledge about which cortical areas are involved in contour integration, it does not allow to tap into the temporal aspects of the grouping processes.

To uncover the time course of contour integration, imaging methods with a high temporal resolution are required. In a MEG study, Tanskanen, Saarinen, Parkkonen, and Hari [178] found that responses to collinear contours embedded in a field of randomly-oriented Gabor elements began to differ from no-contour stimuli after 130 ms, with the largest difference occurring 215 ms after stimulus onset. Earlier responses, 95 ms after stimulus onset, were identical to contour and no-contour stimuli. Their source analysis revealed contour-sensitive regions in the posterior parieto-occipital cortex. Mathes, Trenner, and Fahle [128] found a contour-specific EEG response, starting about 150 ms after stimulus onset, with detectable contours eliciting a negative shift over occipital recording sites (see also [122]).

Although the above MEG and EEG studies have yielded novel insights into the time course of contour integration, they do not provide much insight into the temporal dynamics underlying contour integration. Knowledge about the dynamical interplay between the different mechanisms of contour integration is fundamental to a comprehensive understanding of the mechanisms involved in contour integration. In the current study, we set out to investigate which cortical areas are activated when. Joint independent component analysis (JointICA) on simultaneously recorded

EEG/fMRI data, introduced in [23] and validated in [136] is a promising approach to study the temporal interactions between the cortical regions involved in contour integration. JointICA starts from the assumption that the amplitudes of the event-related potentials (ERP) and the haemodynamic responses covary because they are generated in the same brain region. The shared components can then be disentangled across participants, allowing to link temporally localized electrical activations (ERP peaks) to spatially localized BOLD responses.

In the current study, we apply these methods to reveal the neural underpinnings of local and global mechanisms of contour integration. We believe that local grouping (i.e., binding of neighboring elements) starts early in visual processing, and provides the input for more global grouping processes that evolve later in time and in object-sensitive areas. Grouping on a more global level can facilitate the ongoing grouping processes in retinotopic areas through recurrent feedback mechanisms.

## 7.2 Methods

### 7.2.1 Participants

15 participants (7 female and 8 male, aged 23-44, with a mean and standard deviation of respectively 27.4 and 5.2) with no history of neurological or cardiological disorders volunteered for this study. All participants reported normal or corrected-to-normal vision. Written informed consent was obtained in accordance with the KU Leuven Ethics Committee guidelines.

### 7.2.2 Task Paradigm

To investigate the mechanisms behind contour integration, a task was used in which two types of contour stimuli were alternated with no-contour stimuli (with the two types of contours in distinct runs). Below, first, a detailed description of the construction of these stimuli is given, after which the experimental procedure that was followed, is explained.

**Stimuli** The detailed description of the task used in this chapter was explained in 5.2.1. Here, only a short description is given, so that the following text can be more easily followed.

The employed stimuli were arrays of oriented and non-overlapping Gabor elements (see Fig. 5.4), created with MATLAB and GERT, the Grouping Elements Rendering Toolbox [59]. The stimuli were presented centrally on a uniform grey screen with a randomized alternation between local+global contour (LG), global-only contour

(GO), no contour (NC) and catch stimuli. NC stimuli were dense matrices of isolinear non-structure elements as shown in Fig. 5.4(a). Catch stimuli looked similar but included a small circle in the Gabor array (Fig. 5.4(d)). There were two types of structure stimuli, thereby distinguishing between two versions of task blocks. In LG, structure stimuli were dense matrices with curvilinear contour elements and isolinear non-structure elements (Figure 5.4(b)). GO task showed structure stimuli corresponding to dense matrices with alternating curvilinear and orthogonal contour elements and isolinear non-structure elements (Fig. 5.4(c)). For more details on similar stimulus construction, see [121].

**Experimental Procedure** The Gabor arrays explained above were presented centrally on a uniform gray screen, during a passive-viewing task. To ensure that the participants' attention was kept to the displays during passive viewing, an undemanding orthogonal catch task was used: while fixating in the middle of the screen, participants were instructed to press a response button when a circle was present in the array (as illustrated in Fig. 5.4(d)). To avoid that participants would focus on a small region of the display, the position of the circles was randomized across catch trials. Catch trials were not included in the analyses.

As such, each experimental run consisted of contour trials (frequency = .24), no contour trials (frequency = .48), catch trials (frequency = .08), and blank trials (frequency = .20). LG and G conditions were presented in separate runs, four of each type. The stimulus order within each run was optimized using the approach suggested in [98], slightly modified to allow for a random inter-trial duration.

A contour stimulus was always preceded by 1 to 5 no contour stimuli with identical Gabor positions, and was always followed by a no contour stimulus with different Gabor positions. To ensure that all effects pertain only to differences in element orientation (and not to differences in element position), the first no contour stimulus following a contour stimulus was not included in the analyses. The positions of Gabor elements in successive no contour arrays did not change, while their orientations did (each element was rotated at least 30 degrees away from its previous orientation).

Each stimulus was presented for 200 ms. The duration of the inter-trial interval was uniformly sampled between 2000 and 2400 ms. A central fixation cross was shown during the inter-trial interval. The experiment was run using the Presentation software (Neurobehavioral Systems, Albany, CA, USA). A Barco projected the stimuli on a translucent screen attached to the bore of the scanner. Responses to the catch trials were registered using a response box.

**Localizer Exeriments** In addition to our task paradigm focusing on contour integration, fMRI data were acquired during four more runs especially intended

to accurately define certain regions of interests (ROIs). Two types of these so-called localizer experiments were performed (two of each type). In the first, the meridian mapping experiments, horizontal and vertical wedges filled with black-and-white patterns of circles and squares were presented to the participants. These stimuli specifically activate the borders of the early visual regions, thus allowing an accurate localization of the early visual areas (EVAs) V1 and V2. Second, the contrast between presented objects and scrambled images during object-localizer experiments was employed to extract the lateral occipital complex (LOC, including LO and pFs) and co-lateral sulcus (CoS) areas, involved in object detection.

To sum up, a complete experiment consisted of 12 runs of about 5 minutes each: eight runs involving contour integration, two meridian-mapping and two object-localizer runs. The order of runs was randomized across participants.

### 7.2.3 Electrophysiology

The EEG acquisition and preprocessing is thoroughly explained in Chapter 4. Here we outline shortly the preprocessing steps used in this study.

**EEG recording** The EEG data were collected from 62 standard scalp sites using the MR-compatible BrainAmp MR+ system (BrainProducts,Munich, Germany) with a sampling rate of 5 $kHz$. Two additional electrodes were placed below the left eye and on the left upper back to monitor eye blinks and the electrocardiogram (ECG), respectively. All 64 channels were recorded with FCz as reference and Iz as ground. Electrode impedances were kept below 10 $k\omega$.

**EEG preprocessing** The acquired EEG data were subjected to the following preprocessing steps, of which the first ones were intended to remove the scanner-related artifacts in EEG simultaneously measured with fMRI data. Preprocessing as well as artifact removal were performed in the MATLAB (v 7.7; The MathWorks, Natick, MA, USA) environment with the EEGLAB 5.03 toolbox [58].

First, gradient artifacts were removed with the average template subtraction method [2], as implemented in the Bergen EEG-fMRI EEGLAB plug-in [142]. After filtering the data between 1 and 30 Hz and downsampling to 250 $Hz$, ballistocardiogram (BCG) artifacts were reduced with a combination of the Optimal Basis Set (OBS) method [147] and ICA [185]. In addition, eye artifacts were reduced with ICA [96] and data were rereferenced to the average of TP9 and TP10 (the closest electrodes to the mastoids in the present electrode setup).

To extract task-related event-related potentials (ERPs), all available blocks per subject and per condition were merged together and data were segmented from 100

$ms$ before until 500 $ms$ after stimulus onset. Baseline correction was performed based on the 100 $ms$ pre-stimulus interval and low quality trials were rejected by thresholding trials at 150 $\mu V$. Thereafter, an average ERP for each stimulus type was computed.

### 7.2.4 Functional MRI

The fMRI acquisition and preprocessing is thoroughly explained in Chapter 4. Here, the parameters used for this particular study are shortly outlined.

**fMRI acquisition** To acquire the fMRI images, a Philips 3T Intera whole-body scanner (Royal Philips Electronics, Amsterdam, the Netherlands) was used. The acquisition parameters differed between the experimental (related to contour integration) and the localizer runs. For each of the experimental runs, 155 echo-planar images (EPI) composed of 36 slices of 3 x 3 x 3 mm voxel size and 3 mm slice thickness were recorded with ascending slice order with 2 s repetition time (TR) and 29.8 ms echo time (TE). For the localizer runs, 110 images were acquired composed of 48 slices of 3 x 3 x 3 mm voxel size and 2 mm slice thickness with TR = 3 s and TE = 29.8 ms. In addition to the functional data, a full brain anatomical image was obtained with the magnetization prepared rapid gradient echo (MPRAGE) imaging sequence (182 coronal slices, TE = 4.6 ms, TR = 9.7 s).

**fMRI preprocessing** fMRI analysis was performed with the statistical parametric mapping software (SPM5, Wellcome Department of Cognitive Neurology, London, UK). The EPI time series were slice-time corrected, realigned, co-registered with anatomical images, normalized to a template and smoothed with a 6-mm FWHM Gaussian kernel. Next, fMRI activation maps were retrieved via a general linear model (GLM) analysis with stick-functions based on the onset times of the different stimuli. More specifically, percent signal change (PSC) maps were derived for each subject and stimulus.

**Definition of Regions of Interest** To define the regions of interest, first, the anatomical images of all participants were segmented and flat-maps were derived using the Caret5 software (Van Essen Laboratory, Washington University, St. Louis, USA). Subsequently, the SPM-derived activation maps (T-maps) from the object-localizer and meridian-mapping runs were projected onto these flat-maps, and thresholded based on a p-value of 0.001. The resulting overlays allowed deriving the CoS and LOC ROIs (for the object-localizer maps) and the ROIs in the early visual regions V1 and V2 (for the meridian-mapping maps).

### 7.2.5 Data analysis part 1: Correlation Study

The correlations are computed between the task-related fMRI activation in the ROIs extracted using localizers, and the time-instants in the average ERPs computed for the corresponding task in the following way. Concerning the fMRI data, in each of the ROIs, the 100 most sensitive voxels are selected from the fMRI PSC map. The median of these selected voxels is then used to for the correlation with the ERP data. The ERP data, are divided in $4ms$ windows. These data points for each subject, are then correlated with the fMRI activations from the ROIs, and this is performed for all the three recorded conditions (LG - local+global, GO - only global and NC).

### 7.2.6 Data analysis part 2: JointICA

To extract spatio-temporal information from the EEG and fMRI data acquired in this study, the JointICA approach, as originally proposed by Calhoun et al. (2006) [23] and validated by Mijović et al. (2012) [136], was used. JointICA starts from the assumption that the amplitudes of the ERPs and the hemodynamic responses co-vary when they are generated in the same brain region.

In order to apply JointICA, the fMRI PSC map obtained with the SPM GLM analysis for every subject and stimulus, was vectorized and concatenated with the average ERP for the same subject and stimulus. For each stimulus separately, the subject-specific concatenated ERP-fMRI vectors were then arranged together in one matrix and fed into the JointICA algorithm (freely available from http://icatb.sourceforge.net). As such, joint independent component maps were obtained as in Eq. 7.1, incorporating both spatial and temporal information about the stimulus-related processes.

$$\left[\mathbf{X}^{fMRI}\mathbf{X}^{EEG}\right] = \mathbf{A} \cdot \left[\mathbf{S}^{fMRI}\mathbf{S}^{EEG}\right] \tag{7.1}$$

The reliability of the JointICA decomposition was checked by calculating the stability index ($Iq$) using ICASSO [87], as proposed by Mijović et al. (2012) [136]. The $Iq$ index was computed for all the extracted independent components, both based on the complete dataset (15 participants), and when one of the participants was left out. In addition, this ICASSO analysis also allowed estimating the number of underlying components, based on the computation of the R-index [87].

### 7.2.7 Data analysis part 3: Modified JointICA

The application of JointICA explained above, was performed for each condition separately. However, the three different conditions present in this study (LG, GO and NC) are similar to a certain extent, such that they might invoke the same underlying neural sources. For this reason, it would be interesting to perform the analyses on the data from the different conditions simultaneously, in other words, to jointly estimate their mixing matrices and sources. As such, we could focus the method specifically on similarities and differences across conditions.

To explain this in more detail, let us denote the matrices representing the EEG and fMRI data from all subjects, induced by condition LG, with and , respectively (and analogously for the conditions GO and NC). We then propose to combine the data from the different conditions in a single matrix and perform the ICA analysis, as shown in Eq. 7.2:

$$\begin{bmatrix} \mathbf{X}_{LG}^{fMRI} & \mathbf{X}_{LG}^{EEG} \\ \mathbf{X}_{GO}^{fMRI} & \mathbf{X}_{GO}^{EEG} \\ \mathbf{X}_{NC}^{fMRI} & \mathbf{X}_{NC}^{EEG} \end{bmatrix} = \begin{bmatrix} \mathbf{A}_{LG} \\ \mathbf{A}_{GO} \\ \mathbf{A}_{NC} \end{bmatrix} \cdot \begin{bmatrix} \mathbf{S}^{fMRI} & \mathbf{S}^{EEG} \end{bmatrix} \tag{7.2}$$

with $\mathbf{A}_{LG}$, $\mathbf{A}_{GO}$ and $\mathbf{A}_{NC}$ the parts of the mixing matrix, corresponding to the conditions LG, GO and NC, respectively, and $\mathbf{S}^{EEG}$ and $\mathbf{S}^{fMRI}$ the EEG and fMRI portions of the extracted independent components. By modifying the JointICA analysis in this way, the information embedded in the source signals is assessed jointly for all conditions.

Subsequently, to extract the information in the independent sources, corresponding to a particular condition, the above-mentioned condition-specific parts of the estimated mixing matrix can be used. For example, by combining the LG-specific part of the mixing matrix A with the EEG and fMRI data from this same condition, the independent sources specific for this condition, can be extracted. This is illustrated in Eq. 7.3, with $\mathbf{A}_{LG}^{-1}$ the pseudo-inverse of the LG-specific part of the mixing matrix.

$$\begin{bmatrix} \mathbf{S}_{LG}^{fMRI} \mathbf{S}_{LG}^{EEG} \end{bmatrix} = \mathbf{A}_{LG}^{-1} \cdot \begin{bmatrix} \mathbf{X}_{LG}^{fMRI} \mathbf{X}_{LG}^{EEG} \end{bmatrix} \tag{7.3}$$

In this way, the information embedded in the source signals is going to be assessed jointly for all the conditions. If one remembers Eq. 2.19, all the columns of

the unmixing matrix ($w_i$) are estimated together, maximizing the entropy of the output. This procedure enables us to jointly maximize the likelihood of $\hat{\mathbf{S}}$ as $(p_x(\mathbf{WX})|\det \mathbf{W}|)$, instead of first estimating $\mathbf{W}_{LG}$, $\mathbf{W}_{GO}$ and $\mathbf{W}_{NC}$, such as to maximize the likelihood od $\hat{\mathbf{S}}_{LG}$, $\hat{\mathbf{S}}_{GO}$ and $\hat{\mathbf{S}}_{NC}$ as $p_{x_{LG}}(\mathbf{W}_{LG}\mathbf{X}_{LG})|\det \mathbf{W}_{LG}|$, $p_{x_{GO}}(\mathbf{W}_{GO}\mathbf{X}_{GO})|\det \mathbf{W}_{GO}|$ and $p_{x_{NC}}(\mathbf{W}_{NC}\mathbf{X}_{NC})|\det \mathbf{W}_{NC}|$ and then trying to make a link between the estimates. Therefore, the rows of the mixing matrix $\mathbf{A}$ (mixing matrix is computed as the pseudo-inverse of the unmixing matrix) are also calculated jointly.

## 7.3 Results

### 7.3.1 Visualization of Employed EEG and fMRI data

Fig. 7.2 shows the localized V1/V2, LOC and CoS areas obtained from the localizer analysis. The color bar depicts the number of subjects whose localized areas overlap at the particular voxel.

To illustrate the data that have been used to obtain the results below, Fig. 7.3 shows visual depictions of both the ERP and fMRI signals, averaged across subjects. First, the top panel of Fig. 7.3 shows the grand average ERPs corresponding to, from left to right, the LG, GO and NC condition. In addition, their standard deviation across subjects is illustrated in gray. Next, in the middle panel, the scalp distributions of these grand average ERPs at two different latencies are included. More specifically, for each of the conditions, the topography is displayed around a latency of 90 (top) and 190 $ms$ (bottom) after stimulus onset. Finally, the fMRI results of a second-level SPM analysis are visualized from three different views (ventral, medial and lateral) in the bottom panel. Furthermore, the contours of the group-ROIs, obtained by analyzing the data from the localizer runs, are illustrated in these same figures in different colors. More specifically, the contour of the V1 ROI is marked with a purple line, the V2 ROI is shown in green, a red line is used for the LOC ROI, and the CoS ROI is shown in black. The group-ROIs are defined as the overlapping areas between the individual ROIs from at least 10 subjects.

### 7.3.2 Correlations

The results from the correlation study are shown in Fig. 7.4. The inverse values of the corresponding p-values ($p^{-1}$) are shown in Fig. 7.5. In these plots, a value larger than 20, implies that the p-value is lower than 0.05.

The plots show three panels, corresponding to the conditions LG, GO, and NC from top to bottom, on the interval 0-400 $ms$. Different ROIs are color-coded. It

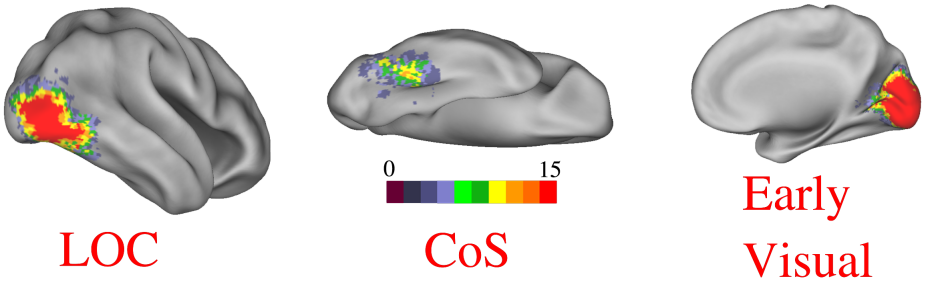


Figure 7.2: The regions of interest (ROIs) derived using the localizers, projected onto an inflated anatomical brain template. The color represents the number of subjects which have the active localizer area in the current voxel.

is to be noted that if the ERP and fMRI changes are positively correlated, then the sign of the correlation should correspond to the sign of the ERP amplitude at the particular time-instant. If the signs differ, that implies that the activation in the particular ROI is negatively correlated with the amplitude of the ERP at the particular time-point. The average ERPs for different conditions are shown in the bottom panels of Fig. 7.3.

These results imply that there exists a significant correlation between the ERP wave around 130 $ms$ and the EVA and LOC ROIs for the LG condition. Also, there is a significant negative correlation between the CoS ROI and the ERP wave at around 170 $ms$. In addition, significant negative correlations are observed with the EVA ROI around 350 $ms$ and the LOC ROI around 370 $ms$.

As for the GO condition, significant correlations are observed with the EVA ROI around 70 $ms$. The CoS ROI is correlated with the ERP wave at the latency of around 270 - 300 $ms$, and EVA and LOC show the correlations around 330 $ms$.

Concerning the NC condition, the significant correlations exist only in the time-interval between 0 and 50 $ms$.

### 7.3.3 JointICA

The JointICA results are shown in Figures 3-5 for the conditions LG, GO and NC, respectively. As explained above, for each case, the stability index Iq from the ICASSO analysis was computed for the complete dataset as well as after leaving out one subject. In all cases, the calculated values were higher than 0.9, implying a good reliability of the obtained results. The R-index of the ICASSO analysis

estimated the number of components to be derived on 15, for all three conditions in this study.

Fig. 7.6 shows both the temporal (ERP) and spatial (fMRI) part of five independent components resulting from applying JointICA to the data from the LG condition. Together with the ERP part of the independent components, also the grand average ERP corresponding to this same condition is shown. The components are ordered according to their temporal behavior.

From this figure, it becomes clear that the EVA regions (both V1 and V2) are activated around 60 $ms$ and 250 $ms$ (panels 1 and 5, respectively). Activations of the CoS area are visible around 200 and 250 $ms$ (panels 4 and 5), and the LOC is mainly activated around 70, 170 and 200 $ms$ (panels 1, 3 and 4). In addition, negative visual activations are visible around 130 $ms$ and 370 $ms$ (panel 2). These negatively activated areas should be interpreted as that the ERP and fMRI components are "contra-related", meaning that larger ERP peaks correspond to smaller fMRI activations and vice-versa.

In a similar way as for the LG condition in Fig. 7.6, Fig. 7.7 shows the JointICA results from the data corresponding to the GO condition. For this condition, EVA activations are mainly found around 170 $ms$, 270 $ms$ and 330 $ms$ (panels 2, 3 and 4). Furthermore, the component shown in panel 4 also shows a small peak around 70 $ms$, revealing additional EVA activation at this latency. The CoS area shows peak activations around 200 $ms$ and 270 $ms$ (panels 2 and 3) and LOC activations are visible around 200 and 330 $ms$ (panels 2 and 4). The activations around 70 $ms$, 200 $ms$ and 250 $ms$ are very similar to the activations shown earlier in Fig. 7.6, but there is a clear difference visible in the ERPs around 330 $ms$. More specifically, at this latency there is a clear negative peak for the GO condition, which cannot be seen in the LG results. For the GO condition, this peak corresponds to activations in LOC and EVA.

The JointICA results for the NC condition are summarized in Fig. 7.8. Also here, both the temporal and spatial parts of the independent components are shown, the former together with the grand average ERP waveform. Here, EVA activations are found around 170 $ms$ and 370 $ms$ (panels 1 and 3), CoS activations around 200 $ms$ (panel 2) and LOC activations around 170 $ms$ (panel 1). The late activation (around 370 $ms$) of the EVA ROI was also present for the LG condition (see Fig. 7.6, panel 2), but in the case of the LG condition, the relation between ERP and fMRI activations was negative, whereas for the current condition (NC) it is positive.

### 7.3.4 Modified JointICA

Fig. 7.9 shows the results of applying the modified JointICA approach to the data from all conditions simultaneously. The number of independent sources to

be derived was estimated to 23. For 6 independent components, the upper part of the figure shows the condition-specific fMRI results for (from top to bottom) the LG, GO and NC condition, respectively. The condition-specific ERP results are shown below in the figure, together with their grand average ERP waveforms. As explained above, a paired t-test is used to compare the condition-specific distributions across subjects of each component. In the figure, only p-values corresponding to significantly different distributions across subjects ($p < 0.05$) are included. Their subscripts specifically indicate the two conditions that were compared.

The components in the first and third panel (from left to right) show the same distribution across subjects for the three conditions ($p > 0.05$). The component in the first panel shows activations in the early visual areas around 70 $ms$ after stimulus onset. This activation could not be separated in the original JointICA analysis for the NC and GO conditions (Figs. 7.7 and 7.8). The component in the third panel reveals activations in higher visual areas and CoS around 200 $ms$. This same component was also found in the results obtained with the original JointICA analysis for all conditions (as shown in Figs. 7.6-7.8).

The component in the second panel shows activations in the LOC and EVA ROIs around 170 $ms$ after stimulus onset. Similar to the component shown in panel 3, also this component was found in the individual JointICA analyses for all conditions (see Figs. 7.6-7.8). However, as opposed to this previously explained component, the distribution across subjects of the current one is significantly different for the LG and NC conditions, implying that the processes behind these activations are physiologically different. By closer look at the activated regions, it is obvious that, although the EVA and LOC ROIs are activated for all three conditions, the activation in the LOC ROI is the same for LG and GO, but different from NC. Also the activation of the EVA region is the same for LOC and GO, but different for the LG condition.

The component presented in the fourth panel of Fig. 7.9, with the ERP part peaking around 240 $ms$ after stimulus onset, shows significantly different distributions across subjects for all three conditions. The NC-specific ERP part of this IC is a flat line with zero amplitude, implying no activation for this condition around this latency. The difference between the GO- and LG-specific parts of this IC is in the amplitude of their ERP peaks at 240 $ms$. In addition, the GO condition shows activations in the CoS and EVA areas, whereas for the LG condition, also the LOC area is activated.

The fifth panel of Fig. 7.9 shows a component that is only characteristic for the GO condition, with activations in the LOC and EVA ROIs. This component corresponds to a component retrieved with the individual JointICA analysis for this condition, as can be seen from panel 4 in Fig. 7.7. The advantage of the modified JointICA analysis, however, is that the flat lines available from the LG-

and NC-specific parts of the ERP information, confirm the exclusiveness of this component for the GO condition.

Finally, the rightmost panel of Fig. 7.9 shows an IC with not significantly different distributions across subjects for the three conditions. All three conditions reveal activations in the CoS and EVA areas. However, the EVA ROI activations for the NC and GO conditions are positive, whereas these same activations are negatively related to the ERP waveforms for the LG condition. This observation could not be made based on the results from the individual JointICA analyses and suggests the presence of very late activations of the early visual areas specifically for GO and NC.

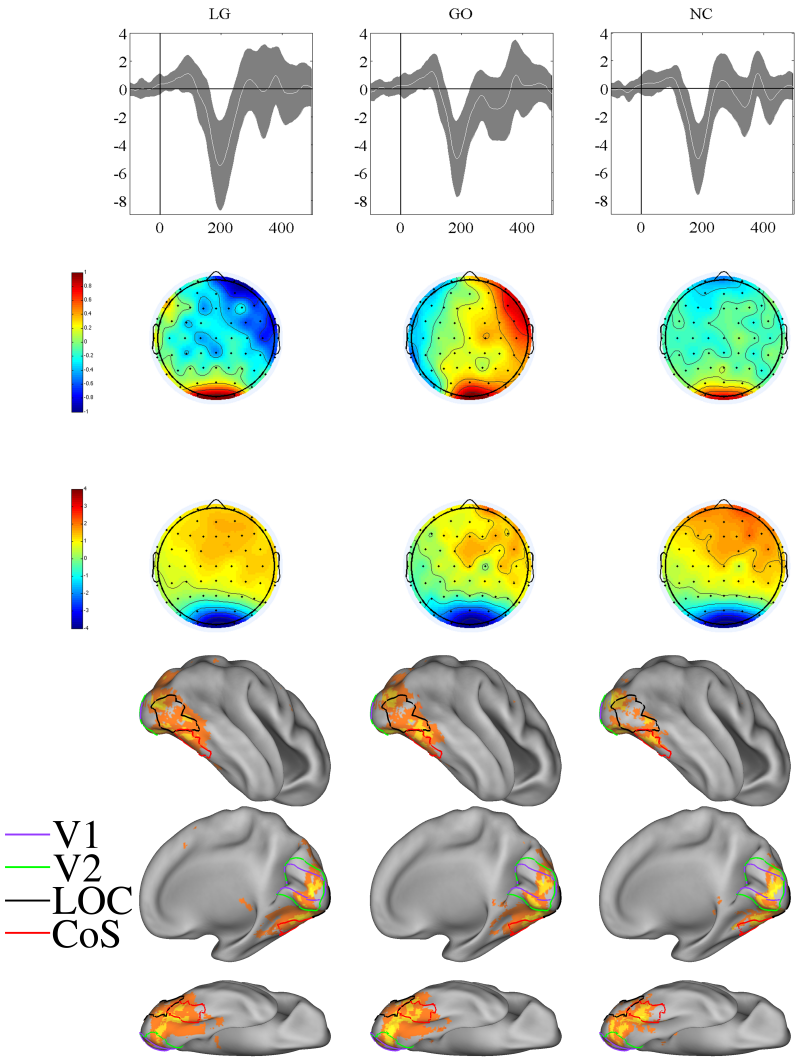


Figure 7.3: Top panel: ERP waveforms for each of the three conditions (LG = local and global, GO = global only and NC = no contour) on channel Oz. For each case, the grand average is shown in white and the standard deviation across subjects is colored in gray. Middle panel: Scalp distributions around 90 (top) and 190 $ms$ (bottom) after stimulus onset for each of the three conditions. Bottom panel: Results from a 2nd-level SPM analysis on the fMRI data from each of the three conditions (ranging from orange to yellow) together with the contours of the ROIs of interest for this study in different colors. These group-ROIs are defined as the overlapping areas between the individual ROIs from at least 10 subjects.

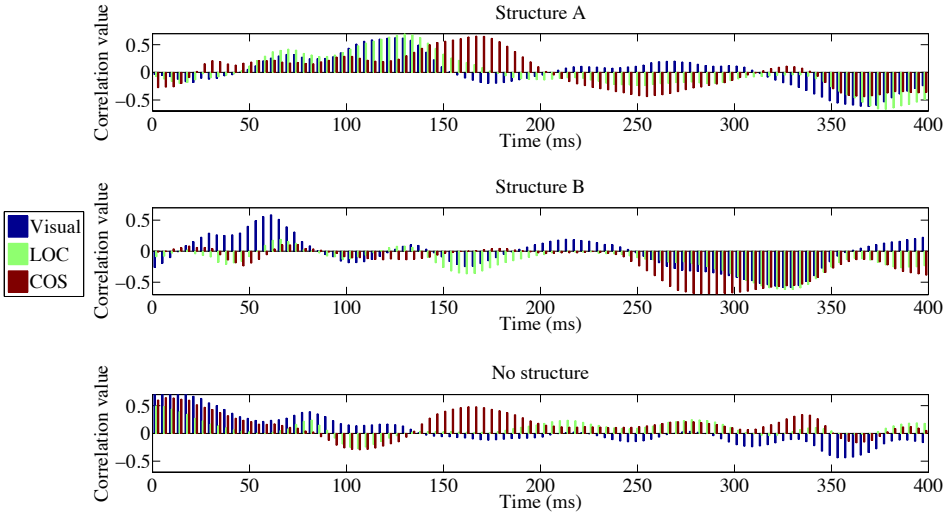


Figure 7.4: The correlation between the activations in a specific ROI and the ERP values at specific time points. The bin-length in the ERPs is 4 milliseconds. Different ROIs are shown in different colors. The early visual area (EVA) ROI is shown in blue, LOC ROI in green and CoS ROI in brown.

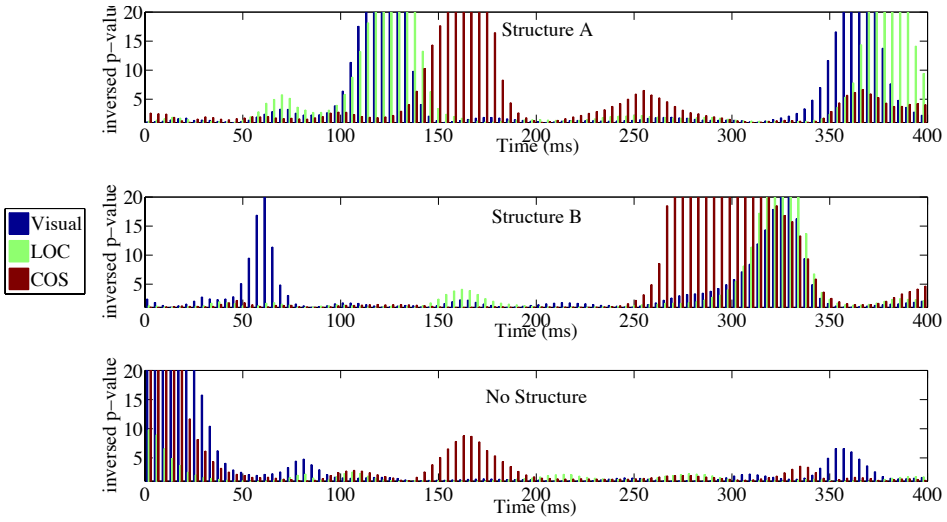


Figure 7.5: The p-values of the correlations from Fig. 7.4.The color codes are the same as in Fig. 7.4.

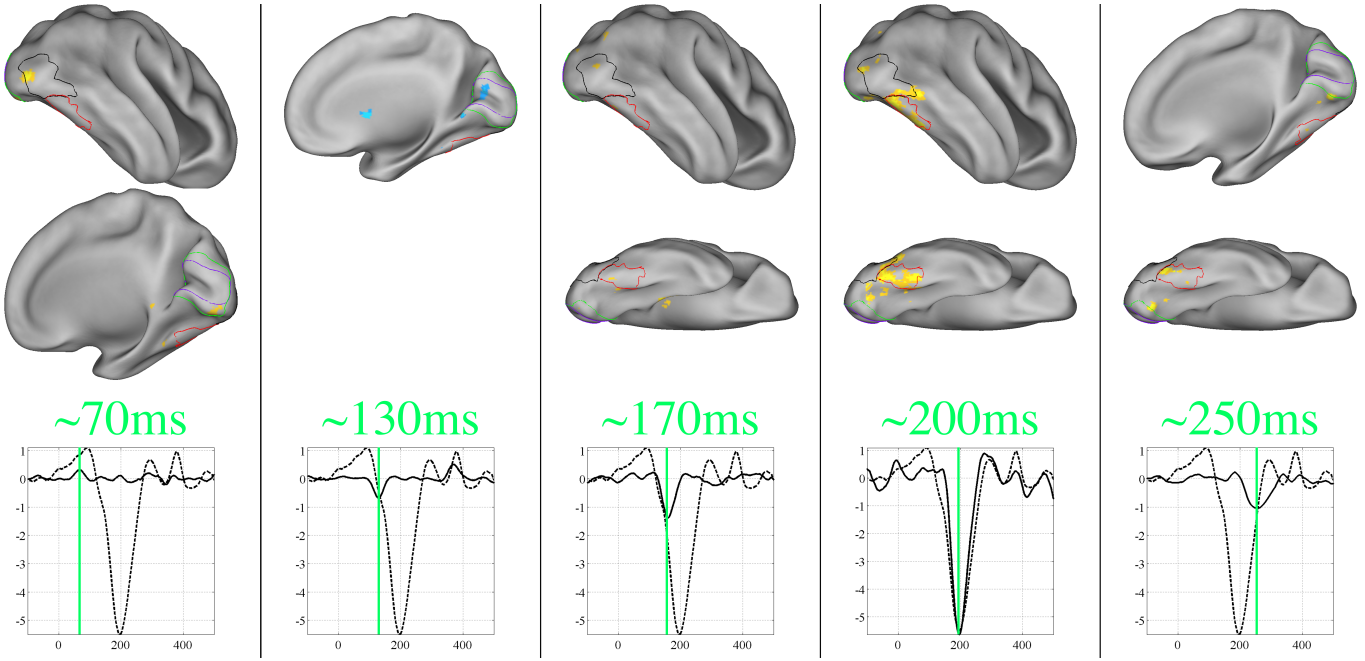


Figure 7.6: Results of the JointICA analysis applied to the data in response to the LG stimulus. Five different components are shown, ordered according to their temporal contribution. For each component the upper panel of the figure shows the spatial (fMRI) part, whereas the bottom panel represents the temporal (ERP) part together with the average ERP waveform (solid versus dotted line, respectively). The fMRI figures show yellow-orange colors for positive activations and blue ones for negative activations and also include the contours of the ROIs of interest in the same colors as in Fig. 7.3. Only activations, of which the absolute value exceeds 3 times the standard deviation of the activation values in all voxels, are shown.

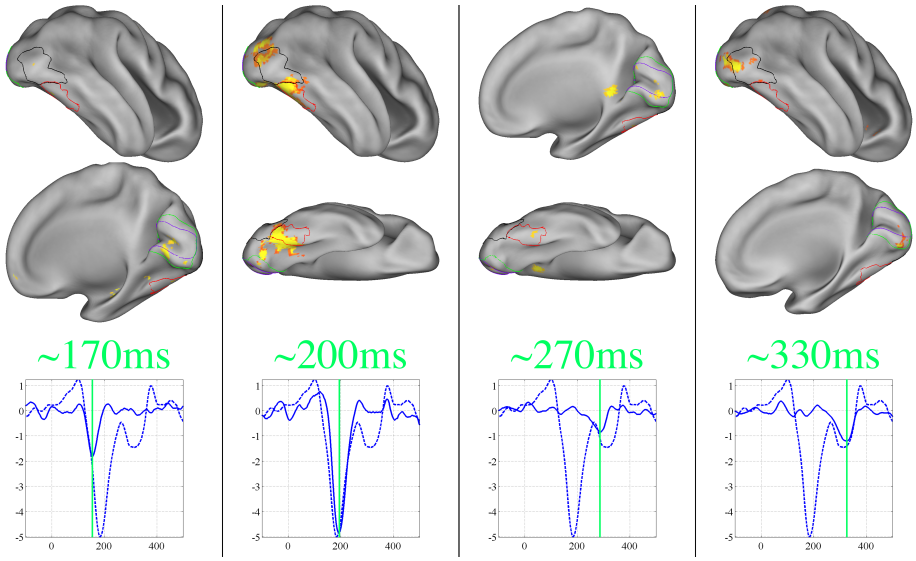


Figure 7.7: Results of the JointICA analysis applied to the data in response to the GO stimulus. Four different components are shown, ordered according to their temporal contribution. For each component the upper panel of the figure shows the spatial (fMRI) part, whereas the bottom panel represents the temporal (ERP) part together with the average ERP waveform (solid versus dotted line, respectively). The fMRI figures show yellow-orange colors for positive activations and blue ones for negative activations and also include the contours of the ROIs of interest in the same colors as in Fig. 7.3. Only activations, of which the absolute value exceeds 3 times the standard deviation of the activation values in all voxels, are shown.

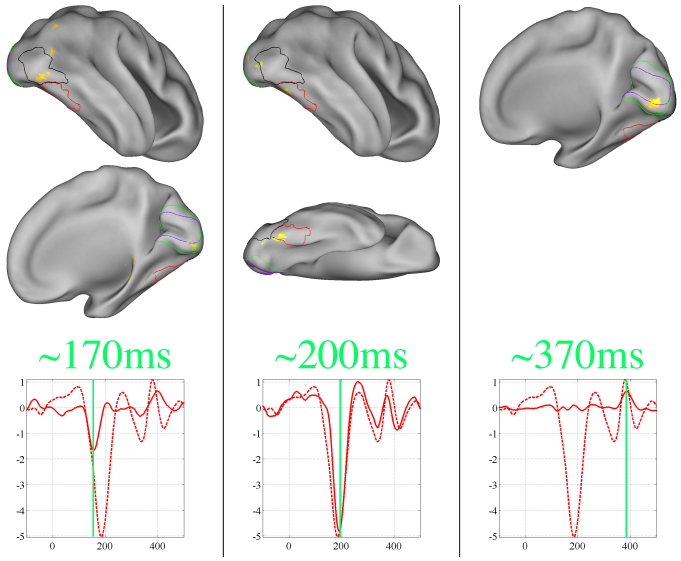


Figure 7.8: Results of the JointICA analysis applied to the data in response to the NC stimulus. Three different components are shown, ordered according to their temporal contribution. For each component the upper panel of the figure shows the spatial (fMRI) part, whereas the bottom panel represents the temporal (ERP) part together with the average ERP waveform (solid versus dotted line, respectively). The fMRI figures show yellow-orange colors for positive activations and blue ones for negative activations and also include the contours of the ROIs of interest in the same colors as in Fig. 7.3. Only activations, of which the absolute value exceeds 3 times the standard deviation of the activation values in all voxels, are shown.

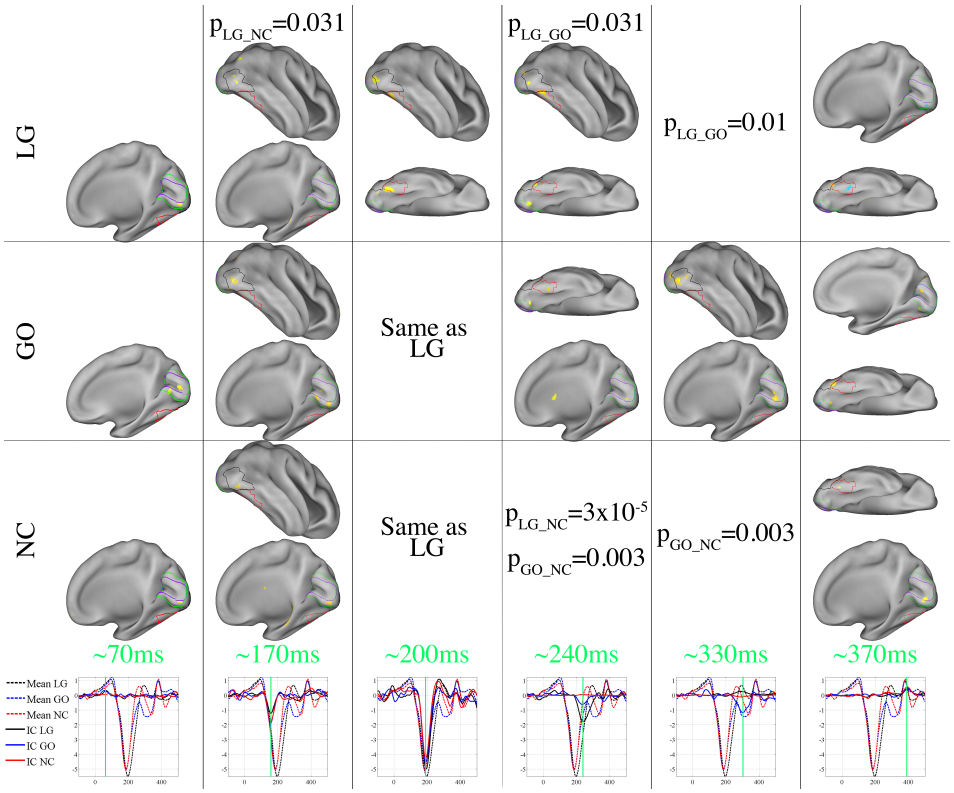


Figure 7.9: Results of the modified JointICA analysis, performed jointly on the data from all three conditions (LG = local and global, GO = global only and NC = no contour). The upper panels show the spatial (fMRI) results from the condition-specific independent components, for (from top to bottom) the LG, GO and NC conditions. For each case, the results are only depicted from those angles that show the major part of the activation (as before, only those parts of the activation are shown that exceed 3 times the standard deviation of all activation values). P-values are only mentioned if they are below 0.05. The bottom panel presents the temporal (ERP) parts of the independent components, with different colors distinguishing between the different conditions. These colors correspond to those used in Figs. 7.6-7.8. Together with the independent components (solid line), also the grand average ERPs for all conditions are plotted (dashed line). Like in Figs. 7.6-7.8, also here the components are ordered according to their temporal peak behavior. The empty fMRI sections in panels 4 and 5 correspond to components for which the ERP part is a flat line.

## 7.4 Discussion

To not only identify the brain regions involved in contour integration, but also unravel their temporal interactions, a fully integrated analysis of simultaneously acquired EEG and fMRI data, is needed. In this study, therefore, data acquired during a perceptual grouping experiment, were analyzed with JointICA, a method that has been previously successfully introduced and validated on several datasets [23, 136]. In addition, to specifically investigate the differences between distinct conditions included in the task paradigm, a modified version of the JointICA approach was applied. The results of these studies are also compared to those of a standard correlation analysis.

Our results showed that, although the employed conditions were similar to a certain extent in their temporal activation of involved brain areas, very apparent differences could be found at specific latencies. More specifically, the independent component peaking at latency of 240 $ms$, activating the CoS area, is specific for the LG and GO stimuli, but not for NC. Further, the IC corresponding to the latency of 330 $ms$, shows late activation of the LOC and EVA ROIs, particularly for the GO condition. Finally, late visual activations around 370 $ms$ are specific for GO and NC stimuli, and the LG condition shows negative correspondence.

The modified JointICA allowed us to focus on the similarities and differences across conditions and to perform statistical analyses. An additional benefit of this approach relates to data dimensionality. It has been shown by Mijović et al. (2012) [136] that if the number of subjects, included in the JointICA analysis, is not sufficiently large, the estimated sources will be accurate, but some sources may be joined together into one independent component. This is usually the case when the number of subjects in the study is lower than approximately 25. However, by combining the data from the different conditions in one analysis, as was explained in Eqs. 7.2 and 7.3, the number of available subjects is artificially enhanced to 45 not linearly dependent subjects, therefore making the analysis more robust.

Finally, we compared the performance of the correlation analysis, to JointICA. The results from these two analyses correspond to a certain extent. For example, negative correlation of the EVA ROI and the ERP wave at the latencies of 130 $ms$ and 370 $ms$ for the LG ROI are obtained by both JointICA and the correlation analysis. Further, the results for the GO condition also partly correspond between the two analyses. However, the correlation analysis did not provide any significant correlations for the NC condition.

The reason for this incomplete performance of the correlation analysis may be found in the fact that overlapping of several different activations may highly influence the correlation measure, yielding no significant correspondence. On the other hand, the JointICA analysis, instead of only computing a parameter, aims at disentangling the contributions from different processes into a linear mixture of independent

components. Therefore, JointICA allows that different sources overlap, and is able to separate them into different independent components, yielding more robust and detailed analysis.

## 7.5 Conclusion

The JointICA method, validated and explored in chapter 6 is used in this chapter for the novel perceptional grouping study. The results from JointICA analysis are compared to the results from the correlation analysis. It is shown that JointICA results are more complete and easier to interpret than the the correlation results. Also a modification of JointICA for simultaneous analysis of different paradigms is proposed. The results from this modified analysis agree with the results obtained by regular JointICA. However, the new method is able to emphasize the similarities and differences in the joint EEG-fMRI activations, belonging to different task conditions.

# Chapter 8

# Conclusion and Future Work

*This chapter provides an overview of the work presented in this thesis. Additionally, it states the remaining questions, and proposes approaches towards solutions of these problems.*

## 8.1 EMD-based source separation techniques

In Chapter 2, we demonstrated the application of empirical mode decomposition (EMD) as a tool for exploring the sources of single-channel signals. In this thesis, EMD is used to map the single-channel data into a two-dimensional space. This is used as a preprocessing tool within a novel single-channel BSS method EEMD-ICA, introduced in Chapter 3. The performance of the algorithm in extracting sources from EEG signals is shown, as well as in removal of the ECG artifact from the EMG signals. Thereafter, the extension of the method to 2-channel signals is proposed.

It has been shown that the EEMD as a preprocessing tool outperforms wavelets, due to its data-driven nature. The comparison is provided on a number of simulation and several real-life physiological signals. Also, the nature of the EEMD algorithm allows for better extraction of the oscillatory-type signals, and therefore is superior in this case, compared to wavelets.

The performance of the 2-channel EMD-ICA approach is shown on the EEG data. It is shown that this approach can also solved an under-determined ICA problem, when only two channels are available. Also, it is shown that this extended method outperforms the single-channel method in case that 2 channels are available. Also the potential of using this method for cleaning the ECG artifact from the EMG channels is shown.

This approach may be beneficial for the neonatal EEG processing, in which case, due to small dimensions of the neonatal head, only a small number of EEG-channels are available. In most cases, this number goes up to 8 channels. However, in the polysomnographic (PSG) recordings, usually up to only two EEG electrodes are used. Additionally, nowadays there is a tendency towards developing new devices with wireless transmission of the physiological data. In this case, in order to avoid the overload of the wireless links, only a few channels of the PSG recordings is available. In these cases, such an approach can also be beneficial.

As already mentioned in Chapter 2, the multichannel EMD (multivariate EMD - MEMD) has been developed by Rehman and Mandić [160]. This approach separates the multichannel signal into its oscillatory modes (IMFs) such that the common modes are extracted to the corresponding IMFs. In that group, some work has already been done with applying this approach to the EEG data [162]. This method can be used for a number of useful data-extraction applications from the EEG data. For example, De Vos et al. [51] used the combination of wavelets and parallel factor analysis (PARAFAC) to detect the seizure onset zone from the EEG recordings. In the case of oscillatory seizures, multivariate EMD may have an advantage compared to wavelets as used in combination with PARAFAC.

Additionally, the MEMD algorithm has been shown to exhibit interesting properties that can be used to avoid the mode-mixing problem in EMD. As mentioned in Chapters 2 and 3, the extraction of the IMFs is improved by introducing ensemble EMD (EEMD [191]). However, the mode-mixing problem still remains. Recently, Rehman and Mandić showed that this problem may be solved by using, so-called, Noise Assisted MEMD (NA-MEMD) [161]. The problem appears to be solved by artificially generating a number of white Gaussian noise channels, and feeding these channels as inputs to MEMD, together with the original signal. For more information about the method, the reader is referred to [161]. This method can potentially be used as an improvement of EEMD, as the first step of the algorithms proposed in Chapter 3.

We showed the potential of PARAFAC as a brain computer interface (BCI) tool in [186]. In that work, the automatic clustering of the checkerboard stimuli presented in left or right visual field was shown with the classification accuracy of above 90 percent for the data recorded outside the scanner magnetic field and around 80 percent for the data recorded simultaneously with fMRI. It is also shown that the data between all four quadrants (upper-left, upper-right, down-left and down-right) can be distinguished. The classification is significantly better than the one obtained on the raw data (p-alues below 0.05).

The EMD and bivariate EMD have also shown potential to be used as BCI tools in [167] and [119] respectively. In [119], the gamma-band synchronization is proposed as a selective attention features, both in energy and phase domains. This is one extra reason to exploit the joint performance of the EMD (or MEMD) and

PARAFAC.

Since MEMD by definition extracts joint oscillatory sources from multichannel signals, its application may be useful in the alpha activity removal from the EEG recordings. It is well known that the alpha-band spontaneous activity ($8-12Hz$) strongly overlaps in the frequency spectrum with the event-related potentials (ERPs), and that it is detectable among several channels. Due to this effect, the single-trial ERP estimates can be highly corrupted, and such a method might be able to produce better signal quality for the EEG-fMRI integration applications.

Also, the removal of the ballistocardiogram (BCG) artifacts from the EEG data simultaneously recorded with the fMRI represents a big challenge in the EEG-fMRI research comunity. Several algorithms for this purpose have already been proposed (the overview is given in Chapter 4 [185]). However, although the signal quality is fair, the residual artifacts are still large, making the EEG data recorded outside the scanner room way more reliable (see for example Chapter 6, [136]). This artifact is also oscillatory in nature, and the application of MEMD or combination of MEMD with PARAFAC may be useful for its removal.

The major drawback of these approaches is the computational complexity of the EMD algorithm. Several groups have focused their research towards a solution of this problem. For the single-channel case, Lee et al. [108] developed a hardware implementation of EMD using digital signal processors (DSP) and field programmable gate arrays (FPGA). They also demonstrated the performance of their implementation for on-line ECG denoising systems.

## 8.2 BSS techniques for multimodal EEG-fMRI fusion

The introduction to BSS techniques for EEG-fMRI is given in Chapter 4. The application of these methods to the detection and grouping task (presented in Chapter 5) are shown in Chapters 6 and 7. It was shown that the JointICA algorithm can be successfully used for unravelling the time-space characteristics of brain-activity recorded by EEG and fMRI. Indirectly, that is a proof of the assumption that the EEG and fMRI task-related responses are mutually correlated across subjects, as proposed e.g. in [11].

In Chapter 6 an explanation and discussion is provided on how and why the algorithm performs well, and what are the necessary conditions for applying it to the acquired EEG-fMRI dataset. Further, it is discussed what one can expect if the dimensionality of the acquired data is not large enough, and how the dataset quality influences the JointICA result. The superiority of the Infomax [15] algorithm to the JADE [31] is validated and explained. Also, it is shown that the number of participants in such an analysis should be as high as possible. However, even if

the number of subjects is insufficient for a *full decomposition*, a physiologically meaningful decomposition can still be obtained.

After this extensive validation, we used the technique in an optimal way to derive novel neuroscientific conclusions in the study of perceptual grouping. We also proposed a modification in order to statistically compare results from EEG-fMRI recordings during different task-conditions. The results of this study are shown in Chapter 7, and a discussion is provided.

Several JointICA questions are still left unanswered, and need further exploration. For example, it is interesting to find an automatic way to select the significant components (this can be done by, e.g. explained variance of the particular component in the particular brain areas). Also, so far, only one electrode is used in the JointICA setup. In this way the spatial information coming from the EEG modality is completely lost. Therefore, using more electrodes in the JointICA setup would be beneficial. In an analogue way, the time information coming from the fMRI modality is also lost, and it would be interesting to incorporate this in the JointICA framework. Finally, the use of JointICA-like methods for single-trial EEG-fMRI fusion may bring additional improvements in the neuroscience signal-processing research.

## 8.3 Future work in the single-trial EEG-fMRI area

The work on EEG-fMRI integration presented in this thesis is mostly directed towards average EEG or fMRI responses. However, as mentioned in Chapter 4, future work will also be concentrated on the investigation of single-trial EEG-fMRI activations. Highly cited papers [55, 67] show that single-trial variations related to physiological processes can be identified in EEG and fMRI, and confirm that integrated EEG-fMRI on a single-trial basis is conceptually possible. However, there is no consensus if single-trial variations as a response to identical stimuli can be reliably studied with current signal processing techniques. Therefore, it is important to focus on improving signal processing concepts to identify single-trial variations and validate them by correlating it with variations from another modality.

In order to improve the quality of the single-trial estimates, it is necesary to remove as much as possible non task-related activations from the fMRI and EEG data. Some ideas for improving the quality of the single-trial ERP estimates are stated in Section 8.1. Nowadays, fMRI analysis is mainly based on assessing the statistical significance of a trigger-based model across subjects. However, in the cases of single trials, statistical models cannot be used. This calls for new techniques to investigate the single-trial variations. So far, little has been done to optimize the

quality of the single-trial fMRI data. There is, however, an indication that BSS techniques may be exploited for this purpose.

Most of the currently available BSS algorithms for the fMRI processing are mostly used fully blindly, without incorporating any of the available prior knowledge during the source extraction. Some semi-blind approaches for the processing of the fMRI data are reported, which incorporate stimulus timing constraints into the BSS techniques [25]. Although they showed to outperform standard BSS techniques in extracting task-related activation maps, they are not able to extract spontaneous brain activity, since no prior information about the time-course is available in this case. Also, the BSS approaches to processing of the fMRI recordings are mostly either spatial or temporal, although the fMRI information of interest is embedded in both domains.

It is crucial to extract well the spontaneous fMRI activity to achieve better quality of the single-trial fMRI maps. An additional importance of extracting these spontaneous fluctuations is in the study of behavioural responses. Several studies indicate that the fluctuations in single trial estimates (together with the overlapping spontaneous activity) are responsible for the changes in human behavioural responses. It can make our responses faster or slower, it can make that sometimes we see the stimulus, and sometimes not. However, it is not fully explored to which extent these changes are coupled to intrinsic single-trial variations and what is the influence of the overlapping spontaneous brain activity. Currently, the correlation-based methods (seeding approaches) are used to extract this spontaneous activity from resting states. However the extraction of these maps is more difficult in case where task-related activations are also present for several reasons. Therefore, the aim of future research would be to first separate both the single-trial fluctuations and the spontaneous brain activity from each other, as well as from other brain fluctuations which are not of interest.

As already mentioned, this decoupling of spontaneous activity and single-trial BOLD estimates is additionally important for the coupling of fMRI and electrical (EEG) brain activity. There are certain indications from the literature that the ongoing spontaneous brain activity is coupled with power oscillations in the electrical brain activity [170, 171, 13], and that the single-trial BOLD activity is related to the single-trial changes in ERP [117]. This hypothesis is not yet fully explored, and the findings from such a study may lead to a new focus to the field of EEG-fMRI research.

According to what is stated in this section, several objectives for further research can be proposed:

1. Developing new BSS techniques to optimize the extraction of fMRI sources in both the spatial and temporal domain simultaneously. Currently, there are numerous ICA algorithms with different assumptions on the extracted

independent components (e.g., components are sparse or fluctuating). The techniques should be introduced to best match the behaviour of the fMRI spatio-temporal maps, and allow introducing constraints as prior knowledge. These constraints are to be extracted from the data itself. For example, during this spatio-temporal source separation, it is possible to allow the temporal ICA algorithm to use prior information obtained from the spatial separation, and vice versa.

2. These techniques can consequently be used to extract the spontaneous activity maps from the recordings where the subjects perform a particular task and compare the results with or without additional constraints obtained from the well-known patterns of ongoing brain activity. These patterns can also be obtained during the recording of the resting-state maps, when only the spontaneous activity maps are present.

3. These estimates can then be used to optimize the quality of single-trial estimates, and decouple the single-trial and spontaneous brain activity.

4. It is important to provide answers to how single-trial estimates are connected to subjects' responses (behaviour), and to which extent these behavioural responses are caused by the spontaneous activity.

5. Unravelling the basis of the fMRI-EEG coupling. This also means providing the answer to how much overlap is there between spontaneous brain activity and single-trial activations recorded with fMRI, on the one hand, and the electrical power oscillations in different bands and the single trial ERP estimates, on the other hand. Also, it is important to find which features recorded with fMRI and EEG do not correspond to each other (which are specific to only one modality). This can be done for example by comparing (correlating) both modalities by behavioural features.

6. Finally, with all the previously stated questions being answered, one can compare the possible improvements obtained with different methods and develop new BSS techniques for single-trial EEG-fMRI coupling.

In the personal opinion of the author, it is important to focus on these basic, yet not well-established concepts in current neuroscience research. The understanding of these relations is crucial and will yield new insight into basic brain functioning and connectivity. The goal is also that these techniques allow us understanding more about spontaneous activity during performing a task. On a long term, understanding how the fluctuations in spontaneous activity influence human behaviour will open the door to possible applications for studying neuro-feedback.

From the algorithm development point of view, besides the continuation of the work on matrix BSS techniques, we also aim at exploring tensorial setups for solving a EEG-fMRI fusion BSS problem. The first major challenge here is to map

this multimodal data to be best represented in this mutlidimensional space. One approach is to fit the data meaningfully in only one tensor, similarly as JointICA arranges the data in a single matrix, and then perform the decomposition. Another approach would be to use separate tensors for each modality, and then to solve the "coupled" tensorial problem. Several "coupled" cannonical decomposition approaches, which might serve as ideas to solve this multimodal problem are already proposed in [193, 1]. Finally, the second challenge is then how to perform a tensor decomposition, such that the newly obtained mathematical components are physiologically interpretable.

# Bibliography


[1] E. Acar, T. Kolda, and D. Dunlavy. All-at-once optimization for coupled matrix and tensor factorizations. In *In Proceedings of Mining and Learning with Graphs*, 2011.

[2] P. Allen, O. Josephs, and R. Turner. A method for removing imaging artifact from continuous EEG recorded during functional MRI. *NeuroImage*, 12:230–239, 2000.

[3] P. Allen, G. Polizzi, K. Krakow, D. Fish, and L. Lemieux. Identification of EEG events in the MR scanner: the problem of pulse artifact and a method for its subtraction. *NeuroImage*, 8:229–239, 1998.

[4] M. Altaf, T. Gautama, T. Tanaka, and D. Mandić. Rotation-invariant complex empirical mode decomposition. volume 3, pages 1009–1012, 2007.

[5] C. F. Altmann, H. H. Blthoff, and Z. Kourtzi. Perceptual organization of local elements into global shapes in the human visual cortex. *Current Biology*, 13(4):342–349, 2003.

[6] K. Anami, T. Mori, F. Tanaka, Y. Kawagoe, J. Okamoto, M. Yarita, T. Ohnishi, M. Yumoto, H. Matsuda, and O. Saitoh. Stepping stone sampling for retrieving artifact-free electroencephalogram during functional magnetic resonance imaging. *NeuroImage*, 19:281–295, 2003.

[7] A. Angelucci and P. C. Bressloff. Contribution of feedforward, lateral and feedback connections to the classical receptive field center and extra-classical receptive field surround of primate V1 neurons. *Progress in Brain Research*, 154:93–120, 2006.

[8] A. Angelucci, J. Levitt, E. Walton, J. Hupé, J. Bullier, and J. Lund. Circuits for local and global signal integration in primary visual cortex. *The Journal of Neuroscience*, 22:8633–8646, 2002.

[9] S. Assecondi, K. Vanderperren, N. Novitskiy, J. Ramautar, W. Fias, P. Stiers, S. Sunaert, S. Staelens, S. Van Huffel, and I. Lemahieu. Effect of the static

magnetic field of the MR-scanner on ERPs: evaluation of visual, cognitive and motor potentials. *Clinical Neurophysiology*, 121(5):672–685, 2010.

[10] F. Auger and P. Flandrin. The why and how of time-frequency reassignment. In *Time-Frequency and Time-Scale Analysis, Proceedings of the IEEE-SP International Symposium on*, pages 197–200, October 1994.

[11] A. Bagshaw and T. Warbrick. Single trial variability of EEG and fMRI responses to visual stimuli. *NeuroImage*, 38(2):280–292, 2007.

[12] R. Barr, B. Hopkins, and J. Green. Crying as a sign, a symptom and a signal. *Mac Keith Press.*, pages 143–146, 2000.

[13] R. Becker, M. Reinacher, F. Freyer, A. Villringer, and P. Ritter. How ongoing neuronal oscillations account for variability of evoked fMRI responses. *Journal of Neuroscience*, 32(30):11016–11027, 2011.

[14] A. Bell and T. Sejnowski. An information-maximization approach to blind separation and blind deconvolution. *Neural Computation*, 7(6):1129–1159, 1995.

[15] A. Bell and T. Sejnowski. An Information-Maximization approach to blind separation and blind deconvolution. *Neural Computation*, 7(6):1129–1159, 1995.

[16] C. Bellieni, R. Sisto, B. Codelli, and G. Buonocore. Cry features reflect pain intensity in term newborns: an alarm threshold. *Pediatric Research*, 55:142–146, 2004.

[17] C. Bénar, C. Grova, E. Kobayashi, A. Bagshaw, Y. Aghakhani, F. Dubeau, and J. Gotman. EEG-fMRI of epileptic spikes: Concordance with EEG source localization and intracranial EEG. *NeuroImage*, 30(4):1161–1170, 2006.

[18] C. Bénar, D. Schön, S. Grimault, B. Nazarian, B. Burle, M. Roth, J. Badier, P. Marquis, C. Liegeois-Chauvel, and J. Anton. Single-trial analysis of oddball event-related potentials in simultaneous EEG-fMRI. *Human Brain Mapping*, 28:602–613, 2007.

[19] M. Blanco-Velasco, B. Weng, and K. Barner. Ecg signal denoising and baseline wander correction based on the empirical mode decomposition. *Computers in Biology and Medicine*, 38:1–13, 2008.

[20] C. Bledowski, D. Prvulovic, K. Hoechstetter, M. Scherg, M. Wibral, R. Goebel, and D. Linden. Localizing P300 generators in visual target and distractor processing: a combined event-related potential and functional magnetic resonance imaging study. *The Journal of Neuroscience*, 24:9353–9360, 2004.

[21] V. Calhoun and T. Adali. Unmixing fMRI with independent component analysis. *IEEE Engineering in Medicine and Biology Magazine*, 25:79–90, 2006.

[22] V. Calhoun, T. Adali, L. Hansen, J. Larsen, and J. Pekar. ICA of Functional fMRI data: An Overview. In *Proceedings of the International Workshop on Independent Component Analysis and Blind Signal Separation*, pages 281–288, Nara, Japan, 2003.

[23] V. Calhoun, T. Adali, G. Pearlson, and K. Kiehl. Neuronal chronometry of target detection: fusion of hemodynamic and event-related potential data. *NeuroImage*, 30:544–553, 2006.

[24] V. Calhoun, T. Adali, G. Pearlson, and J. Pekar. A Method for Making Group Inferences from Functional MRI Data Using Independent Component Analysis. *Human Brain Mapping*, 14:140–151, 2001.

[25] V. Calhoun, T. Adali, M. Stevens, K. Kiehl, and J. Pekar. Semi-blind ICA of fMRI: A method for utilizing hypothesis-derived time courses in a spatial ica analysis. *NeuroImage*, 25:527–538, 2005.

[26] V. Calhoun, J. Liu, and T. Adali. A review of group ICA for fMRI data and ICA for joint inference of imaging, genetic, and ERP data. *NeuroImage*, 45(1 Suppl):163–172, 2009.

[27] V. Calhoun, J. Liu, and T. A. T. A review of group ICA for fMRI data and ICA for joint inference of imaging, genetic, and ERP data. *Neuroimage*, 45(1):163–172, 2009.

[28] V. Calhoun, L. Wu, K. Kiehl, T. Eichele, and G. Pearlson. Aberrant processing of deviant stimuli in schizophrenia revealed by fusion of fMRI and EEG data. *Acta Neuropsychiatrica*, 22(3):127–138, 2010.

[29] J. Cardoso. Infomax and maximum likelihood for source separation. *IEEE Letters on Signal Processing*, 4:112–114, 1997.

[30] J. Cardoso and A. Souloumiac. Blind beamforming for non-Gaussian signals. *IEE Proceedings-F*, 140(6):362–370, 1993.

[31] J. Cardoso and A. Souloumiac. Blind beamforming for non gaussian signals. *Radar and Signal Processing, IEE Proceedings F*, 140(6):362–370, 1993.

[32] V. Clark, S. Fan, and S. Hillyard. Identification of early visual evoked potential generators by retinotopic and topographic analyses. *Human Brain Mapping*, 2(3):170–187, 1995.

[33] M. Cohen, R. Goldman, and J. Engel Jr. Simultaneous EEG and fMRI made easy. In *Proceedings of the seventh international conference on functional mapping of the human brain*, Brighton, England, 2001.

[34] P. Comon. Independent component analysis - a new concept? *Signal Processing*, 36:287–314, 1994.

[35] N. Correa, T. Adali, and V. Calhoun. Performance of Blind Source Separation Algorithms for fMRI using a Group ICA Method. *Magnetic Resonance Imaging*, 25(5):684–694, 2007.

[36] N. Correa, Y. Li, T. Adali, and V. Calhoun. Canonical Correlation Analysis for Feature-Based Fusion of Biomedical Imaging Modalities and Its Application to Detection of Associative Networks in Schizophrenia. *IEEE Journal of Selected Topics in Signal Processing*, 2(6):998–1007, 2008.

[37] N. Correa, Y. Li, T. Adali, and V. Calhoun. Canonical Correlation Analysis for Data Fusion and Group Inference. *IEEE Signal Processing Magazine*, 27(4):39–50, 2010.

[38] K. Coughlin and K. Tung. 11-year solar cycle in the stratosphere extracted by the empirical mode decomposition method. *Advances in Space Research*, 32:323–329, 2004.

[39] M. Czisch, T. Wetter, C. Kaufmann, T. Pollmacher, F. Holsboer, and D. Auer. Altered processing of acoustic stimuli during sleep: reduced auditory activation and visual deactivation detected by a combined fMRI/EEG study. *NeuroImage*, 16:251–258, 2002.

[40] I. Daubechies. *Ten Lectures on Wavelets*. SIAM, Philadelphia, 1992.

[41] I. Daubechies, J. Lu, and H. Wu. Synchrosqueezed wavelet transforms: An empirical mode decomposition-like tool. *Applied and Computational Harmonic Analysis*, 30:246–261, 2011.

[42] I. Daubechies, E. Roussos, S. Takerkart, S. Benharrosh, C. Golden, K. D'Ardenne, W. Richter, J. Cohen, and J. Haxby. Independent component analysis for brain fMRI does not select for independence. *Proceedings of the National Academy of Sciences of the United States of America*, 106(26):10415–10422, 2009.

[43] J. Daunizeau, C. Grova, G. Marrelec, J. Mattout, S. Jbabdi, M. Pélégrini-Issac, J. Lina, and H. Benali. Symmetrical event-related eeg/fmri information fusion in a variational bayesian framework. *NeuroImage*, 36:69–87, 2007.

[44] M. E. Davies and C. J. James. Source separation using single channel ICA. *Signal Processing*, 87(8):1819 – 1832, 2007. Independent Component Analysis and Blind Source Separation.

[45] W. De Clercq, A. Vergult, B. Vanrumste, W. Van Paesschen, and S. Van Huffel. Canonical Correlation Analysis applied to remove muscle artifacts from the electroencephalogram. *IEEE Transactions on Biomedical Engineering*, 53(12):2583–2587, 2006.

[46] L. De Lathauwer, J. Castaing, and J.-F. Cardoso. Fourth-order cumulant based underdetermined independent component analysis. *IEEE Transactions on Signal Processing*, 55:2965–2973, 2007.

[47] L. De Lathauwer, B. De Moor, and J. Vandewalle. A multilinear singular value decomposition. *SIAM journal on Matrix Analysis and Applications*, 21(4):1253–1378, 2000.

[48] F. De Martino, A. de Borst, G. Valente, R. Goebel, and E. Formisano. Predicting EEG single trial responses with simultaneous fMRI and relevance vector machine regression. *NeuroImage*, 56(2):826–836, 2011.

[49] M. De Vos, S. Riès, K. Vanderperren, B. Vanrumste, F.-X. Alario, S. Van Huffel, and B. Burle. Removal of muscle artifacts from EEG recordings of spoken language production. *Neuroinformatics*, 8(2):135–150, 2010.

[50] M. De Vos, J. Thorne, G. Yovel, and S. Debener. Let's face it, from trial to trieal: Comparing different procedures for n170 single trial estimation, submitted.

[51] M. De Vos, A. Vergult, L. De Lathauwer, W. De Clercq, S. Van Huffel, P. Dupont, A. Palmini, and W. Van Paesschen. Canonical decomposition of ictal scalp EEG reliably detects the seizure onset zone. *NeuroImage*, 37(3):844–854, 2007.

[52] S. Debener and M. De Vos. The benefits of simultaneous EEG-fMRI for EEG analysis. *Clinical Neurophysiology*, 122(2):217–218, 2011.

[53] S. Debener, A. Strobel, B. Sorger, J. Peters, C. Kranczioch, A. Engel, and R. Goebel. Improved quality of auditory event-related potentials recorded simultaneously with 3 T fMRI: removal of the ballistocardiogram artifact. *NeuroImage*, 34:587–597, 2007.

[54] S. Debener, M. Ullsperger, M. Siegel, and A. Engel. Single-trial EEG-fMRI reveals the dynamics of cognitive function. *Trends in Cognitive Sciences*, 10(12):558–563, 2006.

[55] S. Debener, M. Ullsperger, M. Siegel, K. Fiehler, D. von Cramon, and A. Engel. Trial-by-trial coupling of concurrent electroencephalogram and functional magnetic resonance imaging identifies the dynamics of performance monitoring. *Journal of Neuroscience*, 25(50):11730–11737, 2005.

[56] W. Deburchgraeve, P. Cherian, M. De Vos, R. Swarte, J. Blok, G. Visser, P. Govaert, and S. Van Huffel. Neonatal seizure localization using PARAFAC decomposition. *Clinical Neurophysiology*, 120:1787–1796, 2009.

[57] W. Deburchgraeve, P. J. Cherian, M. De Vos, R. M. Swarte, J. H. Blok, G. H. Visser, P. Govaert, and S. Van Huffel. Automated neonatal seizure detection mimicking a human observer reading EEG. *Clinical Neurophysiology*, 119(11):2447 – 2454, 2008.

[58] A. Delorme and S. Makeig. EEGLAB: an open source toolbox for analysis of single-trial EEG dynamics including independent component analysis. *Journal of Neuroscience Methods*, 134:9–21, 2004.

[59] M. Demeyer and B. Machilsen. Creating perceptual grouping displays with GERT. In *Perception, 40; ECVP Abstract Supplement*, page 179, 2011.

[60] M. Dempsey and B. Condon. Thermal injuries associated with MRI. *Clinical Radiology*, 56:457–465, 2001.

[61] F. Di Russo, A. Martínez, and S. Hillyard. Source analysis of event-related cortical activity during visuo-spatial attention. *Cerebral Cortex*, 13(5):486–499, 2003.

[62] F. Di Russo, A. Martinez, M. Sereno, S. Pitzalis, and S. Hillyard. Cortical sources of the early components of the visual evoked potential. *Human Brain Mapping*, 15:95–111, 2002.

[63] F. Di Russo, S. Pitzalis, G. Spitoni, T. Aprile, F. Patria, D. Spinelli, and S. Hillyard. Identification of the neural sources of the pattern-reversal VEP. *NeuroImage*, 24(3):874–886, 2005.

[64] N. Doñamayor, U. Heilbronner, and T. Münte. Unmixing concurrent eeg-fmri with parallel independent component analysis. *International Journal of Psychophysiology*, 67(3):222–234, 2008.

[65] D. Duffy. The application of hilbert-huang transforms to meteorological datasets. *Journal of Atmospheric and Oceanic Technology*, 21:599–611, 2004.

[66] C. Eckart and G. Young. The approximation of one matrix by another of lower rank. *Psychometrika*, 1:211–218, 1936.

[67] T. Eichele, V. Calhoun, M. Moosmann, K. Specht, M. Jongsmae, R. Q. Quiroga, H. Nordby, and K. Hugdahl. Unmixing concurrent EEG-fMRI with parallel independent component analysis. *International Journal of Psychophysiology*, 67(3):222–234, 2008.

[68] M. Ellingson, E. Liebenthal, M. Spanaki, T. Prieto, J. Binder, and K. Ropella. Ballistocardiogram artifact reduction in the simultaneous acquisition of auditory ERPS and fMRI. *NeuroImage*, 22:1534–1542, 2004.

[69] F. Esposito, E. Formisano, E. Seifritz, R. Goebel, R. Morrone, G. Tedeschi, and F. Di Salle. Spatial independent component analysis of functional mri time-series: To what extent do results depend on the algorithm used?

[70] A. Fachini, C. Belineli, C. Marchettini, F. Pulselli, and E. Tiezzi. Relating pain intensity of newborns to onset of non-linear phenomena in cry recordings. *Phys Lett*, 338:332–337, 2005.

[71] J. Felblinger, J. Slotboom, R. Kreis, B. Jung, and C. Boesch. Restoration of electrophysiological signals distorted by inductive effects of magnetic field gradients during mr sequences. *Magnetic Resonance in Medicine*, 41:715–721, 1999.

[72] D. J. Field, A. Hayes, and R. F. Hess. Contour integration by the human visual system: Evidence for a local "association field". *Vision Research*, 33:173–193, 1993.

[73] B. Fisch. The source of the EEG. In *Fisch and Spelhmann's EEG Primer*, chapter 1, pages 3–17. Elsevier, third edition, 1999.

[74] D. Fitzpatrick. The functional organization of local circuits in visual cortex: Insights from the study of tree shrew striate cortex. *Cerebral Cortex*, 6:329–341, 1996.

[75] P. Flandrin and P. Goncalves. Empirical Mode Decomposition as data-driven Wavelet-like expansion. *Int. J. of Wavel., Multires. and Inf. Proc.*, 2(4):477–496, 2004.

[76] M. Fox and M. Raichle. Coherent spontaneous activity accounts for trial-to-trial variability in human evoked brain responses. *Nature Reviews in Neuroscience*, 8:700–711, 2007.

[77] M. Fox, A. Snyder, J. Vincent, and M. Raichle. Intrinsic fluctuations within cortical systems account for intertrial variability in human behavior. *Neuron*, 56:171–184, 2007.

[78] M. Fox, A. Snyder, J. Zacks, and M. Raichle. Coherent spontaneous activity accounts for trial-to-trial variability in human evoked brain responses. *Nature Neuroscience*, 9:23–25, 2005.

[79] A. Franco, J. Ling, A. Caprihan, V. Calhoun, R. Jung, G. Heileman, and A. Mayer. Multimodal and Multi-Tissue Measures of Connectivity Revealed by Joint Independent Component Analysis. *IEEE Journal of Selected Topics in Signal Processing*, 2(6):986–997, 2008.

[80] O. Friman. *Adaptive Analysis of Functional MRI data*. PhD thesis, Department of Biomedical Engineering, Linköping University (Sweden), 2003.

[81] K. Friston, J. Ashburner, S. Kiebel, T. Nichols, and W. Penny. *Statistical Parametric Mapping: The Analysis of Functional Brain Images*. Academic Press, 2007.

[82] R. Goldman, J. Stern, J. Engel, and M. Cohen. Acquiring simultaneous EEG and functional MRI. *Clinical Neurophysiology*, 111:1974–1980, 2000.

[83] R. Goldman, J. Stern, J. Engel, and M. Cohen. Simultaneous EEG and FMRI of the alpha rhythm. *NeuroReport*, 13:2487–2492, 2002.

[84] R. F. Hess, W. H. Beaudot, and K. T. Mullen. Dynamics of contour integration. *Vision Research*, 41:1023–1037, 2001.

[85] R. F. Hess and D. J. Field. Integration of contours: New insights. *Trends in Cognitive Sciences*, 3:480–486, 1999.

[86] J. Himberg and A. Hyvärinen. Icasso: software for investigating the reliability of ica estimates by clustering and visualization.

[87] J. Himberg, A. Hyvärinen, and F. Esposito. . validating the independent components of neuroimaging time-series via clustering and visualization.

[88] `http://www.radiopaedia.org/`, August 2011.

[89] N. E. Huang, S. S. Shen, S. R. Long, M. L. Wu, H. Shih, Q. Zheng, N. Yen, C. Tung, and H. Liu. The Empirical Mode Decomposition and the Hilbert spectrum for nonlinear and non-stationary time series analysis. *Proc. of Royal Soc. London*, 454A(1971):903–995, 1998.

[90] A. Hyvärinen. New approximations of differential entropy for independent component analysis and projection pursuit.

[91] A. Hyvärinen, J. Karhunen, and E. Oja. *Independent component analysis*. Wiley and Sons, 2001.

[92] A. Hyvarinen and E. Oja. Independent Component Analysis: algorithms and applications. *Neural Networks*, 13(4-5):411 – 430, 2000.

[93] J. Ives, S. Warach, F. Schmitt, R. Edelman, and D. Schomer. Monitoring the patient's EEG during echo planar MRI. *Electroencephalography and Clinical Neurophysiology*, 87:417–420, 1993.

[94] H. Jasper. The Ten-Twenty Electrode System of the International Federation. *Electroencephalography and Clinical Neurophysiology*, 10(2):371–375, 1958.

[95] P. Jezzard, P. Matthews, and S. Smith. *Functional MRI : An Introduction to Methods*. Oxford University Press, 2002.

[96] C. Joyce, I. Gorodnitsky, and M. Kutas. Automatic removal of eye movement and blink artifacts from EEG data using blind component separation. *Psychophysiology*, 41(2):313–325, 2004.

[97] T. Jung, S. Makeig, C. Humphries, T. Lee, M. McKeown, V. Iragui, and T. Sejnowski. Removing electroencephalographic artifacts by blind source separation. *Psychophysiology*, 37:163–178, 2000.

[98] M. Kao, A. Mandal, N. Lazar, and J. Stufken. Multi-objective optimal experimental designs for event-related fmri studies. *NeuroImage*, 44:849–856, 2009.

[99] S. Karch, R. Feuerecker, G. Leicht, T. Meindl, I. Hantschk, V. Kirsch, M. Ertl, J. Lutz, O. Pogarell, and C. Mulert. Separating distinct aspects of the voluntary selection between response alternatives: N2- and P3-related BOLD responses. *NeuroImage*, 51:356–364, 2010.

[100] K. Koffka. *Principles of Gestalt psychology.* Routledge & Kegan Paul, Ltd., 1935.

[101] T. Kolda and B. Bader. Tensor decompositions and applications. *SIAM Reviews*, 51:455–500, 2009.

[102] Z. Kourtzi, A. Tolias, C. Altmann, M. Augath, and N. Logothetis. Integration of local features into global shapes: Monkey and human fMRI studies. *Neuron*, 37(2):333–346, 2003.

[103] I. Kovács and B. Julesz. A closed curve is much more than an incomplete one: Effect of closure in figure-ground segmentation. *Proceedings of the National Academy of Sciences of the United States of America*, 90:7495–7497, 1993.

[104] K. Krakow, D. Messina, L. Lemieux, J. Duncan, and D. Fish. Functional MRI activation of individual interictal epileptiform spikes. *NeuroImage*, 13:502–505, 2001.

[105] L. LaGasse, A. Neal, and B. Lester. Assessment of infant cry: acoustic cry analysis and parental perception. *Ment Retard Dev Disabil Res Rev.*, 11:83–93, 2005.

[106] H. Laufs, J. Holt, R. Elfont, M. Krams, J. Paul, K. Krakow, and A. Kleinschmidt. Where the bold signal goes when alpha eeg leaves. *NeuroImage*, 31:1408–1418, 2006.

[107] H. Laufs, A. Kleinschmidt, A. Beyerle, E. Eger, A. Salek-Haddadi, C. Preibisch, and K. Krakow. EEG-correlated fMRI of human alpha activity. *NeuroImage*, 19:1463–1476, 2003.

[108] M. Lee, K. Shyu, P. Lee, C. Huang, and Y. Chiu. Hardware implementation of EMD using DSP and FPGA for online signal processing. *IEEE Transactions on Industrial Electronics*, 58:2473 – 2481, 2011.

[109] X. Lei, C. Qiu, P. Xu, and D. Yao. A parallel framework for simultaneous eeg/fmri analysis: methodology and simulation.

[110] L. Lemieux, K. Krakow, and D. Fish. Comparison of spike-triggered functional MRI BOLD activation and EEG dipole model localization. *NeuroImage*, 14:1097–1104, 2001.

[111] M. Lewicki. A review of methods for spike sorting: the detection and classification of neural action potentials. *Computation in Neural Systems*, 9(4):R53–R78, 1998.

[112] J. Li, L. Zhang, and Q. Zhao. Pattern Classification of Visual Evoked Potentials Based on Parallel Factor Analysis. In R. Wang, E. Shen, and F. Gu, editors, *Advances in Cognitive Neurodynamics ICCN 2007*, pages 571–575. Springer Netherlands, 2008.

[113] W. Li and C. D. Gilbert. Global contour saliency and local colinear interactions. *Journal of Neurophysiology*, 88:2846–2856, 2002.

[114] E. Liebenthal, M. Ellingson, M. Spanaki, T. Prieto, K. Ropella, and J. Binder. Simultaneous ERP and fMRI of the auditory cortex in a passive oddball paradigm. *NeuroImage*, 19:1395–1404, 2003.

[115] J. Lin and A. Zhang. Fault feature separation using Wavelet-ICA filter. *NDT & E International*, 38(6):421 – 427, 2005.

[116] J. Liu and V. Calhoun. Parallel independent component analysis for multimodal analysis: Application to fmri and eeg data. In *Biomedical Imaging: From Nano to Macro, 4th IEEE International Symposium on,*, pages 1028–1031, 2007.

[117] N. Logothetis, J. Pauls, M. Augath, T. Trinath, and A. Oeltermann. Neurophysiological investigation of the basis of the fMRI signal. *Nature*, 412:150–157, 2001.

[118] S. Long. *Applications of HHT in image analysis*, volume 5. (N.E. Huang and S.S.P. Shen, eds.), 2005.

[119] D. Looney, C. Park, Y. Xia, P. Kidmose, M. Ungstrup, and D. P. Mandić. Time-frequency and synchrony analysis of responses to steady-state auditory and musical stimuli from multichannel EEG. In *The 2010 International Joint Conference on Neural Networks (IJCNN)*, pages 1–5, July 2010.

[120] S. Luck. *An introduction to the event-related potential technique*. The MIT Press, Cambridge, MA, 2005.

[121] B. Machilsen, M. Pauwels, and J. Wagemans. The role of vertical mirror symmetry in visual shape detection. *Journal of Vision*, 9(12:11):1–11, 2009.

[122] B. Machilsen and J. Wagemans. Integration of contour and surface information in shape detection. *Vision Research*, 51(1):179–186, 2011.

[123] J. Malmivuo and R. Plonsey. *Bioelectromagnetism: Principles and Applications of Bioelectric and Biomagnetic Fields*. Oxford University Press, New York - Oxford, 1995.

[124] H. Mandelkow, P. Halder, P. Boesiger, and D. Brandeis. Synchronization facilitates removal of MRI artefacts from concurrent EEG recordings and increases usable bandwidth. *NeuroImage*, 32:1120–1126, 2006.

[125] D. Mantini, M. Perrucci, S. Cugini, A. Ferretti, G. Romani, and C. D. Gratta. Complete artifact removal for EEG recorded during continuous fMRI using independent component analysis. *NeuroImage*, 34:598–607, 2007.

[126] A. Martínez, F. D. Russo, L. Anllo-Vento, M. Sereno, B. Buxton, and S. Hillyard. Putting spatial attention on the map: timing and localization of stimulus selection process in striate and extrastriate visual areas. *Vision Research*, 41(10-11):1437–1457, 2001.

[127] E. Martínez-Montes, P. Valdés-Sosa, F. Miwakeichi, R. Goldman, and M. Cohen. Concurrent EEG/fMRI analysis by multiway Partial Least Squares. *NeuroImage*, 22(3):1023–1034, 2004.

[128] B. Mathes, D. Trenner, and M. Fahle. The electrophysiological correlate of contour integration is modulated by task demands. *Brain Research*, 1114(1):98–112, 2006.

[129] S. Mayhew, S. Dirckx, R. Niazy, G. Iannetti, and R. Wise. EEG signatures of auditory activity correlate with simultaneously recorded fMRI responses in humans. *NeuroImage*, 49(1):849–864, 2010.

[130] M. McKeown, T. Sejnowski, A. Makeig, G. Brown, T. Jung, S. Kindermann, A. Bell, and T. Sejnowski. Analysis of fMRI Data by Blind Separation Into Independent Spatial Components. *Human Brain Mapping*, 6:160–188, 1998.

[131] M. Mendez, J. Corthout, S. Van Huffel, M. Matteucci, A. Bianchi, T. Penzel, and S. Cerutti. Automatic screening of obstructive sleep apnea from the ecg based on empirical mode decomposition and wavelet analysis. *Physiological Measurement*, 31:273–289, 2010.

[132] M. Mennes, H. Wouters, B. Vanrumste, L. Lagae, and P. Stiers. Validation of ICA as a tool to remove eye movement artifacts from EEG/ERP. *Psychophysiology*, 47:1142–1150, 2010.

[133] V. Meriläinen. Magnetic resonance imaging with simultaneous electroencephalography recording: safety issues. Master's thesis, Department of electrical and communications engineering, Helsinki University of Technology (Finland), 2003.

[134] B. Mijović, M. De Vos, I. Gligorijević, J. Taelman, and S. Van Huffel. Source separation from single-channel recordings by combining empirical mode decomposition and independent comnponent analysis. *IEEE Transaction on Biomedical Engineering*, 57:2188 – 2196, 2010.

[135] B. Mijović, M. De Vos, I. Gligorijević, and S. Van Huffel. Combining emd with ica for extracting independent sources from single channel and two-channel data. pages 5387 – 5390, 2010.

[136] B. Mijović, M. De Vos, K. Vanderperren, N. Novitskiy, B. Vanrumste, P. Stiers, B. Van den Bergh, J. Wagemans, L. Lagae, S. Sunaert, and S. Van Huffel. The Why and How of JointICA: Results from a Visual Detection Task. *NeuroImage*, 60:1171–1185, 2012.

[137] B. Mijović, M. De Vos, K. Vanderperren, and S. Van Huffel. Improving spatiotemporal characterisation of cognitive processes with data-driven eeg-fmri analysis. *Prilozi, Proceedings of Macedonian Academy of Sciences, accepted for publication.*

[138] B. Mijović, M. Silva, B. Van den Bergh, K. Allegaert, J. Aerts, D. Berckmans, and S. Van Huffel. Assessment of pain expression in infant cry signals using empirical mode decomposition. *Methods of Information in Medicine*, 49:448–452, 2010.

[139] S. Moller and R. Schonweiler. Analysis of infant cries for the early detection of hearing impairment. *Speech Com*, 28:175–193, 1999.

[140] M. Moosmann, T. Eichele, H. Nordby, K. Hugdahl, and V. Calhoun. Joint independent component analysis for simultaneous EEG-fMRI: principle and simulation. *International Journal of Psychophysiology*, 67(3):212–221, 2008.

[141] M. Moosmann, P. Ritter, I. Krastel, A. Brink, S. Thees, F. Blankenburg, B. Taskin, H. Obrig, and A. Villringer. Correlates of alpha rhythm in functional magnetic resonance imaging and near infrared spectroscopy. *NeuroImage*, 20:145–158, 2003.

[142] M. Moosmann, V. Schonfelder, K. Specht, R. Scheeringa, H. Nordby, and K. Hugdahl. Realignment parameter-informed artefact correction for simultaneous EEG-fMRI recordings. *NeuroImage*, 45:1144–1150, 2009.

[143] E. Moulines, J. F. Cardoso, and E. Gassiat. Maximum likelihood for blind separation and deconvolution of noisy signals using mixture models. In *IEEE International Conference on Acoustics, Speech, and Signal Processing, ICASSP-97*, volume 5, pages 3617–3620 vol.5, Apr 1997.

[144] C. Mulert, L. Jäger, R. Schmitt, P. Bussfeld, O. Pogarell, H. Möller, G. Juckel, and U. Hegerla. Integration of fMRI and simultaneous EEG: towards a

comprehensive understanding of localization and time-course of brain activity in target detection. *NeuroImage*, 22:83–94, 2004.

[145] C. Mulert and L. Lemieux. *EEG-fMRI: Psychological Basis, Technique and Applications*. Springer, 2010.

[146] M. NessAiver. *All you really need to know about MRI Physics*. University of Maryland, Baltimore, 1996.

[147] R. Niazy, C. Beckmann, G. Iannetti, J. Brady, and S. Smith. Removal of FMRI environment artifacts from EEG data using optimal basis sets. *NeuroImage*, 28:720–737, 2005.

[148] D. Nishimura. *Principles of Magnetic Resonance Imaging*. Stanford University, 1996.

[149] N. Novitskiy, J. Ramautar, K. Vanderperren, M. De Vos, M. Mennes, B. Mijovic, B. Vanrumste, P. Stiers, B. Van den Bergh, L. Lagae, S. Sunaert, S. Van Huffel, and J. Wagemans. The BOLD correlates of the visual P1 and N1 in single-trial analysis of simultaneous EEG-fMRI recording during a spatial detection task. *NeuroImage*, 54(2):824–835, 2011.

[150] M. Nuwer, G. Comi, R. Emmerson, A. Fuglsang-Frederiksen, J.-M. Gue, H. Hinrichs, A. Ikeda, F. Jose, and C.Luccas. IFCN standards for digital recording of clinical EEG. *Electroencephalography and Clinical Neurophysiology*, 106(3):259–261, 1998.

[151] A. Papoulis. *Probability, Random Variables, and Stochastic Processes*. McGraw-Hill, 3rd edition, 1991.

[152] B. Pearlmutter and L. Parra. Maximum likelihood blind source separation: A context-sensitive generalization of ICA. *Advances in Neural Information Processing Systems*, 9:613–619, 1997.

[153] K. Pearson. On lines and planes of closest fit to systems of points in space. *Philosophical Magazine*, 2:559–572, 1901.

[154] M. W. Pettet. Shape and contour detection. *Vision Research*, 39:551–557, 1999.

[155] M. W. Pettet, S. P. McKee, and N. M. Grzywacz. Constraints on long range interactions mediating contour detection. *Vision Research*, 38:865–879, 1998.

[156] D.-T. Pham, P. Garrat, and C. Jutten. Separation of a mixture of independent sources through a maximum likelihood approach. In *EUSIPCO*, pages 771–774, 1992.

[157] D. Plewes and W. Kucharczyk. The Animated Physics of MRI - Spin Gymnastics. *http://www.sunnybrook.ca/files/RESH_DBP_Spin_gymnastics.pdf*, 2003.

[158] U. Polat, K. Mizobe, M. W. Pettet, T. Kasamatsu, and A. M. Norcia. Collinear stimuli regulate visual responses depending on cell's contrast threshold. *Nature*, 391:580–584, 1998.

[159] N. Rehman and D. Mandić. Empirical mode decomposition for trivariate signals. *IEEE Transactions on Signal Processing*, 58:1069–1068, 2010.

[160] N. Rehman and D. Mandić. Multivariate empirical mode decomposition. *Proceedings of the Royal Society A*, 466:1291–1302, 2010.

[161] N. Rehman and D. Mandić. Filter bank property of multivariate empirical mode decomposition. *IEEE Transactions on Signal Processing*, 59:2421–2426, 2011.

[162] N. Rehman, Y. Xia, and D. Mandić. Application of multivaritate empirical mode decomposition for seizure detection in EEG signals. In *Proceedings of the IEEE Engineering in Medicine and Biology Society, EMBS 2010*, pages 1650–1653, August-September 2010.

[163] G. Rilling, P. Flandrin, P. Goncalves, and J. M. Lilly. Bivariate empirical mode decomposition. *IEEE Signal Processing Letters*, 14:936–939, 2007.

[164] G. Rilling, P.Flandrin, and P. Goncalves. On empirical mode decomposition and its algorithms. In *IEEE-EURASIP Workshop on Nonlinear Signal and Image Processing NSIP03*, Jun 2003.

[165] C. Roy and C. Sherrington. On the regulation of the blood-supply of the brain. *Journal of Physiology*, pages 85–108, 1889.

[166] U. Rutishauser, E. M. Schuman, and A. N. Mamelak. Online detection and sorting of extracellularly recorded action potentials in human medial temporal lobe recordings, in vivo. *Journal of Neuroscience Methods*, 154:204–224, 2006.

[167] T. Rutkowski, A. Cichocki, F. Vialatte, J. Dauwels, and D. Mandić. Time-frequency and synchrony analysis of responses to steady-state auditory and musical stimuli from multichannel EEG. In *Proceedings of Neural Information Processing Systems, NIPS '07*, 2007.

[168] B. Sadeh, I. Podlipsky, A. Zhdanov, and G. Yovel. Event-Related Potential and Functional MRI Measures of Face-Selectivity are Highly Correlated:A Simultaneous ERP-fMRI Investigation. *Human Brain Mapping*, 31(10):1490–1501, 2010.

[169] M. Schabus, T. Dang-Vu, G. Albouy, E. Balteau, M. Boly, J. Carrier, A. Darsaud, C. Degueldre, M. Desseilles, Gais, C. Phillips, G. Rauchs, C. Schnakers, V. Sterpenich, G. Vandewalle, A. Luxen, and P. Maquet. Hemodynamic cerebral correlates of sleep spindles during human non-rapid eye movement sleep. *Proceedings of Natlional Academy of Sciences, USA*, 104:13164–13169, 2007.

[170] R. Scheeringa, P. Fries, K. Petersson, R. Oostenveld, I. Grothe, D. Norris, P. Hagoort, and M. Bastiaansen. Neuronal dynamics underlying high- and low-frequency eeg oscillations contribute independently to the human bold signal. *Neuron*, 69:572–583, 2011.

[171] R. Scheeringa, A. Mazaheri, I. Bojak, D. Norris, and A. Kleinschmidt. Modulation of visually evoked cortical fmri responses by phase of ongoing occipital alpha oscillations. *Journal of Neuroscience*, 31:3813–3820, 2011.

[172] K. E. Schmidt, R. Goebel, S. Löwel, and W. Singer. The perceptual grouping criterion of colinearity is reflected by anisotropies of connections in the primary visual cortex. *European Journal of Neuroscience*, 9:1083–1089, 1997.

[173] M. Seeck, F. Lazeyras, C. Michel, O. Blanke, C. Gericke, J. Ives, J. Delavelle, X. Golay, C. Haenggeli, N. de Tribolet, and T. Landis. Non-invasive epileptic focus localization using EEG-triggered functional MRI and electromagnetic tomography. *Electroencephalography and Clinical Neurophysiology*, 106(6):508–512, 1998.

[174] M. Silva, B. Mijović, B. Van Den Bergh, K. Allegaert, J. Aerts, S. Van Huffel, and D. Berckmans. Decoupling between fundamental frequency and energy envelope of neonate cries. *Early Human Development*, 86:35–40, 2010.

[175] G. Srivastava, S. Crottaz-Herbette, K. Lau, G. Glover, and V. Menon. ICA-based procedures for removing ballistocardiogram artifacts from EEG data acquired in the MRI scanner. *NeuroImage*, 24:50–60, 2005.

[176] J. Taelman, A. Spaepen, and S. Van Huffel. Wavelet-Independent Component Analysis to remove electrocardiography contamination in surface electromyography. In *Proceedings of Engineering in Medicine and Biology Society*, pages 682–685, 2007.

[177] T. Tanaka and D. Mandić. Complex empirical mode decomposition. *IEEE Signal Processing Letters*, 14(2):101–104, 2006.

[178] T. Tanskanen, J. Saarinen, L. Parkkonen, and R. Hari. From local to global: Cortical dynamics of contour integration. *Journal of Vision*, 8(7:15):1–12, 2008.

[179] L. Tong, G. Xu, and T. Kailath. Blind identification and equalization based on second-order statistics: a time domain approach. 40:340 – 349, 1994.

[180] M. Ullsperger and S. Debener. *Simultaneous EEG and fMRI: Recording, Analysis, and Application*. Oxford University Press, New York, 2010.

[181] `http://rcada.ncu.edu.tw/research1_clip_program.html`. Ensembleemd algorithm.

[182] `http://www.cis.hut.fi/projects/ica/fastica/code/dlcode.shtml`. Fastica graphical user interface.

[183] K. Van Dijk, T. Hedden, A. Venkataraman, K. Evans, S. Lazar, and R. Buckner. Intrinsic functional connectivity as a tool for human connectomics: theory, properties, and optimization. *Journal of Neurophysiology*, 103:297–321, 2010.

[184] K. Vanderperren. *Improving data-driven EEG-fMRI analyses for the study of cognitive functioning*. KU Leuven, 2011.

[185] K. Vanderperren, M. De Vos, J. Ramautar, N. Novitskiy, M. Mennes, S. Assecondi, B. Vanrumste, P. Stiers, B. Van den Bergh, J. Wagemans, L. Lagae, S. Sunaert, and S. Van Huffel. Removal of BCG artifacts from EEG recordings inside the MR scanner: a comparison of methodological and validation-related aspects. *NeuroImage*, 50(3):920–934, 2010.

[186] K. Vanderperren, B. Mijović, N. Novitskiy, B. Vanrumste, P. Stiers, B. Van den Bergh, J. Wagemans, L. Lagae, S. Sunaert, S. Van Huffel, and M. De Vos. Single trial ERP reading based on Parallel Factor Analysis. Technical report, submitted.

[187] T. Wager and T. Nichols. Optimization of experimental design in fMRI: a general framework using a genetic algorithm. *NeuroImage*, 18:293–309, 2003.

[188] T. Warbrick, A. Mobascher, J. Brinkmeyer, F. Musso, N. Richter, T. Stoecker, G. Fink, N. Shah, and G. Winterer. Single-trial P3 amplitude and latency informed event-related fMRI models yield different BOLD response patterns to a target detection task. *NeuroImage*, 47:1532–1544, 2009.

[189] M. Wertheimer. Untersuchungen zur Lehre von der Gestalt. *Psychologische Forschung*, 4:301–350, 1923.

[190] P. Wolf. The natural history of crying and other vocalization in early infancy. *Determinants of infant behavior*, pages 81–109, 1969.

[191] Z. Wu and N. E. Huang. Ensemble empirical mode decomposition: a noise-assisted data analysis method. *Advances in Adaptive Data Analysis*, 1(1):1–41, 2009.

[192] L. Xu, G. Pearlson, and V. Calhoun. Joint source based morphometry identifies linked gray and white matter group differences. *NeuroImage*, 44(3):777–789, 2009.

[193] K. Yilmaz, A. Cemgil, and U. Simsekli. Generalized coupled tensor factorization. In *In Proceedings of Neural Information Processing Systems (NIPS2011)*, 2011.

[194] Y. Yu. Neural computation in visual pathway. `http://camelot.mssm.edu/~ygyu/research.html`.

[195] P. Zhou and T. Kuiken. Eliminating cardiac contamination from myoelectric control signals developed by targeted muscle reinnervation. *Physiological Measurement*, 27:1311–1327, 2006.

# List of Publications

## Papers in international journals

1. **B. Mijović**, M. De Vos, K. Vanderperren, N. Novitskiy, B. Vanrumste, P. Stiers, B.R.H. Van den Bergh, J. Wagemans, L. Lagae, S. Sunaert and S. Van Huffel. *The Why and How of JointICA: Results from a Visual Detection Task.* NeuroImage, vol. 60, no. 2, 2012, pp. 1171–1185.

2. **B. Mijović**, M. De Vos, K. Vanderperren, and S. Van Huffel. *Improving spatiotemporal characterisation of cognitive processes with data-driven EEG-fMRI analysis.* Prilozi, Proceedings of Macedonian Academy of Sciences, 2012, to appear.

3. N. Novitskiy, J.R. Ramautar, K. Vanderperren, M. De Vos, M. Mennes, **B. Mijović**, B. Vanrumste, P. Stiers, B.R.H. Van den Bergh, L. Lagae, S. Sunaert, S. Van Huffel and J. Wagemans. *The BOLD correlates of the visual P1 and N1 in single-trial analysis of simultaneous EEG-fMRI recordings during a spatial detection task.* NeuroImage, vol. 54, no. 2, 2011, pp. 824-835.

4. **B. Mijović**, M. De Vos, I. Gligorijević, J. Taelman and S. Van Huffel. *Source Separation from Single-Channel Recordings by Combining Empirical Mode Decomposition and Independent Comnponent Analysis.* IEEE Transaction on Biomedical Engineering, vol. 57, no. 9, 2010, pp. 2188 - 2196.

5. **B. Mijović**, M. Silva, B.R.H. Van den Bergh, K. Allegaert, J.M. Aerts, D. Berckmans and S. Van Huffel. *Assessment of pain expression in infant cry signals using Empirical Mode Decomposition.* Methods of Information in Medicine, vol. 49, no. 5, 2010, pp. 448-452.

6. M. Silva, **B. Mijović**, B.R.H. Van den Bergh, K. Allegaert, J.M. Aerts, S. Van Huffel and D. Berckmans *Decoupling between fundamental frequency and energy envelope of neonate cries.* Early Human Development, vol. 86, no. 1, 2010, pp. 35-40.

7. **B. Mijović**, M.B. Popović and D.B. Popović. *Synergistic control of forearm based on accelerometer data and artificial neural network.* Brazilian Journal of Medical and Biological Research, vol. 41, no. 5, 2008, pp. 389-397.

## Papers submitted to international journals

8. K. Vanderperren, **B. Mijović**, N. Novitskiy, B. Vanrumste, P. Stiers, B.R.H. Van den Bergh, L. Lagae, S. Sunaert, J. Wagemans, S. Van Huffel and M. De Vos. *Single trial ERP reading based on Parallel Factor Analysis.* Psychophysiology, submitted, Oct. 2011

9. I. Gligorijević, J.P. van Dijk, **B. Mijović**, S. Van Huffel, J.H. Blok, M. De Vos. *A computationally efficient approach towards surface EMG decomposition* Medical and Biological Engineering and Computing, submitted, submitted, Nov. 2011.

## Papers in proceedings of international conferences

10. I. Gligorijević, B.T.H.M. Sleutjes, M. De Vos, J.H. Blok, I. Montfoort, **B. Mijović**, M. Signoretto and S. Van Huffel. *Correcting electrode displacement errors in motor unit tracking using high density surface electromyography (HDsEMG).* 7th International Workshop on Biosignal Interpretation (BSI2012), Como, Italy, July 2012.

11. **B. Mijović**, M. De Vos, V. Matić and S. Van Huffel. *Independent Component Analysis as a Preprocessing step for Data Compression of Neonatal EEG.* in Proc. of the 33rd Annual International Conference of the IEEE Engineering in Medicine and Biology Society (IEEE EMBS Boston), Boston, Massachusetts, Aug. 2011, pp. 7316-7319.

12. I. Gligorijević, M. De Vos, J.H. Blok, **B. Mijović**, J.P. van Dijk and S. Van Huffel. *Automated way to obtain motor units? signatures and estimate their firing patterns during voluntary contractions using HD-sEMG.* in Proc. of the 33rd Annual International Conference of the IEEE Engineering in Medicine and Biology Society (IEEE EMBS Boston), Boston, Massachusetts, Aug. 2011, pp. 4090-4093.

13. J. Taelman, **B. Mijović**, S. Devuyst, T. Dutoit and S. Van Huffel. *ECG Artifact Removal from Surface EMG Signals by combining empirical mode decomposition and independent component analysis.* in Proc. of the International Conference on Bio-inspired Systems and Signal Processing, subconference of the 4th International Joint Conference on Biomedical

Engineering Systems and Technologies (BIOSTEC 2011), Rome, Italy, Jan. 2011, pp. 421-424.

14. **B. Mijović**, M. De Vos, I. Gligorijević and S. Van Huffel. *Combining EMD with ICA for Extracting Independent Sources from Single Channel and Two-Channel Data.* in Proc. of the 32rd Annual International Conference of the IEEE Engineering in Medicine and Biology Society (IEEE EMBS Buenos Aires), Buenos Aires, Argentina, Aug. 2010, pp. 5387-5390.

15. K. Vanderperren, M. De Vos, **B. Mijović**, J.R. Ramautar, N. Novitskiy, B. Vanrumste, P. Stiers, B.R.H. Van den Bergh, J. Wagemans, L. Lagae, S. Sunaert and S. Van Huffel. *PARAFAC on ERP data from a visual detection task during simultaneous fMRI acquisition.* Proceedings of the International Biosignal Processing Conference, Berlin, Germany, Jul. 2010, vol. 103, pp. 1-4.

16. **B. Mijović**, M. Silva, B.R.H. Van den Bergh, K. Allegaert, J.M. Aerts, D. Berckmans and S. Van Huffel. *Assessment of pain expression in infant cry signals using Empirical Mode Decomposition.* in Proc. of the 6th International Workshop on Biosignal Interpretation (BSI2009), New Haven, CT, USA, Jun 2009, pp. 128-131.

17. **B. Mijović**, J. Corthout, S. Vandeput, M. Mendez, S. Cerutti and S. Van Huffel. *Detection of Obstructive Sleep Apnea by Empirical Mode Decomposition on Tachogram.* in Proc. of European Congress of the International Federation for Medical and Biomedical Engineering (ECIFMBE), Antwerp, Belgium, Sep. 2008 pp. 247-251.

## Abstracts in proceedings of international conferences

18. **B. Mijović**, M. De Vos, K. Vanderperren, N. Novitskiy, B. Vanrumste, P. Stiers, B.R.H. Van den Bergh, J. Wagemans, L. Lagae, S. Sunaert and S. Van Huffel. *Combined Analysis of Electrophysiological and Hemodynamic Signals.* Proceedings of the $2^{nd}$ International Seminar for Magnetic Resonance Imaging in the Republic of Macedonia, Ohrid, Republic of Macedonia, Jun. 2011, p. 22.

19. V. Matić, **B. Mijović**, S. Van Huffel and M. De Vos. *Sparse Approximation of Neonatal EEG.* Workshop on Signal Processing with Adaptive Sparse Structured Representations - SPARS11, Edinburgh, Scotland, UK, June 2011.

20. **B. Mijović**, M. Silva, G. Naulaers, S. Van Huffel and K. Allegaert. *Empirical mode decomposition to assess the association between coupling in infants cry signals and pain expression quantified by a pain score.* The $3^{rd}$ congress of

the Eurpean Academy of Pediatric societies (EAPS). Copenhagen, Denmark, Oct. 2010.

21. **B. Mijović**, M. De Vos, K. Vanderperren, N. Novitskiy, B. Vanrumste, P. Stiers, B.R.H. Van den Bergh, J. Wagemans, L. Lagae, S. Sunaert and S. Van Huffel. *Influence of the stimulus onset asynchrony for the analysis of fMRI with independent component analysis.* Proceedings of the $16^{th}$ Annual Meeting of the Organization for Human Brain Mapping, Barcelona, Spain, Jun. 2010.

22. L. Lagae, **B. Mijović**, K. Jansen, K. Brown, J. Vervishc, S. Van Huffel and J. Penders. *Wireless multichannel miniaturized EEG in the assessment of childhood epilepsy.* $63^{rd}$ annual meeting of American Epilepsy Society, Boston, MA, USA, Dec. 2009.

23. **B. Mijović**, K. Vanderperren, M. De Vos, J.R. Ramautar, N. Novitskiy, B. Vanrumste, P. Stiers, B.R.H. Van den Bergh, J. Wagemans, L. Lagae, S. Sunaert and S. Van Huffel. *Influence of the stimulus onset asynchrony in fMRI experiment to the independent component analysis results.* Proceedings of the $8^{th}$ Belgian Day on Biomedical Engineering, Brussels, Belgium, Dec. 2009, p. 39.

24. M.B. Popović, D.B. Popović, **B. Mijović**, L. Schwirtlih and S. Jović. *Assessment of arm motion for evidence-based rehabilitation.* Book of Abstracts, Clinical Neurophysiology Simposium, Belgrade, Serbia, Oct. 2008, vol. 120, no. 3, pp. e132 No. 22.

## Papers submitted to international conferences

25. G. Strobbe, J.D. López, P. Van Mierlo, K. Vanderperren, B. **Mijović**, M. De Vos, S. Van Huffel, H. Hallez and S. Vandenberghe. *Comparison of BEM and FDM head modeling in EEG source reconstruction based on free energy.* $18^{th}$ International Conference on Biomagnetism (BIOMAG2012), Paris, France, July 2012.

26. Hunyadi B., **Mijović** B., Tousseyn S., Dupont P., Van Paesschen W., Van Huffel S., De Vos M. *ICA component selection based on sparse activelet reconstruction for fMRI analysis in refractory focal epilepsy.* $2^{nd}$ International Workshop on Pattern Recognition in NeuroImaging (PRNI 2012), London, UK, July 2012.

# Curriculum Vitae

Bogdan Mijović was born in Belgrade, Serbia on February 21, 1983. He received the MSc. degree in Electrical Engineering from the University of Belgrade, Serbia in May 2007. His master thesis "Determination of Synergies During Reaching and Grasping Using Inertial Sensors (Accelerometers)" was performed in BMIT research group, faculty of electrical engineering, Belgrade university, Serbia.

In October 2007, he joined the SISTA research group at the department of electrical engineering (ESAT), KU Leuven, Belgium as a predoctoral student. In March 2008, he started his PhD program with the emphasis on data-driven signal processing techniques with a focus on electroencephalography (EEG) and functional magnetic resonance imaging (fMRI) analyses. As such, he has been involved in the KU Leuven EEG-fMRI IDO project (Interdisciplinary Research Program - 05/010), for which the KU Leuven EEG-fMRI website is created, available through www.esat.kuleuven.be/scd/eegfmri.

**Arenberg Doctoral School of Science, Engineering & Technology**
Faculty of Engineering
Department of Electrical Engineering (ESAT)
SISTA
Kasteelpark Arenberg 10 — 2446, 3001 Heverlee, Belgium




